BRNO UNIVERSITY OF TECHNOLOGY
VYSOKÉ UČENÍ TECHNICKÉ V BRNĚ

CENTRAL EUROPEAN INSTITUTE OF TECHNOLOGY BUT
STŘEDOEVROPSKÝ TECHNOLOGICKÝ INSTITUT VUT

HIGH FREQUENCY ELECTRON SPIN RESONANCE SPECTROSCOPY
SPEKTROSKOPIE VYSOKOFREKVENČNÍ REZONANCE SPINŮ ELEKTRONŮ

DOCTORAL THESIS
DIZERTAČNÍ PRÁCE

AUTHOR Ing. Jakub Hrubý
AUTOR PRÁCE

SUPERVISOR doc. Ing. Petr Neugebauer, Ph.D.
ŠKOLITEL

BRNO 2021

Abstract

Electron spin resonance (ESR) is a non-invasive magnetic-resonance-based spectroscopic technique. It is used in many scientific fields such as biology, chemistry, and physics to investigate systems with unpaired electrons. This doctoral thesis deals with high-frequency electron spin resonance (HF-ESR) spectroscopy and its use on paramagnetic coordination compounds. The first part outlines theoretical basics with literature research in this field and shows the HF-ESR applications. Afterwards, methods used to study systems of interest are presented. Herein, the complementary spectroscopic methods (XPS, RS, UV-VIS, AFM, SEM) are described, and the design of a newly built high-vacuum (HV) sublimation chamber was developed for the preparation of thin films of coordination compounds on surfaces. The next part deals with results obtained by HF-ESR on molecular quantum bits [$Cu(dbm)_2$], single-molecule magnets [CoX_2(dppf)], [Co(4MeO-L)$_2$Cl$_2$], and vision of graphene-based bolometers for detection of this class of compounds is outlined. The results are further discussed, and their implications are summarised in conclusions. Finally, references and the author's outputs make up the final chapters of this work.

Abstrakt

Elektronová spinová rezonance (ESR) je neinvazivní spektroskopická technika založená na magnetické rezonanci. Používá se v mnoha vědních oborech jako biologie, chemie a fyzika pro zkoumání systémů s nepárovými elektrony. Tato dizertační práce se věnuje spektroskopii vysokofrekvenční rezonance spinů elektronů (HF-ESR) a jejímu použití na paramagnetické koordinační sloučeniny. V první části je představen teoretický základ s rešerší literatury v této oblasti a jsou představeny aplikace HF-ESR. Dále jsou představeny metody použité ke studování těchto systémů. Zde jsou popsány doplňující metody (XPS, RS, UV-VIS, AFM, SEM) pro zkoumání vzorků a je představen návrh nové sublimační komory vysokého vakua, která byla sestavena pro tvorbu tenkých vrstech koordinačních sloučenin na površích. Následují výsledky dosažené pomocí HF-ESR na molekulárních kvantových bitech [$Cu(dbm)_2$], jednomolekulárních magnetech [CoX_2(dppf)], [Co(4MeO-L)$_2$Cl$_2$] a je nastíněna vize bolometrů na bázi grafenu pro detekci této třídy sloučenin. Výsledky jsou diskutovány a jejich implikace jsou shrnuty v závěru. Reference a autorské výstupy pak uzavírají celou tuto práci.

Keywords

electron spin resonance, magnetochemistry, single-molecule magnet, quantum bit, spectroscopy, nanotechnology

Klíčová slova

elektronová spinová rezonance, magnetochemie, jednomolekulární magnet, kvantový bit, spektroskopie, nanotechnologie

HRUBÝ, Jakub. *High Frequency Electron Spin Resonance Spectroscopy.* Brno, 2021. 119 s. Doctoral thesis. Brno University of Technology. Central European Institute of Technology BUT. Supervisor: Petr NEUGEBAUER.

I hereby declare that I have written my doctoral thesis topic on the theme of *High Frequency Electron Spin Resonance Spectroscopy* independently, under the guidance of the thesis supervisor, doc. Ing. Petr Neugebauer, Ph.D., and using literature and other sources of information which are all properly quoted in the thesis and detailed in the list of literature at the end of the thesis.

Ing. Jakub Hrubý

First and foremost, special thanks goes to my life partner Terka, family, and friends who supported me all the way.
I acknowledge all colleagues and support staff who helped me to carry out this work. Especially, my home CEITEC MOTES research group and all the groups I cooperated with during my studies, namely group of Prof. van Slageren at the University of Stuttgart, group of Prof. Mannini at the University of Florence, group of Prof. Barbara in Washington D.C., and Dr. Peter Šiffalovič at Slovak Academy of Sciences in Bratislava.
This work has been financially supported: by the Ministry of Education, Youth and Sports of the Czech Republic under the project CEITEC 2020 (LQ1601), CzechNanoLab project LM2018110 funded by MEYS CR, LTAUSA19060 in the INTER-EXCELLENCE Programme, internal grant of Brno University of Technology CEITEC-VUT-J-20-6514, and the EU COST Action CA15128 MOLSPIN.

Ing. Jakub Hrubý

Contents

1. Introduction

The fundamentals of electron spin resonance (ESR), sometimes also called electron paramagnetic resonance (EPR), date back to the end of the 19th century and the discovery of spectral lines splitting in the presence of an external magnetic field by P. Zeeman [1]. The ESR technique as such can be then treated as an extension of the Stern–Gerlach experiment. They demonstrated in 1922 that the magnetic moment of an electron in an atom can acquire only discrete orientations in a magnetic field [2]. Subsequently, Uhlenbeck and Goudsmit linked the electron magnetic moment to the electron spin angular momentum [3]. The next contributors were Breit and Rabi that described the energy levels of a hydrogen atom in a magnetic field [4]. Afterwards, they studied transitions between energy levels induced by an oscillating magnetic field [5]. This can be considered as the first observation of magnetic resonance.

Finally, the first observations of an electron spin resonance peak were made in 1944 by Zavoisky, who detected a radio frequency absorption line from $CuCl_2 \cdot 2\,H_2O$ and $MnSO_4$ salts [6]. He discovered a resonance at the magnetic field $B = 4.76\,\mathrm{mT}$ for the frequency $\nu = 133\,\mathrm{MHz}$. For this case, the g factor in Zeeman splitting term was approximately 2 [7]. Later on, Frenkel interpreted Zavoisky's results as showing spin resonance absorption [8]. Subsequent experiments with higher magnetic fields of $100-300\,\mathrm{mT}$ demonstrated the advantage of using higher magnetic fields and frequencies [9].

The rapid development of electron spin resonance started after World War II due to the widespread availability of microwave technology used for military purposes. For instance, technology for X-band (i.e. $8-12\,\mathrm{GHz}$) was widely used for radars, and thus components were easy to obtain at reasonable costs. The field of high frequency/field electron spin resonance (HF-ESR) has grown since 1970s/1980s thanks to Y. S. Lebedev and L. G. Oransky, who designed a 2-mm (corresponds to D-band $\approx 140\,\mathrm{GHz}$) band ESR spectrometer containing superconducting solenoid at the Institute of Chemical Physics in Russia used for physical-chemical investigations [10, 11]. Nowadays, state-of-the-art instruments for ESR detection benefit from the development of related fields such as information technology, microwave sources, precise machining, and sensitive detectors. All of this pushes every new ESR instrument to a higher level and allows for a deeper, quicker, and more sophisticated investigation of diverse materials.

HF-ESR has become a powerful tool in the spectroscopic investigation of paramagnetic species such as radicals, single-molecule magnets (SMMs), quantum bits (qubits), and samples with unpaired electrons in general. The principle is the same as in the standard X-band ESR method operating at the frequency of 9.6 GHz, in which a system with unpaired electrons is placed in an external magnetic field and irradiated by a microwave. However, the broadband HF-ESR spectrometers are usually home-built and operate in the frequency range from 90 GHz to 1000 GHz in high magnetic fields of 10 T and higher and low temperatures of units of kelvin [12, 13]. HF-ESR is especially beneficial for the determination of intrinsic magnetic properties and anisotropy of molecular nanomagnets.

This thesis is divided into 6 main chapters, in which the first chapter: Introduction (1) gives a brief historical background to ESR spectroscopy with extension to high-frequency ESR. The second chapter: Aims of thesis (2) outlines the goals set by this work and methods in order to accomplish them. The chapter: Theoretical background (3) leads the reader through fundamental physical phenomena connected to ESR spectroscopy such as the connection of electron spin to statistics, magnetic moments, the spin of an electron, spin Hamiltonian, molecular magnetism, single-molecule magnets and ends with a short review on applicability of HF-ESR spectroscopy to various systems. The following chapter: Methods (4) then introduces two approaches of preparation of thin films used to obtain results for this work – namely, wet-chemistry method of Langmuir-Blodgett and thermal sublimation in high-vacuum. Characterisation techniques used to probe prepared samples are then briefly introduced: HF-ESR spectrometer, X-ray photoelectron spectroscopy (XPS), Raman spectroscopy (RS), ultraviolet-visible spectroscopy (UV-VIS), atomic force microscopy (AFM) and scanning electron microscopy (SEM). The next chapter: Results obtained (5) describes the main results obtained during my doctoral studies. The last chapter: Conclusions (6) summarises results and concludes about the main topic of the thesis, HF-ESR spectroscopy. Additional chapters include References, Author publications and outputs, List of abbreviations and Appendices.

2. Aims of thesis

The goal of this doctoral thesis was to prepare suitable samples and establish deposition routes for HF-ESR measurements of single-molecule magnets (SMMs) and quantum bits on surfaces, including layered materials such as graphene. It was carried out by applying a chain of techniques to achieve the required samples measurable by a novel HF-ESR spectrometer located at CEITEC Brno. The route can be divided into three following objectives:

1. The first objective was the preparation of suitable samples for HF-ESR spectroscopy. Suitable samples are usually in the form of a pellet, single-crystals or solutions. However, in order to be able to probe on surface capabilities of prepared novel molecular materials, deposition on various surfaces is needed. Therefore, the effort was put on mastering and creating a working chain of procedures for making thin films of layered materials, SMMs, and quantum bits on selected surfaces. There are two routes of depositing such materials: the wet-chemistry approach by dissolving the compound of interest in a solvent with subsequent deposition and by thermal sublimation from as-synthesised powder. To probe both paths, we used a glove-bag filled with inert gas and developed our own high-vacuum (HV) sublimation chamber.

2. Samples prepared either by wet-chemistry or sublimation methods, depending on their stability, were characterised for their physical and chemical properties on surfaces. For the surface-sensitive characterisation of thin films, I used available in-house instruments located in CEITEC Nano core facility: X-ray electron spectroscopy (XPS) - Kratos Analytical Axis Supra, Atomic force microscopy (AFM) - Bruker Dimension Icon, Raman spectroscopy (RS) - WITec Alpha 300 R, Scanning electron microscope (SEM) - High-resolution FEI Verios 460L, and MOTES ESR laboratory: a home-built sublimation chamber for preparation of thin films (part of this thesis) and a home-built HF-ESR spectrometer featuring a Virginia diode (VDI) signal generator, amplifier-multiplier chain, a quasi-optical bridge (Thomas Keating), Cryogenics 16 T solenoid cryomagnet and a VDI heterodyne detector.

3. Once a suitable sample was prepared and characterised in the bulk form and on a surface, the final objective was to advance the field of HF-ESR spectroscopy and its applicability to thin films and layered materials by using various spectrometer setups and make use of its full capacity. This came hand in hand with theoretical simulations and the fitting of experimentally measured data.

3. Theoretical background

3.1. Electron spin and statistical physics

ESR is a spectroscopic technique based on the interaction of the electron spin with a magnetic field. The spin is a quantum mechanical property of an electron, which belongs to the family of subatomic particles called fermions. These particles obey Pauli's exclusion principle, which implies that in an atom, there cannot be two fermions with the same quantum state (i.e. same set of the quantum numbers, including the spin S). An electron spin is an intrinsic form of angular momentum. The corresponding measurable spin projections are half-integer: $-\frac{1}{2}$ and $\frac{1}{2}$. The connection of spin with statistics was demonstrated by the spin-statistics theorem in 1940 [14]. This connection was important because ESR measurements are usually performed on an ensemble of spins of paramagnetic species. Electrons are governed by the Fermi–Dirac distribution, however, in an approximation far from the Heisenberg uncertainty limit, one can use Boltzmann–Maxwell distribution. Let us assume that paramagnetic centres are in thermal equilibrium, the population of spins in a sample can be expressed as follows:

$$n_{\text{diff}} = \frac{n_{\text{upper}}}{n_{\text{lower}}} = \exp\Big(-\frac{E_{\text{upper}} - E_{\text{lower}}}{k_{\text{B}}T}\Big) = \exp\Big(-\frac{\Delta E}{k_{\text{B}}T}\Big) = \exp\Big(-\frac{h\nu}{k_{\text{B}}T}\Big), \tag{3.1}$$

where n_{diff} is the ratio between number of paramagnetic centres occupying the upper E_{upper} and lower E_{lower} energy levels, h is the Planck constant, ν is the microwave frequency matching the energy levels difference, k_{B} is the Boltzmann constant, and T is the thermodynamic temperature.

The following examples illustrate the difference between states with higher and lower energy on a system with unpaired electrons at given temperatures and frequencies:

1. X-band: $\nu = 10\,\text{GHz}$ and $T = 300\,\text{K}$, then $n_{\text{diff}} = 0.998$,
2. X-band: $\nu = 10\,\text{GHz}$ and $T = 2\,\text{K}$, then $n_{\text{diff}} = 0.787$,
3. HF-ESR: $\nu = 1000\,\text{GHz}$ and $T = 300\,\text{K}$, then $n_{\text{diff}} = 0.852$,
4. HF-ESR: $\nu = 1000\,\text{GHz}$ and $T = 2\,\text{K}$, then $n_{\text{diff}} = 3.8 \times 10^{-11}$.

This is one of the reasons why ESR measurements on paramagnetic samples usually take place at very low temperatures close to absolute zero. The aim is to put as many spins to the ground state as possible. This results in the increased sensitivity and higher possibility of observing the excitation from a ground state to the first excited energy level within the sample. The increase in sensitivity during low-temperature HF-ESR measurements compared to conventional low frequency and magnetic field ESR setups is significant.

Figure (3.1) shows how ESR sensitivity can be greatly improved by higher frequencies and low temperatures.

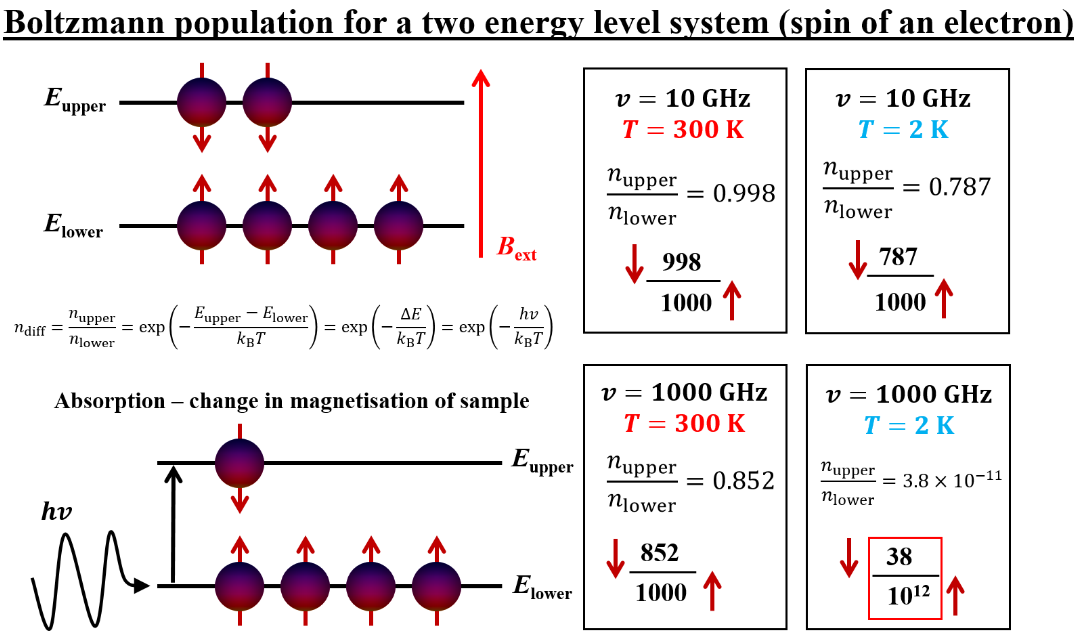

Figure 3.1: Application of Boltzmann population distribution in ESR of non-interacting paramagnetic unpaired electrons. This difference causes the observation of an absorption, which is the change in magnetisation of the probed sample.

3.2. Magnetic moments

Let us consider a case of a classical particle with mass m and charge q rotating with speed v in a circle of radius r. The circle lies in the xy plane. The circulating electric current I can be considered as generating a magnetic field equivalent to the magnetic field produced by a point magnetic dipole as shown in Figure (3.2).

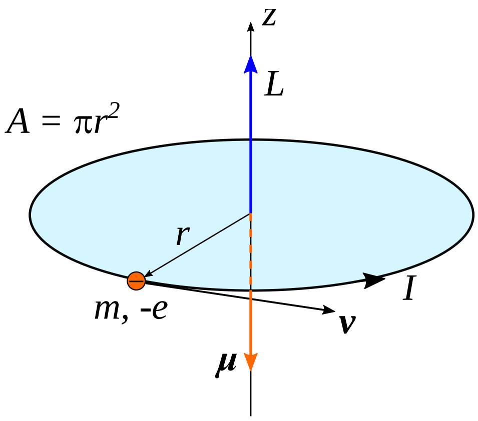

Figure 3.2: A classical model of particle with mass m and charge $q = -e$ such as electron moving in a circle with radius r and velocity $\boldsymbol{v}$. Such charged and moving particle has an angular momentum $\boldsymbol{L} = \boldsymbol{r} \times \boldsymbol{p}$, where $\boldsymbol{p}$ is its linear momentum $\boldsymbol{p} = m\boldsymbol{v}$. Particle's motion is equivalent to a current loop with an associated magnetic dipole moment $\boldsymbol{\mu}$ that has opposite direction to orbital angular momentum $\boldsymbol{L}$.

The charge flow per unit time (effective current) is $I = qv/2\pi r$. This magnetic dipole has a magnetic moment $\mu = IA$ normal to the plane, with $A = \pi r^2$ being the area of the circle. The magnetic moment pointing along the z-axis can be then expressed as:

$$\mu_z = IA = \frac{qv\pi r^2}{2\pi r} = \frac{q}{2m}mvr = \frac{q}{2m}L_z, \tag{3.2}$$

where L_z is the orbital angular momentum along the z-axis and the sign choice depends on the direction at which the particle rotates. The magnetic moment, due to the motion of the charge, is proportional to the orbital angular momentum $\boldsymbol{L} = \boldsymbol{r} \times \boldsymbol{p}$ as:

$$\boldsymbol{\mu} = \frac{q}{2m}\boldsymbol{L}, \tag{3.3}$$

where $\boldsymbol{p} = m\boldsymbol{v}$ is the momentum of a particle with mass m and velocity $\boldsymbol{v}$. The proportionality constant is $\gamma = q/2m$ which is called the gyromagnetic ratio (units in SI: $\mathrm{C \cdot kg^{-1} = s^{-1} \cdot T^{-1}}$). This factor γ converts angular momentum to magnetic moment. When such magnetic moment is placed in an external magnetic field $\boldsymbol{B}_{\text{ext}}$ it will experience a torque $\boldsymbol{\tau}$:

$$\boldsymbol{\tau} = \frac{d\boldsymbol{L}}{dt} = \boldsymbol{\mu} \times \boldsymbol{B}_{\text{ext}} = -\frac{q}{2m}\boldsymbol{B}_{\text{ext}} \times \boldsymbol{L} = \boldsymbol{\omega}_L \times \boldsymbol{L}, \tag{3.4}$$

where $\boldsymbol{\omega_L}$ is the Larmor frequency:

$$\boldsymbol{\omega}_L = -\frac{q}{2m}\boldsymbol{B}_{\text{ext}} = -\gamma\boldsymbol{B}_{\text{ext}}, \tag{3.5}$$

at which a magnetic moment precesses about an external magnetic field.

If we compare Larmor frequency for proton spin and electron spin as illustrated in Figure (3.3). We get the comparison for two magnetic resonance techniques: NMR vs ESR. The energy necessary to polarise electron spins is approximately 1000× higher than to polarise proton spins.

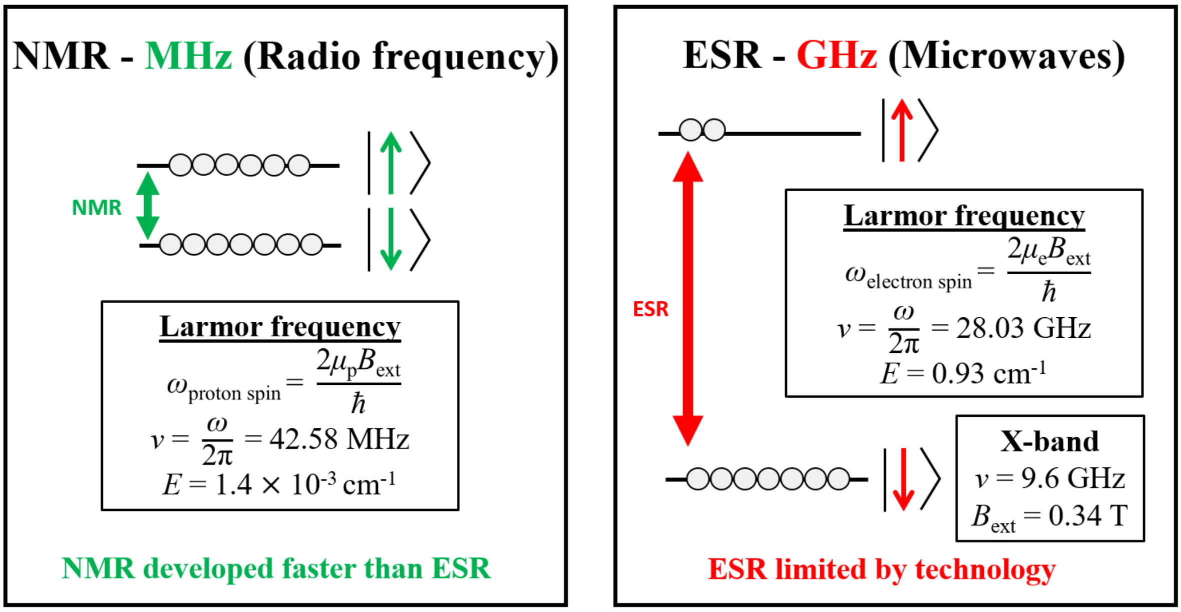

Figure 3.3: Comparison of Larmor frequency for NMR and ESR. The technological consequence is that NMR instrumentation was developed much faster. This is because the energy necessary to polarise electron spins is higher in ESR than for NMR. The typical X-band measurements take place at around $B_{\text{ext}} = 0.34\,\text{T}$ and frequency $\nu = 9.6\,\text{GHz}$ which meets the resonant condition for electron spin polarisation for samples with g-factor of radicals close to 2.

The total magnetisation $\boldsymbol{M} = \sum_{i=1}^{N} \frac{\boldsymbol{\mu}_i}{V}$, where $\boldsymbol{\mu}_i$ are all individual magnetic dipole moments, and its change in time can be written as follows:

$$\frac{d\boldsymbol{M}}{dt} = \gamma \boldsymbol{M} \times \boldsymbol{B}_{\text{ext}}. \tag{3.6}$$

The spin relaxation can be described by following Bloch Equations (3.7), (3.8), (3.9) that describe magnetisation $\boldsymbol{M} = (M_{\text{x}},\, M_{\text{y}},\, M_{\text{z}})$ as a function of time with two relaxation times τ_1 and τ_2. τ_1 is longitudinal spin-lattice relaxation time and τ_2 is transverse spin-spin relaxation time [15]. Bloch equations in the rotating frame x', y', z' with ω frequency of the microwave field B_1, and ω_L being the Larmor frequency can be written as follows:

$$\frac{dM'_{\text{x}}}{dt} = (\omega - \omega_L)\, M'_{\text{y}} - \frac{M'_{\text{x}}}{\tau_2}, \tag{3.7}$$

$$\frac{dM'_{\text{y}}}{dt} = -\,(\omega - \omega_L)\, M'_{\text{x}} - \frac{M'_{\text{y}}}{\tau_2} + \gamma B_1 M'_{\text{z}}, \tag{3.8}$$

$$\frac{dM'_{\text{z}}}{dt} = -\gamma B_1 M'_{\text{y}} - \frac{M'_{\text{z}} - M_0}{\tau_1}, \tag{3.9}$$

where M_0 is the magnetisation in thermal equilibrium and τ_1 with τ_2 are relaxation times.

The solutions of Equations (3.7, 3.8, and 3.9) for the stationary state: $dM'_{\text{x}}/dt = dM'_{\text{y}}/dt = \\ = dM'_{\text{z}}/dt = 0$ are as follows:

$$M'_{\text{x}} = \frac{\gamma B_1 (\omega_L - \omega)\tau_2^2}{1 + (\omega_L - \omega)^2 \tau_2^2 + \gamma^2 B_1^2 \tau_1 \tau_2} M_0, \tag{3.10}$$

$$M'_{\text{y}} = \frac{\gamma B_1 \tau_2}{1 + (\omega_L - \omega)^2 \tau_2^2 + \gamma^2 B_1^2 \tau_1 \tau_2} M_0, \tag{3.11}$$

$$M'_{\text{z}} = \frac{1 + (\omega_L - \omega)^2 \tau_2^2}{1 + (\omega_L - \omega)^2 \tau_2^2 + \gamma^2 B_1^2 \tau_1 \tau_2} M_0. \tag{3.12}$$

The transformation back to laboratory frame gives:

$$\boldsymbol{M} = \begin{pmatrix} M'_{\text{x}} \\ M'_{\text{y}} \\ M'_{\text{z}} \end{pmatrix} = \begin{pmatrix} M'_{\text{x}}\cos(\omega t) + M'_{\text{y}}\sin(\omega t) \\ -M'_{\text{x}}\sin(\omega t) + M'_{\text{y}}\cos(\omega t) \\ M'_{\text{z}} \end{pmatrix}. \tag{3.13}$$

The transverse magnetisation has one component M'_{x} which rotates synchronously with B_1 about z-axis, while M'_{y} is shifted by 90°. Therefore, M'_{x} is the dispersion χ' in complex magnetic susceptibility $\chi = \chi' - i\chi''$ while M'_{y} is the absorption χ'':

$$\chi' = \frac{M'_{\text{x}}}{2B_1}, \tag{3.14}$$

$$\chi'' = \frac{M'_{\text{y}}}{2B_1}. \tag{3.15}$$

Without saturation $\gamma^2 B_1^2 \tau_1 \tau_2 << 1$ we obtain:

$$\chi'' = \frac{\gamma \tau_2 M_0}{2[(1 + (\omega - \omega_L)^2 \tau_2^2]}, \tag{3.16}$$

$$\chi' = \frac{\gamma (\omega - \omega_L) \tau_2 M_0}{2[(1 + (\omega - \omega_L)^2 \tau_2^2]}, \tag{3.17}$$

$$M_z = M_0. \tag{3.18}$$

Figure (3.4) The absorption χ'' and dispersion χ' plotted against $(\omega - \omega_L)\tau_2$. χ'' was plotted as Lorentzian line shape $f(x) = 1/(1 + x^2)$. The Lorentzian shape is the line shape of a homogeneous EPR line [16].

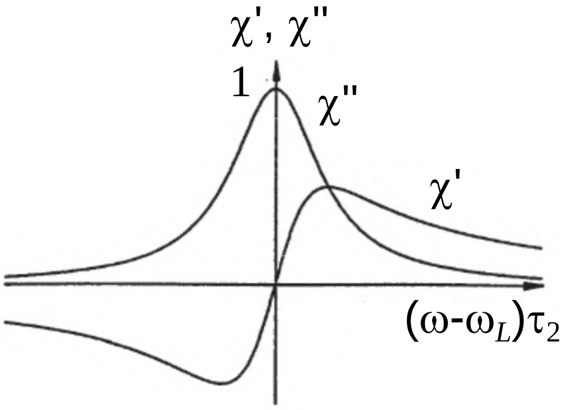

Figure 3.4: Line shape for the real and imaginary part of the complex susceptibility χ' and χ'', respectively. χ'' has a Lorentzian line shape, which is the line shape measured for a homogeneous ESR line. Taken and adapted from [16].

The half width of homogeneously broadened line is:

$$\Delta\omega_{1/2} = \frac{2}{\tau_2}, \tag{3.19}$$

and maximum value χ'' is for $\omega = \omega_L$:

$$\chi''_{\max} = \frac{1}{2}\gamma\tau_2 M_0 = \frac{1}{2}\chi_0\omega_L\tau_2 = \frac{\chi_0\omega_L}{\Delta\omega_{1/2}}, \tag{3.20}$$

where

$$\chi_0 = M_0/B_{\text{ext}}. \tag{3.21}$$

Figure (3.5) illustrates the relaxation of magnetisation.

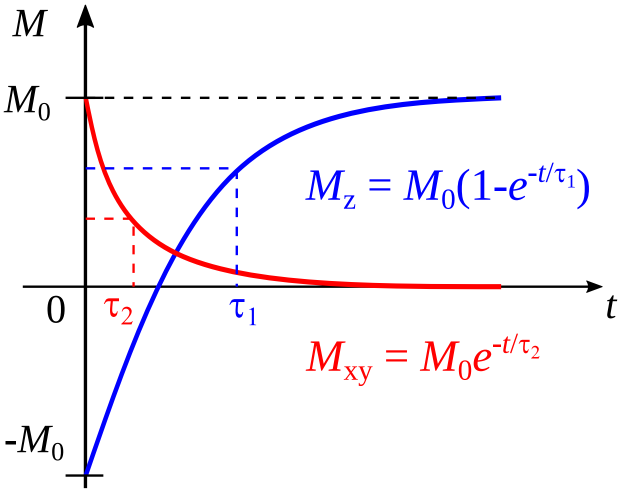

Figure 3.5: Scheme of relaxation of magnetisation in time for the longitudinal spin–lattice relaxation time τ_1 and transverse spin-spin relaxation time τ_2.

In the typical X-band ESR measurement, a resonant cavity with a sample placed inside is used. This enables to adjust phase and filter dispersion before the measurement takes place. On the contrary, in an HF-ESR experiment with a non-resonant cavity mixing of both components, dispersion χ' and χ'' is present. This makes the subsequent spectral analysis difficult. In the latter case, the post-measurement evaluation of detected signals and adjustment of phase is usually necessary.

In quantum mechanics, the total (or generalised) angular momentum operator $\hat{\boldsymbol{J}}$ can be written as:

$$\hat{\boldsymbol{J}} = \hat{\boldsymbol{L}} + \hat{\boldsymbol{S}}, \tag{3.22}$$

where $\hat{\boldsymbol{L}}$ is the orbital angular momentum operator and $\hat{\boldsymbol{S}}$ is the spin angular-momentum operator. The precession of total angular momentum is shown in Figure (3.6).

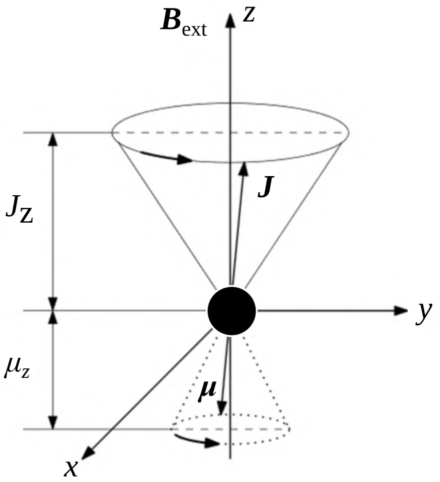

Figure 3.6: The precession of an electron with the total angular momentum $\boldsymbol{J}$ and the total magnetic moment vector $\boldsymbol{\mu}$ with their z-component projections in applied external magnetic field $\boldsymbol{B}_{\text{ext}}$.

At this place, it is important to note that all of operators mentioned in Equation (3.22) are quantised:

$$\hat{L} = \hbar\sqrt{L(L+1)} \quad L = 0, 1, 2, \cdots \tag{3.23}$$

$$\hat{S} = \hbar\sqrt{S(S+1)} \quad S = 0, \frac{1}{2}, 1, \frac{3}{2}, \cdots \tag{3.24}$$

$$\hat{J} = \hbar\sqrt{J(J+1)} \quad J = 0, \frac{1}{2}, 1, \frac{3}{2}, \cdots, \tag{3.25}$$

where $\hbar = \frac{h}{2\pi}$ is the reduced Planck constant, J is the angular momentum quantum number, and S is the spin quantum number. The allowed values of the component of $\hat{J}$ are restricted by the quantum number m_J, with increments of $-J$ to $+J$. This gives in total $2J+1$ possible components.

The quantisation phenomena arise from the Heisenberg uncertainty principle, as it can be shown that it is possible to measure one projection and the square of the operator at the same time (e.g. $\hat{L}_z$, $\hat{L}^2$). This is best understood by the operation of commutation. Two operators commute if:

$$[\hat{A}, \hat{B}] = \hat{A}\hat{B} - \hat{B}\hat{A} = 0. \tag{3.26}$$

Commuting quantities can be measured at the same time. This is, however, not the case of individual components of angular momentum:

$$[\hat{L}_x, \hat{L}_y] = i\hbar\hat{L}_z. \tag{3.27}$$

The same applies to other variations of components. They do not commute, and thus they cannot be measured at the same time.

On the contrary, an arbitrary projection and square:

$$[\hat{L}_z,\hat{L}^2] = 0 \tag{3.28}$$

commute, and thus they can be measured at the same time. Therefore, it is relevant to consider arbitrary projection or square of quantised angular-momentum components [9], [17].

An electron in an atom carries two distinctive momenta. The first one is orbital angular momentum due to its motion about the nucleus. The second already mentioned is intrinsic angular momentum called spin. Orbital magnetic dipole moment $\boldsymbol{\mu}_L$ and orbital angular momentum $\boldsymbol{L}$ are proportional to each other both in classical and quantum mechanics, giving the following expression:

$$\boldsymbol{\mu}_L = -\mu_{\mathrm{B}}\boldsymbol{L}, \tag{3.29}$$

where the proportionality constant is Bohr magneton $\mu_{\mathrm{B}} = \frac{e\hbar}{2m_{\mathrm{e}}} \doteq 9.274 \times 10^{-24} \mathrm{J} \cdot \mathrm{T}^{-1}$, taking into account elementary charge e, mass of an electron m_{e}, and $\hbar$ is the reduced Planck constant. An electron also possesses a spin magnetic dipole given by:

$$\boldsymbol{\mu}_S = -g_{\mathrm{e}}\mu_{\mathrm{B}}\boldsymbol{S}, \tag{3.30}$$

where g_{e} is the electron g-factor and $\boldsymbol{S}$ is the electron spin angular momentum. The total magnetic dipole momentum can be then written as:

$$\boldsymbol{\mu} = -\mu_{\mathrm{B}}(\boldsymbol{L} + g_{\mathrm{e}}\boldsymbol{S}). \tag{3.31}$$

The quantised spin angular momentum obeys the abovementioned Equation (3.24), then the magnetic spin quantum number m_S in general follows $m_S = -S, (-S+1), ..., +S$. The spin of an electron has $S = \frac{1}{2}$, therefore it can possess states given by magnetic quantum numbers of values $m_S = \pm\frac{1}{2}$. When such spin is placed in an external magnetic field $\boldsymbol{B}_{\mathrm{ext}}$ aligned along the z-axis in the Cartesian coordinate system such as $\boldsymbol{B}_{\mathrm{ext}} = (0, 0, B_{\mathrm{ext}})$ the energy of a magnetic dipole will be as follows:

$$E = -\boldsymbol{\mu} \cdot \boldsymbol{B}_{\mathrm{ext}}, \tag{3.32}$$

$$E = -\mu_z B_{\mathrm{ext}}, \tag{3.33}$$

the quantised projection of such spin along z-axis is $S_z = m_S$. If we consider $L = 0$, we obtain the energy of the specific electronic spin state:

$$E_S = g_{\mathrm{e}}\mu_{\mathrm{B}}B_{\mathrm{ext}}m_S, \tag{3.34}$$

which is the basics of ESR resonance and will be further elaborated in the following section.

3.3. Spin Hamiltonian

The spin Hamiltonian (SH) approach expresses the Hamiltonian in powers of abstract spin-operators, absorbing the different (spatially dependent) interactions in effective parameters and thus reducing the complexity of the problem. It is an effective approach where only the lowest-lying energy states are considered. ESR is a phenomenon that can be described as selective absorption of electromagnetic wave by an unpaired electron placed in an external magnetic field.

Figure (3.7) shows the simplest Zeeman energy-level diagram in case of ESR studies for a particle with a spin $\frac{1}{2}$ (one electron) placed in an external magnetic field B_{ext}.

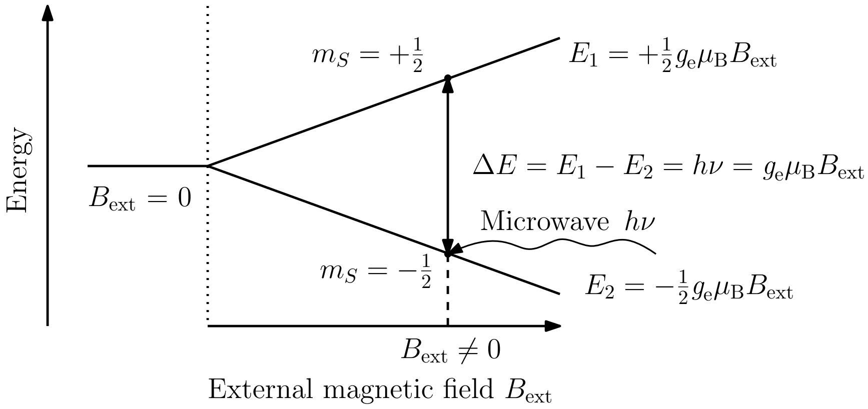

Figure 3.7: Scheme of Zeeman energy-level diagram for a free electron as a function of external magnetic field B_{ext}. E_1 and E_2 are energies corresponding to $m_S = \pm\frac{1}{2}$ states. The spin quantum number S is the characteristics of an electron in this case. g_{e} is the g factor for an electron, μ_{B} is the Bohr magneton, and h is the Planck constant.

The Zeeman term in SH can be written as:

$$\hat{\mathcal{H}}_{\text{Zeeman}} = \mu_{\text{B}} \boldsymbol{B}_{\text{ext}} \cdot \tilde{\boldsymbol{g}} \cdot \hat{\boldsymbol{S}}, \tag{3.35}$$

where μ_{B} is Bohr magneton, $\boldsymbol{B}_{\text{ext}}$ is applied external magnetic field, $\tilde{\boldsymbol{g}}$ is a tensor linking the magnetic field and the spin vectors, and $\hat{\boldsymbol{S}}$ is the electron spin operator.

By varying the magnetic field, it is possible to change the energy-level separation. Resonant absorption is observed for the frequency satisfying $E = h\nu$, where ν is the frequency of incident microwave radiation. The magnitude of the transition equals the energy that must be absorbed from the radiation in order to excite spins from the lower state to the upper state. Usually, many simple unpaired-electron systems require the field of approximately 0.34 T for the resonance to occur at $\nu = 9.5\,\text{GHz}$. This stems from the electron spin polarisability. The important implication of the abovementioned Zeeman splitting is that frequency of incident microwave radiation is linearly dependant on the applied external magnetic field: $\nu \propto B_{\text{ext}}$. Therefore, with increasing the radiation frequency, the necessity of higher magnetic fields is obvious. This principle is the basics of ESR spectroscopy.

Figure (3.8) illustrates the further splitting of energy levels due to the hyperfine interaction. It is caused by the interaction between nuclear spin dipole moment and electron spin dipole moment and contributes to the SH as:

$$\hat{\mathcal{H}}_{\text{HFI}} = \hat{\boldsymbol{I}} \cdot \tilde{\boldsymbol{A}} \cdot \hat{\boldsymbol{S}}, \tag{3.36}$$

where $\hat{\boldsymbol{I}}$ is the nuclear spin operator, $\tilde{\boldsymbol{A}}$ is the hyperfine tensor of interaction between nuclear spin magnetic dipole and the electron spin magnetic dipole, and $\hat{\boldsymbol{S}}$ is the electron spin operator.

Another key SH contribution comes from zero-field splitting (ZFS), which is crucial for spectroscopy of single-molecule magnets (SMMs). They can be imagined as molecular magnets. Every molecule in SMMs can act as a nanomagnet. The preparation route for such systems is by means of synthetic coordination chemistry. They are coordination organometallic compounds consisting of the metallic centre, usually transition metal, lanthanide, or actinide, surrounded by various organic ligands. The change in the local environment of a metal centre causes a change in the potential energy of the whole molecule, which can be addressed in SH. HF-ESR is an essential technique in the investigation of SMMs, as it can probe magnetic anisotropy at the molecular level. After application of an external magnetic field to a SMM, the magnetisation will be aligned parallel to an easy-axis, which is the most favourable direction in the term of energy for the spontaneous magnetisation.

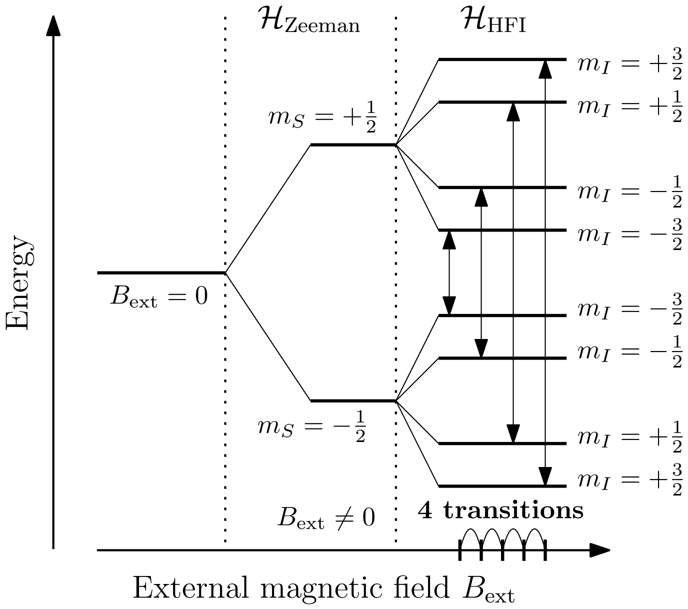

Figure 3.8: Scheme of hyperfine interaction in a system with electron spin $S = \frac{1}{2}$ and nuclear spin $I = \frac{3}{2}$.

Figure (3.9) illustrates the ZFS in the system with total spin $S = \frac{3}{2}$. It describes variations in energy levels in a system originating from the presence of more than one unpaired electron $S > \frac{1}{2}$.

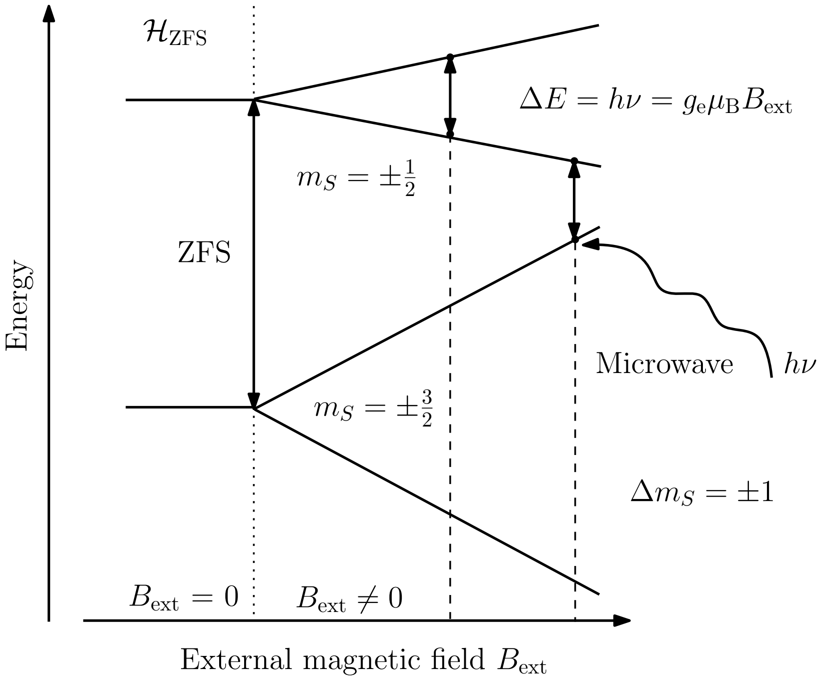

Figure 3.9: Scheme of ZFS interaction in a system with electron spin $S = \frac{3}{2}$ and $D < 0$.

The ZFS interaction term in the SH can be written as:

$$\hat{\mathcal{H}}_{\text{ZFS}} = \hat{\boldsymbol{S}} \cdot \tilde{\boldsymbol{D}} \cdot \hat{\boldsymbol{S}}, \tag{3.37}$$

where $\hat{\boldsymbol{S}}$ is the electron spin operator, $\tilde{\boldsymbol{D}}$ is the axial component of magnetic dipole-dipole interaction, it is symmetric and traceless matrix, which can be diagonalised. The Equation (3.37) can be rewritten as follows:

$$\hat{\mathcal{H}}_{\mathrm{ZFS}} = D\hat{S}_z^2 + E(\hat{S}_x^2 - \hat{S}_y^2), \tag{3.38}$$

where $\hat{S}_x$, $\hat{S}_y$, and $\hat{S}_z$ are spin operators and:

$$D = D_{zz} - \frac{1}{2}D_{xx} - \frac{1}{2}D_{yy} \quad \text{and} \quad E = \frac{1}{2}(D_{xx} - D_{yy}). \tag{3.39}$$

By subtracting the constant $DS(S+1)/3$ from Equation (3.38), the Hamiltonian is

$$\hat{\mathcal{H}}_{\mathrm{ZFS}} = D\left[\hat{S}_z^2 - \frac{1}{3}S(S+1)\right] + E(\hat{S}_x^2 - \hat{S}_y^2). \tag{3.40}$$

In axial symmetry, $D_{xx} = D_{yy}$, and thus $E = 0$. Equation (3.38) is then

$$\hat{\mathcal{H}}_{\mathrm{ZFS}} = D\hat{S}_z^2. \tag{3.41}$$

Therefore, in axial symmetry, only the D parameter is needed to express the energies of the $(2S+1)$ spin levels of the S multiplet at this approximation. The effect of the Hamiltonian in Equations (3.38) and (3.39) is that of splitting the $(2S+1)$ levels even in the absence of an applied magnetic field. It is common to limit variation of $|D|$ and $|E|$:

$$-1/3 \leq E/D \leq +1/3, \tag{3.42}$$

where D can be either positive or negative. Positive D corresponds to the easy-plane magnetic anisotropy, negative D to the easy-axis type magnetic anisotropy. The latter mentioned easy-axis anisotropy is required in order to chemically tailor useful SMMs. The spin anisotropy is expressed as the energy barrier that spins must overcome when they switch from parallel to anti-parallel alignment and can be written as $U_{\mathrm{eff}} = |D| \times S^2$ for integer spin number, and $U_{\mathrm{eff}} = |D| \times (S^2 - \frac{1}{4})$ for half-integer spin number [18]. There are two parameters that can be changed in general, the total spin number S and the ZFS parameter D, in order to increase the barrier. It was demonstrated that it is convenient to focus on increasing D rather than S as there is a fundamental connection between D and S approximately given by $D \propto \frac{1}{S^2}$ [19]. However, it needs to be stressed out that energy barrier U_{eff} is not always proportional to blocking temperature T_{b} as many relaxation mechanisms for magnetisation usually occur. This was shown for many lanthanide-based SMMs in previous studies [20–26]. Therefore, careful considerations have to be made when correlating energy barriers with blocking temperatures of SMMs.

For systems with $S > \frac{1}{2}$ the ZFS occurs and is usually expressed as the second-order parameters D and E. In general, it is necessary to include also fourth, sixth, etc., order terms in the Hamiltonian in order to sufficiently reproduce energy levels. The expansion is applicable only for even-order terms in the zero-field when calculating the effects on states of the same configuration. Therefore, it is sufficient to include only terms of order

$$N = 2,\ 4,\ 6, \ldots,\ 2S. \tag{3.43}$$

A good approximation is obtained by considering that higher-order terms are relatively smaller than the lower order terms. Formally, exact expansion can be done by including higher-order operators such as $\hat{S}_z^4$, $\hat{S}_x^4$, etc. The best way to exploit point group symmetry is to use so-called Stevens operator equivalents:

$$\hat{\mathcal{H}}_{\mathrm{HO}} = \sum_{N,k} B_N^k \hat{\boldsymbol{O}}_N^k, \tag{3.44}$$

where the sum is over all N values defined in Equation (3.43) and the integer k satisfies

$$-N \leq k \leq +N. \tag{3.45}$$

B_N^k are parameters, and $\hat{\boldsymbol{O}}_N^k$ are so-called Stevens operators. The N numbers are limited according to Equation (3.43), while the k values depend on the point group symmetry [27].

There are also other terms contributing to the SH, however, they are usually very small and can be often neglected. It is the nuclear Zeeman interaction $\hat{\mathcal{H}}_{\mathrm{NZI}}$:

$$\hat{\mathcal{H}}_{\mathrm{NZI}} = \mu_{\mathrm{n}} \boldsymbol{B}_{\mathrm{ext}} \cdot \tilde{\boldsymbol{g}}_{\mathrm{n}} \cdot \hat{\boldsymbol{I}}, \tag{3.46}$$

which describes the interaction of a nuclear spin with the external magnetic field, it is analogous to the Zeeman splitting for an electron. Another component is nuclear quadrupole interaction $\hat{\mathcal{H}}_{\mathrm{NQI}}$:

$$\hat{\mathcal{H}}_{\mathrm{NQI}} = \hat{\boldsymbol{I}} \cdot \tilde{\boldsymbol{Q}} \cdot \hat{\boldsymbol{I}}, \tag{3.47}$$

where $\tilde{\boldsymbol{Q}}$ is the traceless nuclear quadrupole tensor, which describes the interaction of the electric quadrupole moment of nuclei with spin $I > \frac{1}{2}$ with the electric field gradient. This electric field gradient arises from uneven distributions of electric charges around the nucleus. The last interaction mentioned here is the electron-electron interaction $\hat{\mathcal{H}}_{\mathrm{EEI}}$:

$$\hat{\mathcal{H}}_{\mathrm{EEI}} = \hat{\boldsymbol{S}}_{\mathbf{1}} \cdot \tilde{\boldsymbol{J}} \cdot \hat{\boldsymbol{S}}_{\mathbf{2}}, \tag{3.48}$$

where the $\tilde{\boldsymbol{J}}$ tensor describes the exchange interaction between the two electron spins by including the isotropic, antisymmetric, and symmetric interactions. By combining all the contributions, the giant SH can be created:

$$\hat{\mathcal{H}} = \hat{\mathcal{H}}_{\mathrm{Zeeman}} + \hat{\mathcal{H}}_{\mathrm{HFI}} + \hat{\mathcal{H}}_{\mathrm{ZFS}} + \hat{\mathcal{H}}_{\mathrm{HO}} + \hat{\mathcal{H}}_{\mathrm{NZI}} + \hat{\mathcal{H}}_{\mathrm{NQI}} + \hat{\mathcal{H}}_{\mathrm{EEI}}. \tag{3.49}$$

The list of SH contributions is exhausting, fortunately, usually only $\hat{\mathcal{H}}_{\mathrm{Zeeman}}$, $\hat{\mathcal{H}}_{\mathrm{ZFS}}$, and $\hat{\mathcal{H}}_{\mathrm{HFI}}$ are used for the fit of an observed spectrum. The ESR fit to measured data can be done by using simulation software such as EasySpin [28], which is a toolbox to the MATLAB program. To conclude this part, the SH approach provides an insight into the description of magnetic interactions within molecular magnets. HF-ESR is a key technique in the precise determination of the g factor, which plays a vital role in ESR spectroscopy. It can be imagined as a dimensionless magnetic moment. It is a unique characteristic of examined material. For an electron $|g_e| = 2.00231930436182$, it is one of the most precisely determined physical constant up to date [29]. Lastly, ZFS parameters D and E can be almost exclusively determined by HF-ESR. They are crucial for the magnetic characterisation of SMMs.

3.4. Molecular magnetism

This chapter provides an introduction to molecular magnetism by describing its characteristic properties. The notation was taken from the book: Molecular Nanomagnets [27] and review: Introduction to Molecular Magnetism [30].

Molecular magnetism as a scientific field is a rather new approach, fully developing since 1990s, describing magnetic behaviour at the scale of individual molecules and molecular clusters. It is an interdisciplinary field, where inorganic and organic chemists design and synthesise new coordination compounds with increasing complexity based on feedback from physicists that usually perform and develop experimental measurements in order to model the novel material properties associated with molecular materials. The rise of this approach is also closely related to the rising interest in the field of nanotechnology, which spans from natural sciences and the industrial needs of miniaturisation processes connected to the rapid development of computers.

Along with the need for smaller components in devices, also the need for principles of quantum mechanics when describing these systems becomes relevant. Both theoretical and experimental parts are necessary for understanding and controlling matter at the nanoscale.

Figure (3.10) illustrates the transition from the region of permanent magnets with magnetic domains containing a huge number of spins to molecular clusters with hundreds of individual spins.

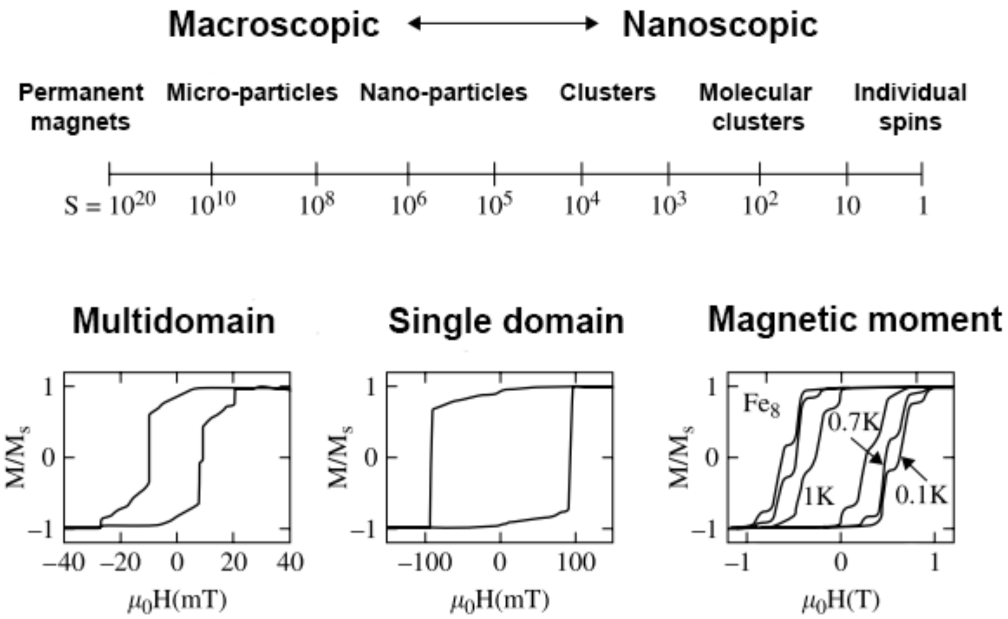

Figure 3.10: The transition from macroscopic to nanoscopic magnets. Change in appearance of hysteresis loops for multidomain (left), single domain (middle), and individual magnetic moment (right). Adapted from [27].

At the macroscale, the particles constituting bulk magnets contain billions of individual spins that are coupled and respond collectively to external stimuli. The magnetic energy is minimised by forming domains. Regions within all the individual magnetic moments are parallel (anti-parallel) to each other. The orientation of magnetic moment in magnetic domains of a paramagnet is random in the absence of an external magnetic field, and thus the magnetisation of the sample is zero. When the sample is magnetised, all the individual moments will be parallel to each other, and the magnetisation reaches its saturation value. If the field is decreased, the magnetisation will not be zero, as in the non-magnetised case, but it will exhibit remanent magnetisation. Demagnetisation of the sample is possible by going to the negative field, which is called the coercive field. This is used in order to classify bulk magnets. A small coercive field is typical for soft magnets (i.e. they do not tend to stay magnetised) and large in the case of hard magnets (i.e. permanent). The M/H plot, shown in Figure (3.10) on the left, shows a hysteresis loop, which gives us information that the value of magnetisation of the sample is dependant on its history. This is the basis for the use of magnets for storing information.

When reducing the size of magnetic particles, magnetic anisotropy A of the sample comes into play:

$$A = KV, \tag{3.50}$$

where V is the volume of the particle, and K is the anisotropy constant of the material.

Figure (3.11) shows the energy of the system as a function of the orientation of the magnetic moment. The anisotropy of the magnetisation is of the Ising type (i.e. the stable orientation of the magnetic moment of the particle is parallel to a given z direction).

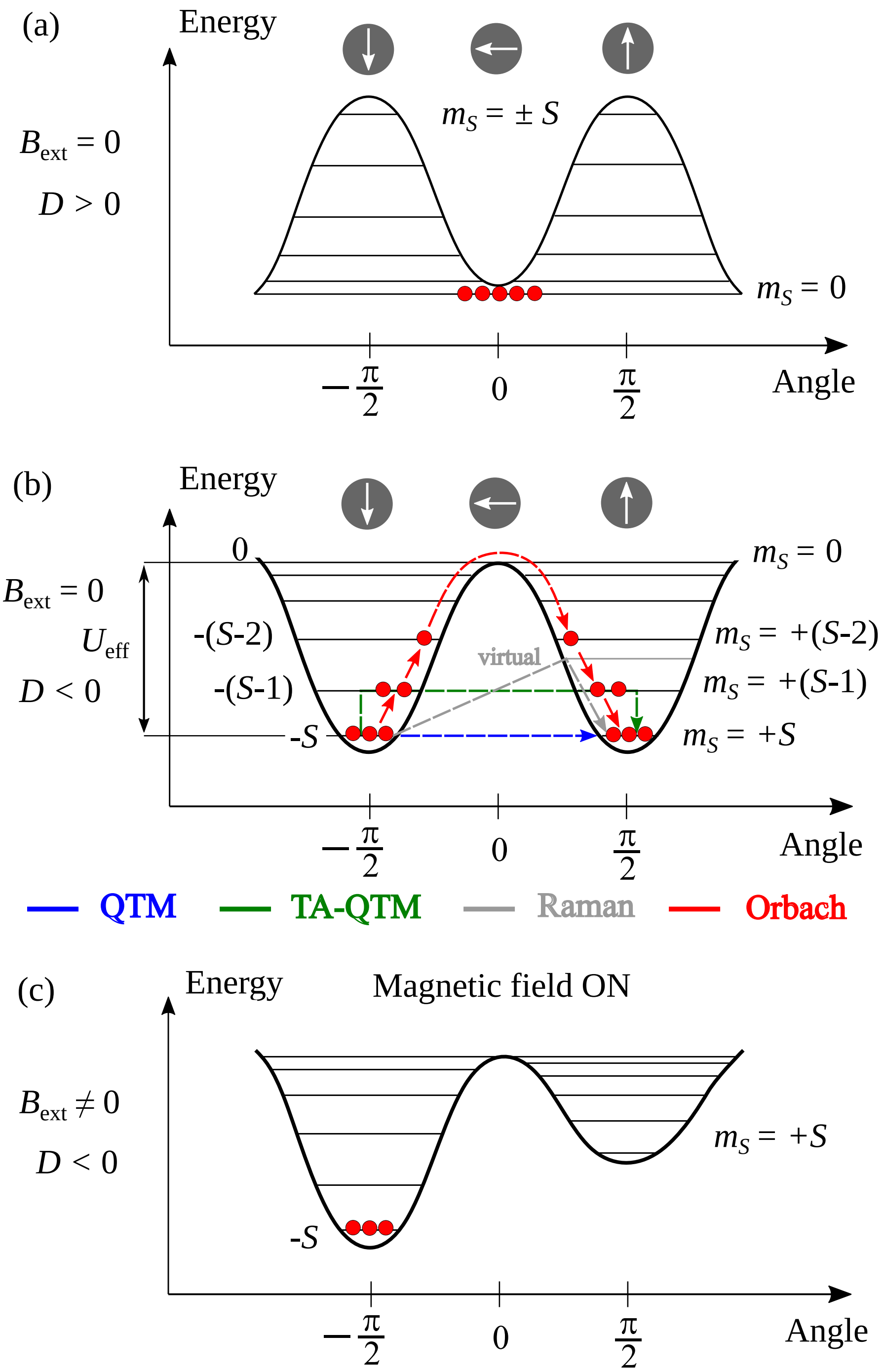

Figure 3.11: Energy of an Ising (easy axis) - white arrows in grey circles as a function of the angle of the magnetisation from the easy axis. Quantum double-well potential for three cases. (a) Case for zero external magnetic field $B_{\text{ext}} = 0$ and positive $D > 0$ parameter. The ground states m_S are located in the minimum of potential well and spin states are inseparable. (b) The second case for zero external magnetic field $B_{\text{ext}} = 0$ and negative $D < 0$ parameter. The spin states are separated by energy barrier U_{eff}. The relaxation mechanisms of magnetisation are depicted for this case: quantum tunnelling of magnetisation (QTM) - blue arrow, thermally assisted quantum tunnelling of magnetisation (TA-QTM) - green arrow, Raman process involving relaxation from virtual states - grey arrow, and Orbach process over the barrier - red arrows. (c) The third case for non-zero external magnetic field $B_{\text{ext}} \neq 0$ and negative $D < 0$ parameter. This case with external magnetic field lifts the degeneracy of energy levels.

The bottom-left well represents energy minimum for magnetisation down, the bottom-right well energy minimum for magnetisation up, and the top between wells represent energy maximum for the magnetisation at 90 ° from the easy axis. When reducing the size of the sample, the barrier for the reorientation of the magnetisation becomes comparable to the thermal energy. If the sample is prepared with up magnetisation (right well), some of the particles with enough energy can jump over the barrier and reverse their magnetisation. After a while, the equilibrium between up and down is established (i.e. half of them will be in the left and half in the right well) because the two minima have the same energy. The system will no longer be magnetised in zero magnetic field as a paramagnet. If, however, an external magnetic field is applied, one of the two wells will lower its energy, and the other will increase it. The two wells will have different populations, and the system behaves as a paramagnet, but since the response to the external perturbation of the system comes from all the individual magnetic centres, it will be large. These particles are called superparamagnets with interesting applications in magnetic drug delivery, magnetic separation of cells, and as a contrast agent for magnetic resonance imaging. The size of particles needed to observe this superparamagnetic behaviour ranges from 2 to 30 nm.

An important feature of the superparamagnet is whether the observation of either static or dynamic magnetic behaviour depends on the time-scale of the experiment used for such an investigation. For example, during AC magnetic susceptibility measurement with the oscillating field at $\nu = 100\,\mathrm{Hz}$, static behaviour with a blocked magnetisation is observed if the characteristic time required for the particle to overcome the barrier is longer than $\tau_\mathrm{m} = (2\pi\nu)^{-1}$. On the contrary, dynamic behaviour is observed for shorter τ_m. The characteristic time for the reorientation of the magnetisation can be calculated, assuming thermally activated process, as an exponential dependence on the energy barrier with Arrhenius behaviour, as observed in many other thermally activated and chemical processes:

$$\tau_\mathrm{N} = \tau_0 \exp \frac{KV}{k_\mathrm{B} T}, \tag{3.51}$$

where τ_N is the Néel relaxation time - the time it takes to randomly flip magnetisation, τ_0 is the attempt time - material property, KV is magnetic anisotropy - energy barrier of magnetisation, k_B Boltzmann constant and T absolute temperature.

For the case of $\tau_\mathrm{m} >> \tau_\mathrm{N}$ the magnetisation will flip many times and the total magnetisation of observation will be zero. In the case of $\tau_\mathrm{m} << \tau_\mathrm{N}$ the magnetisation will not flip during the measurement and we observe the initial magnetisation. The blocking temperature can be then defined as the temperature at which the relaxation time of the magnetisation $\tau_\mathrm{N} = \tau_\mathrm{m}$. The blocking temperature can be obtained from Equation (3.51) by expressing for temperature:

$$T_\mathrm{B} = \frac{KV}{k_\mathrm{B} \ln(\frac{\tau_\mathrm{m}}{\tau_0})}. \tag{3.52}$$

Every molecule of SMM can act as a nanomagnet. The preparation route is by means of synthetic chemistry. The structure of such SMM is the following: the metallic centre, usually transition metal, lanthanide, or actinide, is surrounded by various organic ligands.

3.5. Single-molecule magnets

Single-molecules magnets (SMMs) are coordination complexes composed of transition metals or lanthanides/actinides containing central magnetic atoms (e.g. Co, Mn, Fe, Cu, Gd, Er, Tb, Dy) surrounded by organic ligands. Their magnetic properties exhibit highly anisotropic magnetisation, directional preference, similarly to regular bar magnets. Such magnet placed to an external magnetic field becomes magnetised along their easy axis of magnetisation. A molecules with temperature below blocking temperature (usually tens of kelvin) preserves its magnetisation even for years, and the molecule behaves as a nanoscopic magnet - a single-molecule magnet. Figure (3.12) illustrates the first molecule $[Mn_{12}O_{12}(O_2CCH_3)_{16}(H_2O)_4]$ - shortly Mn_{12} for which such behaviour was observed and described [31]. Since this milestone, SMMs have become widely studied in the field of magnetism. They can have a long relaxation time (years at temperatures below 2 K) [32] and can exhibit an atypical hysteresis curve with apparent steps stemming from quantum tunnelling of magnetisation. These attributes make them promising for future applications in data storage and quantum computing.

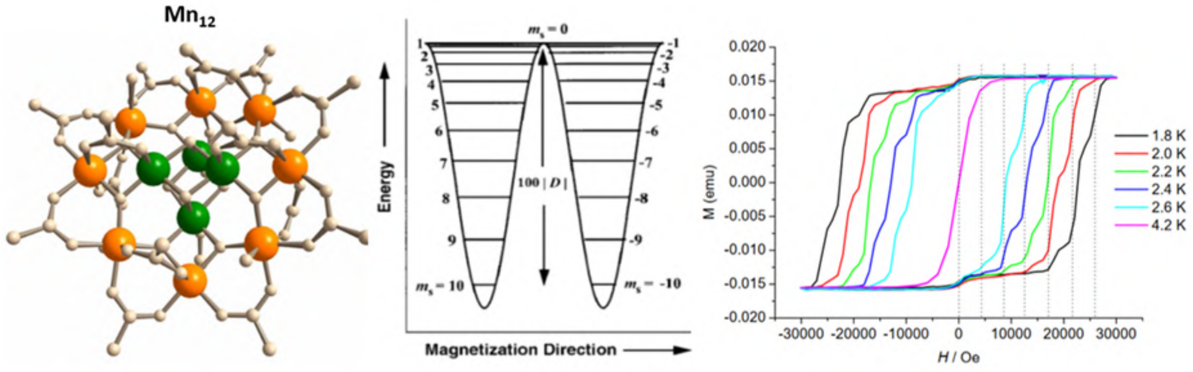

Figure 3.12: Left: depiction of Mn_{12} molecule. Green spheres represent four Mn(IV) ions and orange spheres are eight Mn(III), the rest represent twelve oxygens and octane ligands. Middle: potential energy barrier dependency of magnetisation direction of molecule giving rise to overall spin $S = 10$ in non-zero external magnetic field. Right: atypical hysteresis curve of magnetisation M dependency on magnetic field H. This hysteresis is typical for SMMs at low temperature and illustrates quantum tunnelling of magnetisation with apparent step-like character. Taken and adapted from [31–33].

Thanks to the dimension of individual molecules, the increase in data storage capacity would be significant compared to current technologies. Let us consider a monolayer of $[Mn_{12}]$ on a substrate. There are 2 molecules per unit cell 17×17^2 [34]. Therefore, we can calculate how many molecules - bits could be placed on the area of one m^2:

$$\text{Area density} = \frac{2}{(17 \times 10^{-10})^2} \simeq 700\,000\,\text{Tbit/m}^2. \tag{3.53}$$

This is of course theoretically speaking, and many other issues must be dealt with, but increase of approximately 400× might be expected compared to an affordable solid-state drive (SSD) as of 2021 with the density of 1.2 Tbit/in^2 = 1860 Tbit/m^2.

At this point, it is convenient to summarise optimal conditions to be met by a system in order to be considered as a single-molecule magnet, which is generally a class of metal-organic compounds with the following features [30]:

1. It is a molecule that exhibits slow relaxation of the magnetisation of purely molecular origin.

2. It can be magnetised in a magnetic field, and that will remain magnetised even after switching off the magnetic field.

3. It is inherent molecular property, and no interaction between molecules is necessary for this phenomenon to occur.

4. It can be dissolved in a solvent or put in a matrix (polymer), and it will still exhibit properties listed above.

3.6. Quantum bits

The term quantum bit - shortly a qubit is the basic unit of quantum information. It is the quantum version of the classic binary bit 0 or 1. A qubit is a two-state quantum-mechanical system such as the spin of an electron or the polarisation of a single photon. The word quantum bit was firstly used in the seminal work on quantum coding [35]. Following Equation (3.54) The linear combination of states is called superposition, and it is the working principle of qubits:

$$|\psi\rangle = \alpha|0\rangle + \beta|1\rangle, \tag{3.54}$$

where α and β are complex numbers. The $|0\rangle$ and $|1\rangle$ are basis states. The output of a qubit measurement can still only be 0 with probability $|\alpha|^2$ or 1 with probability $|\beta|^2$. The probabilities sum to one, and thus: $|\alpha|^2 + |\beta|^2 = 1$. With this knowledge we can rewrite the Equation (3.54) as:

$$|\psi\rangle = e^{i\gamma}\left(\cos\frac{\Theta}{2}|0\rangle + e^{i\varphi}\sin\frac{\Theta}{2}|1\rangle\right), \tag{3.55}$$

where Θ, φ and γ are real numbers. The phase factor $e^{i\gamma}$ does not change the expected values of measurement and by omitting we get:

$$\cos\frac{\Theta}{2}|0\rangle + e^{i\varphi}\sin\frac{\Theta}{2}|1\rangle, \tag{3.56}$$

with Θ and φ defining a point on the unit 3D-sphere, a Bloch sphere as shown in Figure (3.13).

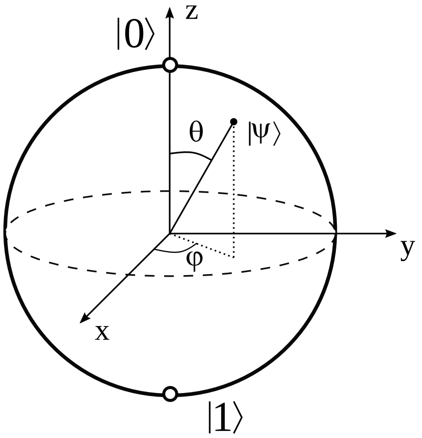

Figure 3.13: Bloch sphere representing a qubit.

In this first part, we have introduced qubits and their representation on a Bloch sphere. Now we can briefly explain what multiple qubits can be used for and how quantum computing can be achieved with them. In the case of two qubits we have four computational basis states: $|00\rangle$, $|01\rangle$, $|10\rangle$, and $|11\rangle$. The vector describing the two qubits is then as follows [36]:

$$|\psi\rangle = \alpha_{00}|00\rangle + \alpha_{01}|01\rangle + \alpha_{10}|10\rangle + \alpha_{11}|11\rangle. \tag{3.57}$$

The physical realisation of qubits for quantum computing was postulated in 2000 with five plus two criteria required to be met before a feasible quantum computing can be implemented [37]. It is also necessary to bear in mind that not all computational tasks can benefit from quantum computing [38]. However, it can be very helpful for tasks that can be sped up, such as locating an entry in a database of n entries [39] or factoring an n-digit number [40]. The proposed criteria are as follows:

1. **A scalable physical system with well-characterised qubits** - this first condition implies that it should be possible to scale up the system and have control over the physical properties of such system. Many physical systems can be implemented as qubits such as the photon, electron spin, nuclear spin, Josephson junction or quantum dots.

2. **Ability to initialise the state of the qubits to a simple fiducial state, such as $|000...\rangle$** - this requirement involves the ability to start computation with zeroed states, having a fresh supply of qubits in the low-entropy state such as $|0\rangle$ state.

3. **Long relevant decoherence times** - decoherence time τ_2 is characteristics of qubit interaction with its environment, it indicates how long a qubit stays in the knows state unaffected by impairing effects, and thus for how long the quantum computation can be performed.

4. **A universal set of quantum gates** - quantum logic gates are building blocks for computing. They represent a set of unitary (e.g. rotation in Bloch sphere) transformations, each acting on a small number of qubits.

5. **A qubit-specific measurement capability** - this means readability of quantum computation with the ability to measure specific qubits. Ideally, the density matrix is $\varrho = = p|0\rangle\langle 0| + (1-p)|1\rangle\langle 1| + \alpha|0\rangle\langle 1| + \alpha^*|1\rangle\langle 0|$, the outcome should be 0 with probability p and 1 with probability $1-p$, independent of α and any other parameters of the system. This would give a quantum efficiency of 100%. Luckily, much lower efficiencies, even less than 1%, are used for successful quantum computing [41], the final measurement is then done as an ensemble average.

The other two requirements are connected to the ability to inter-convert stationary and flying qubits - which is a qubit that can be sent freely from one node to another (e.g. photon polarisation). It should also be possible to reliably transmit these flying qubits between specified locations. All the abovementioned criteria make a set of strict rules that need to be met in order to implement successful quantum computing. Herein, the part of the thesis focused on the first criterion - selection of a scalable and well characterised molecular quantum bit which is described in the Results section (5).

The path we have explored was the molecular qubits, where one molecule serves as one qubit. Usually, a spin of an unpaired electron in coordination compound with organic ligands as protection against the environment is used. The Figure (3.14) shows temperature dependence of spin-spin relaxation time τ_2 for various qubits from coordination complexes to nitrogen-vacancy centres (NVC) in diamond. The effort is usually in the reduction of nuclear spins in the systems. This can be done by replacing hydrogen in compounds with deuterium.

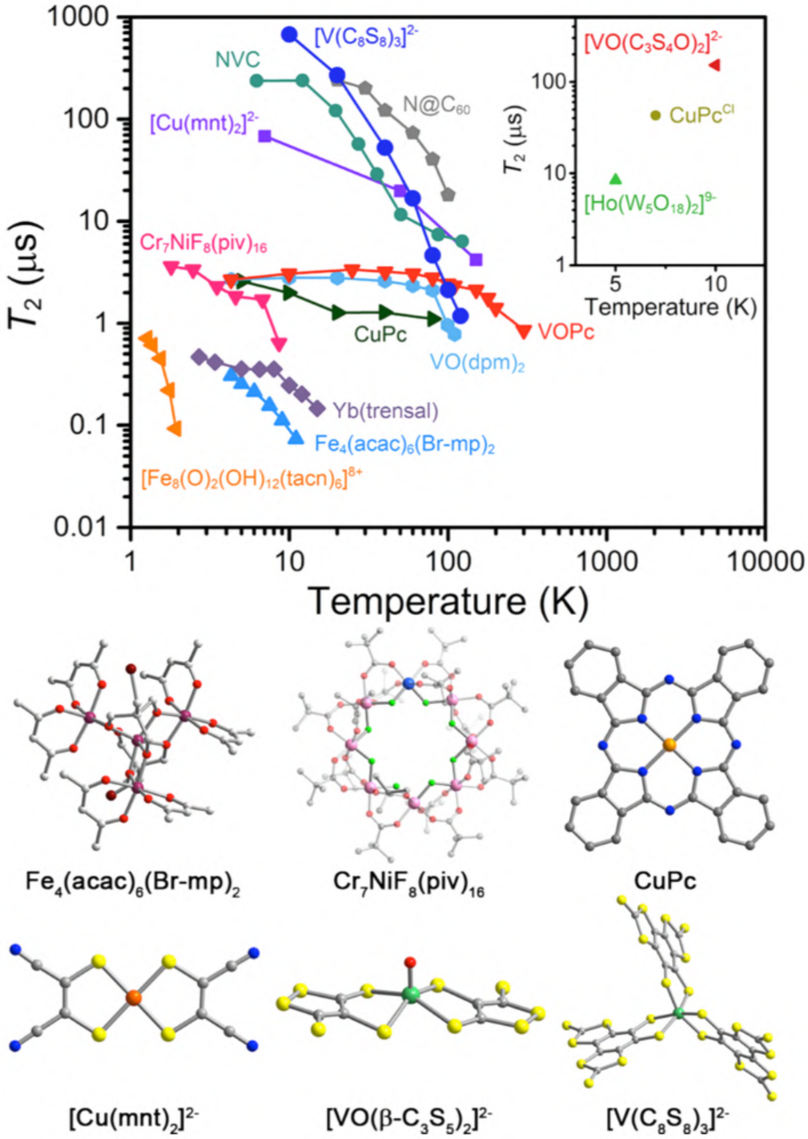

Figure 3.14: Illustration of temperature-dependence of spin-spin relaxation time $T_2 = \tau_2$ for a range of molecular qubit complexes with crystal structure of a few selected. Purple, orange, pink, light blue, green, maroon, light green, blue, yellow, red, and grey spheres represent iron, copper, chromium, nickel, vanadium, bromine, fluorine, nitrogen, sulfur, oxygen, and carbon atoms, respectively. Taken and adapted from [42].

3.7. High-frequency electron spin resonance (HF-ESR) applications

HF-ESR is a powerful tool in the spectroscopic investigation of paramagnetic species such as radicals, SMMs, quantum bits (qubits), and samples with unpaired electrons in general. It is based on the standard X-band ESR technique operating at the frequency of 9.6 GHz, in which a system with unpaired electrons is placed in an external magnetic field and irradiated by an electromagnetic wave in the form of the microwave. These HF-ESR spectrometers are mostly home-built and operate in the frequency range from 100 GHz to 1000 GHz in a high magnetic field (units of tesla) and low temperatures (units of kelvin). They have proved to be crucial in the investigation of magnetic anisotropy of SMMs and their ground states in the pioneer SMM system of Mn_{12} [31]. The microwave frequency of 300 GHz was needed to observe a transition from $m_S = 10$ to $m_S = 9$ in the zero magnetic field [43]. The main parameters obtained from HF-ESR measurements in the context of SMMs are the ZFS parameters D and E, which represent interactions of the energy levels of a molecule/ion resulting from the presence of more than one unpaired electron. ZFS parameter D is the axial component of magnetic dipole-dipole interaction, and E is the transversal component describing the rhombicity of a system [19]. The palette of measurable samples by HF-ESR spans from polynuclear clusters as mentioned before, such as Mn_{12}, to dimers consisting of different transition metal ions such as Cu(II), Cr(III), and Ni(II). For instance, the system with Cu(II) was thoroughly studied in Cu_2Ac by HF-ESR, and the ZFS parameter D was revealed and found to be negative, which is a crucial requirement for the application as a SMM [44]. Besides dimeric compounds, fundamental magnetic properties of many mononuclear complexes single-ion magnets (SIMs) can be unambiguously determined by performing HF-ESR measurements with the subsequent fitting of the system's spin Hamiltonian.

Figure (3.15) shows one of the first HF-ESR applications made on a pioneer molecular cluster with SMM behaviour Mn_{12} [45].

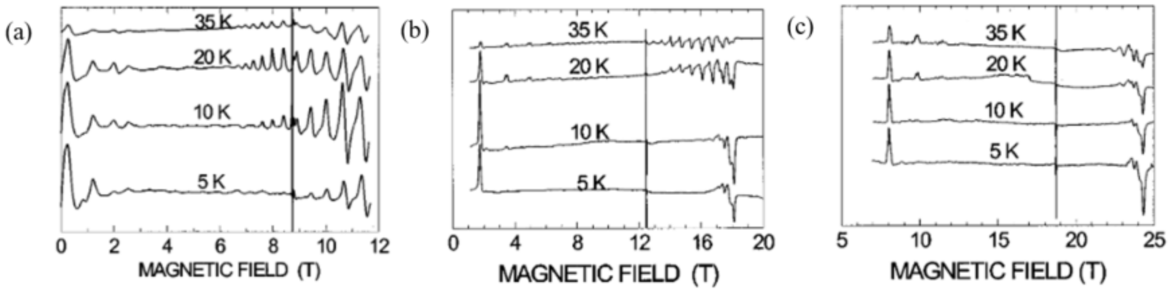

Figure 3.15: Polycrystalline powder HF-ESR spectra of Mn_{12} at different temperatures for selected frequencies of a) 245 GHz, b) 349 GHz, and c) 525 GHz. The narrow signal is given by 1,1-diphenyl-2-picrylhydrazy (DPPH) reference ($g = 2.0037$). Taken and adapted from [45].

The performed measurements helped to understand quantum tunnelling of the magnetisation at low temperatures. Polycrystalline powder spectra of Mn_{12} were recorded at the excitation frequencies of 158 GHz, 245 GHz, 349 GHz, 428 GHz, and 525 GHz, in a spectrometer equipped with a 12 T magnet. The spectra at 35 K show many feature at low field corresponding to the fine structure expected for an $S = 10$ multiplet split in zero field by crystal-field effects. The results showed that HF-ESR is a unique tool for the determination of the crystal-field parameters in large spin clusters.

Figure (3.16) illustrates another study which was focused on multi-frequency HF-ESR study performed on the SMM with chemical formula $[Fe_8O_2(OH)_{12}(tacn)_6]Br_8{\cdot}9H_2O$, in which tacn = 1,4,7-triazacyclononane. Polycrystalline powder spectra allowed for the estimation of the ZFS parameters up to fourth-order terms. The single-crystal spectra have provided the principal directions of the magnetic anisotropy of the cluster. These results have been compared with an evaluation of the intracluster dipolar contribution to the magnetic anisotropy; this suggested that single-ion anisotropy is the main contributor to the magnetic anisotropy [46].

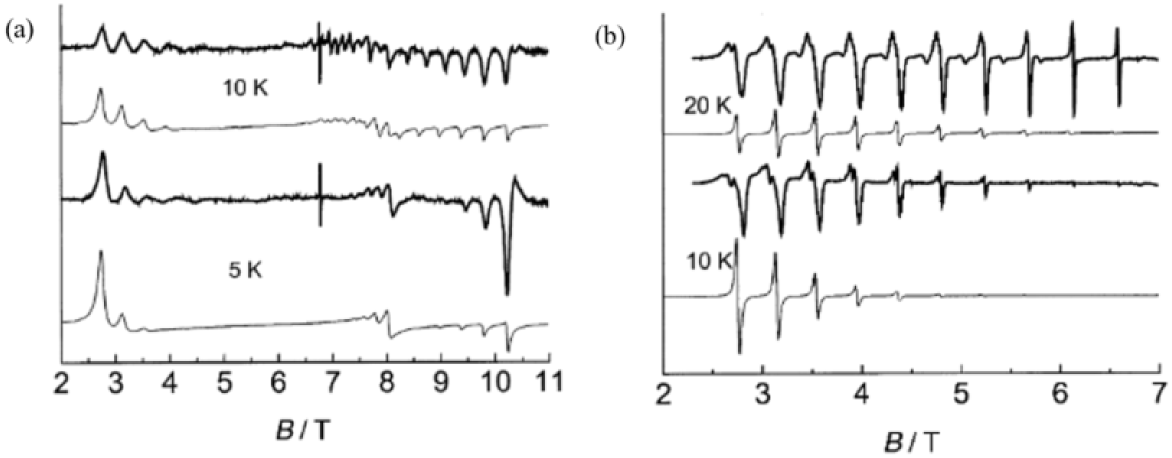

Figure 3.16: a) Experimental (bold) and calculated spectra recorded on a pellet of Fe_8 at 190 GHz. Upper curve at $T = 10\,\mathrm{K}$; lower curve at $T = 5\,\mathrm{K}$. A small DPPH marker was added for field calibration, b) experimental (bold) and calculated spectra of a single crystal at 190 GHz, with the main magnetic field parallel to the easy-axis. The calculated spectra were obtained with the parameters determined from the powder study. Taken and adapted from [46].

As mentioned previously, the HF-ESR technique is especially powerful in determining the parameters of magnetic anisotropy stemming from a spin Hamiltonian. The magnetic behaviour of SIMs is governed by the anisotropic ZFS parameters, D and E, according to the following simplified Hamiltonian: $\hat{\mathcal{H}}_{\mathrm{ZFS}} = D\left[\hat{S}_z^2 - \frac{1}{3}S(S+1)\right] + E(\hat{S}_x^2 - \hat{S}_y^2)$, where D and E are the axial and rhombic ZFS parameters, respectively, S is total spin number, and $\hat{S}_i$ are the spin operators, which describe the spin projection along a given axis. The role of D and E can be thought of as partial removal of the degeneracy of the $2S + 1$ spin microstates associated with a given S, in the absence of an applied magnetic field. When D is negative, the energy difference between $m_S = 0$ and $m_S \pm S$, denoted U, represents an energy barrier to thermal inversion of the magnetic moment. This means that if the thermal energy of a system ($k_{\mathrm{B}}T$) is less than U, the system will be unable to randomly re-orientate its magnetic moment and will thus remain trapped in a potential energy minimum. Under such circumstances, if the system is magnetised under an applied external magnetic field, upon removal of this field, it can retain this magnetisation (provided $k_{\mathrm{B}}T$ never becomes greater than U). This gives rise to a magnetic hysteresis effect at low temperatures of purely molecular origin, which is the defining feature of a SMM/SIM [47].

The HF-ESR applicability is, however, not only limited to SIMs/SMMs but there are also studies on magnetic-field-induced phase transition in $BiFeO_3$, where bismuth ferrite as a magneto-electric material, which simultaneously possesses polarisation and spin ordering, was investigated. HF-ESR was used as a local probe of the magnetic order in the magnetic field range of 0 − 25 T, in the frequency domain of 115 − 360 GHz, and at the temperature of 4.2 K. The data revealed significant changes in the ESR spectra with increasing field, which have been analysed by taking into account the magnetic anisotropy of the crystal and a magneto-electric Dzyaloshinsky-Moria-like interaction. The results demonstrated an induced phase transition from an incommensurately cycloidal modulated state to one with homogeneous spin order [48].

A complex multi-frequency HF-ESR study was published in 2006 and highlighted HF-ESR spectroscopy as a powerful tool to accurately determine ZFS in high-spin transition metal coordination complexes. These studies have been performed on complexes of nearly all high-spin first-row transition metal ions. Advances in instrumentation, such as the use of tunable or quasi-tunable frequency sources, quasi-optical propagation techniques, ever higher fields, and developments in fitting and analytical software have contributed greatly to these advances. Fitting of dense HF-ESR field-frequency data sets allowed determination of spin Hamiltonian parameters with tremendous precision (in ideal cases D, E values better than $\pm 0.001\,\mathrm{cm}^{-1}$, and quite routinely $\pm 0.01\,\mathrm{cm}^{-1}$), significantly greater than results obtainable from magnetometry. More importantly, HF-ESR as a resonance technique provides much greater accuracy in determining all of the spin Hamiltonian parameters (especially the E term and potentially fourth-order terms) than magnetometry. Many of these recent HF-ESR studies have applied ligand-field theory (LFT) to make full use of these parameters to understand the complete electronic structure of these transition metal ion complexes [49].

Figure (3.17) depicts HF-ESR spectra of $\mathrm{CoX(PPh_3)_3}$, X = Cl, Br, that are relatively rare examples of a tetrahedral complex of Co(I), with $S = 1$, as opposed to the more common square planar/pyramidal complexes of $S = 0$ in Co(I).

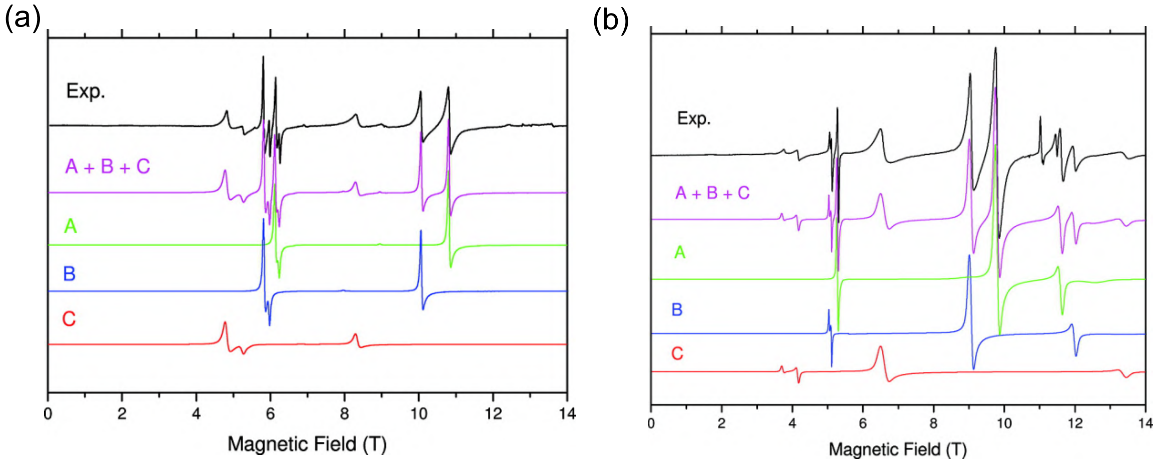

Figure 3.17: HF-ESR spectra of polycrystalline a) $\mathrm{CoX(PPh_3)_3}$ at 406.4 GHz, 10 K, and b) $\mathrm{CoBr(PPh_3)_3}$ at 331.2 GHz, and 10 K. The black traces are experimental results, while the coloured traces represent simulations for the three individual triplet states identified in the sample (green = A, blue = B, red = C), and also their sum (magenta trace). Taken and adapted from [50].

In combination with LFT and quantum chemical calculations by density functional theory (DFT), HF-ESR was used to understand the electronic structure of these and related Co(I) complexes. LFT was used to analyse the electronic absorption spectra of all three complexes quantitatively. The combination of this analysis with HF-ESR allowed them to conclude that the Cl and Br, and likely I, complexes have a $^3A_2[^3T_1(F)]$ electronic ground state (C_{3v} symmetry). The analysis also showed similar bonding interactions, however, weaker than in analogous Ni(II) complexes, and could also reproduce the positive sign of the axial ZFS (D parameter), determined by HF-ESR [50].

Another example shows HF-ESR measurements performed on two binuclear copper complexes, $\mathrm{[Cu(CH_3COO)_2]_2(H_2O)_2}$ and $\mathrm{[Cu(CH_3COO)_2]_2}$(pyrazine). The definitive determination of ZFS parameter D in binuclear copper(II)carboxylates was presented, when contrary to literature reports, the D was found to be negative with the resultant suggestion that D is most likely negative in all binuclear copper carboxylates exhibiting the “paddlewheel” structure [51].

Field-induced hysteresis and quantum tunnelling of the magnetisation in a mononuclear Mn(III) complex is yet another example where HF-ESR can serve as a useful technique. The complete study on synthesis, structural characterization, spectroscopic and magnetic properties, and theoretical calculations of $\mathrm{Ph_4P[Mn(opbaCl_2)(py)_2]}$, where $\mathrm{[H_4opbaCl_2]}$ = N,N’-3,4-dichloro-o-phenylenebis(oxamicacid), py = pyridine, and $\mathrm{Ph_4P^+}$ = tetraphenylphosphoniumcation] was reported [52]. This complex proved to be the first example of a mononuclear Mn(III) complex exhibiting a field-induced slow magnetic relaxation behaviour, thus increasing the number of first-row transition-metal-ion SIMs.

HF-ESR was also successfully applied to probe energy levels in a novel lanthanide-based SIM such as $[C(NH_2)_3]_5[Er(CO_3)_4]\cdot 11\,H_2O$ which was comprehensively studied by means of a large number of different spectroscopic techniques, including far-infrared, optical, and magnetic resonance spectroscopies. A thorough analysis, based on the crystal field theory, allowed an unambiguous determination of all relevant free ion and crystal field parameters. Authors showed that the inclusion of methods sensitive to the nature of the lowest-energy states was essential to arrive at a correct description of the states that are most relevant for the static and dynamic magnetic properties. The spectroscopic investigations also allowed for a full understanding of the magnetic relaxation processes occurring in this system [53].

A SMM behaviour was also observed in a Mn(III) ion with tridentate Schiff-base ligands. The slow magnetic relaxation was observed in the tetraphenylborate salt of $[\mathrm{Mn(3\text{-}OEt\text{-}salme)_2}]^+$, where (salme = N-methyl-N-(3-aminopropyl)-salicylaldiminate), which was the first example of a Mn(III) complex with tridentate donors displaying SIM behaviour by 2016. This choice of a tridentate ligand with three non-equivalent donor atoms should also favour a rhombic distortion, as well as high values of D and E. HF-ESR studies revealed two distinct large axial $D = -4.60\,\mathrm{cm}^{-1}$ for unit A and $D = -4.18\,\mathrm{cm}^{-1}$ for unit B [54].

A recent multi-frequency HF-ESR study, which along with other techniques such as magnetic susceptibility measurements and DFT calculations, probed magnetic properties of Cu(II) ions and their magnetic interactions in the porous metal—organic framework compound $^3_\infty[\mathrm{Cu(prz{-}trz{-}ia)}]$, where prz = pyrazinyle, trz = triazolyl, and ia = isophthalic acid. Two distinct cupric ion species were found to contribute to the overall magnetic susceptibility of the polycrystalline material. The ESR experiments revealed the existence of two distinct copper species, where the 85 % of the copper were antiferromagnetically coupled via the triazole rings with an isotropic exchange coupling $J_1 = 26\,\mathrm{cm}^{-1}$. The magnetic susceptibility measurements provided an intrapair exchange coupling constant in excellent agreement with the value proposed by DFT computations [55].

HF-ESR spectroscopy applied to study pseudotetrahedral Cr(IV) siloxide complex and related homoleptic tetracoordinate $\mathrm{Cr(IV)L_4}$ complexes highlights the necessity of high frequencies in some examples. These complexes are comprised of a variety of donor atoms in their simplest forms, C as alkyl ($\mathrm{L = R_3C{-}}$), N as amide ($\mathrm{L = R_2N{-}}$), and O as alkoxide ($\mathrm{L = RO{-}}$), with L = F included for completeness. Although no thermally stable molecular complex of formula $\mathrm{CrF_4}$ exists, they can be found at a low temperature in a matrix isolated species. They have spin-triplet ground states with a very small magnitude of ZFS so that conventional (e.g. X-band) ESR was sufficient to observe readily interpretable spectra. In contrast, the Cr(IV) siloxido complex, $\mathrm{Cr(DTBMS)_4}$, where DTBMS = $\mathrm{{-}OSiMe^tBu_2}$(di-tert-butylmethylsiloxide), was not amenable to conventional ESR-field/frequency conditions. Only HF-ESR studies on this complex, revealed that $D \approx +0.5\,\mathrm{cm}^{-1}$ [56].

Last but not least, HF-ESR can also be used to study layered materials such as graphene for studying phenomena as cyclotron resonance [57] or recently for the contactless HF-ESR spectroscopy of large-area graphene, which is depicted in Figure (3.18). Shubnikov–de Haas oscillations were compared simultaneously and detected by microwave absorption and by conventional contact Hall bar measurements in magnetic fields up to 15 T on a quasi-free standing, large area ($\approx 25\,\mathrm{mm}^2$) monolayer graphene [58].

To conclude this section, HF-ESR is a useful technique in the investigation of fundamental magnetism and electronic structure in diverse materials ranging from layered materials such as graphene and transition-metal dichalcogenides to SMMs, and qubits. Especially, transition-metal coordination complexes and lanthanide/actinide-based SMMs were mostly investigated by means of HF-ESR as it can very precisely determine ZFS parameters and the sign of the axial D

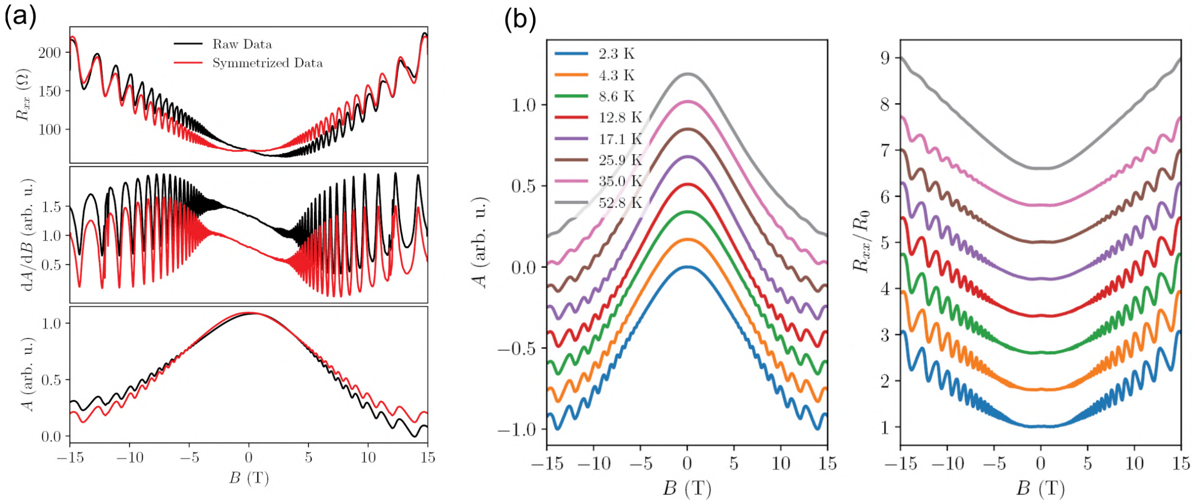

Figure 3.18: a) Top: Hall measurement of the sample, middle: the microwave absorption measurement; since field modulation is used, the derivative of the absorption signal is measured, bottom: the optical absorption of the sample obtained by integrating the spectrum in the middle. The black curves represent the measured data set and red the symmetrised data used for evaluation, b) temperature-dependent transport measurements, left: temperature dependence of the microwave absorption conductivity, the data is normalised and offset for clarity, right: Hall measurements show the same trends as the microwave absorption measurements. The data is normalised, and the offset is shifted for clarity. All measurements were performed at a bath temperature of $T = 2.3\,\mathrm{K}$, a microwave frequency of 320 GHz, a modulation field of $B_{\mathrm{mod}} = 20\,\mathrm{G}$ and an excitation current of $I = 5\ \mu\mathrm{A}$. Taken and adapted from [58].

parameter. In general, all paramagnetic species can be measured and evaluated. There is also a great benefit when using it in combination with quantum chemistry calculation methods and ligand field theory. Current limitations are still in terahertz technology and laboratory demands for a spectrometer. Nowadays, most HF-ESR spectrometers in use are home-built as they require a combination of a superconducting magnet, a precise quasi-optical microwave propagation path, and a terahertz microwave source. Another challenge is related to data acquisition and processing. Whereas most widely spread spectroscopic techniques such as Raman spectroscopy, X-ray photoelectron spectroscopy, ultraviolet-visible spectroscopy, and others are fairly optimised, and their data processing is usually automatised, the HF-ESR is not. Therefore, HF-ESR still offers plenty of room for improvement when it comes to user-friendly experience and data acquisition and its further processing. Despite the rather immature nature of the technique, it has proven to be a versatile and effective spectroscopic method.

4. Methods

This chapter briefly presents methods and techniques used for the preparation and characterisation of samples studied during my doctoral studies. It starts with an overview of sample preparation routes based on wet-chemistry and thermal sublimation.

4.1. Thin film preparation

The as-synthesised coordination compounds, namely single-molecule magnets (SMMs), come in the form of a bulk powder or a single crystal. This form is, however, not suitable for applications nor controlled manipulation. Therefore, there is a need for feasible deposition techniques for these systems in order to be able to deposit in a controlled manner nanostructured layers onto selected substrates. The need for miniaturisation stems from the electronics industry. The current electronics is limited by the quantum tunnelling phenomenon, which occurs for objects as small as units of nanometres and smaller. Such objects can no longer be effectively controlled due to leakage currents. Similar problems appear in magnetic materials with classical domains. When they reach a critical size, the magnetic moments are being switched uncontrollably by thermal fluctuations. The solution to this miniaturisation challenge could be magnets based on magnetic molecules, SMMs [27, 31, 59]. These coordination complexes with central metal atoms surrounded by organic ligands exhibit magnetic bi-stability with slow relaxation of magnetisation of purely molecular origin. The link between magnetism and electronics is an electron. It represents the smallest magnetic dipole moment and electric charge carrier at the same time. The intrinsic angular momentum of an electron is quantised and called spin. The spin electronics (spintronics) deals with the control over electron spin and, together with molecular electronics, promise novel applications [60].

Magnetic properties of SMMs can be very precisely measured in bulk by a high-frequency electron spin resonance (HF-ESR) spectrometer, where the magnetic anisotropy necessary for a molecule to behave as a SMM can be determined. Nowadays, the current effort is put on making thin films, ordered arrays or self-assembled monolayers that would lead to technological applications [61, 62]. The key for this is to understand the behaviour and adsorption of SMMs on surfaces since their exposed surface offers many application possibilities but also brings many challenges as these molecules can oxidise, decompose or degrade in ambient conditions. The current state-of-the-art in the determination of magnetic properties of very thin films is the X-ray magnetic circular dichroism (XMCD) technique, which requires measurements at synchrotron facilities. We aim at making it cheaper and achievable by HF-ES spectroscopy.

There are several ways how to produce nanostructured thin magnetic films. They can be deposited onto a substrate via wet-chemistry protocol from a solution or by thermal sublimation from a solid phase by using an effusion evaporator [63]. Figure (4.1) shows the wet-chemistry based deposition techniques I came across during my studies.

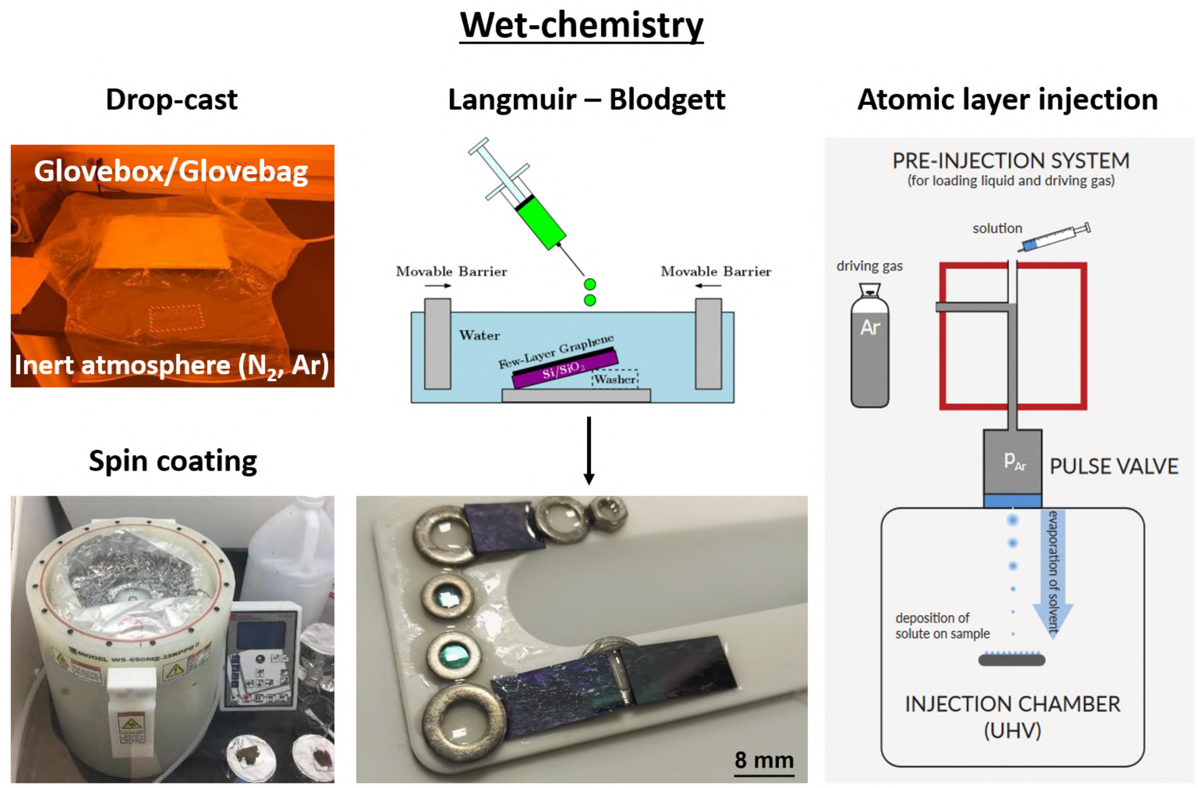

Figure 4.1: Illustration of wet-chemistry based techniques. Drop-cast in inert N_2 or Ar atmosphere and spin coating are the simplest deposition techniques from a dissolved coordination compound in a solution. The following sections will be devoted to the description of the Langmuir-Blodgett technique that proved to be a viable deposition route. The last atomic layer injection is the BihurCrystal's ALI-1000 that utilises mixing solution with a carrier gas and controlled injection onto the substrate in high-vacuum conditions.

Some molecular systems can be transferred onto substrates while maintaining almost unchanged magnetic properties directly by chemical grafting from a solution [64–66]. The latter transfer technique includes thermal treatment with deposition at elevated temperatures by heating the molecular systems promoting their sublimation under vacuum conditions without decomposition [67, 68].

We have shown in previous studies that we are able to determine magnetic properties of organometallic compounds on surfaces with thickness of 100 nm [69, 70] and even a monolayer [71] based on HF-ESR measurements. This is where we want to excel and push the current limits, the precise characterisation of magnetic properties on surfaces. Therefore, our ultimate goal is to be able to fully characterise thin films of magnetic materials inside our lab and in-house within CEITEC BUT, therefore, decreasing the chance of sample damage during transportation and manipulation.

4.1.1. Langmuir–Blodgett deposition

The structure of this section follows book: Langmuir–Blodgett Films: An Introduction [72], and PhD thesis: A Modified Langmuir–Schaefer Method For the Creation of Functional Thin Films [73]. The history of a monolayer-thick film started hundreds of years ago. Already ancient Babylonians created patterns by spreading oil on the water surface. The first technical application of floating organic films dates back to 12th century when coloured dyes composed of sub-micrometre particles (ink) mixed with proteins were spread on a water surface to create patterns. Subsequent horizontal dipping of a paper onto an air-water interface created unique drawings[1]. A detailed report on molecular layers was given by B. Franklin in the first scientific report on surface chemistry in 1774. During his observations of wave attenuation on a water surface (thought to be caused by leaking oil around ships), he noticed a calming effect of oil on water. After depositing a small amount of oil onto a water surface, he observed that area covered by the oil layer was left unaffected by wind and had an attenuating effect on the water surface. If Franklin had calculated the thickness of the oil layer created from the volume of roughly 2 mL spreading over 2000 m^2, he would have found that the layer was approximately 1 nm thick.

The next contributor was Lord Rayleigh, who attempted to measure accurately the quantity of olive oil, which was needed to cover a water surface. He found that 0.81 mg of olive oil was needed to cover an area of 555 cm^2 resulting in a 16 Å thick layer. This length appeared to be a monomolecular layer of the triolein molecule ($C_{57}H_{104}O_6$), which constitutes olive oil. Significant progress was also made by A. Pockels, who created the prototype of today well-known Langmuir–Blodgett trough (shallow container with movable barriers which are used to sweep the surface clean and to compress or relax any thin film).

Finally, the crucial step was made by I. Langmuir, who introduced a novel concept about molecular conformation at the air/water interface[2]. He also mentioned the possibility to transform such a layer at the air/water interface onto a substrate. This was, however, done afterwards by K. Blodgett and published in the Journal of the American Chemical Society (JACS) in 1934 and 1935, respectively. This milestone denoted the birth of the Langmuir–Blodgett (LB) deposition method, and Langmuir film being the expression ascribed to the monomolecular layer at the air/water interface. LB deposition refers to an approach where the sample plate is lowered into the trough vertically. If the sample is inserted horizontally, the technique is called Langmuir–Schaefer (LS). The rebirth of LB and LS deposition starts in 1980s and with numerous modifications still provides a reasonable deposition technique.

Thermodynamic equilibrium

When an arbitrary thermodynamic system is left to itself, properties such as (p – pressure, V – volume, T – temperature) generally change in time. This system, however, after a sufficiently long time, will reach a state of thermodynamic equilibrium. The equilibrium is achieved when the free energy is minimised. For systems at constant volume, this is expressed by the Helmholtz function F:

$$F = U - TS, \tag{4.1}$$

and for constant pressure changes, the free energy is given by the Gibbs' function G:

$$G = H - TS = U + pV - TS, \tag{4.2}$$

where enthalpy H is basically the sum of all the potential and kinetic energies in a system:

$$H = U + pV, \tag{4.3}$$

and U is the internal energy of a system. In both Equations (4.1) and (4.2) mentioned above, S is the entropy. Normally, this represents the heat into or out of a system divided by temperature:

$$\Delta S = \frac{\Delta H}{T}, \tag{4.4}$$

and it is also a measure of the disorder of a thermodynamic system. Equations (4.1) and (4.2) suggest that free energy G can be minimised either by reducing the internal energy U or by increasing the entropy S. At low temperatures, the internal energy of the molecules contributes more to the free energy. On the contrary, at high temperatures, the entropy of the system becomes the predominant influence. Consequently, fluid phases are stable at elevated temperatures even though they constitute higher internal energy configurations than the solid-state.

---

[1] Known as Sumi Nagashi - paper marbling method of Japanese origin.

[2] The Nobel Prize in Chemistry 1932 – "for his discoveries and investigations in surface chemistry."

Gas–liquid interface

Certain molecules can orient themselves at the gas/liquid interface in order to minimise their free energy G. The resulting surface film with a thickness of one molecule is often referred to as a monomolecular layer or monolayer. The boundary between a liquid and a gas phase (e.g. air/water interface) marks a transition between the composition and properties of two different bulk phases. The thickness of this region is of the utmost importance because this is the region where all the processes take place. A molecule at the surface is surrounded by fewer molecules than one in the bulk liquid (see Figure 4.2). Molecules will therefore diffuse initially from the surface. The activation energy for a surface molecule escaping into the bulk will increase until it is equal to the energy of molecules diffusing from the bulk to the surface and finally reaching a state of equilibrium. The line force acting on the surface molecules is the surface tension γ.

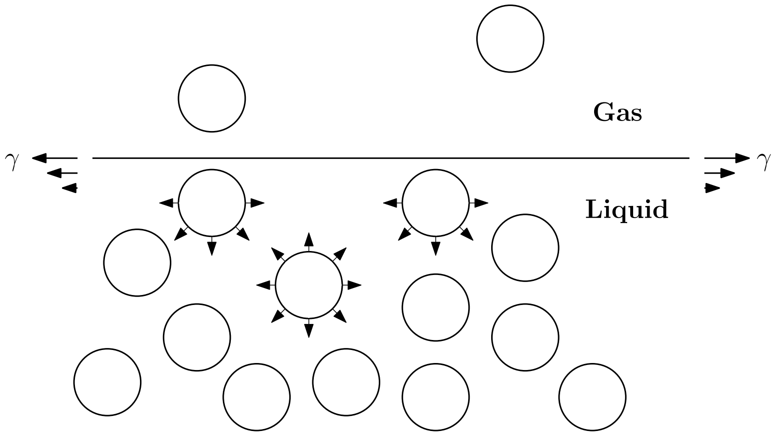

Figure 4.2: Forces in the bulk liquid and at the liquid/gas interface.

At thermodynamic equilibrium, the surface tension of a planar interface can be expressed as partial derivatives of the free energy functions with respect to the area A of the surface:

$$\gamma = \left(\frac{\partial F}{\partial A}\right)_{T,V,n_\mathrm{i}} = \left(\frac{\partial G}{\partial A}\right)_{T,p,n_\mathrm{i}}, \tag{4.5}$$

where pressure p and absolute temperature T are intensive properties, whereas volume V and n_i (e.g. number of moles, entropy, internal energy) are extensive properties.

Surface tension γ is similar to vapour pressure. It remains constant for two phases in equilibrium at the constant temperature but changes with changing temperature. Unlike the vapour pressure, which increases with increasing temperature, γ decreases with increasing temperature and becomes zero at the critical point. The presence of a monolayer on a liquid surface affects the surface tension. Therefore, it is convenient to introduce surface pressure $\mathit{\Pi}$:

$$\mathit{\Pi} = \gamma_0 - \gamma, \tag{4.6}$$

where γ_0 is the surface tension of the pure liquid and γ is the surface tension of the film-covered surface.

Monolayer formation

All compounds can be roughly divided into those that are soluble in water and those that do not dissolve in water. The former compounds are generally polar, and their charge is unevenly distributed. Such molecules possess an electric dipole moment[3] μ. Figure (4.3) shows the case

---

[3] The SI unit of electric dipole moment is (C·m), it is, however, common to use Debye unit ($1\,\mathrm{D} \doteq 3.336 \times 10^{-30}\,\mathrm{C \cdot m}$), electric dipole moment of water is 1.85 D.

for a water molecule. Each of the two hydrogen atoms shares an electron pair with the oxygen atom. The geometry of the shared electron pairs in the outer shell of the oxygen causes the V-shape of a water molecule. The strong electron-withdrawing ability of oxygen causes a local negative charge in the vicinity. Although the water molecule as a whole is electrically neutral, its positive and negative charges are widely separated.

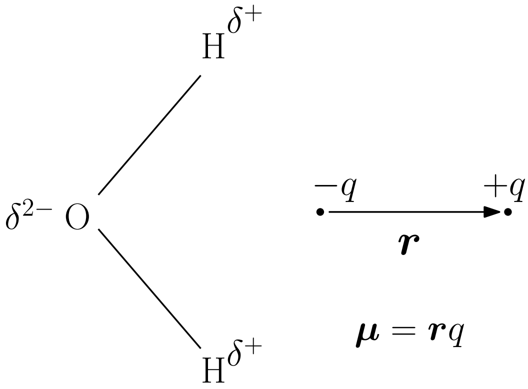

Figure 4.3: Origin of electric dipole moment $\boldsymbol{\mu}$ in a water molecule.

The solvent properties of water are closely related to the attraction between its electric dipoles and the charges associated with the solute. The molecules of most monolayer-forming materials are composed of two main parts: one part is water-soluble (hydrophilic = water-loving), and the opposite one is not (hydrophobic = water-hating). These molecules are called amphiphiles. The most important representatives are soaps and phospholipids.

Water is one of the most widespread and common solvents, and thus it is important to thoroughly describe its properties. In addition, water is also usually used in the LB trough as a sub-phase (i.e. majority liquid, which takes part in a deposition process). Unfortunately, coordination metal complexes, as well as graphite, are not soluble in water. Therefore, it is necessary to use specific organic solvents (e.g. chloroform, dichloromethane, dimethylformamide) in order to dissolve these compounds. When such material is applied firstly onto the water surface, spreading will continue until the surface pressure reaches an equilibrium value. This happens spontaneously, and generally, the material is being added as long as it tends to spread observably on the water surface.

When the monolayer is compressed on the water surface, it will undergo phase transformations. These changes can be observed by monitoring the surface pressure $\mathit{\Pi}$ as a function of the area occupied by the film. This diagram is shown in Figure (4.4) and is unique for every substance and gives information about the formation of the monolayer. Therefore, it is the very first step in the investigation of a new material created at the air/water interface. It is common, in such a plot, to divide the film area A by the total number of molecules N on the water surface to obtain the area per molecule:

$$a = \frac{A}{N} = \frac{A}{nN_\mathrm{A}} = \frac{AM}{mN_\mathrm{A}} = \frac{AM}{cVMN_\mathrm{A}} = \frac{A}{cVN_\mathrm{A}}, \tag{4.7}$$

where n is the amount of a solute in moles, N_A is the Avogadro constant[4], m is mass of a solute, M is the molar mass of a solute, c is the specific molar concentration of a solution, and V is its volume.

---

[4] Avogadro constant in SI units: $N_\mathrm{A} \doteq 6.022\times 10^{23}\mathrm{mol}^{-1}$.

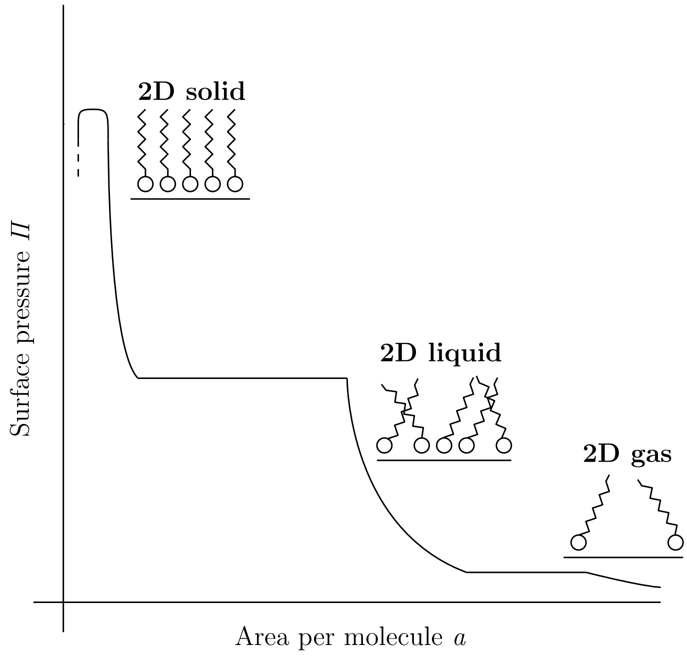

Figure 4.4: Illustration of surface pressure versus area per molecule diagram.

Equation (4.7) is derived from the ideal-gas model by using a two-dimensional variation of conventional kinetic theory. The molecules in the film can move with an average translational kinetic energy of $k_\mathrm{B}T/2$ for each degree of freedom. This leads to the following equation for an ideal 2D gas:

$$\Pi a = N k_\mathrm{B} T, \tag{4.8}$$

where Π is the surface pressure, a is the area per molecule, N is number of molecules, and k_B is the Boltzmann constant[5], and T is the absolute temperature.

Surface pressure measurement

The surface pressure Π is usually measured by the Wilhelmy plate. Figure (4.5) shows the principle, which is as follows: a plate, very often made out of filtration paper, is partially immersed in water. The force acting on this plate is the sum of three force contributions; the gravity F_G and the surface tension F_ST, both are acting downwards, whereas the buoyancy F_B acting on the plate is acting upwards. This can be expressed by the following equations:

$$F = F_\mathrm{G} + F_\mathrm{ST} - F_\mathrm{B} \tag{4.9}$$

$$F = m_\mathrm{p} g + \gamma \cos\alpha P - m_\mathrm{l} g \tag{4.10}$$

for a rectangular plate of dimensions l_p, w_p, t_p, material density ϱ_p, and perimeter P immersed to a depth h in a liquid of density ϱ_l the net force is given by:

$$F = \varrho_\mathrm{p} g l_\mathrm{p} w_\mathrm{p} t_\mathrm{p} + 2\gamma(t_\mathrm{p} + w_\mathrm{p})\cos\alpha - \varrho_\mathrm{l} g t_\mathrm{l} w_\mathrm{l} h, \tag{4.11}$$

where γ is the surface tension of the liquid, α is the contact angle on the solid plate and g is the gravitational constant. By this approach it is possible to measure surface pressure by measuring the change of force F acting on a plate with and without a molecular film at the surface. During a deposition, Wilhelmy plate is completely wetted after a while, that means $\alpha = 0$ and $\cos(0) = 1$. The surface pressure can be subsequently obtained from following equations:

$$F_0 = F_\mathrm{G} + 2\gamma_0(t_\mathrm{p} + w_\mathrm{p}) - F_\mathrm{B}, \tag{4.12}$$

---

[5] Boltzmann constant in SI units: $k_\mathrm{B} \doteq 1.381 \times 10^{-23} \mathrm{J \cdot K^{-1}}$.

$$F = F_\mathrm{G} + 2\gamma(t_\mathrm{p} + w_\mathrm{p}) - F_\mathrm{B}, \tag{4.13}$$

giving the final relation for surface pressure connecting the change in force and the change in surface tension

$$\mathit{\Pi} = \gamma_0 - \gamma = \frac{F_0 - F}{2(t_\mathrm{p} + w_\mathrm{p})}. \tag{4.14}$$

The sensitivity can be increased by using a very thin plate, so that $t_\mathrm{p} \ll w_\mathrm{p}$, and giving the following equation

$$\Delta\gamma = \frac{\Delta F}{2w_\mathrm{p}}. \tag{4.15}$$

The force is then determined by measuring the changes in the mass of the plate, which is directly coupled to a sensitive microbalance.

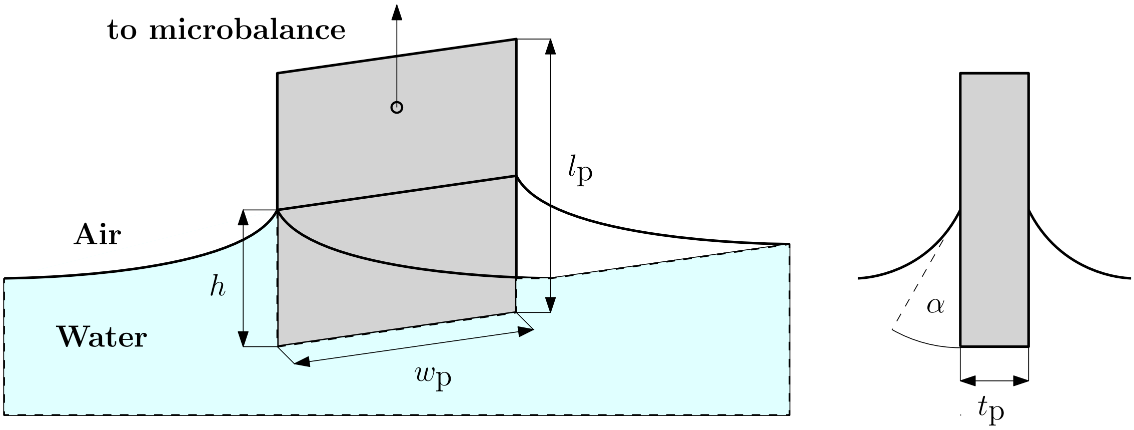

Figure 4.5: A Wilhelmy plate: the perspective view and the side view.

Experimental setup

Figure (4.6) and (4.7) show Langmuir–Schaefer experimental setups. The working principle is as follows: the solution or suspension is injected onto a subphase (deionised water in this case) surface (1). The movable barriers (2) are slowly closed and reduced the surface area of a trough top. The process of layer formation is observed by optical microscope (3) with visual output (4) to a monitor. A Wilhelmy plate (5), usually a piece of filtration paper, is used to measure the surface pressure. A substrate (6) onto which the deposition takes place. The suction pump (7), together with a mounted syringe, pumps out water, and thus the water level is lowered, and the deposition is done. The term modified stands for the deposition carried out by elevating and tilting the substrate. This can be done by placing metal nuts of different sizes underneath the substrates.

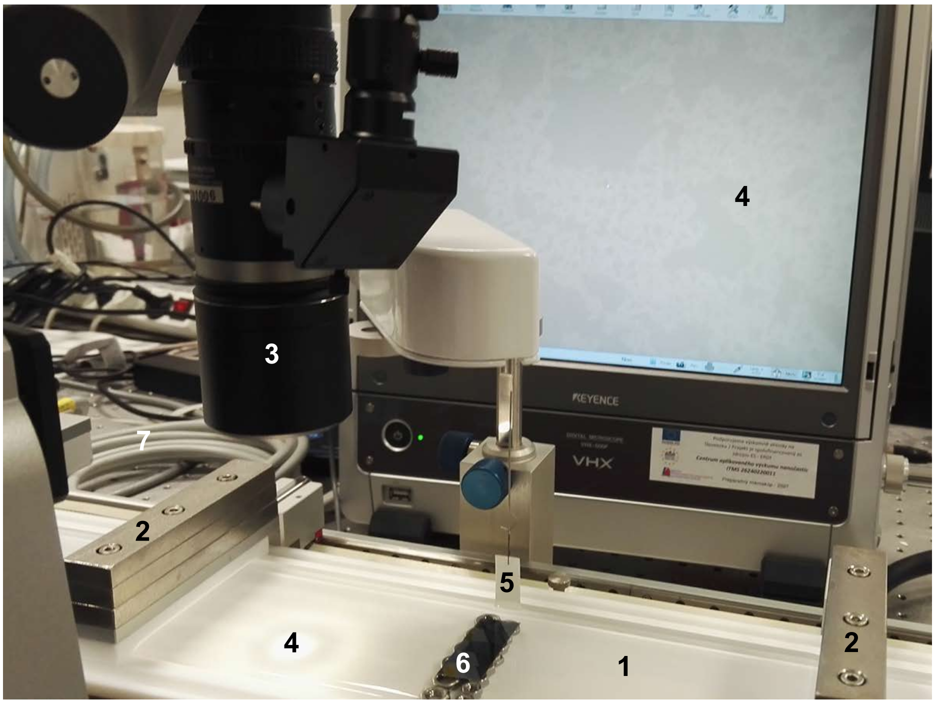

Figure 4.6: Image of Langmuir–Schaefer setup for deposition. Numbers indicate individual components of the trough. (1) Trough top with injected solution/suspension, (2) movable barriers, (3) optical microscope, (4) visual output, (5) surface pressure sensor, (6) substrates for deposition, and (7) suction pump.

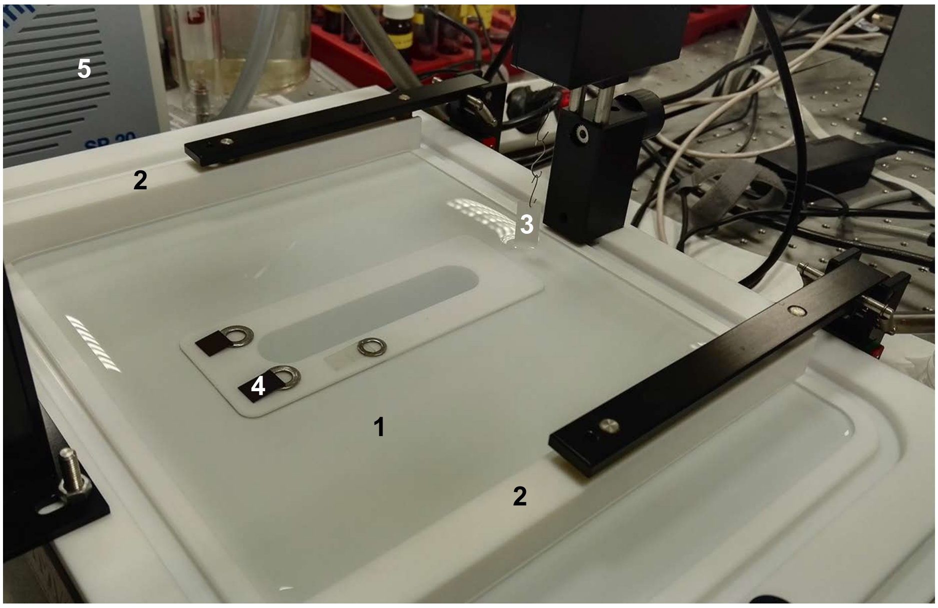

Figure 4.7: Image of Langmuir–Schaefer set-up for molecular deposition. Numbers indicate individual components of the trough. (1) Trough top with injected molecular complexes, (2) movable barriers, (3) surface pressure sensor, (4) graphene-covered Si/SiO_2 substrate, and (5) suction pump.

The main advantage of this wet-chemistry method is the possibility to use many various substrates at the same time during the deposition. I would like to thank Dr. Peter Šiffalovič from the Slovak Academy of Sciences in Bratislava, Slovak Republic, for giving me the opportunity to use such a setup.

4.1.2. Thermal sublimation

Another approach for the deposition of thin films of coordination compounds is by thermal sublimation. A custom sublimation chamber was designed and built to perform controlled thermal sublimation of bulk powder molecular compounds onto various substrates in high-vacuum conditions. The whole sublimation setup was developed as a part of this thesis and includes the following parts that compose the whole assembly as shown and described in Figure (4.8).

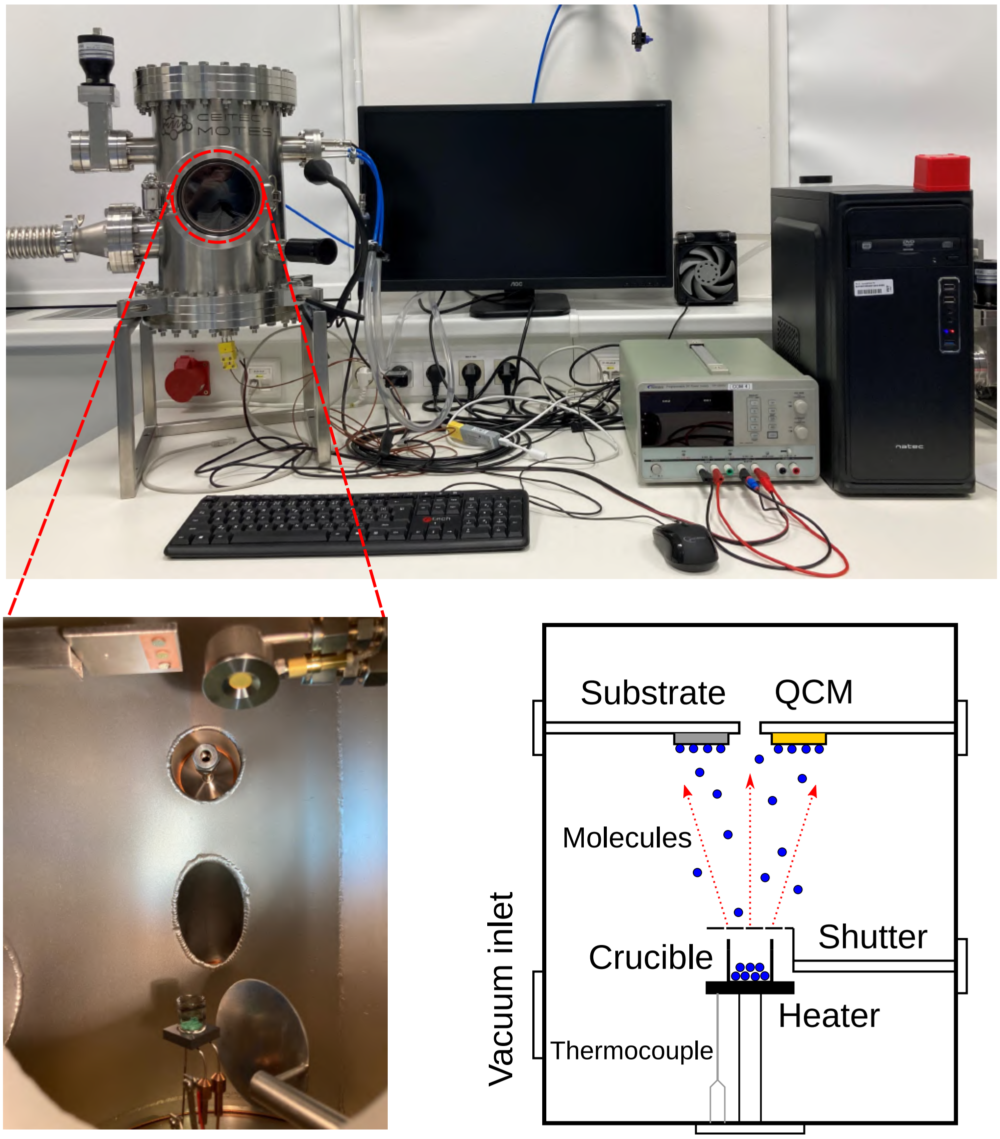

Figure 4.8: The complete sublimation solution consists of the main sublimation chamber based on a frame, a DC power supply, a PC with monitor, a cooling station with a pump and a fan for a quartz crystal microbalance (QCM) cooling during the sublimation. Holder with substrates is placed coaxially with QCM balance to monitor thickness during sublimation. Crucible is placed on a heater with temperature monitored by thermocouple. Molecules heated to specific sublimation temperature sublime, and flux hits substrate and QCM where a thin layer of material grows. The shutter can be either closed or opened.

1. **Stainless steel chamber** (⌀200 mm, manufactured by Activair, Czech Republic):
    - The main part of the setup is described in Figure (4.9).
    - made out of INOX 1.4301 stainless steel designed to meet UHV requirements (1×10^{-9} mbar)

- flanges are connected by tungsten inert gas (TIG) welding, polished by glass microspheres
- the maximum leak rate of 1×10^{-8} Pa·L/s
- the chamber offers following flanges (CF = conflat joint with copper ring sealing, e.g. 16 = $\varnothing$16 mm): 1x CF16, 4x CF40, 1x CF63, 1x CF100, 1x CF200, and 1x CF200 blank to CF40 reduction.

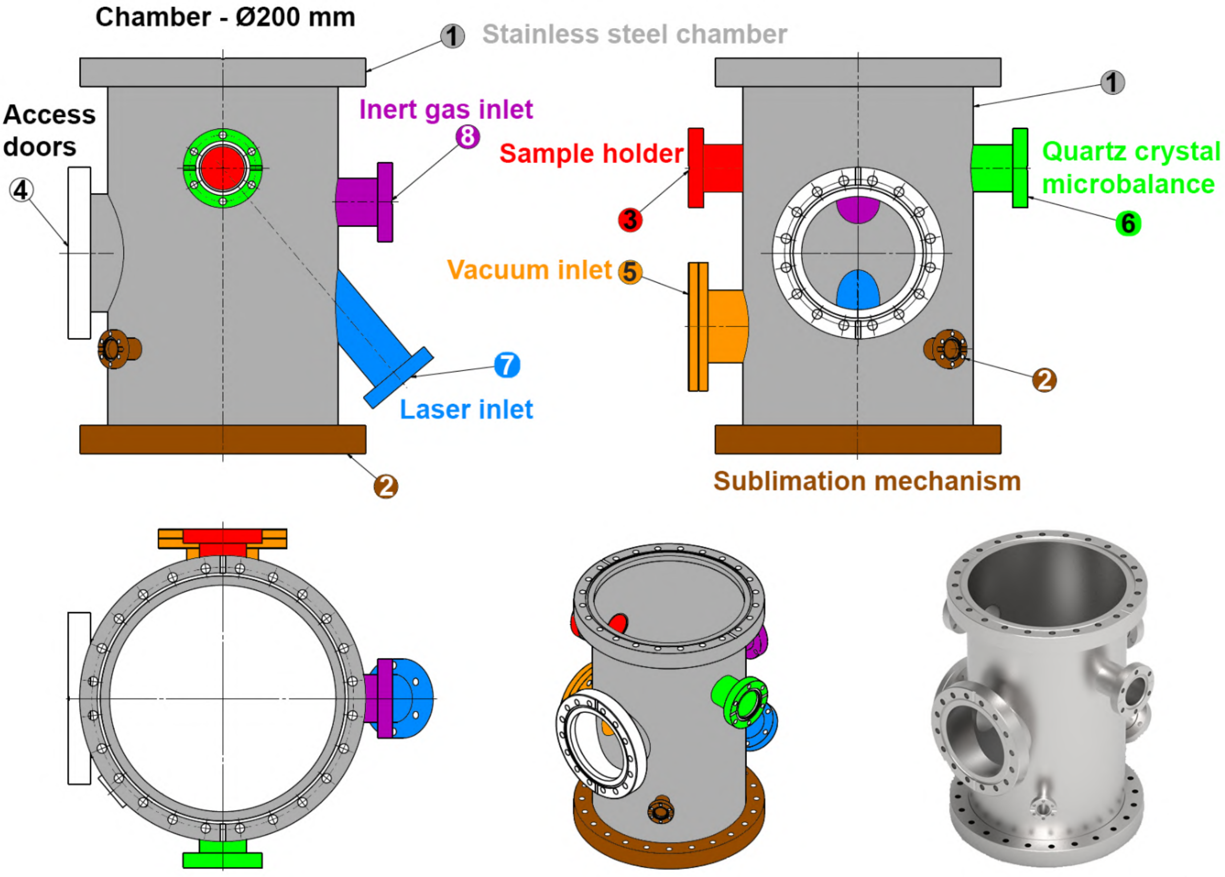

Figure 4.9: Scheme of a custom-built sublimation chamber with numbered parts.

2. **Sublimation mechanism** (CF40): transfers molecular compounds from a bulk power onto a substrate attached to the sample holder:
    (a) **DC powder supply** (Programmable Twintex TP-3305U): a multi-channel programmable power supply with remote access possibility. The detailed scheme of remote pressure readout for the sublimation chamber is in Appendix A: (8).
    (b) **Electrical feedthrough** (LewVac TC F/T type K power 1 kV 25 A Cu): a flange with feedthrough connecting a DC power supply outside of evaporation chamber with a heating basket inside the chamber.
    (c) **Thermocouple** (Omega UTC-USB A/D converter + Omega K-type thermocouple TJM-CA310-M100U-150): connected to the heating element for monitoring of sublimation temperature.
    (d) **Heating element** (Bach Resistor Ceramics): custom-made Si_3N_4 heater.
    (e) **Crucible** (Testbourne): Quartz, carbon or hexa boron nitride inert crucible holding sublimable powder compounds.

   (f) **Crucible shutter** (CF16): attached to the sublimation chamber, blanks the crucible until it reaches the required temperature and prevents from premature sublimation.

3. **Sample holder** (CF40): custom design with the possibility to sublime onto multiple substrates.
    - Custom design holder with the possibility to sublime onto multiple substrates.
    - Stainless steel gate valve (Highvac - 11120-0154) for connection of mobile UHV chamber for connection to HF-ESR spectrometer and other vacuum instruments.

4. **Access doors** (CF100, LewVac FL-QADV-100CFS): located in the middle of the chamber and designed to provide visual control over sublimation and handling of crucible inside the chamber.

5. **Vacuum inlet** (CF63): connection to turbo-molecular vacuum pump Edwards T-station 85 with the base pressure of 1×10^{-6} mbar, UHV accessible by adding ion pump, pressure monitored by wide range gauge connected to the station. The detailed scheme of remote pressure readout for the sublimation chamber is in Appendix B: (8).

6. **Quartz crystal microbalance** (QCM) (CF40, Inficon STM2-USB): a system for monitoring the film thickness and sublimation rate is composed of a controller, sensor head and a sensitive quartz crystal coated by gold with a specific resonance frequency that changes based on its mass difference caused by sublimated material. This important system is coaxially aligned with a sample holder in order to guarantee the same thickness on QCM, as well as on the sample.

7. **Laser inlet** (CF40, option): positioned at 40° with respect to chamber cylinder vertical axis allows us to irradiate sample during the deposition, this can be applied in photochemistry to activate ESR inactive systems to form free radicals measurable in our ESR spectrometers or to create defects in layered materials.

8. **Inert gas inlet** (CF 40): enables us to fill the chamber with an inert atmosphere and create overpressure, which is necessary for the protection of our sample from oxidation and moisture when taking out samples during venting from the chamber.

4.2. Characterisation techniques

4.2.1. HF-ESR spectroscopy

This section will briefly illustrate and describe the HF-ESR spectrometer located at CEITEC BUT. Figure (4.10) shows such HF-ESR setup. It is an example of a continuous-wave (cw) arrangement. There are five main parts of such setup: the tunable microwave sources (1) provide microwave radiation of variable frequency: $\nu = 82 - 1100\,\mathrm{GHz}$, which is propagated by the quasi-optics (2). Higher frequencies are accessed by amplifying and multiplying the microwave base frequency: $\nu = 9 - 14\,\mathrm{GHz}$. The variable temperature insert (VTI) (3), $T = 1.6 - 320\,\mathrm{K}$, is put in a tunable superconductive magnet (4) capable of magnetic fields up to $B = 16\,\mathrm{T}$. The signal detection is provided by a heterodyne receiver which mixes the input signal with a local oscillator tuned to a higher frequency giving a new set of frequencies that are amplified (5).

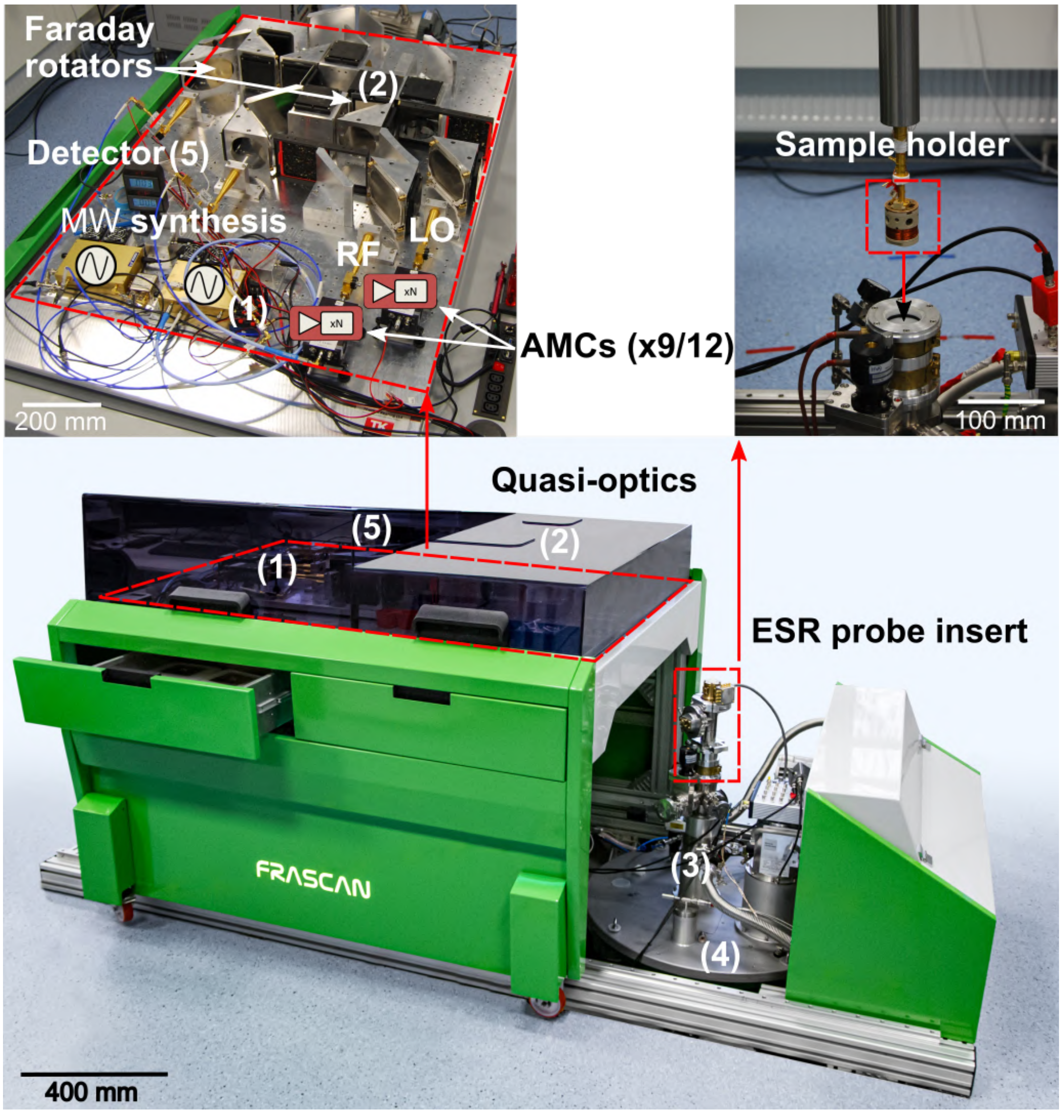

Figure 4.10: The HF-ESR spectrometer with indicated setup components. The top-left inset figure shows the quasi-optics (2) table with MW sources (1) with radio frequency (RF) and local oscillator (LO) arm. The amplification multiplication chain (AMC) is used to multiply the base frequency. The top-right inset shows the insertion of a sample holder to the interlock and further to VTI insert (3) and superconductive magnet (4).

1. **Microwave source**: We use two microwave sources (Virginia Diodes, USA) to generate the microwave radiation. The desired microwave frequency can be obtained by the multiplication of the base frequency $\nu = 9 - 14\,\text{GHz}$ generated by the microwave synthesiser (VDIS0122). The highest accessible frequency of our setup is 1125 GHz. The following Figure (4.11) illustrates the microwave generation and superheterodyne detection.

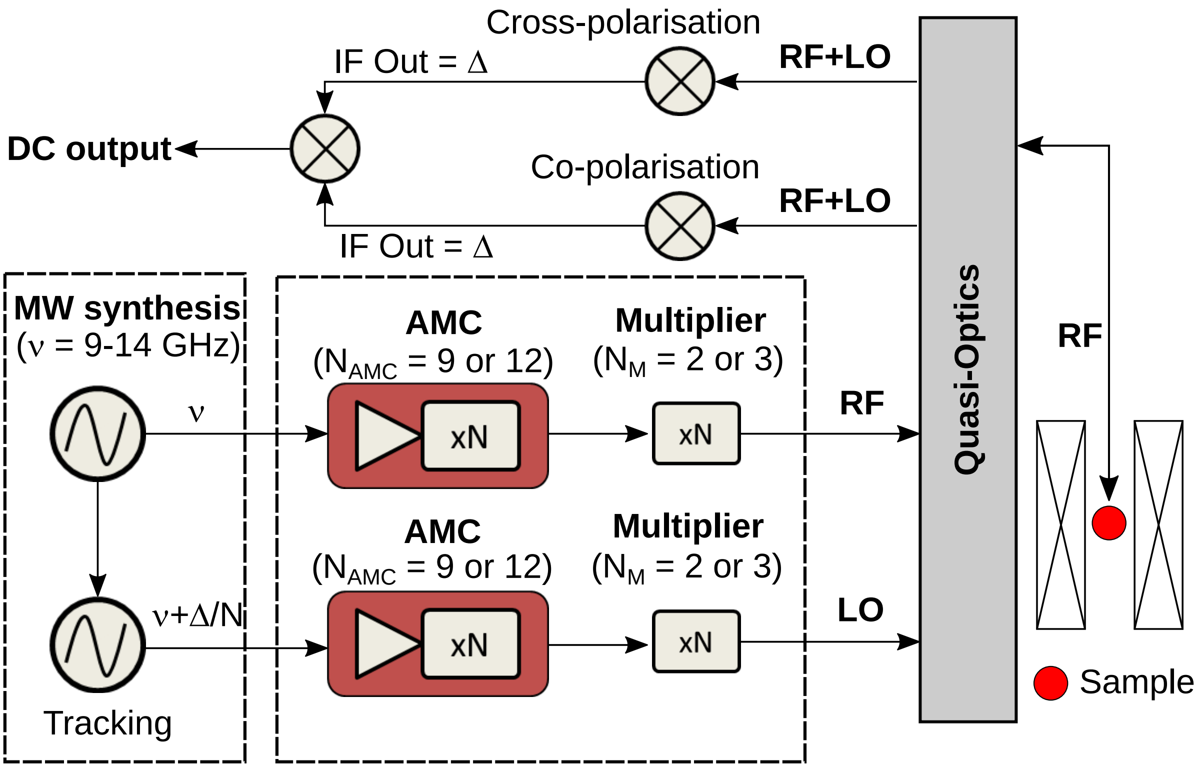

Figure 4.11: Scheme of microwave (MW) propagation from a synthesiser with frequency $\nu = = 9 - 14\,\text{GHz}$. The second MW source is phase-locked with frequency offset Δ/N. The signal from both sources propagate through an amplification-multiplication chain (AMC) with frequency multiplication $N = 9$ or 12 and is further multiplied by multipliers (doublers and triplers). The desired frequency is created by the multiplication of the base frequency ν. The first channel is labelled as radio frequency (RF), and the second is the local oscillator (LO). They both propagate through the quasi-optical table, and the RF arm travels through the sample, whereas LO serves as power feedback. The RF signal changed by a sample is then cross-polarised, and the unchanged signal is co-polarised. Both channels mix in the final mixer, and DC signal output is detected. The intermediate frequency (IF) in our system is $\Delta = 1.8\,\text{GHz}$.

2. **Quasi-optics**: The propagation of a microwave from the source to the sample is provided by a free-space quasi-optical table (Thomas Keating, UK). The Gaussian beam is propagated from feed horns. It is then refocused by elliptical mirrors placed within certain distances. The beam also goes through a series of polarisers that filter out unwanted polarisation components. Metallic mirrors are used to reflect and extend the beam's travel distance. The power losses during the propagation are roughly 3 dBm in our setup. The microwave from a table propagates to a sample through the teflon window and inside the corrugated waveguide within VTI placed in a cryostat inside a superconductive magnet.

3. **Variable temperature insert (VTI)**: A rod housing for a sample holder, wiring, and microwave waveguide on the inside. In the lower part, there is a place for various sample holders for pellet, chip, and single-crystal samples. The special load-lock system is used in this setup to prevent any air and moisture access during the sample removal. VTI

allows for temperature control in the range of $1.6 - 320\,\mathrm{K}$ during the experiment, which is important. The sample properties or the increased sensitivity can be achieved by going to very low temperatures.

4. **Magnetic Field**: The HF-ESR operates with the superconductive cryogen-free magnet (Cryogenics, UK) placed under the laboratory's floor with magnetic fields up to $B = 16\,\mathrm{T}$. When going to these high magnetic fields, it is crucial to ensure stability and avoid interference with other electromagnetic devices.
5. **Detection**: Absorption lines in the ESR spectrum are observed when the separation of two energy levels is equal to (or very close to) the quantum of an incident microwave photon, $E = h\nu$. The absorption of such photons by a sample is then indicated as a change in the detector current. The detection used in our setup is superheterodyne. It is based on mixing the input signal from the first source, which excites a sample and the second source serving as a local oscillator.

The development in the field of HF-ESR spectrometers is rather slow due to the technical requirements on microwave sources, propagation systems, and detectors in the THz range. Up to this date, there are only a few laboratories worldwide capable of HF-ESR measurements on spectrometers that are mostly home-built.

4.2.2. X-ray photoelectron spectroscopy (XPS)

X-ray photoelectron spectroscopy (XPS), also known as Electron Spectroscopy for Chemical Analysis (ESCA), is a widespread spectroscopic technique for the analysis of chemical composition on a sample's surface. It is based on the photoelectric effect, which was firstly observed by H. Hertz in 1887 [74]. Explanation of this effect was enabled with electromagnetic radiation energy quantisation provided by A. Einstein[6] in 1905 [75]. XPS as an analytical instrument was then developed in 1960s by the group of K. Siegbahn[7] at Uppsala University [76].

XPS working principle is depicted in Figure (4.12). A sample is irradiated by an X-ray source with a specific radiation wavelength (usually Al-Kα at 1486.6 eV or Mg-Kα at 1253.6 eV). This radiation penetrates the topmost layers of a sample, usually tens of nanometers, which makes it a perfect characterisation technique for the chemical composition of thin films on surfaces. Photons in these layers interact with matter and cause electron emission based on the photoelectric effect. Emitted electrons have kinetic energy:

$$E_\mathrm{k} = h\nu - (E_\mathrm{B} + \Phi_\mathrm{spec}), \tag{4.16}$$

where $h\nu$ is the energy of incident electromagnetic radiation (h is Planck constant and ν is frequency), E_B is binding energy of electron related to Fermi level and Φ_spec is the work function of the spectrometer which represents the energy necessary to release an electron from Fermi level to vacuum level.

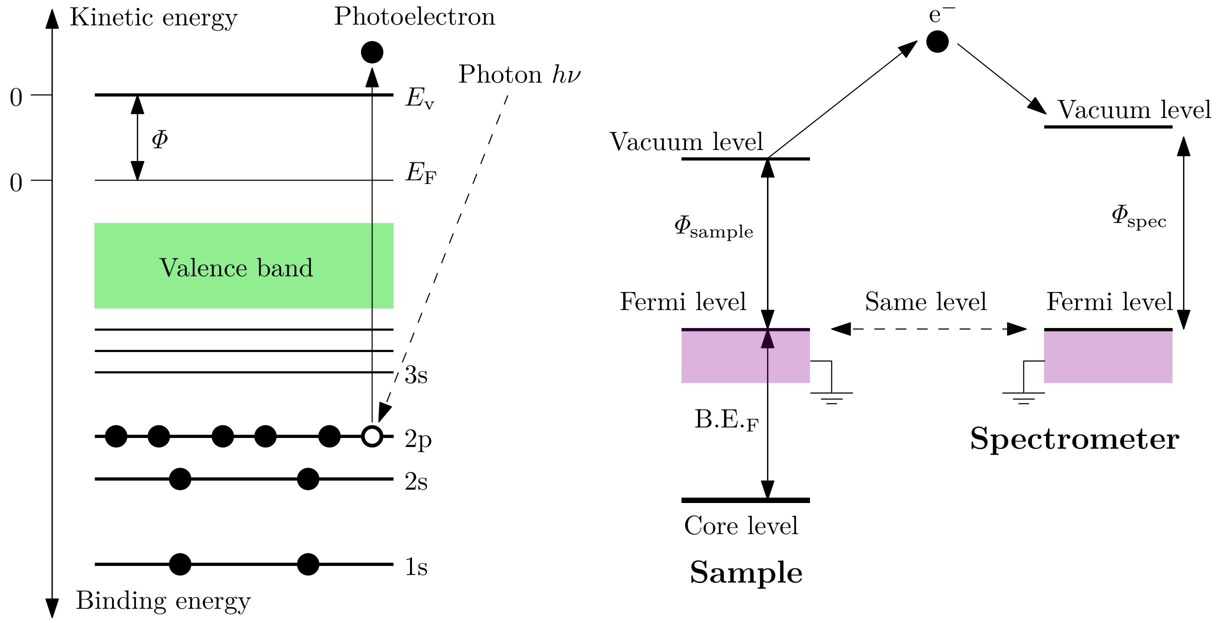

Figure 4.12: Left: scheme of XPS basics with incident photon pulling photoelectron from a sample. Right: illustration of binding energy B.E. reference.

XPS spectra also often incorporate Auger peaks caused by the Auger effect, as shown in Figure (4.13). A photoelectron from the core levels is replaced by a higher energy electron which leads to emission of energy either in the form of photon or can be given to another electron known as Auger electron.

---

[6] 1921 – Nobel Prize in Physics ”for his services to Theoretical Physics, and especially for his discovery of the law of the photoelectric effect.”

[7] 1981 – Nobel Prize in Physics ”for his contribution to the development of high-resolution electron spectroscopy.”

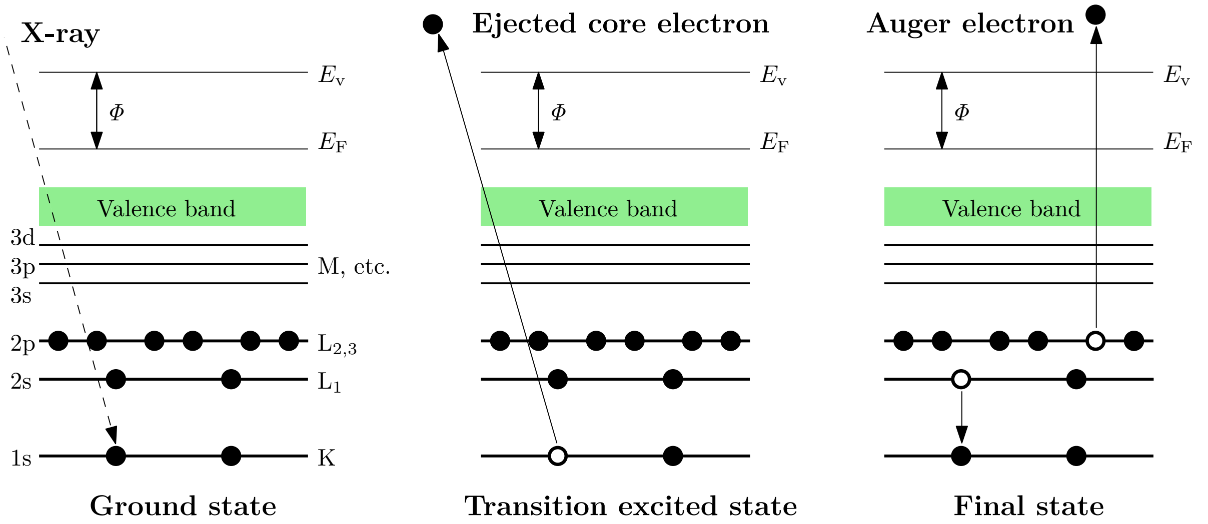

Figure 4.13: Scheme of X-ray induced Auger electrons. Incoming X-ray ejects the core electron and electron from a higher level fills the vacancy resulting in emission of Auger electron.

An example of survey XPS spectrum of a bulk powder tetracoordinate Co(II) complex, with chalcone ligands [Co(4MeO-L)$_2$Cl$_2$], where chalcone imidazole-derivative ligand 4MeO-L = (2E)-3-[4-(1H-imidazol-1-yl)phenyl]-1-(4-methoxyphenyl)prop-2-en-1-on, investigated during my doctorate studies in Chapter 5 (5.3).

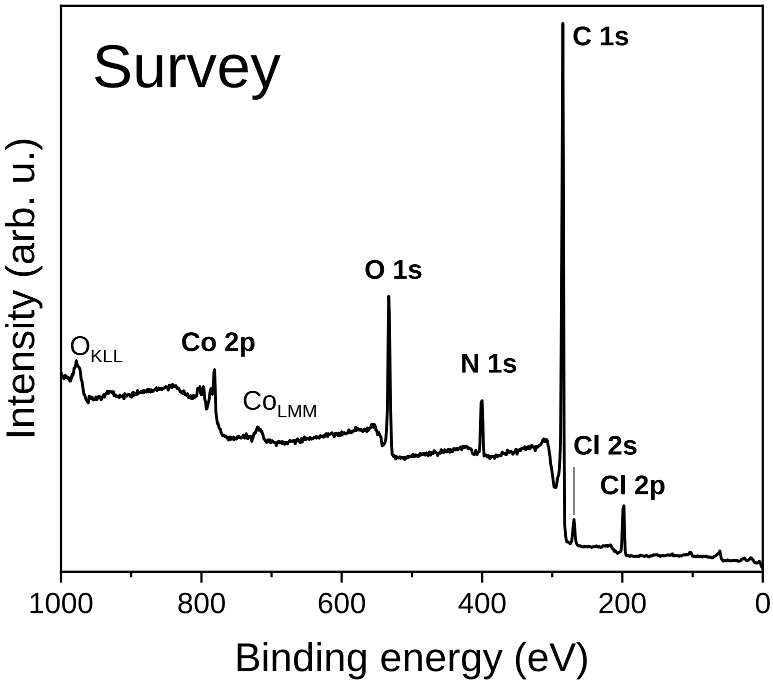

Figure 4.14: Illustration of survey XPS spectrum with visible detected photoelectron and Auger peaks O_{KLL} and Co_{LMM}.

4.2.3. Raman spectroscopy (RS)

Raman spectroscopy is a non-destructive technique for the composition and structure analysis of samples. It is based on inelastic light scattering. This spectroscopy was described by C. V. Raman[8] and his colleague K. S. Krishnan in 1928 [77].

Figure (4.15) shows the basics of Raman scattering schematically. A sample is irradiated by a monochromatic incident source (laser). This light is absorbed by a sample and leads to energy transitions (excitation) in the sample with subsequent relaxation, light emission. The origin of Raman scattering is the inelastic scattering of an incident photon. It is a two-photon process during which annihilation and creation of photons occur. Molecular modes observed by this method are especially molecular vibrations that are characterised by frequency Ω. Every molecule has its own spectra originating from different vibrational modes, and thus Raman scattering can be imagined as a chemical fingerprint of a molecule [78].

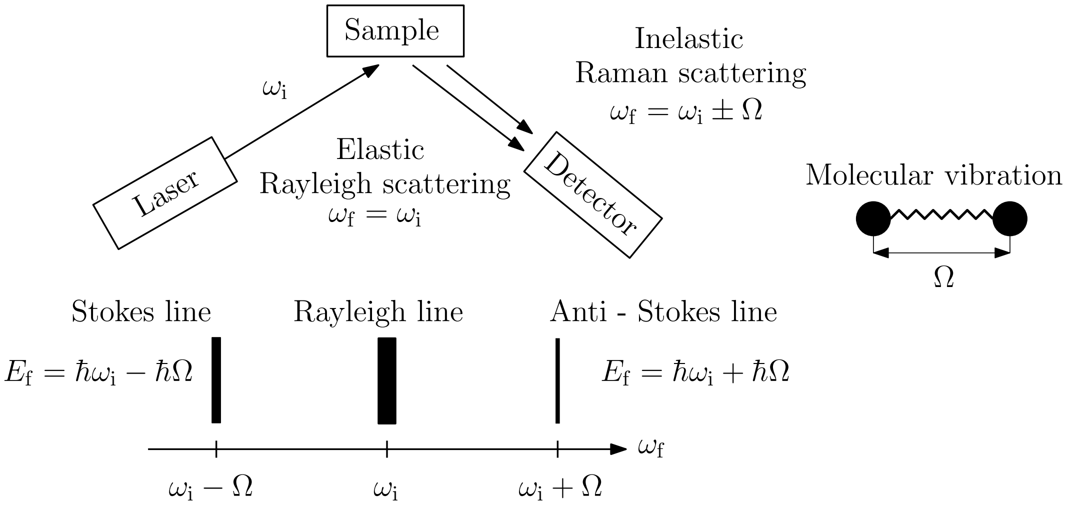

Figure 4.15: Scheme of Raman scattering in a sample. For the case of elastic scattering, the Rayleigh line is observed. Inelastic scattering gives origin to Raman signal. There are two observable lines. The first is Anti-Stokes lines that have higher energy, and the second is Stokes lines with lower energy.

In a typical Raman spectroscopy measurement, spectra show vibrational frequency in wavenumbers $\tilde{\nu}$ (cm^{-1}). Peaks indicate specific chemical groups (i.e. types of bonds). The usable energy range for the Raman scattering is typically $(200 - 4000)\,\mathrm{cm}^{-1}$. The effect as such is very weak. Approximately only 1 out of 10^7 incident photons is inelastically scattered and contributes to the Raman signal. It is also common to consider only Stokes lines, as they have a higher probability of occurrence compared to Anti-Stokes lines. This is given by Boltzmann distribution:

$$p_\mathrm{i} = \frac{e^{\frac{-\varepsilon_\mathrm{i}}{k_\mathrm{B}T}}}{\sum_{i=1}^{M} e^{\frac{-\varepsilon_\mathrm{i}}{k_\mathrm{B}T}}}, \tag{4.17}$$

where p_i is the probability of states i, ε_i the energy of state i, k_B the Boltzmann constant, T the absolute temperature of the system, and M is the number of states accessible to the system [79].

---

[8] 1930 – The Nobel Prize in Physics ”for his work on the scattering of light and for the discovery of the effect named after him.”

Therefore, as shown in Figure (4.15), Stokes lines have lower energy, and hence higher probability of occurrence. The spectra are usually plotted as intensity or counts per second (photons hitting a detector) against Raman shift given in wavenumbers (cm^{-1}) as:

$$\Delta\omega = \frac{1}{\lambda_{\text{incident}}} - \frac{1}{\lambda_{\text{scattered}}}, \tag{4.18}$$

where $\lambda_{\text{incident}}$ is the wavelength of incident light and $\lambda_{\text{scattered}}$ is the wavelength of inelastically scattered light going to the detector, which is usually a charge-coupled device (CCD) camera.

The choice of wavenumbers is apparent as it can be taken as a unit of energy. Figure (4.16) illustrates an example of Si/SiO_2 substrate with highlighted bands. The low signal near zero comes mainly from the laser source and elastic Rayleigh scattering. These signals are, however, very strong in comparison with Stokes lines and thus are filtered out in the Raman setup, usually by a notch filter, which is a band-stop filter for eliminating this huge signal. The main silicon phonon band (TO) at approximately $521\,\mathrm{cm}^{-1}$ is cut off in order to include other less intense signals from other phonon bands [80].

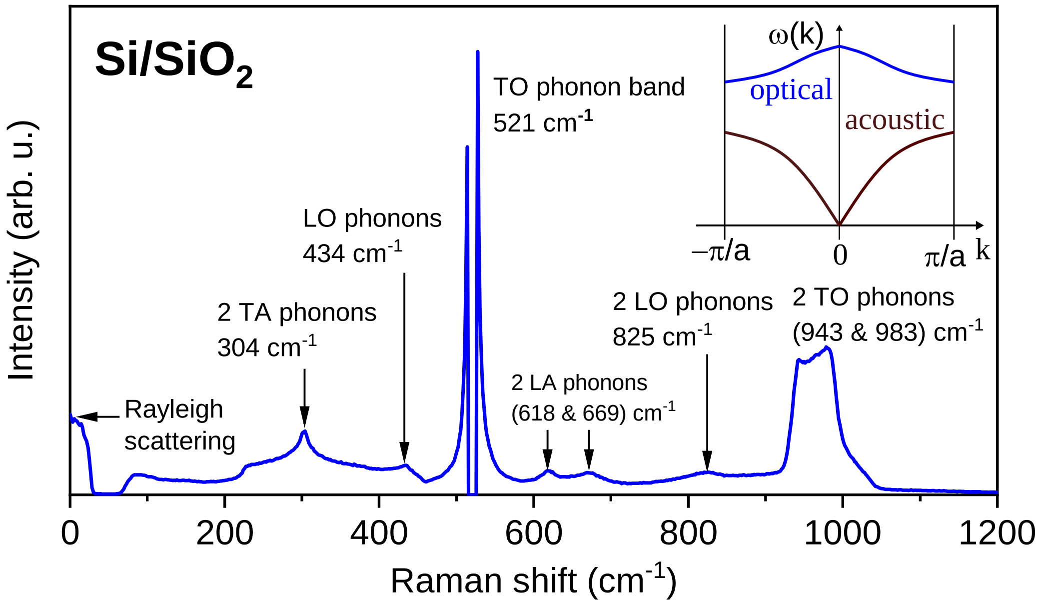

Figure 4.16: Example of Raman spectra for Si/SiO_2 substrate. Here, only Stokes lines are visible, because they produce stronger signal in comparison with Anti-Stokes lines. Inset shows the phonon dispersion relation for a linear diatomic chain with distance a between them with boundaries in Brillouin zone where k is the wavevector $k = 2\pi/\lambda$.

In summary, Raman spectroscopy is a very sensitive spectroscopic method enabling investigation of chemical bonds in a sample based on the transition from the ground state vibrational energy level and ending at a higher vibrational energy level (Stokes scattering). It provides a specific chemical fingerprint of material with fast spectra acquisition in the order of minutes along with easy sample preparation. One of the main advantages is the possibility to examine carbon-based samples (e.g. organic molecules, graphene). Therefore, it is widely used for confirmation of prepared molecular structure, as well as examining the degree of crystallinity in solid-state materials or estimating the quality of prepared structure (defects) that are also visible in the spectra.

4.2.4. Ultraviolet-Visible spectroscopy (UV-VIS)

The ultraviolet-visible spectroscopy (UV-VIS) is a spectroscopic technique in the range from $(200 - 800)\,\mathrm{nm}$ sensitive to excitations of outer electrons in atoms. Figure (4.17) shows the possibilities for a sample illuminated by a light beam with intensity I_0. The intensity of the transmitted beam I_t is lower, and the following processes occur.

- **Absorption** – if the beam frequency is resonant with a ground to excited state transition of the atoms in a sample, a fraction of this intensity is emitted (usually at a lower frequency than that of the incident beam), giving rise to the emission of intensity I_e, the other fraction of the absorbed intensity is lost by non-radiative processes; a heat dissipation.
- **Reflection** – with an intensity I_R from the external and internal surfaces.
- **Scattering** – with a light intensity I_S spread in multiple directions, due to elastic (at the same frequency as the incident beam) or inelastic (at lower and higher frequencies than that of the incident beam – Raman scattering) processes [81].

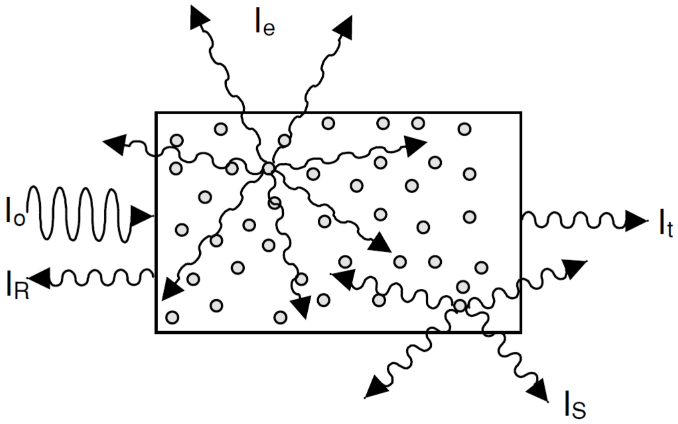

Figure 4.17: Scheme of the possible emerging beams when a sample is illuminated with a beam of intensity I_0. The circles represent atoms and defects that are interacting with the incoming light beam. Adapted from [81].

The absorbance measurement is illustrated in the following Figure (4.18).

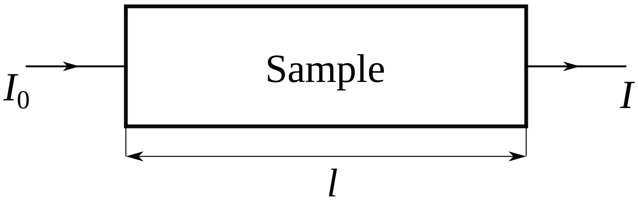

Figure 4.18: The basic scheme where radiation of intensity I_0 falls on the absorption cell of length l containing absorbing material of concentration c. The radiation emerges with intensity I.

The absorbance is defined then by Lambert–Beer law:

$$A = \log_{10}\left(\frac{I_0}{I}\right) = \varepsilon c l, \tag{4.19}$$

where ε is a function of wavenumbers $\tilde{\nu}$ and it is the molar absorption coefficient or molar absorptivity, l is length of the sample, and c is the concentration of sample [82].

A scheme of the components of a typical UV-VIS spectrometer are shown in the following Figure (4.19).

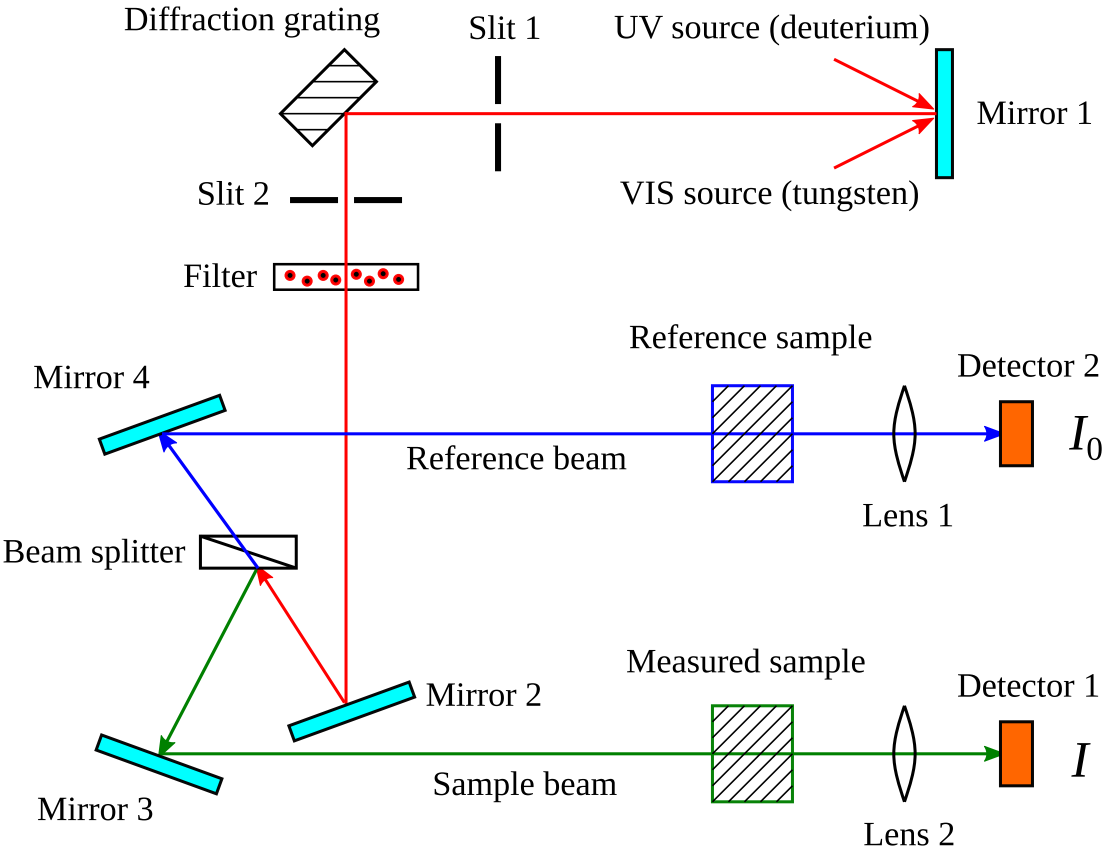

Figure 4.19: The light beam (red) propagates from a light source: ultraviolet (UV) source (deuterium) or visible (VIS) source (tungsten). The UV region scanned is usually in the range $(200 - 400)$ nm and the VIS $(400 - 800)$ nm. This beam is separated into distinct wavelengths by a diffraction grating. Every single monochromatic wavelength is then split into two equal intensity beams by a 50/50 beam splitter. The sample beam (green) passes through a studied sample. The second reference beam (blue) passes through a reference sample. In this regard, for solution samples, quartz cuvettes with $l = 10$ mm are usually used. The reference sample serves as background. The intensities of both light beams are then measured at the detector and compared. The intensity of the reference beam with little to no absorption is I_0 and the intensity of the sample beam is I.

4.2.5. Atomic force microscopy (AFM)

Atomic force microscopy (AFM) is a microscopic technique used for analysing the topography of samples. It was firstly introduced by G. Binnig[9], C. F. Quat, and Ch. Gerber [83] in 1986. The principle is based on mapping the attractive and repulsive forces between atoms of the sample and a tip of a probe. The probe is usually a very sharp, ideally one atom, etched tip attached to a flexible cantilever which is being slightly deflected due to the interactions. The deflection is detected by a laser beam that points at the tip of the cantilever and reflects on the sensitive photodiode. This photodiode is divided into four quadrants in such a way that in the equilibrium position, the measured intensity of the incoming laser beam is the same in individual quadrants. Upon deflection, the laser beam will deviate from the middle and detected intensity in each quadrant will differ. Figure (4.20) illustrates an AFM setup.

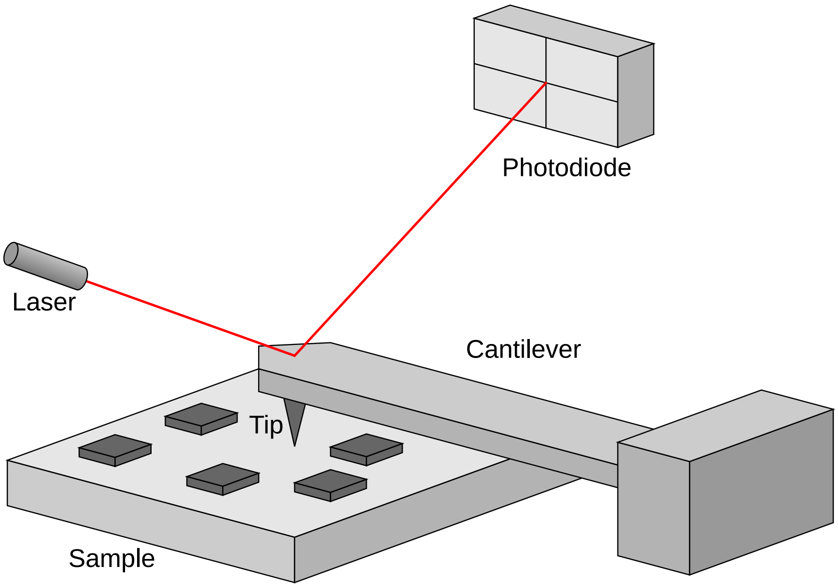

Figure 4.20: Scheme of AFM microscope. Adapted and with permission of my colleague and former bachelor student Šárka Vavrečková [84].

Repulsive or attractive forces dominate based on the tip distance from a surface. These interactions can be approximated by Lennard-Jones potential [85] as follows:

$$\omega(r) = 4\omega_0 \left[\left(\frac{\sigma}{r}\right)^{12} - \left(\frac{\sigma}{r}\right)^{6} \right], \tag{4.20}$$

where r is the distance between tip atoms and a surface, σ is the equilibrium distance between atoms and ω_0 is the minimal potential energy. The force can be derived from the negative derivation of potential energy by r as:

$$F(r) = -\frac{\mathrm{d}\,\omega(r)}{\mathrm{d}\,r} = 24\omega_0 \left[\left(\frac{2\sigma^{12}}{r^{13}}\right) - \left(\frac{\sigma^{6}}{r^{7}}\right) \right]. \tag{4.21}$$

Repulsive forces (consequence of Pauli exclusion principle) are proportional to r^{-13} and attractive forces (van der Waals forces) are proportional to r^{-7}. Figure (4.21) illustrates dependency of Lennard-Jones potential $\omega(r)$ and force $F(r)$ acting between atoms. The repulsive force is above the abscissa, and the attractive is below. The distance r_e denotes minimum potential

---

[9] 1986 – The Nobel Prize in Physics "for design of the scanning tunneling microscope", which is a predecessor of AFM.

energy, and the final forces are zero. The scheme also illustrates different AFM modes: contact, non-contact, and tapping.

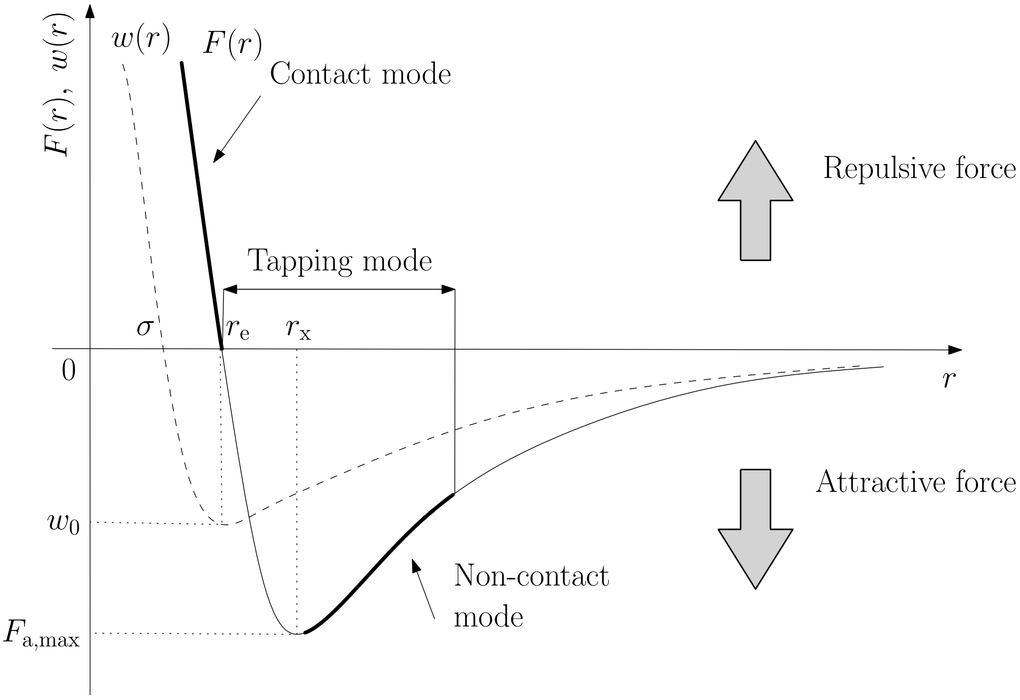

Figure 4.21: Lennard–Jones potential dependency ω and force F for distance r of two atoms. Adapted and with permission of my colleague Igor Turčan [86].

Based on the distance between tip and surface, different AFM modes are distinguished.

- **Contact mode** - the tip moves in the vicinity of the surface, and the cantilever is bent by repulsive force. This mode can be further split into two regimes - constant height or constant force.
- **Non-contact mode** - in this mode, the tip is further from the surface, and the cantilever feels attractive forces. These forces are very small, and the cantilever will oscillate at a resonance frequency. If moved closer to the surface, forces will change resonance frequency and amplitude. This is a safer mode as the probability of damaging the sample or dragging molecules across the sample is minimised, however, at the expense of worse resolution.
- **Tapping mode** - this mode combines the contact and non-contact mode in which the tip oscillates and occasionally touches the surface. It tries to find the sweet spot between surface damage and resolution.

4.2.6. Scanning electron microscopy (SEM)

This part will briefly mention the basics of SEM microscopy and mention the current implementation of AFM to SEM. SEM microscopes use electrons instead of light compared to conventional optical microscopy. This enables much higher magnification but also presents a few drawbacks. The sample has to be vacuum compatible and in contact with conductive tape/holder to drain excessive electrons and thus prevent the sample from charging. The physical interpretation of electron microscopy is elegantly given by using quantum mechanics, especially the de Broglie hypothesis, which introduces wave-particle duality (i.e. every particle can also be considered as a wave). Therefore, visible light used for observations in an optical microscope has wavelength λ of approximately $(360 - 700)\,\mathrm{nm}$. Such an optical system is also limited by diffraction, and thus it is possible to distinguish two points with the distance between them of approximately $d \sim \lambda/2$. This fact, however, limits principally the optical microscopy to have the maximal resolution of approximately 150 nm.

Therefore, by considering electron as the matter wave with the de Broglie wavelength:

$$\lambda = \frac{h}{p}, \tag{4.22}$$

where h is the Planck constant, and p is the momentum of a particles with mass m and speed v. Such an electron is accelerated in the SEM chamber by high voltage U. Kinetic energy of an electron can be expressed as:

$$\frac{1}{2} m_{\mathrm{e}} v^2 = eU. \tag{4.23}$$

When considering a typical accelerating voltage $U = 30\,\mathrm{kV}$, the speed of accelerated electron is obtained by expressing from the Equation (4.23) for v:

$$v = \sqrt{\frac{2eU}{m_{\mathrm{e}}}} \doteq 1 \cdot 10^8\,\mathrm{ms}^{-1}. \tag{4.24}$$

The selection of accelerating voltage determines the penetration depth of the electron beam. For lower voltages such as 1 kV, 2 kV or 5 kV the ultimate resolution is worse, but there is also higher surface sensitivity, and it is usually more convenient to use these lower voltages than high accelerating voltages such as 20 kV or 30 kV. It is also possible to use decelerating voltage at the sample to decelerate electrons for better surface sensitivity.

The speed v obtained by these considerations can be now put into Equation (4.22) with considering the accelerating voltage $U = 30\,\mathrm{kV}$:

$$\lambda = \frac{h}{p} = \frac{h}{m_{\mathrm{e}} v} \doteq 0.01\,\mathrm{nm}. \tag{4.25}$$

This is a theoretical lower limit, and there are several negligences made during this deduction. The first one is that the speed $v \approx c/3$ is very close to the speed of light c. Therefore, it would be necessary to consider also relativistic effects. However, when calculating for corrected electron wavelength, there is a negligible discrepancy in value for this case. The next approximation is made by omitting aberrations such as spherical, chromatic, diffraction, and astigmatism. All of these aberrations are making the final resolution limit worse. Nowadays, instruments come with systems designed to correct aberrations to some extent and order. Despite making several approximations and negligences, the effective resolution limit of SEM can be taken as $< 1\,\mathrm{nm}$, which is, compared to optical microscopy, still many times greater. Electron microscopy has a long tradition in my home town Brno, as of 2021, roughly 1/3 of global electron microscopes production come from Brno, Czech Republic. This production is represented by Thermo Fisher Scientific, TESCAN Orsay Holding and Delong Instruments.

Figure (4.22) shows an interesting hardware and software invention is Nenovision's solution LiteScope, which combines SEM microscope with AFM probe and uses correlative probe and electron microscopy technology (CPEM). This can help with solving the problem of seeing either a hole or a thin layer of material in sole SEM imaging plus adds an extra layer of information to the image. This method proved to be beneficial during studies of thin samples.

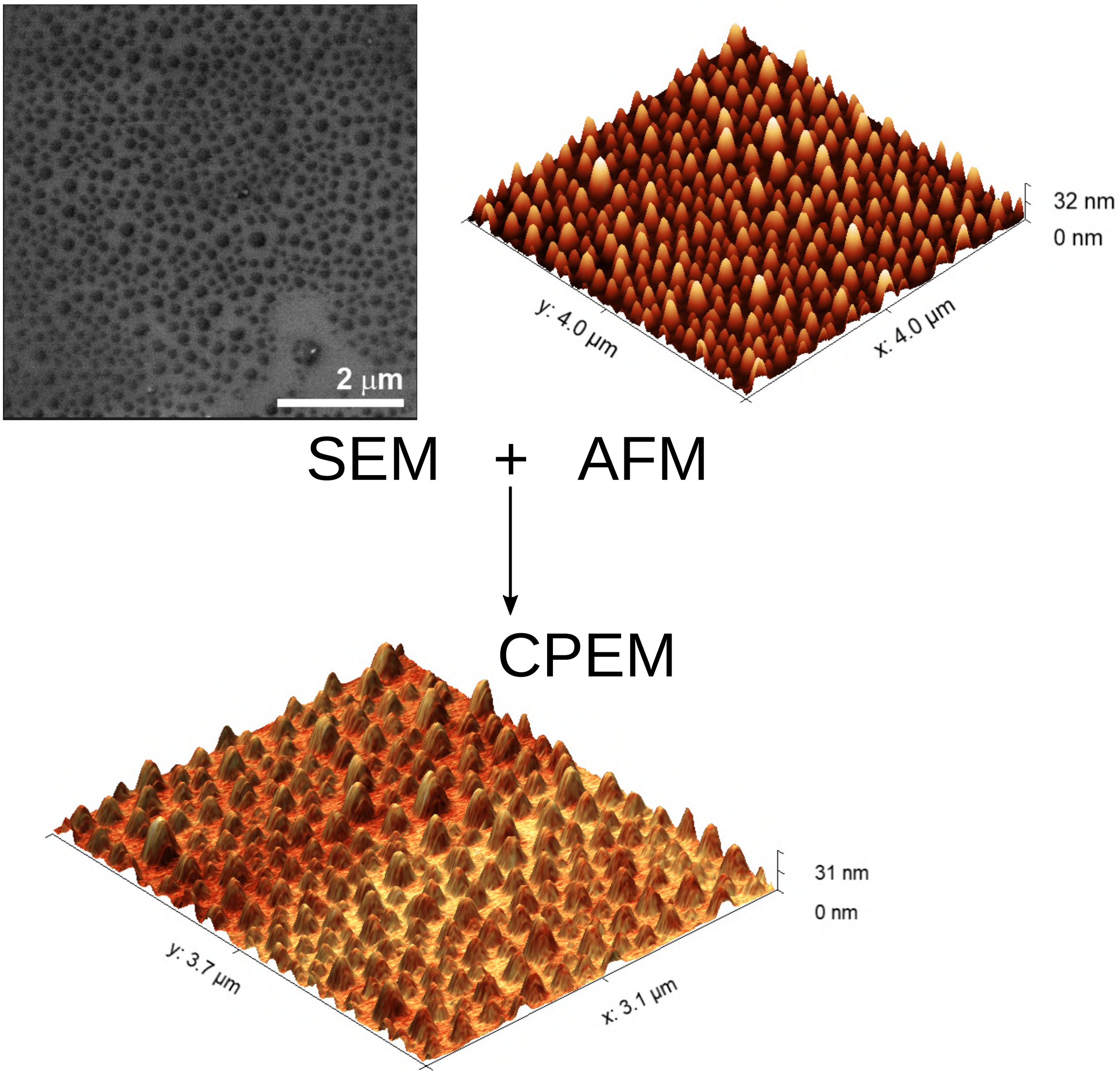

Figure 4.22: Images of sublimated [Co(trenb)(NCS)]Cl, where trenb = tris[2-(benzylamino)ethyl]amine on Si/SiO_2 wafer via SEM, AFM and from LiteScope by using CPEM technology where AFM module is mounted inside SEM microscope and the sample is scanned simultaneously for SEM and AFM with offset. Consequently, the image is overlaid and the final image with an extra layer of information is provided. This is especially beneficial for samples with non-conductive molecules where SEM image does not provide information on whether it is a hole or hill on the surface. The disadvantage is that the image is a bit cropped, as can be seen in the figure from its original size.

To conclude, SEM is a convenient and fast method to check surface with higher magnification than a standard optical microscope, and when combined with AFM, it offers thorough information about the sample's morphology.

5. Results obtained

This chapter presents work based on already published peer-reviewed articles combining spectroscopic and microscopic techniques applied in studies of organometallic compounds in both bulk and deposited on surfaces by wet-chemistry and thermal sublimation. The results herein serve as a commented extraction from published works. For full details, the reader is referenced to a full article with supplementary information at the beginning of each section.

5.1. A graphene-based hybrid material with quantum bits prepared by the double Langmuir–Schaefer method

Following results were obtained in cooperation and published in:

J. Hrubý, V. T. Santana, D. Kostiuk, M. Bouček, S. Lenz, M. Kern, P. Šiffalovič, J. van Slageren and P. Neugebauer: A graphene-based hybrid material with quantum bits prepared by the double Langmuir–Schaefer method, *RSC Adv.*, **9**, 24066-24073 (2019).

Abstract

The scalability and stability of molecular qubits deposited on surfaces is a crucial step for incorporating them into upcoming electronic devices. In this study, we reported on the preparation and characterisation of a molecular quantum bit, copper(II) dibenzoylmethane - $[\mathrm{Cu(dbm)_2}]$, deposited by a modified Langmuir–Schaefer (LS) technique onto a graphene-based substrate. A double LS deposition was used for the preparation of a few-layer-graphene (FLG) on a Si/-$\mathrm{SiO_2}$ substrate with subsequent deposition of the molecules as shown in Figure (5.1). Magnetic properties were probed by high-frequency electron spin resonance (HF-ESR) spectroscopy and found maintained after deposition. Our approach demonstrated the possibility to utilise a controlled wet-chemistry protocol to prepare an array of potential quantum bits on a disordered graphene-based substrate. The deployed spectroscopic techniques showed the robustness of our studied system unambiguously with a potential to fabricate large-scale, intact, and stable quantum bits.

Introduction to topic

Core computational units based on molecular architecture present one way in pursuing a quantum computer, a device which could substantially change all fields of human activity from complex structural biology to finance [87, 88]. The core is based on the principle of quantum superposition in which multiple states can be accessed at the same time, in contrast to classical zeroes and ones, which are used in current linear computational technology. A quantum computer could outperform any classical one in factoring numbers and searching a database [89]. In the search for novel approaches to standard silicon-based electronics, several routes were proposed. One of the promising routes is the merge of electronics controlled by the spin of an electron, spintronics [90], and molecular electronics [60].

Nowadays, there are several approaches in the research of quantum bits (qubits) aiming at controlling spin states which is the origin of magnetism in a matter. Crystal-structure defects

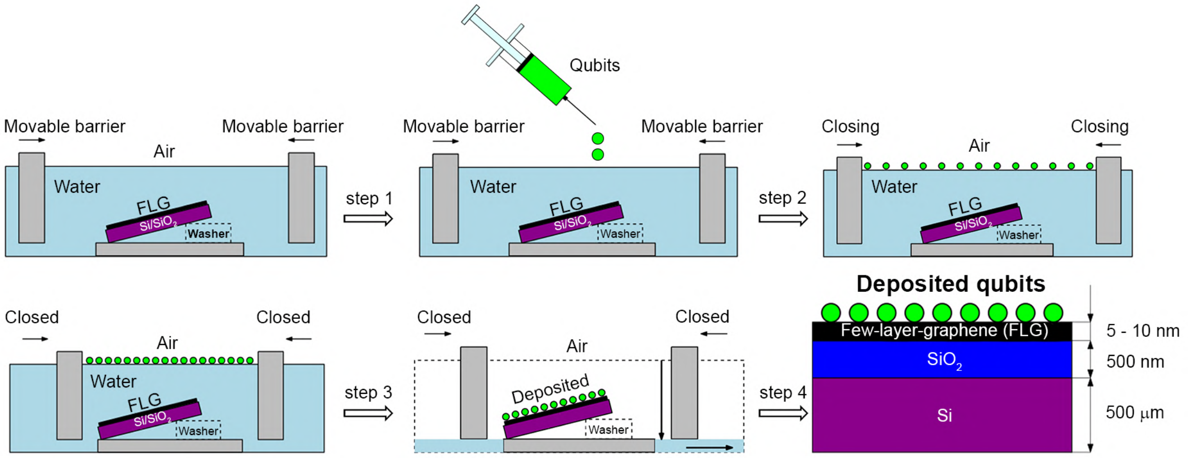

Figure 5.1: Scheme of modified Langmuir–Schaefer deposition process. It started by Langmuir–Blodgett trough filled with deionised water sub-phase. Step 1: the solution of [Cu(dbm)$_2$] in chloroform was injected onto a water subphase. The [Cu(dbm)$_2$] formed an oil-like structure on the water/air interface. Step 2: the movable barriers were closing until the molecules formed a tight layer. Step 3: the movable barriers were fully closed, and the water subphase was carefully pumped out under the movable barrier until the water level reached the substrate and the layer was deposited. Step 4: The final layer was composed of [Cu(dbm)$_2$] qubits deposited onto the FLG-covered substrate.

with a net spin such as nitrogen vacancies in diamond [91] or double vacancies in silicon carbide [92–94] are currently under investigation due to their potential for quantum information processing. However, the issue related to the usability of such centres lies in the production of defects as they can be prepared either by electron or ion bombardment, both of which create a random distribution of defects in the material [95]. These solid-state systems of defect sites prepared by lithographic means offer only limited synthetic control over their electronic and magnetic properties, which is crucial in integration with large scale devices. Another approach relies on using electron spins provided within magnetic molecules with unpaired electrons. The advantages over solid-state systems are mainly the reproducible fabrication, the ability to fine-tune magnetic properties by changing the ligand environment of an active-metal site, and the possibility to form large-scale ordered arrays. Hence, molecular magnets are also promising candidates for qubits as they offer unpaired electrons in a stable molecular environment [96].

Herein, we have decided to challenge the first out of five DiVincenzo's criteria postulated on the brink of quantum computer development era in 2000 [37]. We addressed namely characterisation and scalability of the copper(II)dibenzoylmethane - [Cu(dbm)$_2$], where dbm stands for dibenzoylmethane, with linear chemical formula: $C_{30}H_{22}CuO_4$, which is a transition-metal complex with copper as a central atom surrounded by two dbm ligands. It is a potential qubit with a coherence time of dozens of microseconds at low temperatures [97], which is a time usable for quantum information processing. To circumvent the abovementioned challenges with a host material for spins, we have opted for a few-layer-graphene (FLG) which is a stacked single graphite sheet known as graphene [98] famous for its interesting properties such as high electron mobility, mechanical strength, and thermal conductivity [57, 99–101]. The FLG in our sample provides a conductive substrate for qubits with the possibility to apply a gate voltage in order to have control over spin states. This led us to a production of a graphene-based hybrid material via controlled wet-chemistry protocol with an intact and robust molecular qubit.

Currently, there are several methods of how to prepare graphene, by original micromechanical cleavage [102], chemical vapour deposition (CVD) [103], epitaxial growth from SiC [104] or liquid-phase exfoliation [105]. The last method is possibly the best option for scalable production of graphene-based hybrid materials, thin conductive films, and thermal pastes [106, 107]. In order to obtain exfoliated graphene, there is a need for applying an external force to graphite flakes, such as ultrasonic vibrations [108]. Recently, there has been a growing interest in graphene-based materials that led to the chemically engineered graphene-based magnetic [109], opto-electrical [110, 111], and bio-sensing devices [112–114]. Besides, the supramolecular approach to graphene resulting in physisorption of magnetic materials directly onto the substrate via π–π stacking without any further functionalisation appears to be feasible [115]. The ability to control the magnetic properties of graphene-based hybrid materials is crucial for the further development of carbon-based devices [116, 117].

We have prepared a hybrid structure of a deposited quantum bit represented by organometallic complex [Cu(dbm)$_2$] onto FLG-covered Si/SiO$_2$ substrate and investigated its stability and robustness by Raman spectroscopy, XPS, and HF-ESR. Our proposed wet-chemistry-based approach can be considered as a complementary study to recently published one in which [Cu(dbm)$_2$] was successfully evaporated onto Au(110) substrate by organic molecular beam deposition [71], and thus showing both deposition routes are viable for this qubit.

Synthesis of [Cu(dbm)$_2$]

The synthesis of [Cu(dbm)$_2$] complex followed previously described procedure [118]. Copper(II) chloride dihydrate (1 mmol, 170 mg) was dissolved in water (15 mL). Simultaneously, a solution of dibenzoylmethane (2 mmol, 458 mg) and potassium hydroxide (1.4 mmol, 80 mg) in ethanol/water mixture with 15:1 ratio was added drop-wise to the copper solution. The resultant solution was stirred by a magnetic stirrer for 30 min. Finally, the precipitate was separated by a paper filtration and washed once by pure ethanol and demineralised water with consecutive vacuum filtration for 12 h. The reaction yield of the synthesis was fair (347 mg, 66 %). Elemental analysis performed on [Cu(dbm)$_2$]; Anal. Calc. for $C_{30}H_{22}CuO_4$, $M_w = 510.04$: C – 70.65; H – 4.35. Found: C – 71.73; H – 4.58.

Langmuir–Schaefer (LS) Deposition

The expanded and milled graphite (SGL-Carbon) was dispersed at the concentration of 10 mg/mL in N-Methyl-2-pyrrolidone (NMP) and was sonicated for 60 min at room temperature in an ultrasonic bath. Since the graphene layers tend to re-aggregate due to the weak van der Waals forces acting between them, the stabilisation agent NMP was used as a sonication medium. It prevented graphene layers from re-aggregation by minimising the interfacial tension between the graphene sheets and the medium [119]. The prepared FLG suspension in NMP was centrifuged in order to separate supernatant from sediment. The suspension was centrifuged at 10 320 RPM for 30 min. Afterwards, the supernatant was taken and left further to settle in a fridge $T = (2 - 3)$ °C for a month. The final concentration of graphene in the suspension was 0.1 – 0.2 mg/mL with the average lateral size of nano-sheets: 300 nm and the average thickness of nano-sheets from 5 – 10 nm (i.e. 10 – 20 layers) as shown in Figure (5.2).

The first deposition took place in the first Langmuir–Blodgett trough (KSV NIMA). The experimental setup was described in detail previously (Methods 4.1.1). By this method we deposited FLG onto a boron-doped Si(100) p-type substrate with a 500 nm thick layer of SiO$_2$ and resistivity $\varrho = 10 - 20\ \Omega \cdot \mathrm{cm}$. The 10 mL of FLG dispersion in NMP was gently spread onto the water subphase using a microlitre syringe. The pH of the water subphase was lowered to 4 by the addition of HCl, which is known to improve the floatation of nanoscale materials. The FLG Langmuir film compressed at the surface pressure of 38 mN/m was transferred onto the Si substrates by the controlled removal of the water subphase. Prior to deposition, the Si samples were submersed into the water subphase, having a tilt of approximately 5° with respect to the air/water interface. During the water removal, the tilt of the samples facilitated an increased spatial homogeneity of the deposited FLG layers due to a predefined sliding direction of the

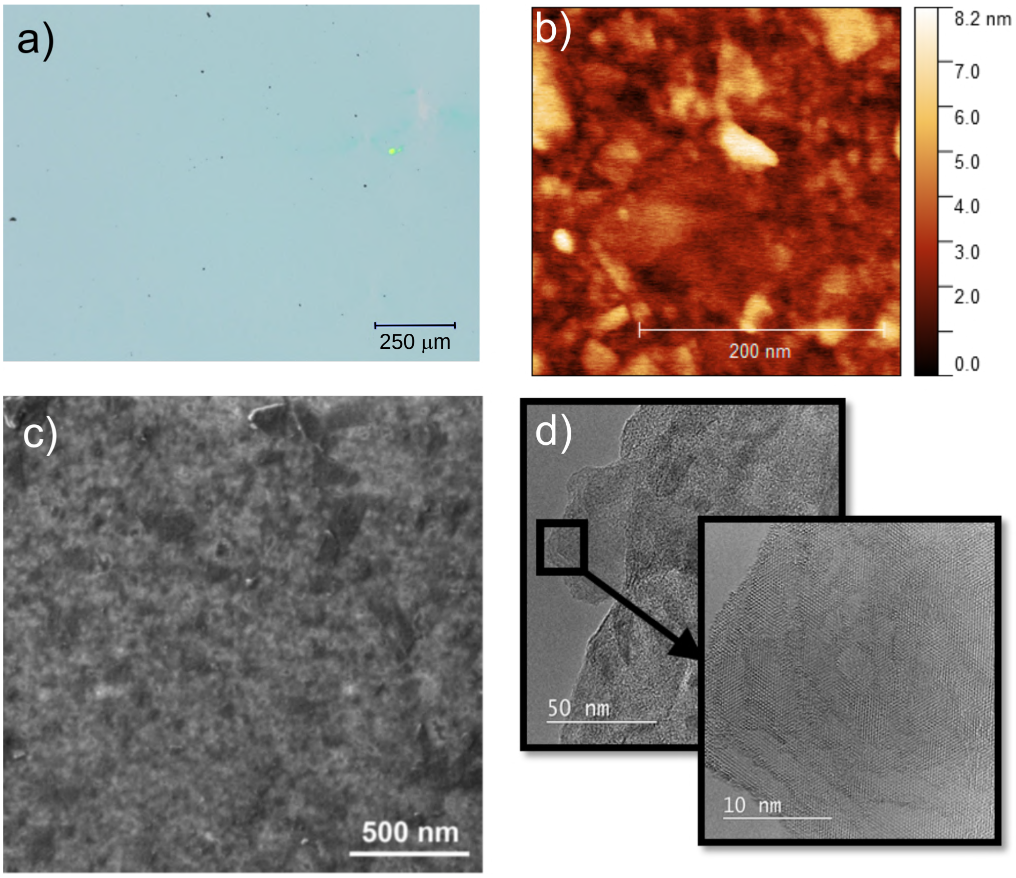

Figure 5.2: Characterisation of FLG layer for its thickness and uniformity by a) optical microscopy, b) AFM image, c) SEM image, and d) HR-TEM image.

three-phase boundary. After the first FLG deposition was made, samples were annealed at 800 °C for 30 min. This step helped to remove the remaining water from the deposition and to stabilise the layer on the substrate.

For the second deposition of where we used the second Langmuir–Blodgett trough for the qubit deposition (KSV NIMA) filled with deionised water (PURELAB Classic ELGA). The 5 mM solution of $[\mathrm{Cu(dbm)_2}]$ in chloroform (AlfaAesar, 99.8 %) was dropped ($V = 1.4\,\mathrm{mL}$) onto a water sub-phase until no further spreading was visible. Compounds formed an oil-like structure on the water/air interface. When the molecular layer was compressed on the water surface, it underwent phase transformations. Figure (5.3) shows these changes by monitoring the surface pressure Π as a function of the area occupied by the film A. The molar concentration for both 'Finding' and 'Deposition' of $[\mathrm{Cu(dbm)_2}]$ was 5 mM. The volume $V_{\mathrm{FINDING}} = 750\,\mu\mathrm{L}$ and $V_{\mathrm{DEPOSITION}} = 1400\,\mu\mathrm{L}$. The isotherm was the very first characteristic of the compound regarding the deposition step. During the 'Finding' deposition, the isotherm was estimated to be at $\Pi = 25\,\mathrm{mN/m}$ (i.e. where the curve starts to saturate). This pressure was then applied during the actual deposition onto substrates. The process of finding a correct isotherm is crucial for the formation of the ideal coverage. This was, however, an uneasy task for metal compounds. Surface pressure is given as follows: $\Pi = \gamma_0 - \gamma$, where γ_0 is the surface tension of the pure liquid, and γ is the surface tension of the film-covered surface.

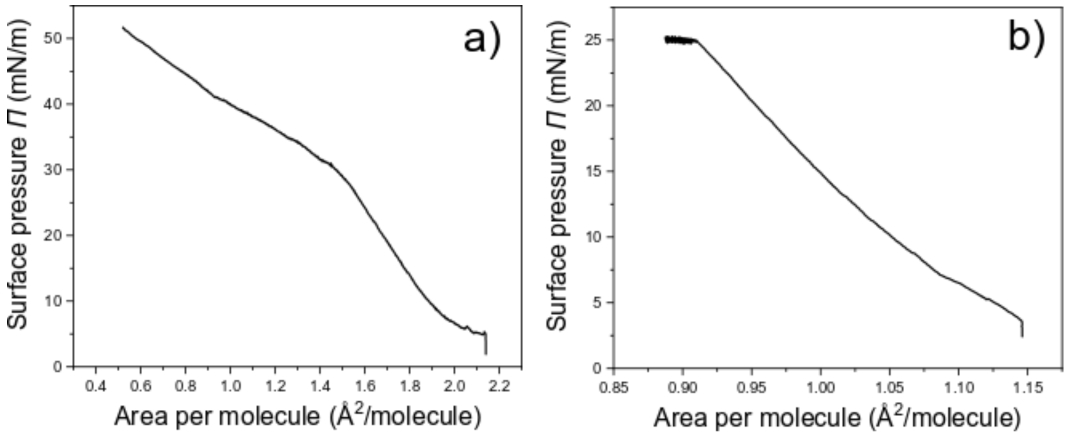

Figure 5.3: Diagram a) and b) show isotherms for [Cu(dbm)$_2$] obtained during the blank deposition and actual deposition onto substrates, respectively.

The main advantage of this method is in the possibility to use a manifold of various substrates at the same time during the deposition, limited only by the dimension of the trough. Figure (5.4) shows the final multi-layered material composed of [Cu(dbm)$_2$] deposited onto the FLG-covered substrate.

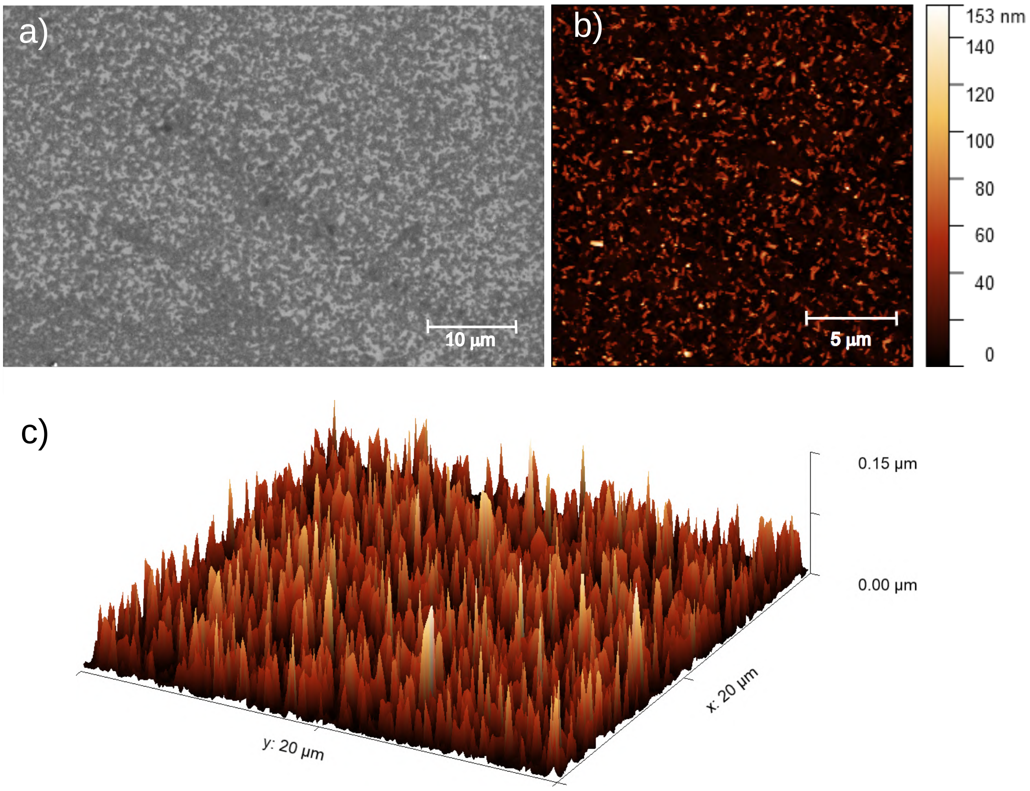

Figure 5.4: Characterisation of deposited [Cu(dbm)$_2$] on FLG. a) SEM image obtained at 5 kV and equipped with secondary electrons detector, b) AFM topography image, c) extracted 3D morphology image.

Raman spectroscopy (RS)

Raman spectra of the reference [Cu(dbm)$_2$] powder were acquired on confocal Raman microscope WITec Alpha300 R+. All other spectra were acquired on a confocal Raman microscope Renishaw inVia. Both instruments were equipped with the excitation laser source with 532 nm wavelength.

We performed Raman spectroscopy to explore vibrational modes of individual components in the resultant hybrid material and made a comparison in order to confirm the intactness of our studied system. Figure (5.5) shows Raman spectra from top to bottom of a bare Si/SiO$_2$ substrate, FLG, [Cu(dbm)$_2$] powder, and the final deposited sample.

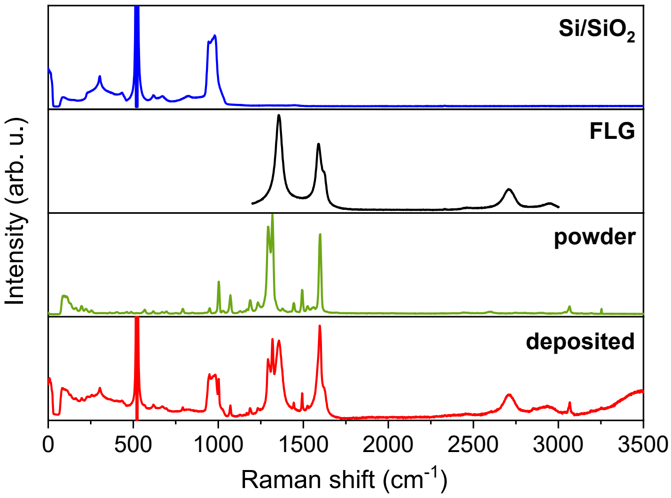

Figure 5.5: Comparison of Raman spectra, from top to bottom, of Si/SiO$_2$ substrate, FLG region, powder [Cu(dbm)$_2$] and deposited [Cu(dbm)$_2$].

For the main comparison purpose the evident 2 transverse acoustic (TA) phonon band at 304 cm^{-1}, the most intense main silicon transverse optic (TO) phonon band at 521 cm^{-1}, and 2 transverse optic phonon band spanning from 943 cm^{-1} to 983 cm^{-1} were observed for the Si/SiO$_2$ substrate [80, 120]. In the case of the FLG, six distinct peaks were found. The D band at 1356 cm^{-1}, G band at 1588 cm^{-1}, D' band at 1621 cm^{-1}, G' band at 2709 cm^{-1}, $G + D$ band at 2953 cm^{-1}, and in multi-layered material 2D' peak which can be attributed to the second-order of the intra-valley D' for graphene layers [121]. In the case of FLG, the disorder-induced D band, which is approximately at half of the frequency of the G' band, is the most intense peak signalling for a largely disordered graphitic substrate. The G band corresponds to doubly degenerate (iTO and LO) phonon mode at the Brillouin zone centre. The G band is the only band coming from a normal first-order Raman scattering process in graphene. On the contrary, the G' and D bands originate from a second-order process involving two iTO phonons near the K point of the first Brillouin zone for the G' band or one iTO phonon and one defect in the case of the D band [122]. All peaks were present both in the bare FLG on Si/SiO$_2$ substrate and the final deposited sample. Peak positions found for [Cu(dbm)$_2$] were in accordance with the previous Raman, infrared and in-depth theoretical studies performed on this system and dbm ligand [123, 124]. Raman spectra confirmed unequivocally all vibrational peaks for [Cu(dbm)$_2$] to be present for both bulk as well as deposited molecules.

X-ray photoelectron spectroscopy (XPS)

X-ray photoelectron (XPS) measurements were carried out with a Kratos Axis Supra spectrometer at room temperature and ultra-high vacuum (UHV) conditions. The instrument was equipped with monochromatic Al Kα source 1486.6 eV (15 mA, 15 kV), and a hemispherical analyser with hybrid magnetic and electrostatic lens for enhanced electron collection. Survey and detailed XPS spectra were acquired at normal emission with the fixed pass energy of 160 eV and 40 eV, respectively. Slot aperture 700 × 300 µm^2 was used during the acquisition. All spectra were charge-corrected to the hydrocarbon peak set to 284.8 eV. The Kratos charge neutraliser system was used on all specimens. The inelastic backgrounds in all spectra were subtracted according to the Shirley method [125]. Data analysis was based on a standard deconvolution method using mixed Gaussian (G) and Lorentzian (L) line shape (G = 70 % and L = 30 %, Gaussian-Lorentzian product) for each component in the spectra. Spectra were analysed using CasaXPS software (version 2.3.18).

The chemical composition of FLG on Si/SiO_2, [Cu(dbm)$_2$] powder, and [Cu(dbm)$_2$] on FLG was probed by means of XPS. Figure (5.6) shows the survey spectra that exhibit O 1s, C 1s, Si 2s, and Si 2p photoelectron peaks and a visible O_{KLL} Auger peak.

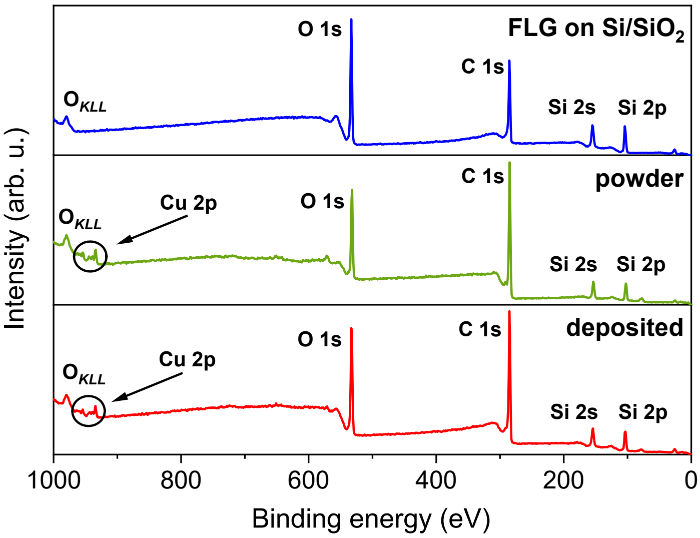

Figure 5.6: XPS survey spectra comparison, from top to bottom, of FLG on Si/SiO_2 substrate, powder [Cu(dbm)$_2$] and deposited [Cu(dbm)$_2$].

Silicon peaks in the [Cu(dbm)$_2$] powder spectra are present due to the silicon adhesive used on polyimide-based double-sided tape, which hosted as-synthesised [Cu(dbm)$_2$] powder. Highly resolved spectra of C 1s, O 1s, and Cu 2p revealed chemical bond types. A slight difference in binding energies for corresponding peaks could be attributed to changed variations in the surrounding chemical environment [126]. The best-fit parameters were found by applying physical constraints to components forming the overall spectrum based on stoichiometry, bond strength, and electronegativity [126, 127]. However, due to the ambient conditions during the LS deposition technique and carbon-based FLG background, we were not able to quantify peak intensities and relate them with molecular structure.

Figure (5.7) shows the chemical structure of [Cu(dbm)$_2$] and detailed XPS spectra characterised by main peaks at 284.8 eV, 532.7 eV, and 934.5 eV for C 1s, O 1s, and Cu $2p_{3/2}$ core levels, respectively. The C 1s and O 1s experience a slight shift towards lower binding energy in the deposited spectra. This can be caused by the image-charge screening effect [128]. The chemical structure suggests expecting components in C 1s from both carbon atoms forming aromatic rings (C-C, C-H) and carbon atoms bound to an oxygen atom (C=O, C-O). Photoelectrons from aromatic rings appear at lower binding energy, whereas carbon atoms bound to oxygen create a strong shoulder feature at 286.8 eV. We have also detected two satellite features S1 and S2, which are typical in photoemission of organic molecules due to relaxation processes resulting in the creation of a core-hole [129]. The increase in the intensity of the S1 satellite at the expense of C-H in the deposited spectrum can be attributed to the physisorption on FLG substrate, image-charge screening effect and charge neutralisation processes.

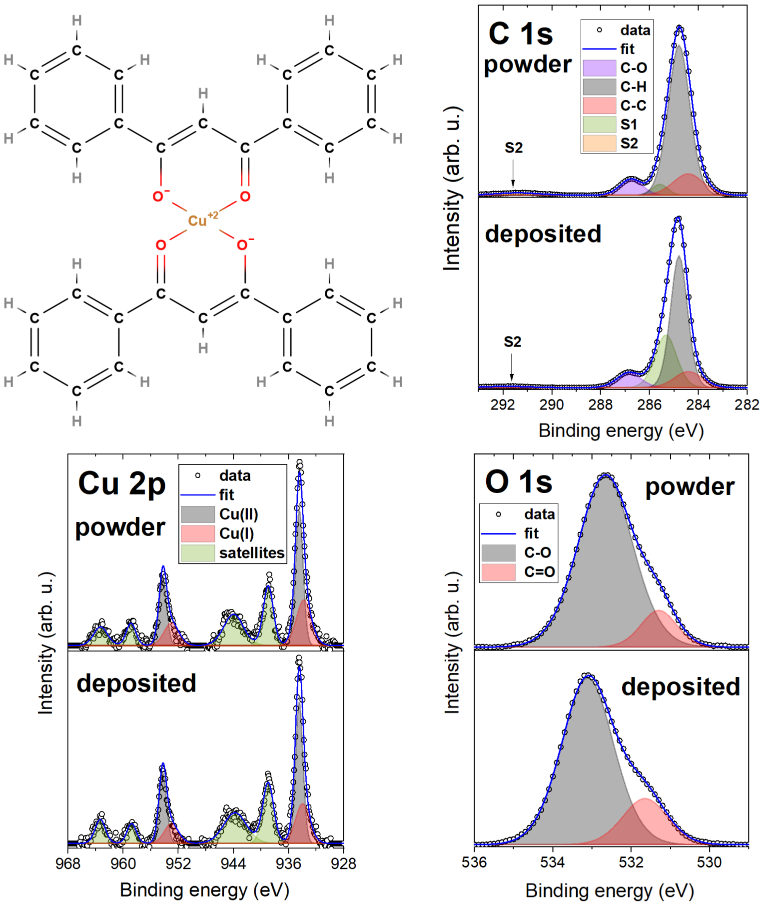

Figure 5.7: Molecular structure of [Cu(dbm)$_2$] with XPS comparison of powder and deposited sample with detailed regions for C 1s, Cu 2p, and O 1s.

The O 1s core-level line showed, besides the main component at 532.7 eV for powder and 533.1 eV for deposited, a shoulder component at lower binding energy, which was identified as C=O bond. The Cu 2p photoemission line features two main peaks Cu 2p$_{3/2}$ and Cu 2p$_{1/2}$ at 934.5 eV and 954.3 eV, respectively, separated by 19.8 eV. We have not evidenced any measurable energy shift in the binding energy of Cu 2p peaks in powder and deposited spectra. Both powder and deposited peaks exhibit a complex satellite structure, which serves as a fingerprint of having Cu atoms with a 2+ oxidation state [130–132]. This corroborates the preserved oxidation state of Cu(II) after the LS deposition process. Strong shake-up satellites visible in regions (937 - 947) eV and (957- 967) eV stem from electronic relaxation effects caused by electron-correlation effects in the open-shell d bands [130]. We have also evidenced a presence of Cu(I) component, shifted towards lower binding energy in comparison with Cu(II). This is a common reduction process for Cu(II)-based systems even without apparent reducing agent [133]. The studied sample was exposed to air, where Cu$_2$O is the final product of air exposure [134], and was in contact with an excessive amount of water during the LS deposition. Cu(II) can also be partially reduced to Cu(I) by excess free electrons in the FLG layer directly in contact with [Cu(dbm)$_2$]. XPS results match the findings recently gained on this system thermally evaporated on Au(110) [71].

Electron spin resonance (ESR)

High-frequency/-magnetic field ESR spectra (HF-ESR) were acquired on a home-built spectrometer featuring a VDI signal generator, a VDI amplifier-multiplier chain (Virginia Diodes, USA), a quasi-optical bridge (Thomas Keating, UK), a 15/17 T solenoid cryomagnet (Oxford Instruments, UK) and an InSb hot-electron bolometer (QMC Instruments, UK) [12]. The reference powder sample of the [Cu(dbm)$_2$] was studied as a pressed teflon-wrapped powder pellet and the final sandwich-like deposited hybrid material as ⌀5 mm sample as shown in Figure (5.8). All ESR spectra were simulated using the EasySpin toolbox for Matlab [28].

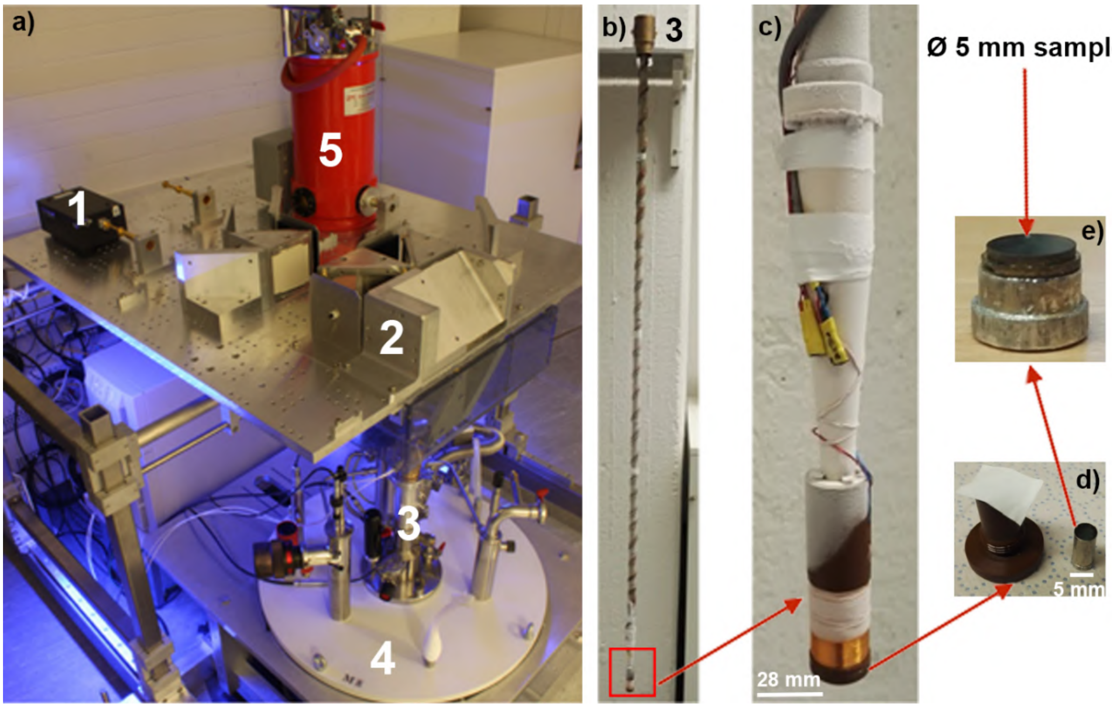

Figure 5.8: The HF-ESR spectrometer in Stuttgart. a) Indication of setup components, b) variable temperature insert (VTI), c) detail of sample-rod head with modulation coil, at which the alternating current (AC) with known noise frequency was applied and formed a lock-in amplification of signal (the first derivative of absorption signal was detected), d) sample insert with support, and e) ⌀5 mm sample in the form of a pressed pellet (for a bulk powder measurements) and a thin film (deposited [Cu(dbm)$_2$] on FLG-covered substrate).

By this method, we have investigated the intrinsic magnetic properties of [Cu(dbm)$_2$] before and after deposition by means of multi-frequency HF-ESR spectroscopy. Figure (5.9) shows HF-ESR spectra for powder [Cu(dbm)$_2$] from which we extracted basic spin Hamiltonian parameters such as g-factor originating from one unpaired electron of Cu(II) ion in 3d^9 electron configuration. Equation (5.1) describes the used spin Hamiltonian constructed by taking into account Zeeman contribution:

$$\hat{H} = \hat{H}_{\mathrm{Zeeman}} = \mu_{\mathrm{B}} \boldsymbol{B}_{\mathrm{ext}} \cdot \tilde{\boldsymbol{g}} \cdot \hat{\boldsymbol{S}}, \tag{5.1}$$

where μ_{B} is Bohr magneton, $\boldsymbol{B}_{\mathrm{ext}}$ is external magnetic field, $\tilde{\boldsymbol{g}}$ is g-factor tensor, $\hat{\boldsymbol{S}}$ is total spin of system, in this case $S = 1/2$. All powder spectra were fitted with the spin Hamiltonian parameters as follows: $g_{\mathrm{x}} = 2.0480$, $g_{\mathrm{y}} = 2.0470$, $g_{\mathrm{z}} = 2.2570$. Parameters used in the fitting procedure are in fair agreement with previously published results [71, 97, 135]. The slight misalignment and intensity decrements in spectra can be attributed to calibration of magnetic field and lock-in phase changes during the measurements. The difference between frequencies can also be assigned to different power distribution profile from a microwave source.

Figure (5.10) shows the HF-ESR spectra of deposited [Cu(dbm)$_2$] onto FLG-covered substrate with additional statistical analysis of resonance lines distribution. We observed a slight difference in g_{x} and g_{y} compared to bulk powder measurements. Both deposited spectra were fitted with the spin Hamiltonian parameters as follows: $g_{\mathrm{x}} = 2.0503$, $g_{\mathrm{y}} = 2.0499$, $g_{\mathrm{z}} = 2.2590$. This shift can be caused by stacking of physisorbed [Cu(dbm)$_2$] on FLG-based substrate.

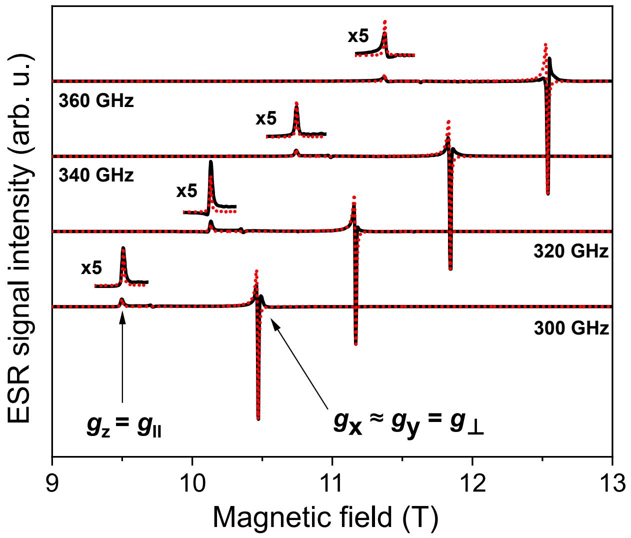

Figure 5.9: HF-ESR powder spectra of [Cu(dbm)$_2$] for four different frequencies, 300 GHz, 320 GHz, 340 GHz, and 360 GHz, respectively, from 9 T to 13 T measured at 5 K.

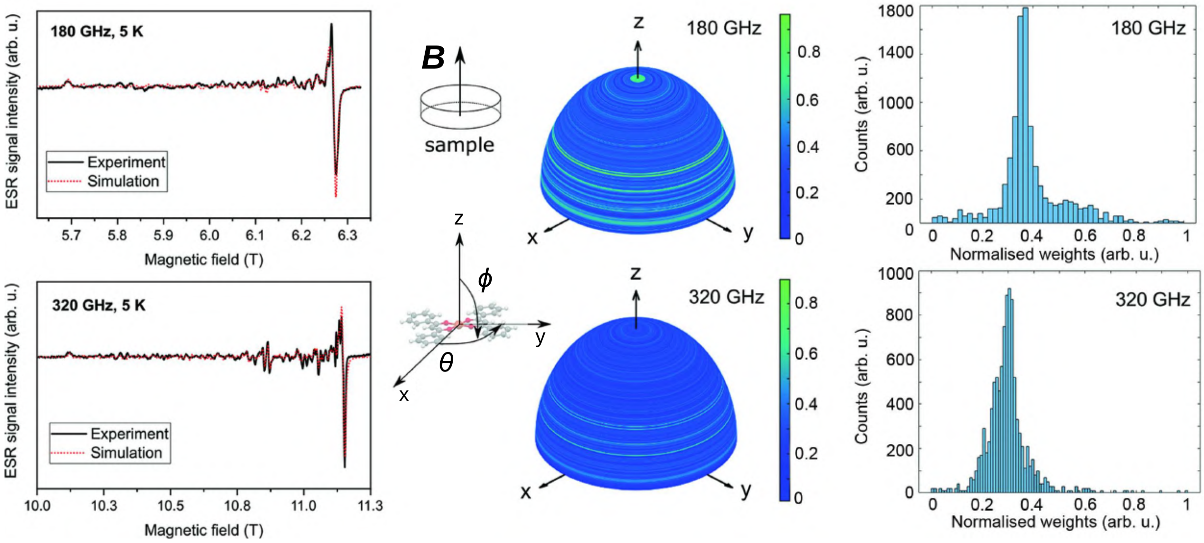

Figure 5.10: Left: HF-ESR spectra of deposited [Cu(dbm)$_2$] for two different frequencies of 180 GHz and 320 GHz measured at 5 K. Middle: visualisation of integration sphere with 10000 equally spaced points illustrating the distribution of resonance lines. In our experimental setup, the external magnetic field $\boldsymbol{B}$ was perpendicular to the surface plane of the sample. The colour scale bar corresponds to the relative weight distribution for the simulated spectra in every direction. The angles $0 < \Theta < 2\pi$ and $0 < \Phi < \pi$ denote the Euler angles. The simulated spectra were expectably sensitive mostly to changing Φ. Right: histogram of assigned weight distribution from an integration sphere, note that 320 GHz is more detailed than 180 GHz, demonstrating that by using higher frequencies, it is possible to get more resolved and finer distribution.

We observed many absorption lines of a small intensity distributed between magnetic field values that correspond to resonances parallel and perpendicular to the plane of the molecules (i.e. between $B_{\text{ext}} \parallel$ z and $B_{\text{ext}} \parallel$ xy plane) for both frequencies 180 GHz and 320 GHz. We statistically evaluated these additional peaks in both spectra by simulating the ESR absorption equivalent to individual micro-crystallites in the sample. We have rotated the $\tilde{\boldsymbol{g}}$ tensor obtained from the bulk powder samples and performed a simulation over a sphere with 10000 equally spaced points generated by the repulsion algorithm [136], attributing weight to the intensity of the spectrum in each direction. The weight is equivalent to the number of molecules at a particular orientation, while the counts in the histogram in Figure (5.10) corresponds to the total number of orientations with a given weight. This result shows that there is not an effective selective orientation of the micro-crystallites formed on the surface, even though about 5 % of them are distributed around the green regions in the integration hemispheres. The other 95 % are randomly distributed when taking into account the roughness of the FLG surface. The effect of the distribution of micro-crystallites is less pronounced at 180 GHz because the magnetic field resolution δB_{ext} between adjacent absorption lines is smaller at lower frequencies ($B_{\mathrm{ext}} = h\nu/g\mu_{\mathrm{B}}$). A simulation made by changing the frequency parameter solely shows that the double intensity at the same directions produces broader and smaller peak-to-peak intensities in the same regions. The pattern on integration hemispheres appears similar for both 180 GHz and 320 GHz spectra, however, the histogram for 320 GHz is more detailed. This can be assigned to an inherent property of going into higher frequencies in ESR in similar cases.

This multi-resonance line effect was also previously observed and discussed for the imperfectly dissolved frozen-solution of [Cu(dbm)$_2$] in chloroform and called as a ”single-crystal effect” [137, 138]. In our case, on a surface, these lines were assigned to an incomplete distribution of the orientations of micro-crystallites. Moreover, we have demonstrated that HF-ESR combined with a statistical approach can be a useful tool for the description of molecular distribution based on magnetic anisotropy on surfaces.

5.2. Co(II)-Based single-ion magnets with 1,1 -ferrocenediyl-bis(diphenylphosphine) metalloligands

Following results were obtained in cooperation and published in:

J. Hrubý, D. Dvořák, L. Squillantini, M. Mannini, J. van Slageren, R. Herchel, I. Nemec, and P. Neugebauer: Co(II)-Based single-ion magnets with 1,1 -ferrocenediyl-bis(diphenylphosphine) metalloligands, *Dalton Trans.*, **49**, 11697-11707 (2020).

Abstract

In this study we reported on magnetic and spectroscopic properties of three heterobimetallic Fe(II)–Co(II) coordination compounds based on the tetracoordinate $\{CoP_2X_2\}$ core encapsulated by dppf metalloligand, where X = Cl (**1**), Br (**2**), I (**3**), dppf = 1,1 -ferrocenediyl -bis(diphenylphosphine) as shown in Figure (5.11). The analysis of static magnetic data has revealed the presence of axial magnetic anisotropy in compounds (**1**) and (**2**), and this was further confirmed by high-frequency electron spin resonance (HF-ESR) spectroscopy. Dynamic magnetic data confirmed that (**1**) and (**2**) behave as field-induced Single-Ion Magnets (SIMs). Together with bulk studies, we have also tested the possibility of depositing (**2**) as thick films on Au(111), glass, and polymeric acetate by drop-casting as well as thermal sublimation, a key aspect for the development of future devices embedding these magnetic objects.

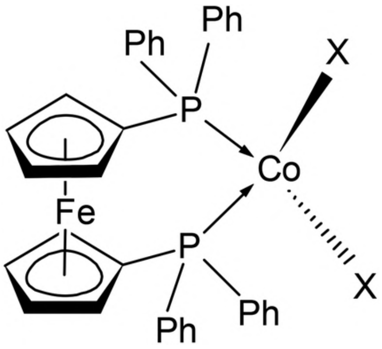

Figure 5.11: Scheme of the molecular structure of compounds (**1**)–(**3**), X stands for halido ligands (X = Cl in (**1**), Br in (**2**) and I in (**3**)). Ph stands for the phenyl rings.

Following Figure (5.12) illustrates splitting of molecular orbitals in high-spin Co(II) in tetrahedral symmetry.

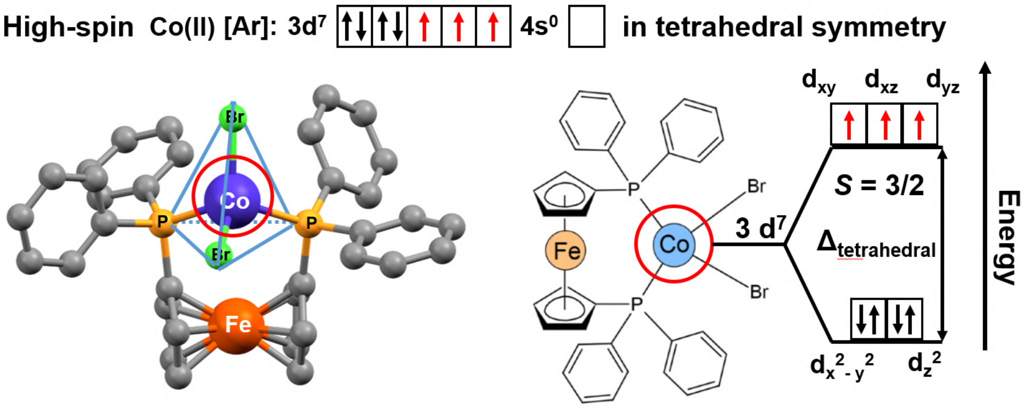

Figure 5.12: Splitting of energy in molecular orbitals of high-spin Co(II) in tetrahedral symmetry.

Introduction to topic

Single-Molecule Magnets (SMMs) feature magnetic bistability at low temperature [27] due to the intrinsic energy barrier (U_{eff}), which is a function of the total spin in the ground state (S) and the axial parameter of the molecular anisotropy (D): $U_{\mathrm{eff}} = |D| \times S^2$ for integer spins and $U_{\mathrm{eff}} = = |D| \times (S^2 - \frac{1}{4})$ for non-integer spins, under the condition that the magnetic anisotropy is axial - $D < 0$. However, it has been reported that D is inversely dependent on S^2 as can be extracted from the relationships describing spin-orbit contributions to D-tensor [19]. Therefore, in parallel with a growing interest in the use of SMM archetypes for the exploration of innovative devices for spintronics [139] and quantum computing [140], research efforts in recent decades have been concentrated on maximising the magnetic anisotropy in novel molecular systems, and thus the dynamic magnetic properties of transition metal-ion and rare-earth-based complexes [22, 47]. As a result, a plethora of 3d or 4f SMMs with one paramagnetic metal centre, called Single-Ion Magnets (SIMs), have been reported [141], including one with the highest blocking temperature, exceeding the temperature of liquid nitrogen [142]. Among the group of 3d SIMs, the Co(II) compounds are the most abundant and the SMM phenomenon was reported for a great variety of the coordination numbers and geometries such as tetracoordinate [143, 144], pentacoordinate [145], hexacoordinate [146], heptacoordinate [147] or even octacoordinate [148].

In these compounds, the ground spin state is split by strong spin-orbit coupling into two Kramers doublets (|3/2,±1/2> and |3/2,±3/2>), which are separated by the energy equal to $2\sqrt{D^2 + 3E^2}$. In the case of tetracoordinate Co(II) compounds with the general formula $[\mathrm{Co(L^{N/P})_2(L1)_2}]$ or $[\mathrm{Co(L^{N/P})(L1)_2}]$, where $\mathrm{L^{N/P}}$ represents mono or bidentate N- or P-donor ligands and L1 is halido or pseudohalido ligands, a magneto-structural correlation was established by Boča and co-workers in 2013 [149]. It reads $\delta = 2\alpha_{\mathrm{Td}}$ - (α), where α_{Td} is the angle of the ideal tetrahedron (109.5°), α is the angle between the two Co-N/P bonds. Despite some limitations [18], this relationship has proved to be successful in the prediction of sign and magnitude of D, such that more negative/positive δ should lead to more negative/positive value of D. Therefore, our attention has focused on compounds with rather large and negative parameter δ, and these were further investigated for their static and dynamic magnetic properties [18, 150]. Therefore, we opted to investigate the compound $[\mathrm{CoCl_2(dppf)}]$ as a suitable SIM candidate, where dppf represents the 1,1 -ferrocenediyl-bis(diphenylphosphine). This complex can be prepared by the reaction between dppf and $\mathrm{CoCl_2}$ where both dppf and the resulting product $[\mathrm{CoCl_2(dppf)}]$ are very well known, thoroughly studied (besides magnetic properties) [151] and even commercially available coordination compounds with CAS numbers: dppf, 12150-46-8; $[\mathrm{CoCl_2(dppf)}]$, 67292-36-8. The crystal structure of $[\mathrm{CoCl_2(dppf)}]$ was reported in 1999 [152] and this compound has tetracoordinate $\mathrm{CoP_2Cl_2}$ arrangement with δ = -4.8°. Therefore, according to the magneto-structural correlation by Boča et al. [149], it should possess negative D. Furthermore, having in mind, the influence of the intermolecular interactions which often effectively decrease U [153] giving also the rise to other relaxation channels [154], another structural property of $[\mathrm{CoCl_2(dppf)}]$ must be emphasised. The crystal structure of this compound is composed of the complex molecules connected only by weak C-H $\cdots$ π and C-H $\cdots$ Cl non-covalent interactions.

Due to the bulkiness of the dppf metalloligand, these interactions are organised in a way (*vide infra*) that they cannot effectively transmit even very weak exchange interactions. The shortest Co $\cdots$ Co separations are longer than 9.6 Å assuring that also dipolar interactions between the Co(II) atoms are negligible. Therefore, we decided to study the static and dynamic magnetic properties of the compound $[\mathrm{CoCl_2(dppf)}]$, (**1**), together with the bromido $[\mathrm{CoBr_2(dppf)}]$, (**2**) and iodido $[\mathrm{CoI_2(dppf)}]$, (**3**) analogues. The precise determination of the magnetic anisotropy parameters was performed by High-Frequency and -Field Electron Spin Resonance (HF-ESR) measurements. We also focused our synthetic strategy on the preparation of the single crystals of compounds (**2**) and (**3**) and the determination of their crystal structures by the X-ray diffraction. The analysis of the experimental data was supported by *ab initio* calculations

(CASSCF/NEVPT2). Furthermore, we tested the deposition of thick films of these complexes on surfaces via both thermal sublimation and wet-chemistry-based protocols.

Synthesis of (1) and (2)

$CoCl_2$ (0.5 mmol, 65 mg) or $CoBr_2$ salt (0.5 mmol, 108 mg) was dissolved in 10 mL of methanol and subsequently, solution of dppf (0.5 mmol, 277 mg) in 25 mL of CH_2Cl_2 was slowly added. The colour of the solution turned green, and it was stirred under heating to boiling for 20 min. Heating together with a stream of nitrogen gas led to a significant reduction of solution volume followed by precipitation of green powder, which was filtered off. The mother liquor was crystallised by slow diffusion of diethyl ether, and this led to the precipitation of hexagonally shaped green crystals, which were filtered off and dried in a desiccator.

(**1**): Anal. Calc. for $C_{34}H_{28}Cl_2CoFeP_2$: $M_w = 684.22\,g\,mol^{-1}$, (in %): C, 59.45; H, 4.33. Observed: C, 59.68; H, 4.12.

(**2**): Anal. Calc. for $C_{34}H_{28}Br_2CoFeP_2$: $M_w = 773.12\,g\,mol^{-1}$, (in %): C, 52.89; H, 3.47. Observed: C, 52.82; H, 3.65. Thermal stability was investigated using differential scanning calorimety and thermogravimetry (DSC-TGA) measurements and the compound is stable up to 260 °C.

UV-VIS spectroscopy

Absorption spectra were acquired using a JASCO V670 UV–VIS-NIR spectrophotometer. The bulk powder of (**2**) was grafted onto filtration paper, and the wet deposition sample was prepared by drop-casting of 1 mL of a 5 mM dichloromethane solution onto a cover glass substrate inside an inert nitrogen atmosphere, and the 30 nm thick film obtained by the sublimation onto acetate substrate. All samples were put into the light beam of the UV-VIS spectrometer filled with a nitrogen atmosphere. UV-VIS spectra of 1 mM solutions of (**1**) and (**2**) in dichloromethane (Sigma Aldrich, 99.8%) were obtained in quartz 10 mm path-length cuvettes as shown in Figure (5.13). The peaks found are in agreement with the previously reported study [151].

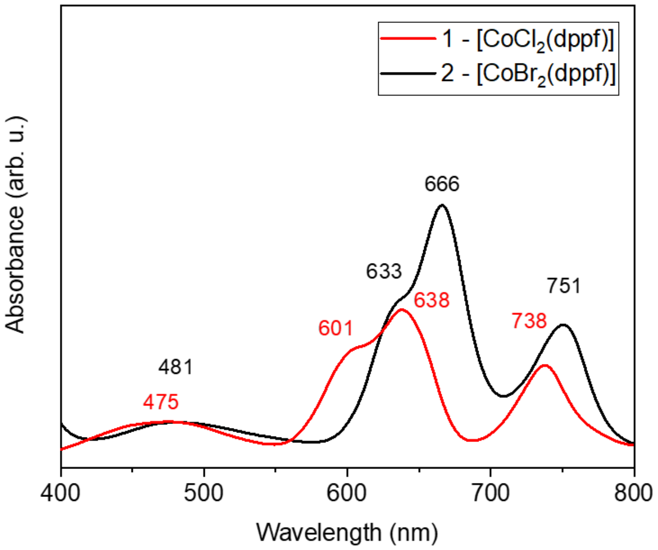

Figure 5.13: UV-VIS spectra for compound (**1**) (red line) and (**2**) (black line) in 1 mM dichloromethane solution.

Static magnetic properties

The temperature and field-dependent magnetic data were collected and analysed for compounds (**1-2**). We were not successful in obtaining the pure phase of the compound (**3**). We believe that partial decomposition of (**3**) occurred, as can be judged from outward reddish-brown and inner green colours of obtained crystals. Temperature dependence of the magnetisation at $B = 0.1\,\mathrm{T}$ from 1.9 to 300 K and the isothermal magnetisations at $T = 2.0$, 5.0 and 10.0 K up to $B = 9\mathrm{T}$ were measured using a PPMS Dynacool with a VSM option. The experimental data were corrected for diamagnetism and the signal of the sample holder.

The temperature dependencies of the effective magnetic moment ($\mu_{\mathrm{eff}}/\mu_{\mathrm{B}}$) are similar for (**1-2**), adopting values ($4.4 - 4.5\mu_{\mathrm{B}}$) larger than spin only value for Co(II) with $\mathrm{e}^4\mathrm{t}_2^3$ configuration in tetrahedral symmetry of the coordination polyhedron ($g = 2.0$, $S = 3/2$, $\mu_{\mathrm{eff}}/\mu_{\mathrm{B}} = 3.87$). The μ_{eff} value was almost constant to cca 20 K and then decrease to cca 3.5 (**1**) and 3.7 (**2**) μ_{B} was observed. The observed decreases of μ_{eff} can only be attributed to the occurrence of the zero-field splitting (ZFS), and thus magnetic anisotropy. Therefore, the magnetic data were fitted for spin Hamiltonian including axial and rhombic ZFS terms:

$$\hat{\mathcal{H}} = \hat{\mathcal{H}}_{\mathrm{Zeeman}} + \hat{\mathcal{H}}_{\mathrm{ZFS}} = \mu_{\mathrm{B}} B_{\mathrm{ext}} g \hat{S}_{\mathrm{a}} + D\left[\hat{S}_z^2 - \frac{1}{3}S(S+1)\right] + E(\hat{S}_x^2 - \hat{S}_y^2), \tag{5.2}$$

where Zeeman term is defined in the direction of a magnetic field as $B_{\mathrm{ext,a}} = B(\sin(\Theta)\cos(\varphi), \sin(\Theta)\sin(\varphi), \cos(\Theta))$ with the help of the polar coordinates, D and E are the single-ion axial and rhombic ZFS parameters. The magnetisation in a-direction of the magnetic field was calculated as follows:

$$M_{\mathrm{a}} = N_{\mathrm{A}} k_{\mathrm{B}} T \frac{\mathrm{d} \ln Z}{\mathrm{d} B_{\mathrm{a}}}, \tag{5.3}$$

where Z is the partition function constructed from the energy levels of the spin Hamiltonian. Then, the averaged molar magnetisation of the powder sample was calculated as the integral (orientational) average:

$$M_{\mathrm{mol}} = \frac{1}{4\pi} \int_0^{2\pi} \int_0^{\pi} M_{\mathrm{a}} \sin\Theta \mathrm{d}\Theta \mathrm{d}\varphi. \tag{5.4}$$

Figure (5.14) shows the best fits found for (**1**) with $g = 2.20$, $D = -11.0\,\mathrm{cm}^{-1}$, $E/D = 0.00$, $\chi_{\mathrm{TIP}} = 10.1 \times 10^{-9}\mathrm{m}^3\mathrm{mol}^{-1}$ and for (**2**) with $g = 2.24$, $D = -8.7\,\mathrm{cm}^{-1}$, $E/D = 0.24$, $\chi_{\mathrm{TIP}} = 6.1 \times 10^{-9}\mathrm{m}^3\mathrm{mol}^{-1}$. These findings confirm the presence of an axial magnetic anisotropy for both compounds (**1**) and (**2**).

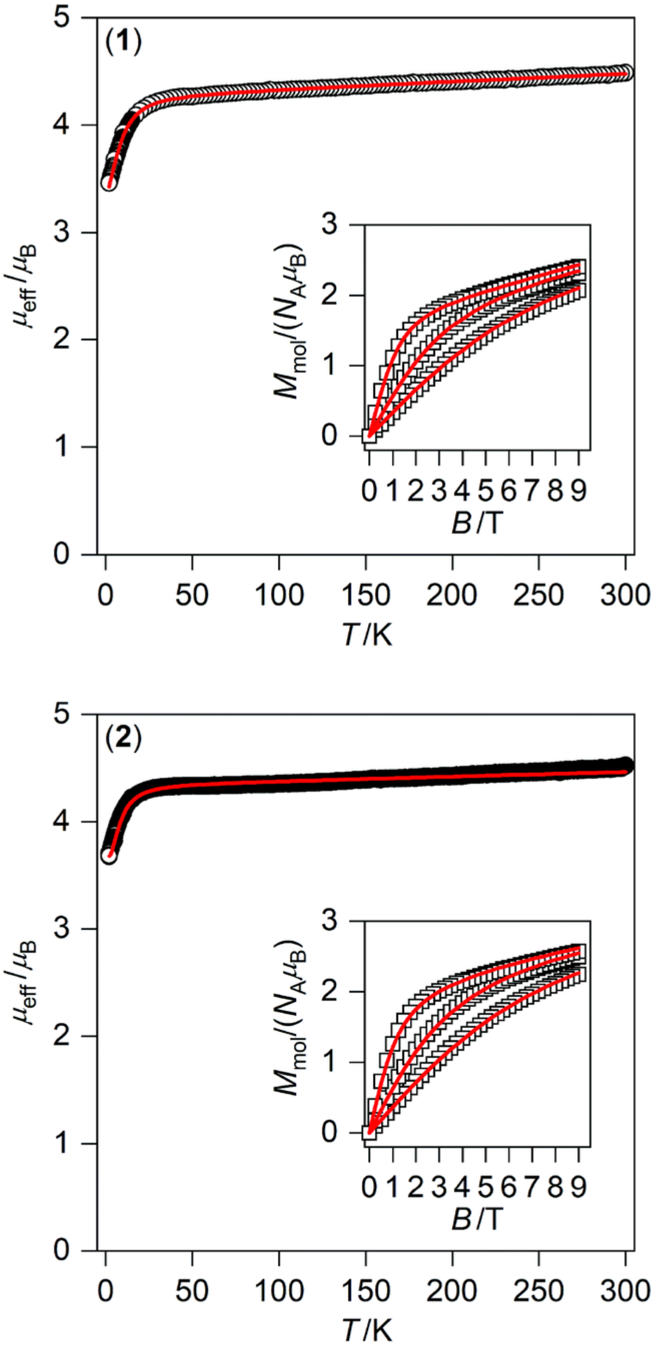

Figure 5.14: Magnetic data for (**1**) (top) and (**2**) (bottom) displayed as the temperature dependence of the effective magnetic moment, and the isothermal molar magnetisation measured at $T = 2$, 5, and 10 K is in the inset. The empty symbols represent the experimental data; red full lines represent the fitted data using Equation (5.2).

Dynamic magnetic properties

To further characterise compounds (**1**) and (**2**), AC susceptibility was measured for both compounds. There were no out-of-phase signals in zero static magnetic field detected. Therefore, the AC susceptibility was measured at $B_{\text{DC}} = 0.1\,\text{T}$ and revealed frequency-dependent maxima of the imaginary susceptibility, and thus confirming the slow relaxation of the magnetisation in (**1**) and (**2**).

Figures (5.15 and 5.16) show the Argand (Cole-Cole) plot for (**1**) and (**2**). The extracted relaxation times follows the Arrhenius law and subsequent analysis yielded these parameters:

$\tau_0 = 5.17 \times 10^{9}\,\mathrm{s}$, $U_{\mathrm{eff}} = 33.3\,\mathrm{K}$ ($23.2\,\mathrm{cm}^{1}$) for (**1**), and $\tau_0 = 1.80 \times 10^{9}\,\mathrm{s}$, $U_{\mathrm{eff}} = 28.8\,\mathrm{K}$ ($20.0\,\mathrm{cm}^{1}$) for (**2**). The one-component Debye's model was applied based on the equation:

$$\chi(\omega) = \frac{\chi_{\mathrm{T}} - \chi_{\mathrm{S}}}{1 + (i\omega\tau)^{1-\alpha}} + \chi_{\mathrm{S}}, \tag{5.5}$$

with isothermal (χ_{T}) and adiabatic (χ_{S}) susceptibilities, relaxation times (τ) and distribution parameters (α).

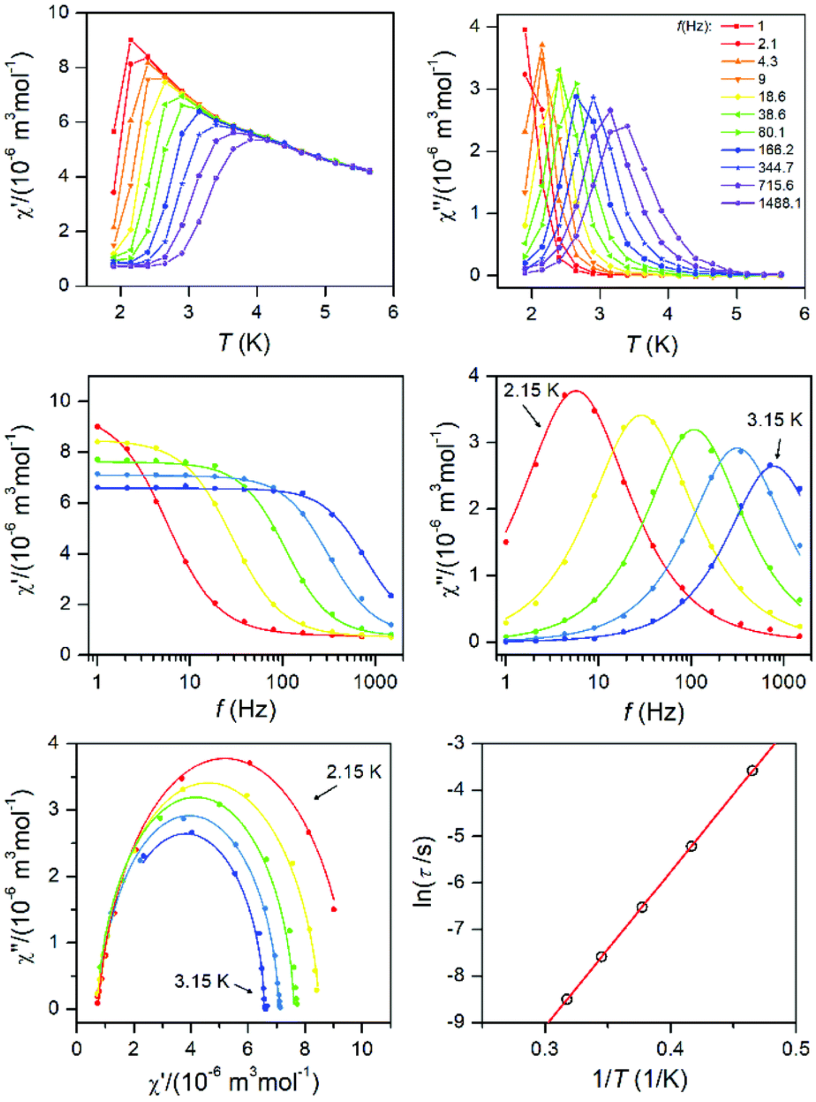

Figure 5.15: AC susceptibility data for (**1**). Top: In-phase χ and out-of-phase χ'' molar susceptibilities at the applied external magnetic field $B_{\mathrm{DC}} = 0.1\,\mathrm{T}$ (full lines are only guides for eyes). Middle: Frequency dependence of in-phase χ and out-of-phase χ'' molar susceptibilities fitted with one-component Debye's model using Equation (5.5) (full lines). Bottom: The Argand (Cole–Cole) plot with full lines fitted with Equation (5.5) and the fit of resulting relaxation times τ with Arrhenius law (red line).

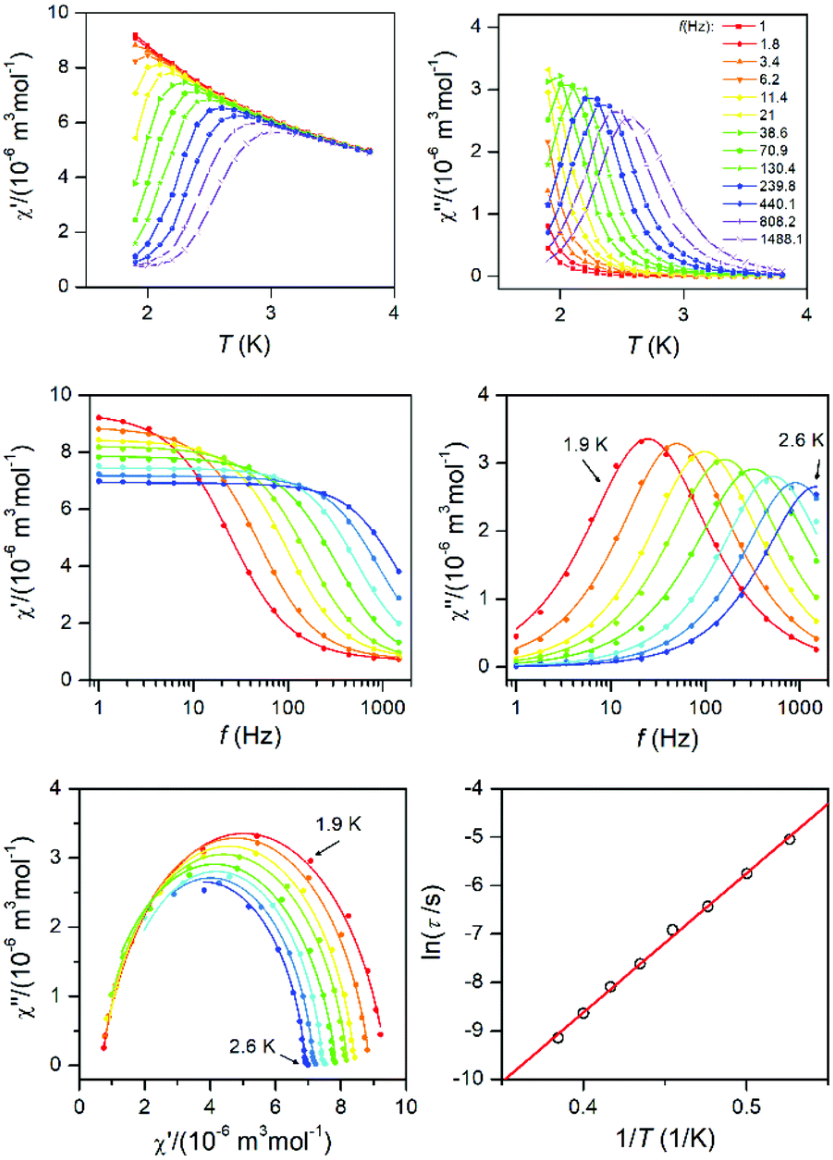

Figure 5.16: AC susceptibility data for (**2**). Top: In-phase χ and out-of-phase χ'' molar susceptibilities at the applied external magnetic field $B_{\mathrm{DC}} = 0.1\,\mathrm{T}$ (full lines are only guides for eyes). Middle: Frequency dependence of in-phase χ and out-of-phase χ'' molar susceptibilities fitted with one-component Debye's model using Equation (5.5) (full lines). Bottom: The Argand (Cole–Cole) plot with full lines fitted with Equation (5.5) and the fit of resulting relaxation times τ with Arrhenius law (red line).

Surface depositions

Deposition of (**2**) on surfaces was investigated by two distinct techniques: by drop-casting under an inert nitrogen atmosphere (drop hereafter) and by thermal sublimation in high-vacuum (subl hereafter). For the preparation of thick films, we used a home-built high-vacuum sublimation chamber. For sublimations of (**2**), a cleaned quartz crucible was used. The base chamber pressure during the sublimation was 1×10^{-7} mbar. We prepared a 30 nm thick molecular film on Au(111) surface deposited on muscovite mica previously treated with a hydrogen flame annealing treatment and a 30 nm thick film on acetate for UV-VIS measurements. The sublimation was performed at 225 °C with a growth rate of 1 Å per 9 min. This was carefully monitored by calibrated quartz crystal microbalance (STM-2, Inficon) placed at the same height as samples inside the vacuum chamber.

Figure (5.17) shows a comparison of UV-VIS spectra of (**2**) as a bulk powder, the deposit obtained from the drop-casting on glass, and the 30 nm thick film obtained by the sublimation onto acetate substrate.

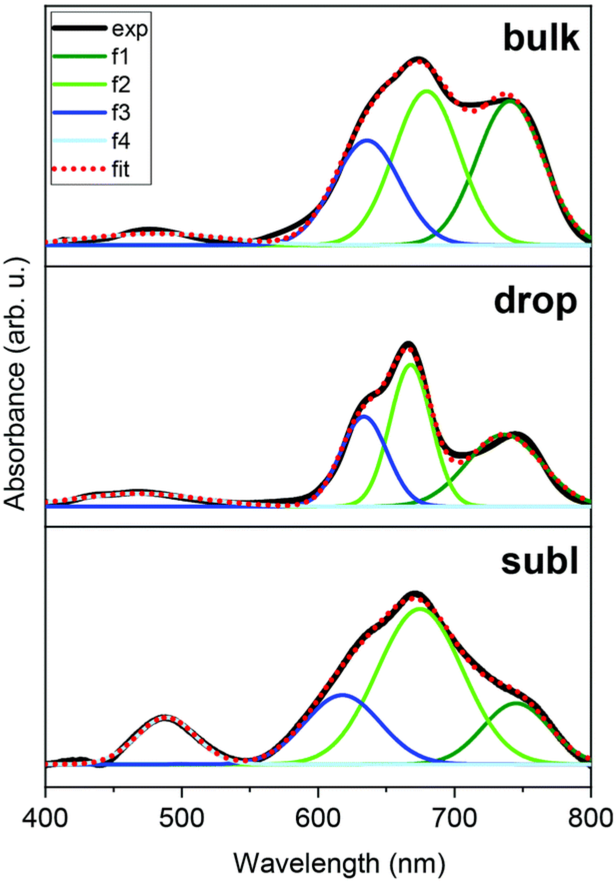

Figure 5.17: UV-VIS spectra of (**2**) as a bulk powder (above), drop-cast layer on glass (middle) and sublimated layer on acetate substrate (below). The results of spectra fitting to four Gaussian primitives (f1 – olive, f2 – green, f3 – blue, f4 – light blue); bulk (top, $\lambda_{\max}$ in nm, absorbance in arb. u.): f1 = 741, 0.1795, f2 = 680, 0.1917, f3 = 636, 0.1295, f4 = 481, 0.012; drop-cast (middle): f1 = 736, 0.0578, f2 = 668, 0.1167, f3 = 634, 0.0730, f4 = 468, 0.0081; sublimated (bottom): f1 = 745, 0.0127, f2 = 675, 0.0326, f3 = 618, 0.0144, f4 = 489, 0.0097.

Spectra of all three solid samples exhibited two dominant absorptions in the visible part of the spectra: the peak around 480 nm, which corresponds to the e_2–e_1 transition in ferrocenyl moiety (in approximate D_{5h} symmetry) [151, 155] and the cluster of peaks between ca. (600 – 800) nm that can be assigned to d–d transitions of the tetracoordinate $3d^7$ central ion [156]. Despite the same absorption bands in all three spectra, it is apparent that the profile of each spectrum is slightly different, e.g. the subl spectra show broader bands and more intense e_2–e_1 transition band than in bulk and drop. Despite being aware of different samples' nature requiring different approaches in acquiring the UV-VIS data, we attempted to fit all three spectra to quantify the observed differences. Each spectrum $(400 - 800)$ nm was fitted using four Gaussian primitives, three peaks (olive – f1, green – f2, blue – f3) sufficiently reconstructed the d–d band [157], while the fourth one (light blue – f4, Figure (5.17)) was used to fit the e_2–e_1 transition. Three rather well-separated components of the d–d band arising from $^4A_2 \rightarrow {}^4T_1(P)$ transition (in ideal T_d symmetry) [158] reflect the lower symmetry of coordination polyhedron, because the parent term $^4T_1(P)$ splits into three terms $^4A_1 + {}^4B_1 + {}^4B_2$ [159] in more realistic C_{2v} symmetry [160]. The peak heights cannot be directly compared among the spectra. Therefore we compared ratios of the peak heights derived for each spectrum.

The f1/f2 ratios are similar for drop (0.49) and subl (0.39) samples, while in bulk, f1/f2 is rather larger (0.94). On the other hand, the f4/f2 ratios are similar for bulk (0.06) and drop (0.07) samples, while f4/f2 is significantly larger in subl (0.30). From the presented UV-VIS data, it is hard to determine if any variations among the spectra, such as one described by f1/f2 ratio, originate from chemical changes or different spectral resolution due to the different nature of the measured sample. However, it must be noted that an increase of f4/f2 in subl spectrum can be reasonably explained by partial decomposition of (**2**) to metalloligand dppf during the sublimation process resulting in a larger abundance of dppf in the deposit.

X-ray photoelectron spectroscopy (XPS)

XPS measurements were carried out at room temperature in a UHV chamber equipped with an X-ray source (non-monochromatic Mg-Kα source, 1253.6 eV) and hemispherical analyser by VSW mounting a 16-channel detector. The X-ray source mounted at 54.44° with respect to the analyser was operated at a power of 120 W (12 kV and 10 mA). Survey and detailed XPS spectra were acquired at normal emission with the fixed pass energy of 44 eV. All bulk powder spectra were referenced to the Cu $2p_{3/2}$ peak at 932.7 eV because it served as a substrate for investigated molecules. Therefore, no change in position for this peak was expected. Drop-cast and evaporated samples were referenced to the Au $4f_{7/2}$ peak at 84.0 eV. The inelastic backgrounds in spectra were subtracted according to the Shirley method [125] except for Fe peaks, where a linear background was used. Data analysis was based on a standard deconvolution method using mixed Gaussian (G) and Lorentzian (L) line shape (G = 70% and L = 30%, Gaussian–Lorentzian product) for each component in the spectra. The elemental composition of the samples was evaluated using a semi-empirical approach. The integrated intensity of each component was corrected with the photoionization cross-section calculated for each atom, neglecting the differences in photoelectron escape length as a function of the kinetic energy [161] Spectra were analysed using CasaXPS software (version 2.3.18).

Figures (5.18) and (5.19) show the chemical composition of bulk (**1**) and (**2**). Figure (5.18) shows the survey spectrum which exhibited O 1s, C 1s, P 2s, P 2p, Cu 2p, Cl 2s, Cl 2p, Fe 2p, and Co 2p photoelectron peaks.

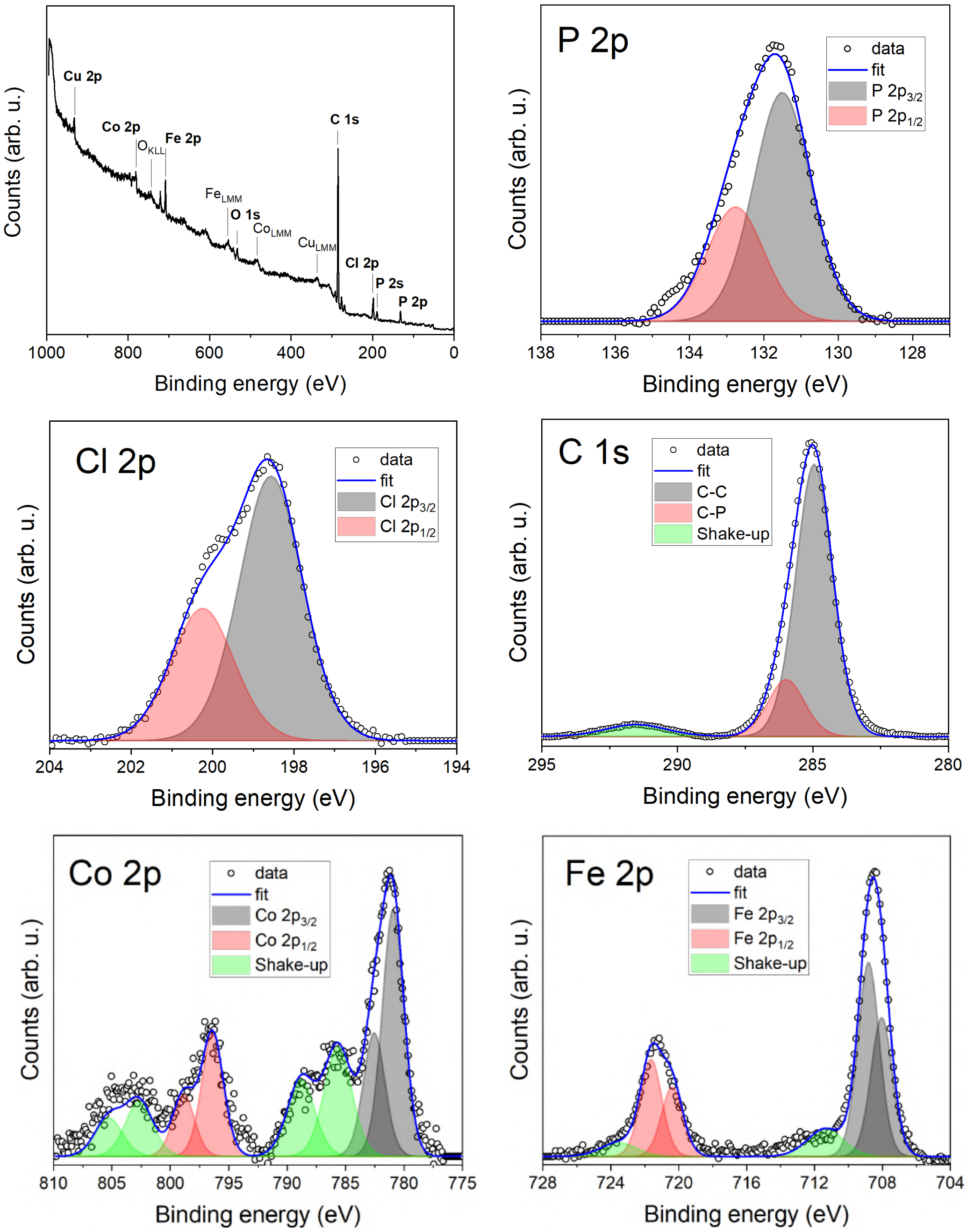

Figure 5.18: XPS spectra for bulk compound (**1**), survey (top left), and then according to elements, spectra for P 2p, Cl 2p, C 1s, Co 2p, and Fe 2p photoelectron peaks.

In the case of (**2**), Br 3d instead of Cl 2p was present in Figure (5.19). Both spectra showed also visible $\mathrm{O_{KLL}}$, $\mathrm{Fe_{LMM}}$, $\mathrm{Co_{LMM}}$, $\mathrm{Cu_{LMM}}$ Auger peaks. Highly resolved spectra of C 1s, P 2p, Cl 2p (or Br 3d), Co 2p, and Fe 2p for both compounds revealed a similar chemical environment through a fitting process by utilising the convolution of Voigt curves to reproduce spectra. The best-fit parameters were found by applying constraints to the components forming the overall spectrum based on the nature of the systems: taking into account the relationship between components area and total angular momentum multiplicity of the final states (for spectra related to orbitals with non-zero angular momentum) and assuming the same FWHM for analogues components in each sample [126, 127]. XPS spectra of bulk (**2**) exhibited main ferrocene peak Fe 2p$_{3/2}$ at 708.5 eV with spin-orbit coupling (SOC) separation of 12.4 eV, which is in agreement with previous studies [162–164]. The Co 2p photoemission line Co 2p$_{3/2}$ at 780.9 eV with SOC of 15.4 eV. Both compounds (**1**) and (**2**) exhibit shake-up features, which serve as a fingerprint of having paramagnetic Co(II) complex in the high-spin state [165–169].

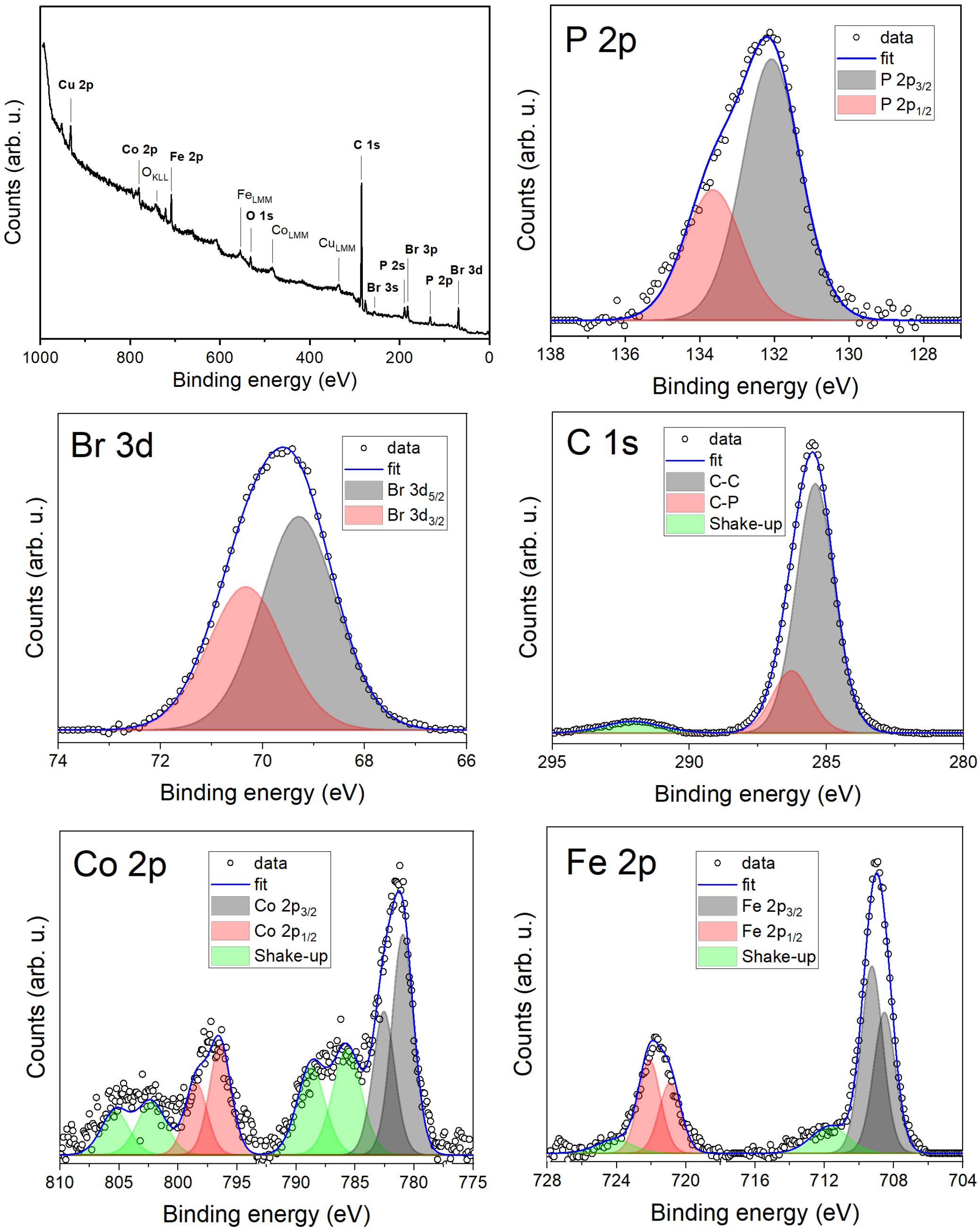

Figure 5.19: XPS spectra for bulk compound (**2**), survey (top left), and then according to elements, spectra for P 2p, Br 3d, C 1s, Co 2p, and Fe 2p photoelectron peaks.

Figure (5.20) shows XPS survey spectra for bulk powder scratched on Cu foil (bulk), drop-cast from a 5 mM solution on Au(111) in a nitrogen atmosphere (drop), and a sublimated 30 nm thick film on Au(111) substrate (subl).

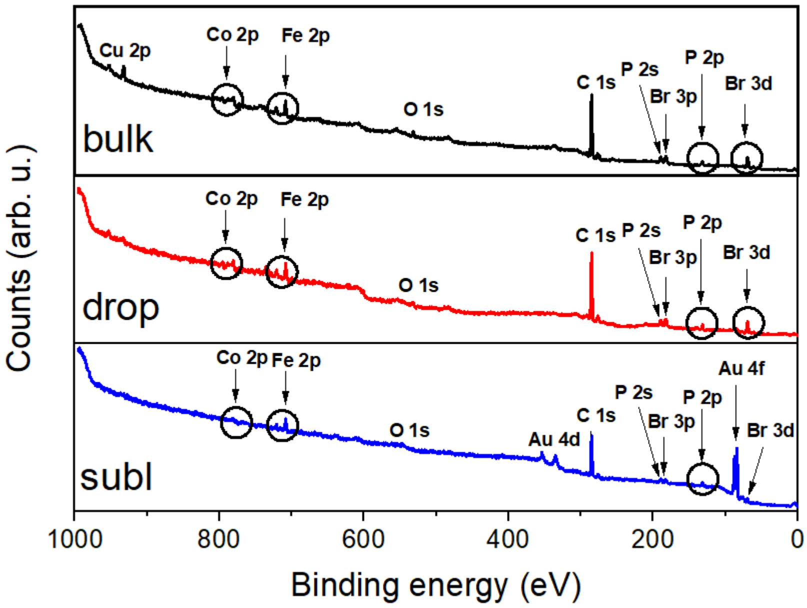

Figure 5.20: XPS survey spectra of (**2**) as a bulk powder (top), drop-cast in nitrogen on Au(111) (middle), and sublimated on Au(111).

Table (5.1) shows a comparison of Fe $2p_{3/2}$ and Co $2p_{3/2}$ peak binding energies with previous studies. For cobalt, a slight shift (0.8 eV) of the $2p_{3/2}$ peak has been observed between the sublimated sample and bulk powder. Considering the direction of the shift (toward lower binding energies), the bromine deficiency, the excess of phosphorous and iron evidenced from stoichiometry evaluations, one scenario might be the partial decomposition of [$CoBr_2$(dppf)]. However, Co $2p_{3/2}$ peak positions are in good agreement with similar systems reported in the literature, with slight shifts due to the differences in the coordination environment.

	Fe $2p_{3/2}$ (eV)	Co $2p_{3/2}$ (eV)
Bulk	708.5	781.0
Drop	708.3	780.6
Subl	708.4	780.2
Ref.	708.5 [170]; 708.1 [171]; 707.9 [172]; 708.0 [163]	780.1 [173]; 780.9 [174]; 781.2 [174]

Table 5.1: Positions of Fe $2p_{3/2}$ and Co $2p_{3/2}$ binding energies.

Detailed XPS spectra for depositions are shown in Figure (5.21) along with a semi-quantitative determination of the elemental composition in Table (5.2). Carbon and oxygen contributions were considered not relevant since they may be affected by adventitious contaminants due to the *ex situ* preparation procedures. The quantitative analysis for an as-synthesised powder of (**2**) and drop-cast in nitrogen atmosphere of (**2**) suggests preserved stoichiometric composition structure, whereas, in the case of sublimated (**2**), the amount of Co and Br was lower than expected, which could be attributed to partial chemical decomposition. In the case of Fe 2p and Co 2p, shake-up satellite features were present in all three investigated samples as expected. No significant shift in binding energies among the different samples has been detected.

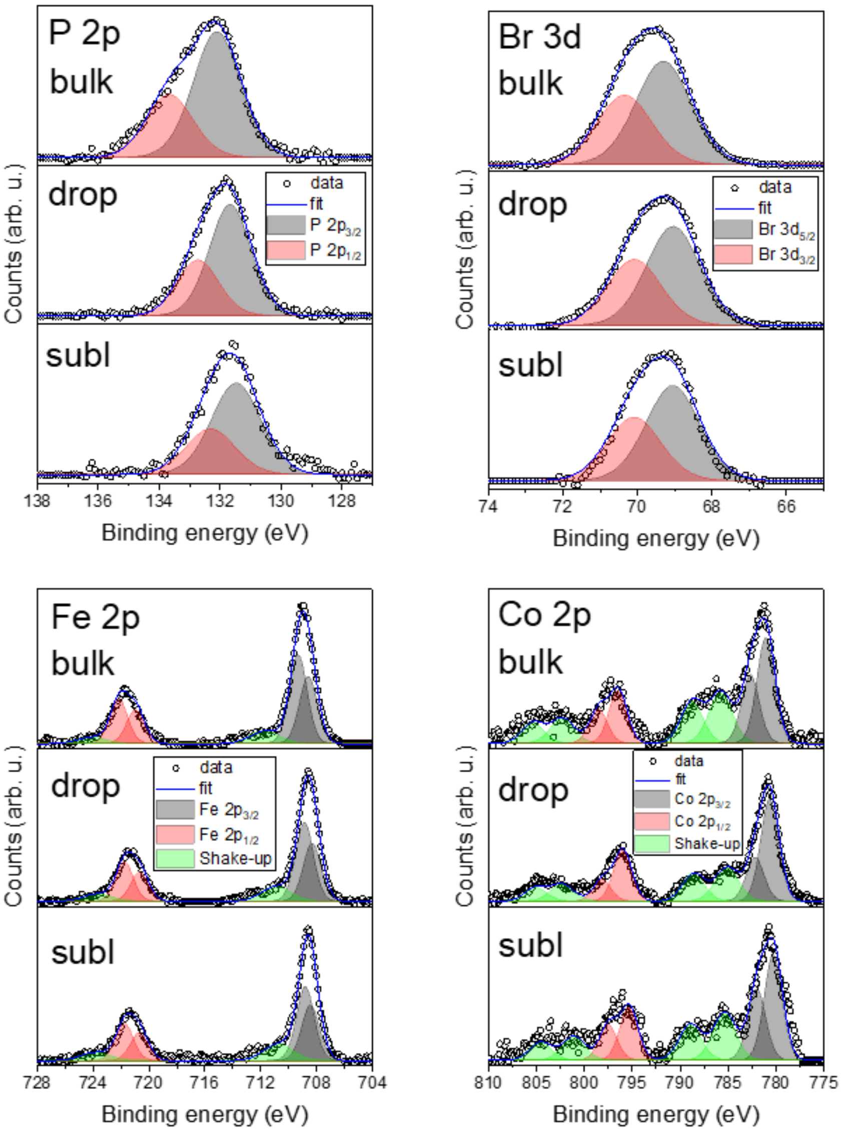

Figure 5.21: Detailed XPS spectra comparison of (**2**) for bulk powder, drop-cast, and sublimation for P 2p, Br 3d, Fe 2p, and Co 2p photoelectron peaks.

Element	Calculated*	1 bulk	2 bulk	2 drop	2 subl
Co	16.7%	12.5%	13.1%	12.3%	10.1%
Fe	16.7%	13.0%	13.1%	14.0%	19.3%
Br*	33.3%	–	34.5%	33.3%	21.6%
P	33.3%	37.1%	39.3%	40.4%	49.0%
Cl*	33.3%	37.4%	–	–	–

Table 5.2: Semi-quantitative determination of the elemental composition. *Chlorine and Bromine content were evaluated respectively only in compound (**1**) and (**2**).

Iron $2p_{3/2}$ peak positions were in good agreement with previous studies addressing the iron in ferrocene molecules (see Table (5.1)). This might be due to the intactness of ferrocene moiety on the surface, even after utilising high vacuum sublimation techniques. However, in the case of the film of (**2**) obtained by sublimation, we observed a shift in binding energies of both elements, which can be attributed to partial decomposition to the thermally stable dppf [164], which serves as a precursor for synthesis. This finding agrees with the decomposition hypothesis deduced from UV-VIS spectroscopy. These findings suggest that films obtained via sublimation are affected by a partial decomposition. Therefore, we may conclude that future deposition attempts should adopt wet-chemistry based protocols preferentially under inert atmosphere [175], which have proven to provide chemically intact deposits of (**2**).

Electron spin resonance (ESR)

High-frequency ESR (HF-ESR) spectra at 5 K, 10 K, 20 K, and 40 K for four frequencies 270 GHz, 320 GHz, 360 GHz, and 380 GHz were recorded on a home-built spectrometer [12] featuring a VDI signal generator, a VDI amplifier-multiplier chain, a Thomas Keating quasi-optical bridge, an Oxford Instruments 15/17 T solenoid cryogenic magnet and a QMC Instruments InSb hot-electron bolometer. Both (**1**) and (**2**) samples were studied as pressed Teflon-wrapped powder pellets. All spectra were simulated using the EasySpin toolbox for Matlab [28].

The bulk magnetic properties of cobalt-ferrocene dimers (CFDs) with linear chemical formula: $[X_2Co(P(C_6H_5)_2C_5H_4)_2Fe]$, where X = Br, Cl, and $(P(C_6H_5)_2C_5H_4)_2Fe$ = dppf] were investigated by HF-ESR. It allowed us to determine the spin Hamiltonian parameters such as the g-tensor and zero-field splitting (ZFS) terms, already defined in the theoretical part, representing intrinsic magnetic properties. Co(II) ions are in tetrahedral $3d^7$ electron configuration in a high-spin state ($S = \frac{3}{2}$). On the contrary, Fe(II) ions are in the $3d^6$ low-spin state ($S = 0$) with no unpaired electrons, and thus only Co(II) contributes to the overall HF-ESR spectrum.

Equation (5.6) describes the used spin Hamiltonian constructed by taking into account Zeeman and ZFS contributions:

$$\hat{H} = \hat{H}_{\mathrm{Zeeman}} + \hat{H}_{\mathrm{ZFS}} = \mu_{\mathrm{B}} \boldsymbol{B}_{\mathrm{ext}} \cdot \tilde{\boldsymbol{g}} \cdot \hat{\boldsymbol{S}} + \hat{\mathcal{H}}_{\mathrm{ZFS}} = D\left[\hat{S}_z^2 - \frac{1}{3}S(S+1)\right] + E(\hat{S}_x^2 - \hat{S}_y^2), \qquad (5.6)$$

where μ_{B} is Bohr magneton, $\boldsymbol{B}_{\mathrm{ext}}$ is applied external magnetic field, $\tilde{\boldsymbol{g}}$ is a tensor linking the magnetic field and the spin vectors, D is the axial component of magnetic dipole-dipole interaction and E is the transversal component describing the rhombicity of a system, and $\hat{S}$ is total spin of the system, in this case $S = \frac{3}{2}$.

Figure (5.22) shows the best fitting parameters found for $[CoCl_2(dppf)]$ (top): $D =$ $= -12.0\,\mathrm{cm}^{-1}$ with $E/D = 0.106$, and $g_{\mathrm{x}} = 2.22$, $g_{\mathrm{y}} = 2.22$, $g_{\mathrm{z}} = 2.28$ and $[CoBr_2(dppf)]$ (bottom): $D = -11.2\,\mathrm{cm}^{-1}$ with $E/D = 0.090$, and $g_{\mathrm{x}} = 2.22$, $g_{\mathrm{y}} = 2.22$, $g_{\mathrm{z}} = 2.31$. The spectra were measured at low temperature of $T = 5\,\mathrm{K}$ and external magnetic field was swept from 0 T to 15 T at 4 different frequencies.

These experimental results are in fair agreement with *ab initio* quantum chemical simulations (CASSCF/NEVPT2). The effective energy barrier for $[CoBr_2(dppf)]$ can be then calculated as: $U_{\mathrm{eff}} = |D| \times (S^2 - \frac{1}{4}) = 22.4\,\mathrm{cm}^{-1}$ and for $[CoCl_2(dppf)]$: $U_{\mathrm{eff}} = 24.0\,\mathrm{cm}^{-1}$. The replacement of the bromine by chlorine also changes the ligand field around the central metal ion, and therefore by chemically engineering the ligands around the metal, a better SMM can be achieved. This is the path that our research group is focused on. To be able to change magnetic properties and adhesion to surfaces by changing the ligand field around metallic centres in SMMs and qubits.

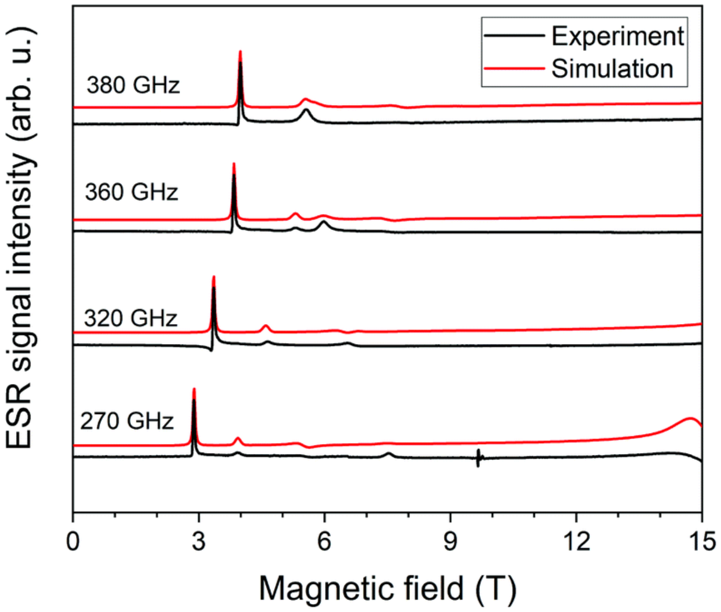

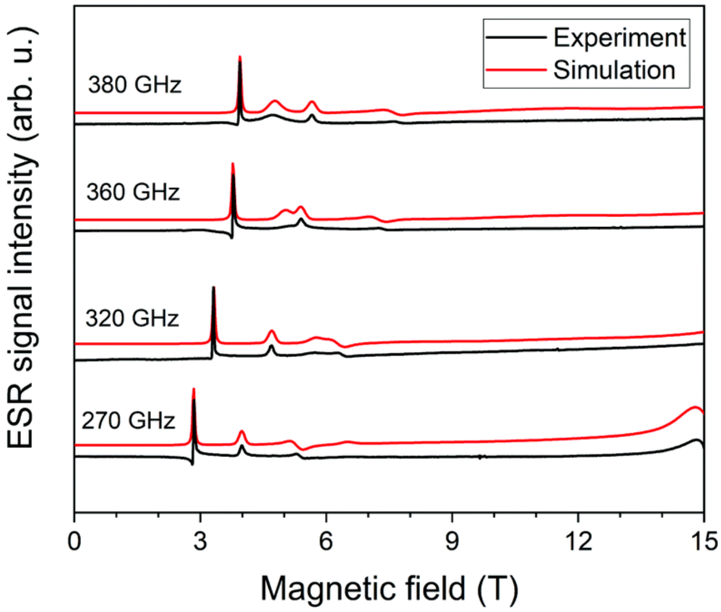

Figure 5.22: HF-ESR powder spectra of [CoCl$_2$(dppf)] - (top) and [CoBr$_2$(dppf)] - (bottom) for four different frequencies, 270 GHz, 320 GHz, 360 GHz, and 380 GHz, respectively, from 0 T to 15 T measured at 5 K.

Figures (5.23) and (5.24) show the temperature dependence in HF-ESR spectra.

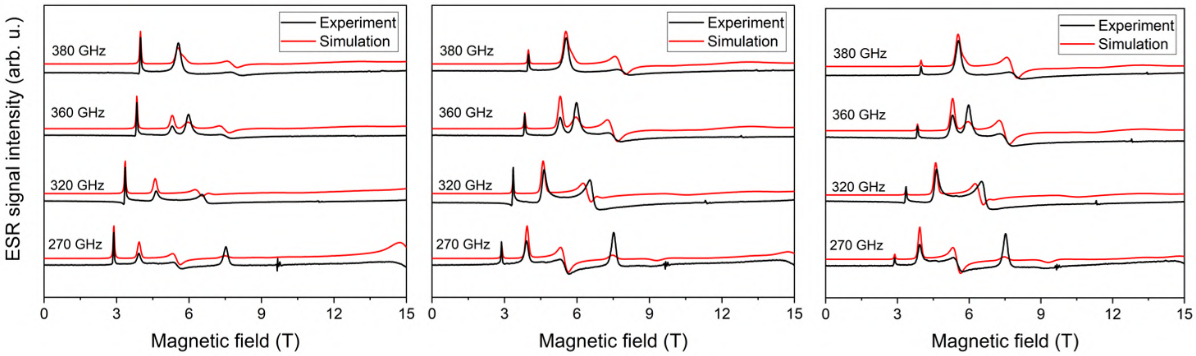

Figure 5.23: HF-ESR spectra of (**1**) at 10 K (left), 20 K (middle), and 40 K (right). The black solid line represents experimental data and the red solid line is the simulation.

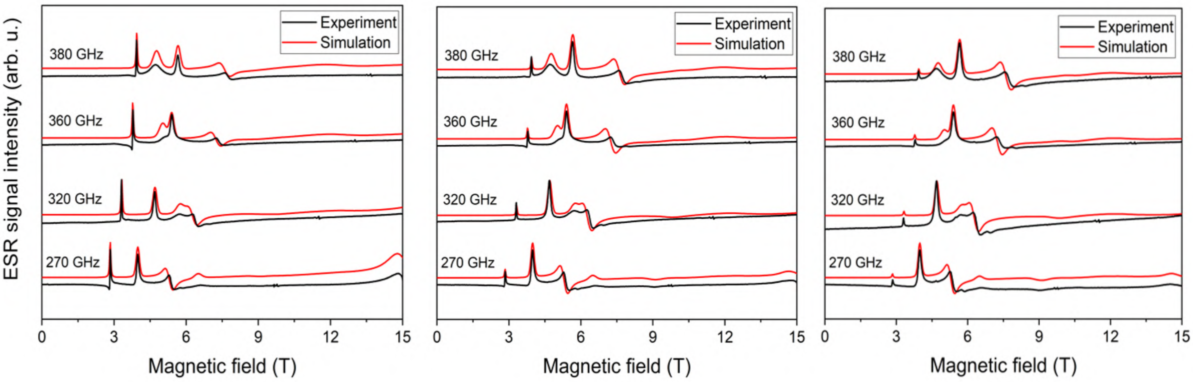

Figure 5.24: HF-ESR spectra of (**2**) at 10 K (left), 20 K (middle), and 40 K (right). The black solid line represents experimental data and the red solid line is the simulation.

5.3. Deposition of tetracoordinate Co(II) complex with chalcone ligands on graphene

Following results were obtained in cooperation and published in:

J. Hrubý, Š. Vavrečková, L. Masaryk, A. Sojka, J. Navarro-Giraldo, M. Bartoš, R. Herchel, J. Moncol, I. Nemec and P. Neugebauer: Deposition of Tetracoordinate Co(II) Complex with Chalcone Ligands on Graphene, *Molecules,* **25**, 5021 (2020).

Abstract

Studying the properties of complex molecules on surfaces is still mostly an unexplored research area because the deposition of metal complexes has many pitfalls. Herein, we probed the possibility to produce surface hybrids by depositing a Co(II)-based complex with chalcone ligands as shown in Figure (5.25) on chemical vapour deposition (CVD)-grown graphene by a wet-chemistry approach and by thermal sublimation under high vacuum. Samples were characterised by high-frequency electron spin resonance (HF-ESR), XPS, Raman spectroscopy, atomic force microscopy (AFM), and optical microscopy, supported with density functional theory (DFT) and complete active space self-consistent field (CASSCF)/N-electron valence second-order perturbation theory (NEVPT2) calculations. This compound's rationale is its structure, with several aromatic rings for weak binding and possible favourable π–π stacking onto graphene. In contrast to expectations, we observed the formation of nanodroplets on graphene for a drop-cast sample and microcrystallites localised at grain boundaries and defects after thermal sublimation.

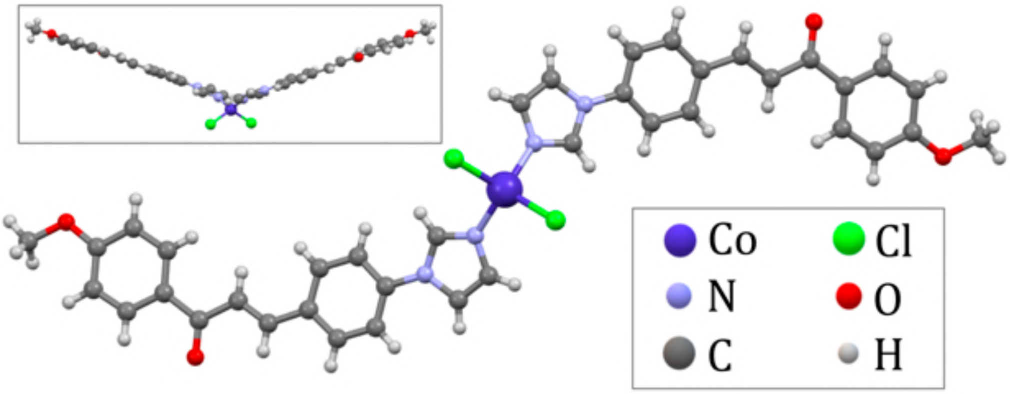

Figure 5.25: Molecular structure of studied Co(II)-based coordination complex.

Introduction to topic

Nearly three decades have already passed since the first description of the slow relaxation of magnetisation in the polynuclear cluster $[Mn_{12}O_{12}(O_2CCH_3)_{16}(H_2O)_4]$ known as Mn_{12} [31, 176, 177], which started the whole new research field of molecular magnetism [27]. These so-called Single-Molecule Magnets (SMMs) exhibit magnetic bi-stability up to a specific blocking temperature manifested by intrinsic spin-reversal barrier energy (U_{eff}). The barrier is a function of the total spin in the ground state (S) and the axial component of magnetic dipole-dipole interaction (D) as follows: $U_{\mathrm{eff}} = |D| \times S^2$ for integer spins and $U_{\mathrm{eff}} = |D| \times (S^2 - \frac{1}{4})$ for non-integer spins, respectively, in axial symmetry. This alone would imply that by increasing the number of magnetic centres, a better SMM would be obtained; however, there is a dependency of $D \propto \frac{1}{S^2}$ that stems from spin-orbit contributions to the D-tensor [19]. This dependency shifted the interest from rather large molecules with many magnetic atoms to Single-Ion Magnets (SIMs) [141]. Several challenges need to be addressed before fully utilising these SIMs in real applications. One of the challenges is increasing the blocking temperature, which was recently found to be 80 K in dysprosium metallocene in 2018 [142]. This temperature, above the boiling point of liquid nitrogen (77 K), already holds promise for possible applications in spintronics [90], quantum computing [89], and molecular electronics [60]. The second challenge is finding the way from bulk material to functional surfaces.

The magnetic properties of magnetic molecules can be precisely measured by high-frequency electron spin resonance (HF-ESR) both in bulk [12, 43, 45, 46, 50, 53–56, 178] and on a surface [69–71]. Primarily, the Zeeman and zero-field-splitting (ZFS) contributions to the spin Hamiltonian with information about the intrinsic magnetic properties of a molecule can be determined. Today, the current effort is focused on making thin films, ordered arrays, or self-assembled monolayers that will lead to technological applications [61, 62]. The key for this is to understand the behaviour and adsorption of complex molecules on surfaces since their exposed surface offers many application possibilities but also brings many challenges, as these molecules can oxidise, decompose, or degrade in ambient conditions. There are two main ways to produce nanostructured magnetic thin films. They can be deposited onto a substrate via a wet-chemistry protocol from a solution [64, 179, 180] or by thermal sublimation in vacuum [67, 68, 181–184].

The electrical addressing of SMMs can be provided via a conductive substrate. A promising candidate is an atomically thin layer of graphite, known as graphene [185], which is an interesting substrate due to its high electron mobility [57, 99], mechanical strength [100], and thermal conductivity [101]. The original preparation technique firstly used to prepare graphene in 2004 was micro-mechanical cleavage [102]. This method is suitable for tens-of-micrometers-large flakes; however, more industrial techniques for large and homogeneous surface coverage soon emerged, such as graphene production by chemical vapour deposition (CVD) [103], on silicon carbide [104], by liquid-phase exfoliation [105], or by large-scale roll-to-roll printing [186]. The perfect graphene is a zero-gap semiconductor, which helps the charge carrier mobility but also limits the applications.

Herein, we reported on the synthesis, crystal structure, magnetic properties, and characterisation of a new tetracoordinate complex $[Co(4MeO\text{-}L)_2Cl_2]$ (**1**) with the chalcone imidazole-derivative ligand 4MeO-L = (2E)-3-[4-(1H-imidazol-1-yl)phenyl]-1-(4-methoxyphenyl)prop-2-en-1-on. The determination of the crystal structure revealed that this compound is tetracoordinate, and its molecules possess a unique shape with a large angle between the coordinated 4MeO-L ligands (*vide infra*). Tetracoordinate Co(II) compounds very often exhibit large easy-axis ($D < 0$) or easy-plane ($D > 0$) magnetic anisotropies [187]. Furthermore, the “flat” molecular shape involving the large aromatic system of the ligands might help to anchor complex molecules on surfaces such as graphene by non-covalent interactions. Therefore, we decided to thoroughly characterise the electronic structure of (**1**) by HF-ESR to investigate both wet-chemistry and thermal sublimation depositions and, thus, to produce a hybrid material composed of highly anisotropic Co(II)-based molecules and graphene. These samples were then characterised by Raman spectroscopy, X-ray photoelectron spectroscopy (XPS), and atomic force microscopy (AFM).

Synthesis of (1)

The chalcone ligand 4MeO-L was prepared by the aldol condensation of 4 -(imidazol-1-yl)benzaldehyde with 4-methoxyacetophenone. The purity and structure of 4MeO-L were confirmed by ^1H and ^{13}C NMR spectroscopy, mass spectrometry, and elemental analysis. The complex (**1**) was synthesised by a reaction between $CoCl_2{\cdot}6H_2O$ and 4MeO-L (molar ratio, 1:2) in methanolic solution, and it precipitated as a blue microcrystalline powder. Recrystallisation from methanol led to the isolation of pale blue crystals suitable for single-crystal diffraction.

Deposition on graphene

Drop-cast sample was prepared by dissolving the bulk compound (**1**) in dichloromethane (98%, Penta, Czech Republic) to make a final solution with a 100 µM concentration. The actual drop-casting was conducted in a mobile glove bag (Merck, Germany) filled with inert nitrogen gas; 10 µL was drop-cast onto a substrate. For the thermal sublimation, we used a home-built high-vacuum sublimation chamber equipped with a quartz crucible heated by tungsten wire, with a thermocouple in thermal contact with the crucible. The base chamber pressure during the sublimation was 2 $\times 10^{-7}$ mbar. The sublimations were performed at 75 °C and 265 °C, respectively.

Raman spectroscopy (RS)

Raman spectra were acquired on a confocal Raman microscope WITec Alpha300 R+ (WITec, Ulm, Germany). All measurements were carried out with the excitation laser source with a 532 nm wavelength and 1 mW power output. Optical images were acquired with a 100× objective (NA 0.9, WD 0.31 mm).

We used CVD graphene (Graphenea, San Sebastian, Spain) on a Si/SiO$_2$ substrate. Figure (5.26) shows the substrate Raman spectra that helped us to determine the defects involved in the graphene. The Si/SiO$_2$ Raman spectrum has a main strong phonon band at 520 cm^{-1} and two medium peaks at 301 cm^{-1} and in the region (946 - 976) cm^{-1} [80, 120]. A spectrum of CVD graphene exhibited the strong peaks D at 1347 cm^{-1}, G at 1595 cm^{-1}, and 2D at 2689 cm^{-1}, with the weaker peaks D at 1627 cm^{-1} and D+D at 2462 cm^{-1}. The presence of a strong G peak and weak D' suggests CVD graphene with defects [121].

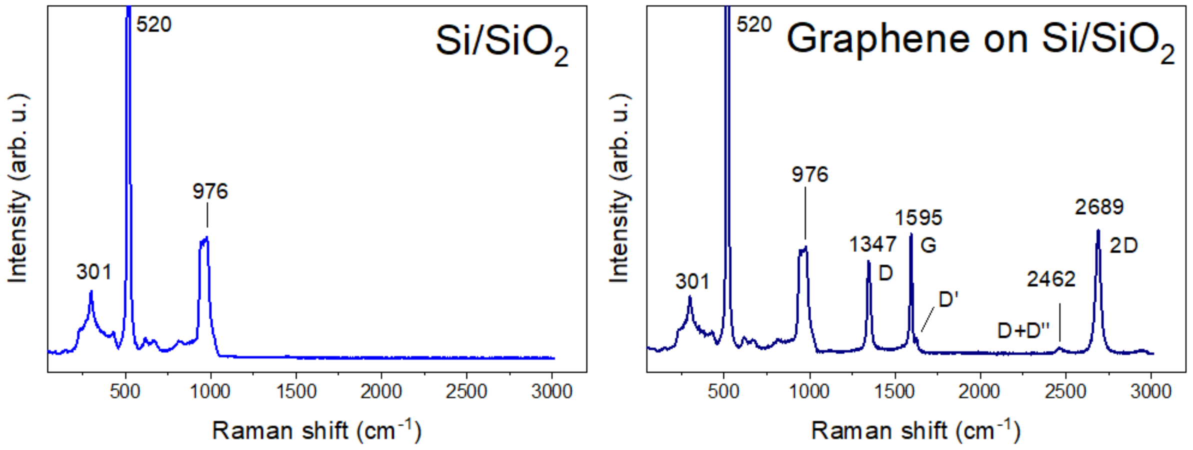

Figure 5.26: Raman spectra of Si/SiO$_2$ substrate and graphene on Si/SiO$_2$ substrate.

Figure (5.27) shows comparison of bulk compound (**1**), drop-cast, and two sublimated samples at 75 °C and 265 °C.

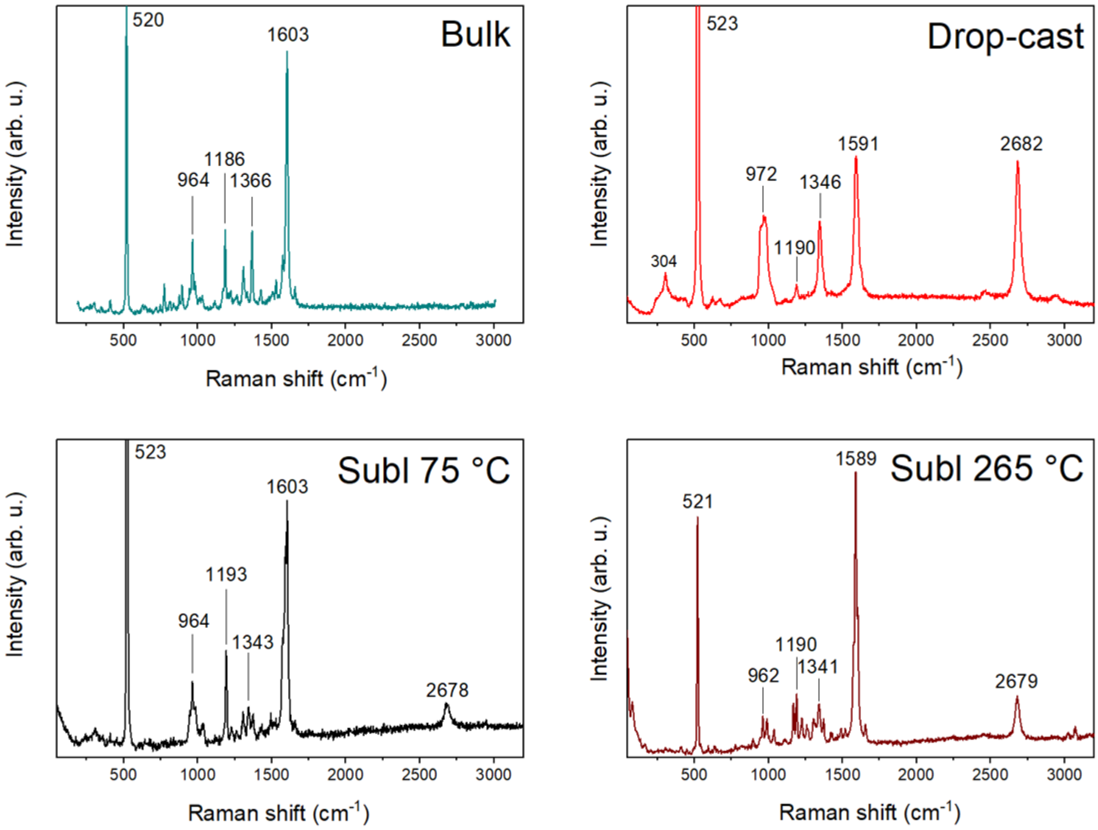

Figure 5.27: Comparison of Raman spectra of bulk compound (**1**), drop-cast, and sublimations at 75 °C and 265 °C.

The Raman spectrum of the bulk compound (**1**) on the Si/SiO$_2$ substrate consists of significant peaks (964, 1186, 1366, and 1603 cm^{-1}) and peaks of Si/SiO$_2$. In the case of the drop-cast sample, significant peaks were overlapped with the peaks of graphene and Si/SiO$_2$, except one (1190 cm^{-1}). By contrast, the Raman spectra of the sublimated samples all showed significant peaks due to measurements on a larger crystal and obtaining a stronger signal.

Optical images of the hybrid material taken along with Raman spectroscopy are shown in Figure (5.28).

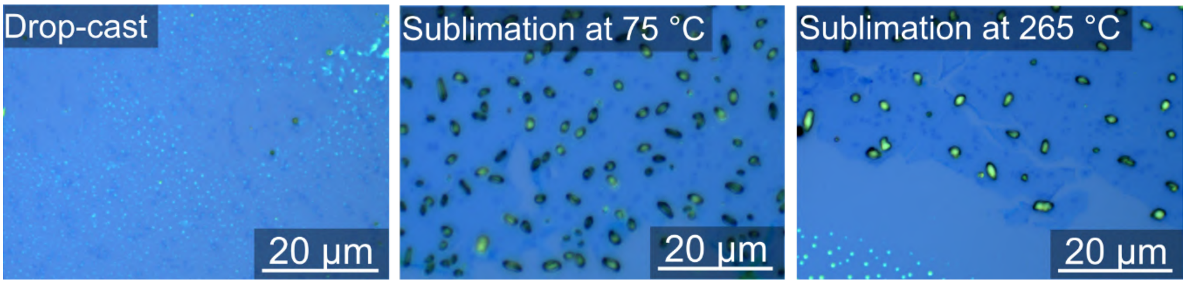

Figure 5.28: Images from the optical microscope of the samples after drop-casting and sublimations at 75 °C and 265 °C.

Atomic force microscopy (AFM)

All topography images and profiles were obtained with the scanning probe microscope Bruker Dimension Icon in tapping mode.

Figure (5.29) shows the AFM images with profiles from white lines. The drop-cast sample consists of nanodroplets up to 50 nm high. On the contrary, sublimated samples resulted in the formation of microcrystals hundreds of nanometers high.

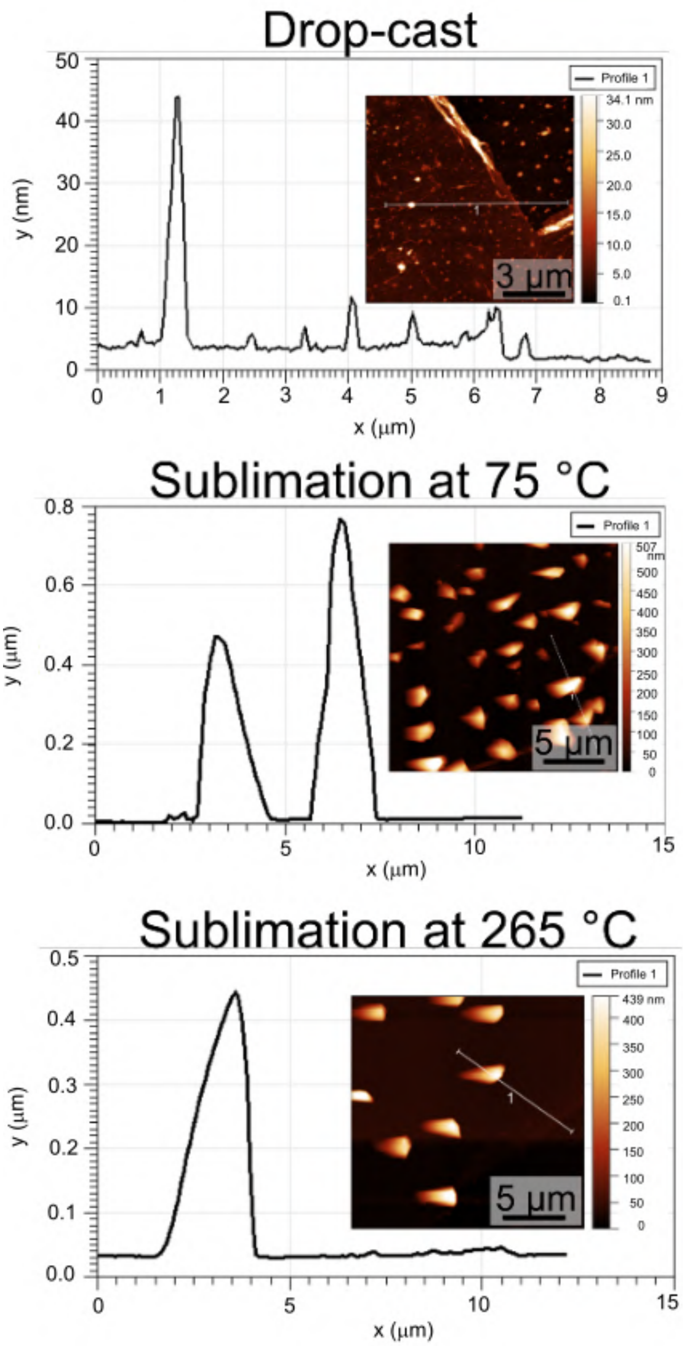

Figure 5.29: AFM images from drop-cast and sublimated samples at 75 °C and 265 °C.

X-ray photoelectron spectroscopy (XPS)

X-ray photoelectron (XPS) measurements were carried out with a Kratos Axis Supra (Kratos Analytical, Manchester, United Kingdom) spectrometer at room temperature and under ultra-high vacuum (UHV) conditions. The instrument was equipped with a monochromatic Al-Kα source of 1486.6 eV (15 mA, 15 kV) and a hemispherical analyser with a hybrid magnetic and electrostatic lens for enhanced electron collection. Survey and detailed XPS spectra were acquired at normal emission with fixed pass energies of 160 eV and 20 eV, respectively. All spectra were calibrated to the hydrocarbon peak set to 284.8 eV. The Kratos charge neutraliser system was used on all specimens. The inelastic backgrounds in all the spectra were subtracted according to the Shirley method [125]. Data analysis was based on a standard deconvolution method using a mixed Gaussian (G) and Lorentzian (L) line shape (G = 70% and L = 30%, Gaussian–Lorentzian product) for each component in the spectra. The elemental composition of the samples was evaluated using a semi-empirical approach. The integrated intensity of each component was corrected with the photoionisation cross-section calculated for each atom, neglecting the differences in photoelectron escape length as a function of the kinetic energy [161]. The spectra were analysed using the CasaXPS software (version 2.3.18).

The chemical composition was probed by XPS. Figure (5.30) shows spectra of bulk compound (**1**). The bulk compound (**1**) spectrum exhibited photoelectron peaks—Co 2p, Cl 2p, N 1s, C 1s, and O 1s—and Augers peaks: $\mathrm{O_{KLL}}$ and $\mathrm{Co_{LMM}}$. The detailed spectra of the selected peaks revealed specific chemical bonds. The N 1s peak was deconvoluted to two components: graphitic N with three neighbouring C atoms and pyrrolic N with two C atoms and one Co bond [188]. The photoelectron peaks emitted from the p, d, and f electronic levels are further split by spin-orbit interactions. This helped us to distinguish, in the Cl 2p spectrum, between organic (Cl–C and Cl–H) and inorganic (Cl–Co) components [189]. Co 2p exhibited two main components and shake-up satellites. The spin-orbit shift of the main components Co $2p_{3/2}$ and Co $2p_{1/2}$ depends on the oxidation state, and with 15.6 eV, the Co(II) high-spin state predominates [169].

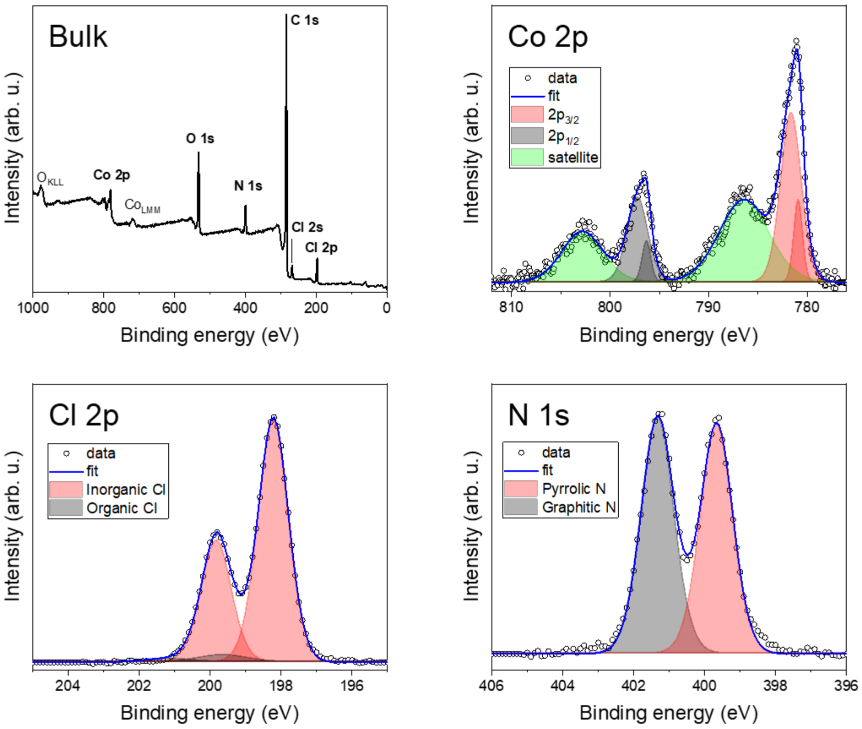

Figure 5.30: Survey XPS spectrum and detailed Co 2p, Cl 2p, and N 1s spectra.

Figure (5.31) shows the comparison of the hybrid samples with CVD graphene: drop-cast, and sublimated at 75 °C and 265 °C, respectively.

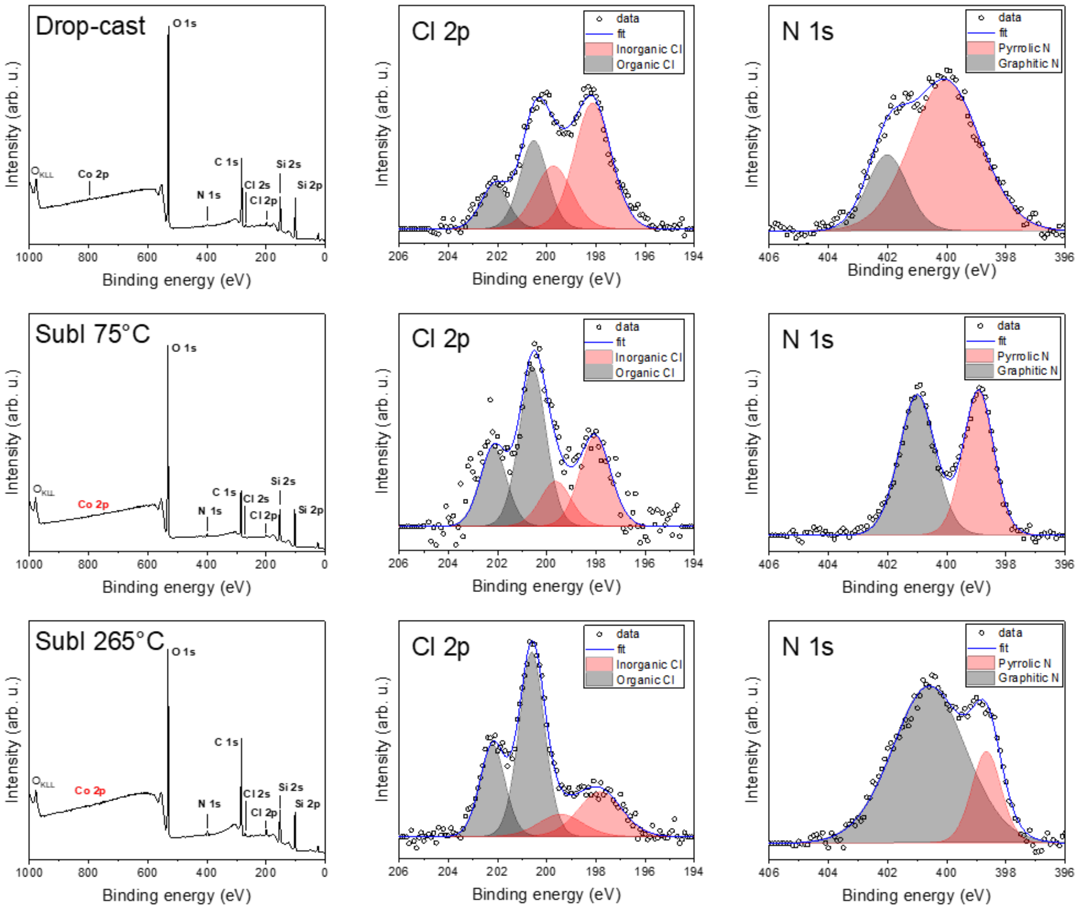

Figure 5.31: Comparison of detailed XPS spectra of drop-cast and sublimated samples at 75 °C and 265 °C.

In the drop-cast sample, we observed a decrease in the graphitic nitrogen component compared to bulk compound (**1**) and an apparent split of chlorine to inorganic and organic contributions. In the case of drop-casting, we detected a weak Co 2p signal on the surface, suggesting a possible complex decomposition as shown in Figure (5.32).

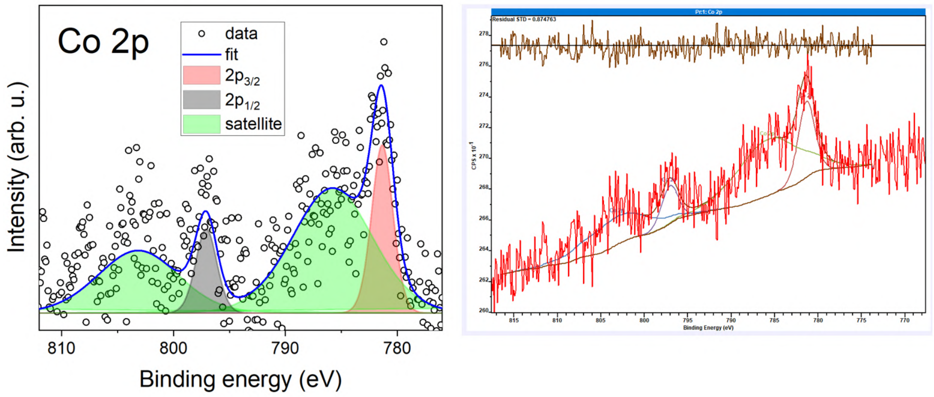

Figure 5.32: Weak signal from Co 2p found on the surface after drop-cast. The right side of the image shows the fit in the CasaXPS program with a weak Co 2p peak detected.

In the case of the sublimated samples, even after several hours of acquisition, we did not obtain any convincing Co 2p peaks for 75 °C and 265 °C. This may be attributed to the possible partial decomposition of the complex or the surface sensitivity of XPS, with the complex outmost layers containing only a very few Co atoms or so-called "dead" layers with oxidized, spoiled molecules. This absence led us to a semi-empirical quantitative analysis of the powder after each sublimation as shown in Figure (5.33) and revealed an increased amount of cobalt and chlorine in the powder from the crucible compared to the bulk powder. This, along with the detected organic chlorine, suggests the possible partial chlorination of the graphene with a partial decomposition of the complex during both deposition processes. Carbon and oxygen contributions were discarded since they might be affected by adventitious contaminants due to the *ex situ* preparation procedures.

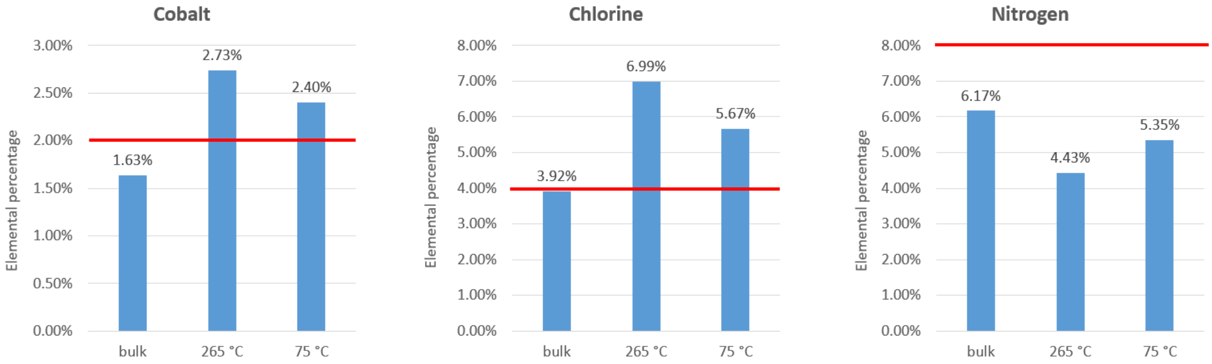

Figure 5.33: Histograms from the semi-empirical quantitative analysis of elemental composition for the studied complex of powder taken from crucible after sublimation at 75 °C and 265 °C. The red line denotes the calculated ideal percental amount of each element from the compound $CoC_{38}H_{32}Cl_2N_4O_4$. Histograms illustrate that cobalt and chlorine content increases as the sublimation temperature rises; this means that cobalt stays in the crucible and supports the observation of no cobalt detected on the surface of microcrystallites after thermal sublimation.

Electron spin resonance (ESR)

HF-ESR spectra were acquired on a newly home-built spectrometer featuring a signal generator (Virginia Diodes, Charlottesville, VA, USA), an amplifier–multiplier chain (Virginia Diodes, Charlottesville, USA), a quasi-optical bridge (Thomas Keating, Billingshurst, UK), and a 16 T solenoid cryomagnet (Cryogenic, London, UK) with heterodyne signal detection. The reference powder sample of the complex was studied as a pressed powder into a ⌀5 mm pellet sample. All ESR spectra were simulated using EasySpin [28], a toolbox for Matlab.

Figure (5.34) shows the HF-ESR spectra acquired for bulk compound (**1**) at four frequencies 380 GHz, 415 GHz, 456 GHz, and 490 GHz while sweeping the magnetic field from 0 to 15 T at 5 K.

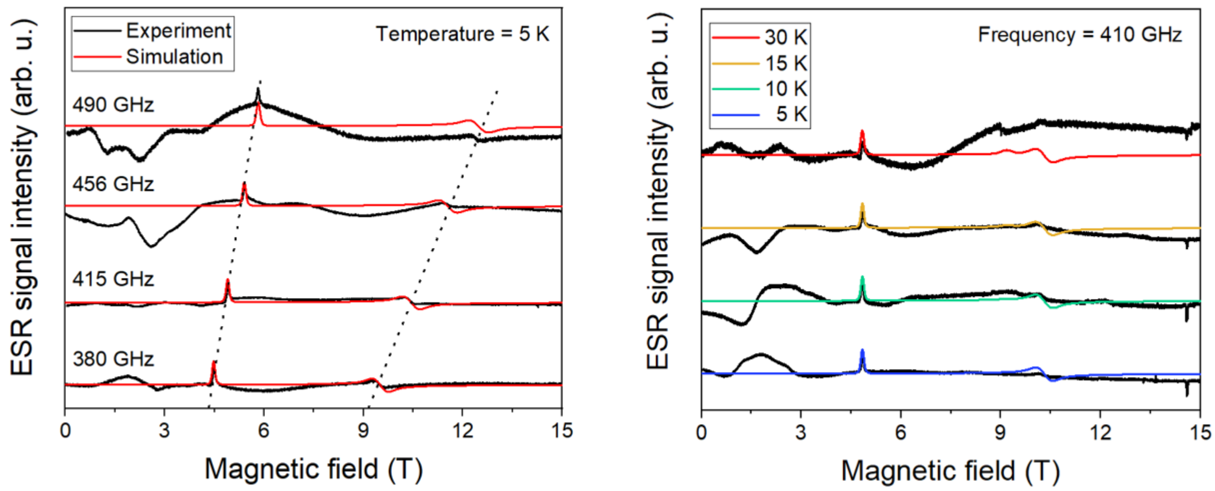

Figure 5.34: Left: high-frequency electron spin resonance (HF-ESR) spectra for four different frequencies at 5 K. The dotted line is guidance for Zeeman splitting. Right: temperature dependence acquired at 410 GHz. Black line in both is experimental, and red/colored line is the simulation.

Equation (5.7) describes the used effective spin Hamiltonian for the simulations:

$$\hat{H} = \hat{H}_{\text{Zeeman}} + \hat{H}_{\text{ZFS}} = \mu_{\text{B}} \boldsymbol{B}_{\text{ext}} \cdot \tilde{\boldsymbol{g}} \cdot \hat{\boldsymbol{S}} + D\hat{S}_z^2 + E(\hat{S}_x^2 - \hat{S}_y^2), \tag{5.7}$$

where μ_{B} is Bohr magneton, $\boldsymbol{B}_{\text{ext}}$ is applied external magnetic field, $\tilde{\boldsymbol{g}}$ is a tensor linking the magnetic field and the spin vectors, $\hat{\boldsymbol{S}}$ is total spin of the system: $S = \frac{3}{2}$, D and E are axial and rhombic zero-field splitting parameters, respectively in this case. The best fit was found for the spin Hamiltonian parameters as follows: $D = 14.6\,\text{cm}^{-1}$ with $E/D = 0.235$, and $g_{\text{x}} = 2.32$, $g_{\text{y}} = 2.38$, and $g_{\text{z}} = 2.16$.

5.4. Nanostructured graphene for nanoscale electron paramagnetic resonance spectroscopy

Following research and results are a part of our cooperation with the University of Georgetown in the USA. The first collaborative work was already published: L. St. Marie, A. E. Fatimy, **J. Hrubý**, I. Nemec, J. Hunt, R. Myers-Ward, D. K. Gaskill, M. Kruskopf, Y. Yang, R. Elmquist, R. Marx, J. van Slageren, P. Neugebauer and P. Barbara: Nanostructured graphene for nanoscale electron paramagnetic resonance spectroscopy, *J. Phys. Mater.*, **3**, 014013 (2020). Our aim here is to use the graphene quantum dot as a bolometric detection device for SMMs and shorten the whole path from a sample to a detector.

Bolometric detectors

Bolometers are very sensitive detection devices for measurements of electromagnetic radiation power in a broad frequency range, including terahertz and infrared bands. The principle is based on heating a material with highly temperature-dependent electrical resistance caused by incident electromagnetic radiation [190]. They are also used in current astrophysics due to their high sensitivity and ability to detect a tiny amount of incident electromagnetic radiation [191]. The applicability also spans to the field of terahertz technology and spectroscopy. There are two important parameters determining the performance of a bolometer. The first is electrical response R (V/W), which defines the efficiency of the bolometer, that is the ability to convert incoming electromagnetic radiation to measurable output (higher is better). The second parameter is the noise-equivalent power NEP ($\mathrm{W}/\sqrt{\mathrm{Hz}}$) which represents the sensitivity (lower is better) [192].

The principle of bolometers can be described in the following way. The incident electromagnetic radiation has power $P = P_0 + \Delta P \cos(\omega t)$. The heat transfer is then as follows:

$$C\frac{\mathrm{d}T}{\mathrm{d}t} = P(t) - G(T - T_0), \tag{5.8}$$

where C is the heat capacity and G is heat conductivity. The temperature change is then:

$$\Delta T = \frac{\Delta P}{G\sqrt{1+\omega^2(C/G)^2}}. \tag{5.9}$$

The responsivity $R(\omega)$ is then:

$$R(\omega) = \frac{\Delta V}{\Delta P} \propto \frac{1}{G\sqrt{1+\omega^2(C/G)^2}}, \tag{5.10}$$

in the case of $\omega << 1/\tau$: $R(\omega) \propto \frac{1}{G}$ and for $\omega >> 1/\tau$: $R(\omega) \propto \frac{1}{\omega C}$, where $\tau = C/G$ is the bolometer constant [193].

Nowadays bolometric detectors (e.g. QMC Instruments Ltd.) work with the following parameters: $R > 5 \times 10^3$ V/W and $NEP < 7.5 \times 10^{-13}$ $\mathrm{W}/\sqrt{\mathrm{Hz}}$ at temperature of 4.2 K. These bolometers are based on (III-V) InSb semiconductors with the use of hot electrons (high kinetic energy) that occur only at very low temperatures, usually units of kelvin. At these temperatures, the electron gas in metal is only weakly bound to phonons. Electrons will get out of equilibrium with phonons after they absorb electromagnetic radiation and create high energy electron gas [194].

The scheme for graphene-based hot-electron bolometer is shown in the following Figure (5.35).

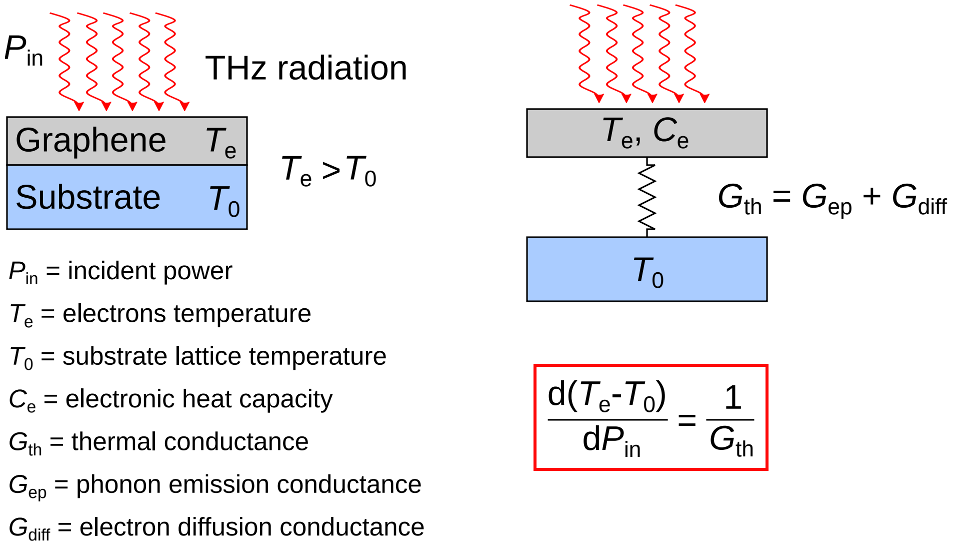

Figure 5.35: Left: the incident power P_{in} from THz radiation hits the graphene with electrons temperature T_{e} on the substrate with temperature T_0. Right: the scheme illustrates the thermal conductance G_{th} from a graphene to the substrate lattice via phonon emission G_{ep} and electron diffusion G_{diff}.

Our interest in bolometric detectors was prompted by the collaborators from Georgetown University, where nanostructured graphene was used for bolometers. Perfect graphene is a pure two-dimensional crystal with hexagonal lattice composed of carbon atoms with distinctive electric, thermal, mechanical properties [195], extraordinary stiffness [100] and high charge carrier mobility which stems from a weak interaction between electrons and phonons [196]. These properties, along with small heat capacity, makes graphene a promising material for very sensitive and responsive bolometers by using hot electrons.

However, monolayer graphene as such is not the best option for functional bolometric devices due to its low temperature-dependent electrical resistance, which changes less than 30 % from 30 mK to room temperature [197]. This property is caused by the abovementioned weak electron-phonon scattering [198]. This would make pure graphene not suitable for bolometric devices. This issue was overcome by dual gate structure on bilayer graphene in such a way to alter the graphene band gap [199], or by creating defects in graphene that cause a strong electron localisation [200].

The milestone in the field of graphene-based bolometers was research conducted by our collaborators where they were able to significantly push the up-to-date performance: 100 000× increase of electrical response R and 10× lower NEP at the temperature of 2.5 K. These results were obtained by using a graphene quantum dot (GQD) [201] which we further use for terahertz spectroscopy of single-molecule magnets. Quantum confinement was used in the setup. Nanostructured graphene quantum dots exhibit a rapid temperature-dependent change of electrical resistance; more than 430 MΩ/K under 6 K. This led to following parameters: $R \approx 1 \times 10^{10}$ V/W and NEP of 2×10^{-16} W/$\sqrt{\mathrm{Hz}}$ at 2.5 K. The advantage of this approach is also the temperature range at which it is still functional, up to 77 K, which makes their applicability more promising compared to other approaches [199, 200]. Bolometers based on graphene quantum dots can also be used as broad band photodetectors [202].

Following Table (5.3) compares parameters of electrical response R - the higher the better, NEP - the lower the better, temperature - the higher the better of commercial InSb bolometer from QMC instruments with state-of-the-art bolometers.

Table 5.3: Comparison of bolometer parameters.

	R (V/W)	NEP (W/$\sqrt{\text{Hz}}$)	Temp. (K)	Ref.
Commercial InSb bolometer	5×10^{3}	7.5×10^{-13}	4.2	QMC
Dual gate on bilayer graphene	2×10^{5}	3.3×10^{-14}	5	[199]
Defects in graphene	6×10^{6}	1.2×10^{-15}	1.5	[200]
Graphene quantum dots	1×10^{10}	2×10^{-16}	2.5	[201]
Magnetic tunnel junction	4×10^{6}	2.4×10^{-12}	uncooled	[203]
Graphene Josephson junction	-	7×10^{-19}	19 mK	[204]
Superconductor graphene junction	-	3×10^{-20}	50 mK	[205]

For our purpose, a bolometer serves as a substrate and an on-chip detector for deposited SMMs. By this step, we aim to increase the sensitivity of spectroscopic information obtained from the active area of graphene quantum dot (GQD). This approach would completely omit the need for the loss of signal path from a sample to the detector, whose power decreases along the way rapidly. Figure (5.36) shows the chip holder with bolometer chip on expander attachable to the ESR probe end. The right column shows SEM images with detail of graphene quantum dot (GQD) and an illustration of bolometer application to detect SMMs.

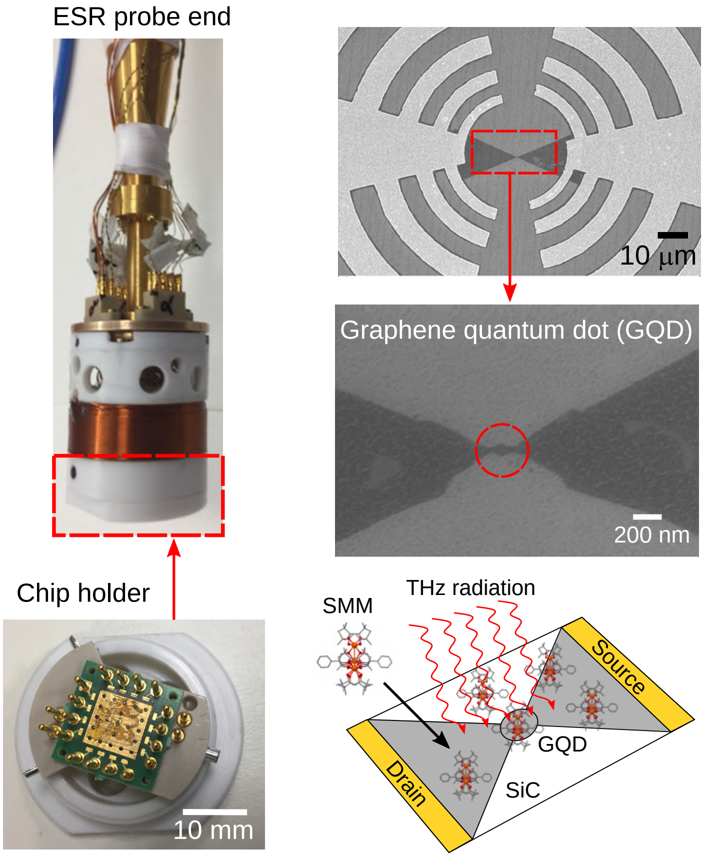

Figure 5.36: Left: insertion of chip holder connected by pins to printed circuit board (PCB) chip expander (SEANT Technology, Brno) with mounted graphene-based bolometer chip on silicon carbide (SiC). Right: SEM image with active graphene quantum dot (GQD) in inset together with a scheme of application on deposited SMMs.

The first characterisation of bolometric chip 9EM2 with several active devices in shown in Figure (5.37).

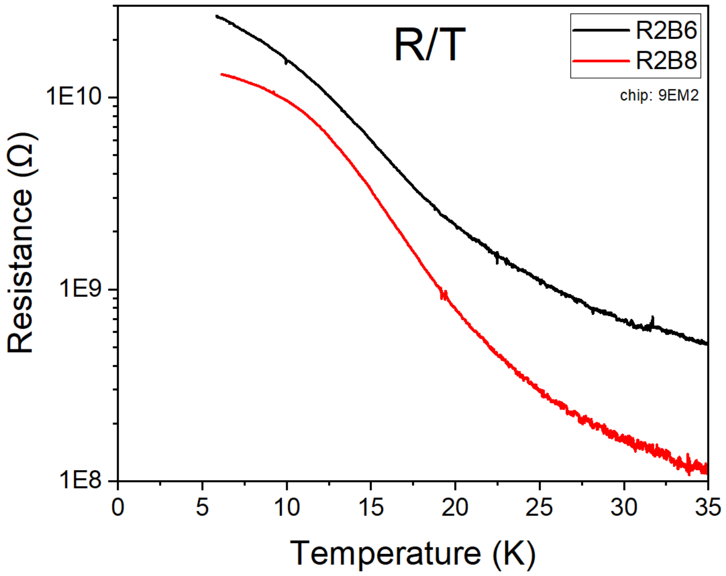

Figure 5.37: Resistance versus temperature for two devices R2B6 and R2B8 on bolometric chip 9EM2. The area of interest is around 15 K for both devices as the there is the most abrupt change of resistance dependency, and thus the most sensitive region for detection of changes.

The next step was to check the response on the microwave irradiation by measuring the I/V characteristics of the device. This is shown in Figure (5.38). At this point, it is necessary to be aware of the heating of the whole sample because of microwave irradiation. During this measurement, an increase of $\Delta T = 0.6\,\mathrm{K}$ was observed, which can be caused by improper cooling by a heat sink or by insufficient feedback on the needle valve control in the VTI.

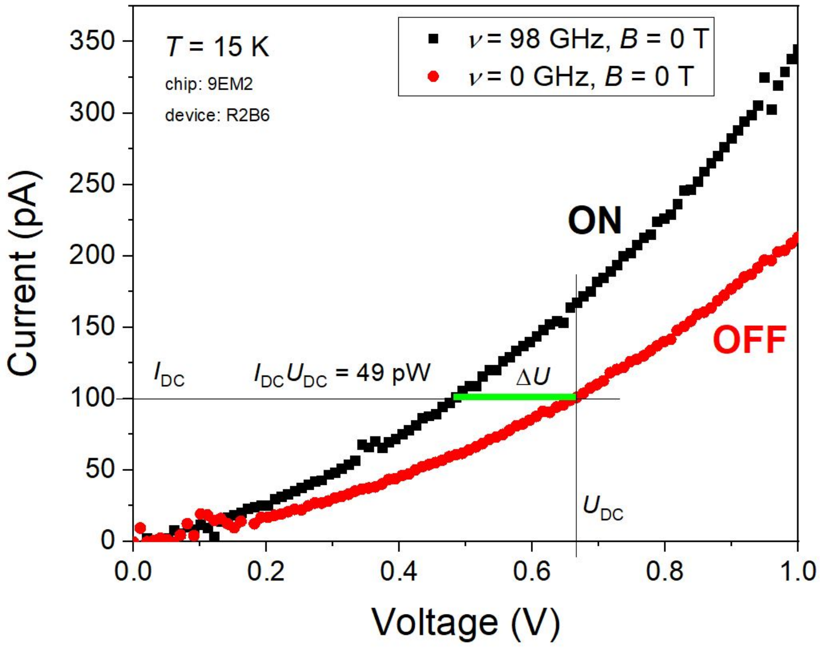

Figure 5.38: I/V characteristics on R2B6 device on 9EM2 chip at 15 K. The frequency applied was 98 GHz at zero external magnetic field.

We have also tested the R2B6 device in an applied external magnetic field of 5, 10, and 15 T as illustrated in the Figure (5.39). We observed almost negligible dependence on the magnetic field applied, which promises usability for the detection of SMMs on the bolometer.

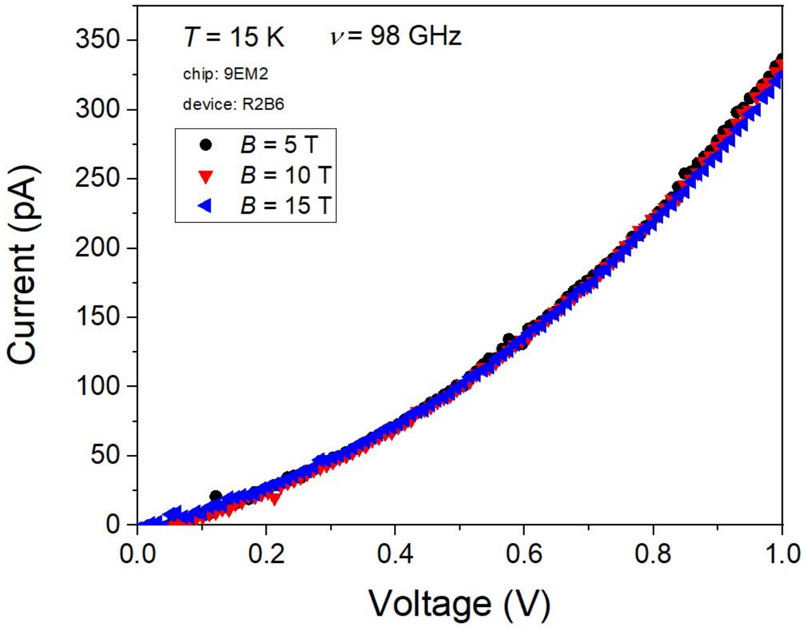

Figure 5.39: I/V characteristics on R2B6 device on 9EM2 chip at 15 K. The frequency applied was 98 GHz at three different external magnetic field intensities of 5, 10, and 15 T.

For the deposition we have chosen a previously well-studied SMM [184, 206, 207] Fe_4Ph with the linear chemical formula $C_{90}H_{146}Fe_4O_{19}$ as shown in Figure (5.40).

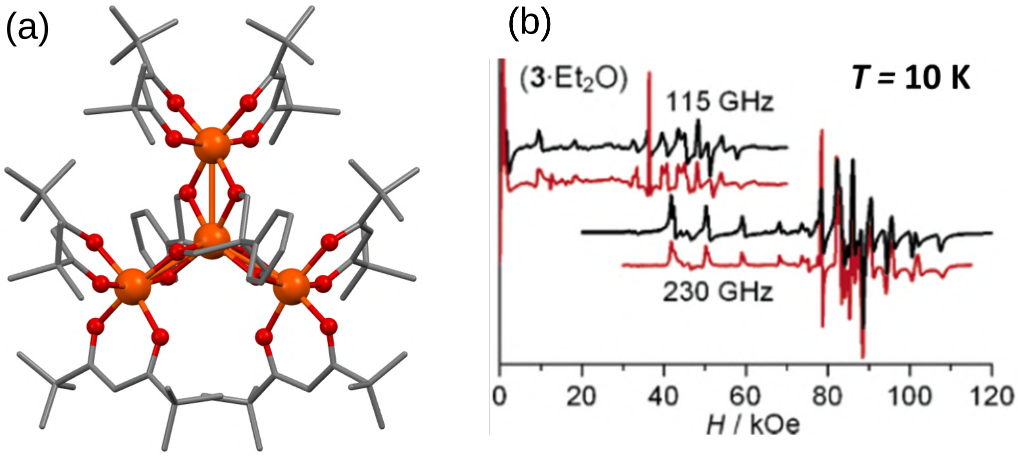

Figure 5.40: (a) Illustration of Fe_4Ph SMM, orange - iron; red - oxygen; grey - carbon, hydrogens are omitted for the sake of clarity, (b) HF-ESR spectra for 2 frequencies 115 GHz and 230 GHz at 10 K, red line is experiment and black simulation. From reference [206].

We have sublimed 15 nm thick film onto the whole bolometer chip 9EM2 at our collaborators prof. Mannini, Dr. Giulia Serrano and others in Florence, Italy. The sublimation took place in the home-built vacuum chamber Ape Cross with a base pressure of 3×10^{-7} mbar. The thickness was monitored by QCM placed at the same distance from the crucible with heated Fe_4Ph. The sublimation started at around 210 °C.

We have tried 2 different ESR schemes as shown in Figure (5.41) for subsequent measurements of Fe_4Ph deposited onto graphene-based bolometer. Unfortunately, neither of these methods gave any reproducible and analysable signal.

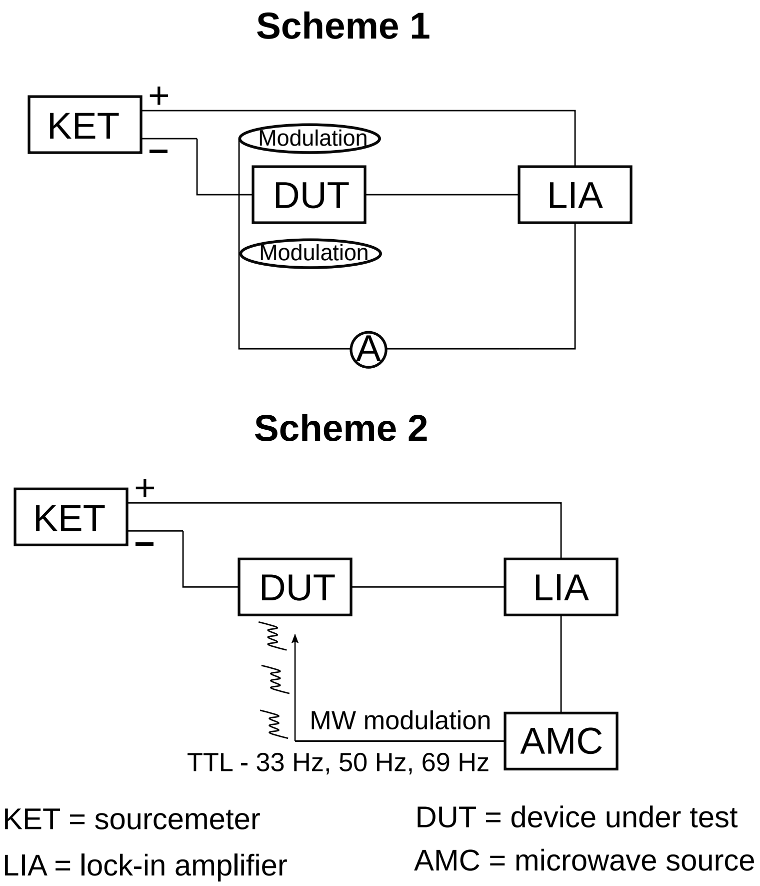

Figure 5.41: Top: the first scheme for testing the device with SMM was with traditional coil modulation on the sample holder. Bottom: the second approach we tried was to modulate microwave directly by in-built TTL modulation of microwave source.

6. Conclusions

To conclude the first result obtained: A graphene-based hybrid material with quantum bits prepared by the double Langmuir–Schaefer method, we have deposited and characterised molecular quantum bit based on Cu(II) ion on a surface. We have demonstrated a possibility to produce large arrays of graphene-based hybrid materials with quantum bits by using a double Langmuir–Schaefer deposition. We have taken advantage of using disordered graphene substrate as a template matrix for physisorption of [Cu(dbm)$_2$], which we have further characterised mainly to pinpoint the intactness and robustness of our system. The biggest advantage of our wet-chemistry based deposition protocol is the scalability and usability of whichever substrate with size limitations only by the dimensions of a LS trough. On the contrary, the access of atmospheric moisture and oxygen in the form of water can lead to abrupt decomposition with a limited amount of systems withstanding the air/water interface and a mixture of solvents during deposition, and thus is not generally applicable to every compound. To the best of our knowledge, there is no established database or a rule helping to determine properties of quantum bits on surfaces, and thus every system has to be treated individually. In this regard, there is space for improving the deposition conditions by using inert nitrogen or argon atmosphere, water purification, as well as to fine-tune deposition parameters in molecular concentration and volume used. Additionally, the potential to use specially tailored ligands surrounding the active Cu(II) ion offers possibilities of adjusting the adhering properties as well as hydrophobicity. Our work demonstrated a scalable deposition of quantum bits onto graphene-based substrate providing promising prospects of a wet-chemistry-based preparation route. Therefore, these molecular qubits in connection with conductive substrate seem to be the potent route in pursuing a quantum computation. Moreover, we have demonstrated that HF-ESR combined with a statistical approach can be a useful tool for the description of molecular distribution based on magnetic anisotropy on surfaces.

To conclude the second result obtained: Co(II)-Based single-ion magnets with 1,1’-ferrocenediyl-bis(diphenylphosphine) metalloligands, we reported on the crystal structure, magnetic properties and field-induced single-molecule magnet behaviour of series of Co(II) tetracoordinate compounds with 1,1 -ferrocenediyl-bis(diphenylphosphine) metalloligand (dppf) and with the general formula [Co(dppf)X], where X = Cl (**1**), Br (**2**), I (**3**). The static and dynamic magnetic properties were thoroughly studied only for complexes (**1**–**2**) because magnetic properties of (**3**) were found to be very sensitive to even slight decomposition of the sample. Investigations by magnetometry and HF-ESR revealed that (**1**–**2**) possess relatively large and axial magnetic anisotropy $D = -12.0\,\mathrm{cm}^{-1}$ in (**1**) and $D = -11.2\,\mathrm{cm}^{-1}$ in (**2**) and significant rhombicity $E/D = 0.106$ in (**1**) and 0.090 in (**2**), in good agreement with *ab initio* quantum chemical calculations. Measurements of dynamic AC susceptibility revealed that both compounds behave as field-induced single-ion magnets with predominant Orbach relaxation of magnetisation. Sublimation in high-vacuum and drop-casting were attempted in order to deposit (**2**) on selected surfaces (Au(111), glass, acetate). Despite the sensitivity to moisture, (**2**) was successfully deposited by drop-casting under an inert nitrogen atmosphere. While attempting thermal sublimation, we observed a partial decomposition of the complex and thus suggesting that nanostructuration of these systems should be operated by the introduction of functional groups allowing the chemisorption from diluted solution and promoting the formation of monolayers on surfaces.

To conclude the third result obtained: Deposition of Tetracoordinate Co(II) Complex with Chalcone Ligands on Graphene, herein we reported on the synthesis, crystal structure, magnetic properties, and characterisation of a new Co(II)-based complex with monodentate chalcone ligands and its deposition on graphene. The magnetic properties were determined from HF-ESR measurements and were found to be in fair agreement with CASSCF/NEVPT2 *ab initio* quantum chemical calculations. The spin Hamiltonian parameters are as follows: $D = 14.6\,\mathrm{cm}^{-1}$ with significant rhombicity $E/D = 0.235$, and $g_\mathrm{x} = 2.32$, $g_\mathrm{y} = 2.38$, $g_\mathrm{z} = 2.16$. Depositions on graphene were attempted by both drop-casting in an inert nitrogen atmosphere and by the thermal sublimation of bulk compound (**1**) in a high vacuum. In both cases, we observed organic chlorine components, suggesting the partial decomposition of the complex or possible chlorination of graphene. On the contrary, the Raman spectra showed a good agreement of the peaks in bulk and on the graphene; however, a few peaks from the complex overlapped with the graphene peaks, which hindered the analysis. In the case of the drop-cast sample, we observed the formation of small nanodroplets about 50 nm high on the graphene. Samples prepared by thermal sublimations revealed the formation of microcrystallites formed mostly at the grain edges and defects on graphene. DFT simulations of the complex at two geometries on the graphene surface confirmed only weak attraction to the graphene surface, with the crucial role of van der Waals forces in the adsorption on graphene. The outlook for the successful deposition of intact complexes on graphene surfaces requires the fine chemical tailoring of ligands, promoting adhesion on graphene, and utilising chelation agents that protect the complex from detrimental effects such as atmospheric moisture, oxidation, and thermal decomposition. The next step after successful deposition is to obtain the magnetic properties of a thin film on the surface, which will be obtained from HF-ESR measurements or from X-ray magnetic circular dichroism (XMCD) at the synchrotron facility.

To outline the future development of HF-ESR technology, I will summarise the advantages and obstacles encountered during HF-ESR systems presented in this thesis. One of the biggest advantages of HF-ESR is the freedom of sample form limited only by the probe head and VTI space. This is unique compared to the standard X-band glass capillaries, suitable usually for powder or liquid measurements. In this regard, samples such as silicon wafer or graphene on a silicon wafer with $\varnothing 5$ mm can be cut by laser dicer for the consequent deposition of molecular compounds or direct HF-ESR measurements. For these depositions, either a wet-chemistry approach or thermal sublimation can be used based on the properties of particular compounds. For the thermal sublimation, the home-built HV chamber was constructed. This chamber serves as the first test of the molecule if it survives the sublimation and thus is suitable to be measured by HF-ESR. The effort made by this work was to be able to prepare and characterise thin films of quantum bits and single-molecule magnets by a combination of HF-ESR spectroscopy and complementary techniques. Transition-metal coordination complexes and lanthanide/actinide-based SMMs are mostly investigated by means of HF-ESR as it can very precisely determine ZFS parameters and a sign of axial D parameter. There is also a great benefit when HF-ESR is used in combination with quantum chemistry calculation methods and ligand field theory. By the graphene bolometers, we want to advance the on-chip sensing of molecular compounds with the potential to revolutionise electronics. This approach would eliminate the whole route of microwave from a sample to the detector by replacing it with direct on-site measurements.

7. References

1. Zeeman, P. The effect of magnetisation on the nature of light emitted by a substance. *Nature* **55,** 347. ISSN: 0028-0836. doi:10.1038/055347a0 (1897).
2. Gerlach, W. & Stern, O. Der experimentelle Nachweis der Richtungsquantelung im Magnetfeld. *Zeitschrift für Physik* **9,** 349–352. ISSN: 1434-6001. doi:10.1007/BF01326983 (1922).
3. Uhlenbeck, G. E. & Goudsmit, S. Ersetzung der Hypothese vom unmechanischen Zwang durch eine Forderung bezüglich des inneren Verhaltens jedes einzelnen Elektrons. *Die Naturwissenschaften* **13,** 953–954. ISSN: 0028-1042. doi:10.1007/BF01558878 (1925).
4. Breit, G. & Rabi, I. I. Measurement of Nuclear Spin. *Physical Review* **38,** 2082–2083. ISSN: 0031-899X. doi:10.1103/PhysRev.38.2082.2 (1931).
5. Rabi, I. I., Zacharias, J. R., Millman, S. & Kusch, P. A New Method of Measuring Nuclear Magnetic Moment. *Physical Review* **53,** 318–318. ISSN: 0031-899X. doi:10.1103/PhysRev.53.318 (1938).
6. Salikhov, K. M. & Zavoiskaya, N. E. Zavoisky and the discovery of EPR. *Resonance* **20,** 963–968. ISSN: 0971-8044. doi:10.1007/s12045-015-0264-6 (2015).
7. Zavoisky, E. Spin-magnetic resonance in paramagnetics. *J. Phys. USSR* **3,** 211–245 (1945).
8. Frenkel, J. Viscous flow of crystalline bodies under the action of surface tension. *Journal of Physics (Moscow)* **9,** 385–391 (1945).
9. Weil, J. & Bolton, J. *Electron Paramagnetic Resonance: Elementary Theory and Practical Applications* 2nd, 664. ISBN: 978-0471754961. doi:10.1002/0470084987 (John Wiley & Sons, New Jersey, 2007).
10. Galkin, A. A., Grinberg, 0. Y., Dubinski, A. A., Kabdin, N. N., Krimov, V. N., Kurochkin, V. I., Lebedev, Y. S., Oranski, L. G. & Shuvalov, V. F. Two-millimeter wave band spectrometer for chemical investigations. *Prib. Tekh. Eksp.* **4** (1977).
11. Krinichnyi, V. I. *2-mm Wave Band EPR Spectroscopy of Condensed Systems* 1st, 1–223. ISBN: 978-1351069373. doi:10.1201/9781351069373 (CRC Press, Boca Raton, 2018).
12. Neugebauer, P., Bloos, D., Marx, R., Lutz, P., Kern, M., Aguilà, D., Vaverka, J., Laguta, O., Dietrich, C., Clérac, R. & Van Slageren, J. Ultra-broadband EPR spectroscopy in field and frequency domains. *Physical Chemistry Chemical Physics* **20,** 15528–15534. ISSN: 1463-9076. doi:10.1039/c7cp07443c (2018).
13. Sojka, A., Šedivý, M., Laguta, O., Marko, A., Santana, V. T. & Neugebauer, P. in *Electron Paramagnetic Resonance* 214–252 (2020). ISBN: 9781839161711. doi:10.1039/9781839162534-00214.
14. Pauli, W. The Connection Between Spin and Statistics. *Physical Review* **58,** 716–722. ISSN: 0031-899X. doi:10.1103/PhysRev.58.716 (1940).
15. Bloch, F. Nuclear Induction. *Physical Review* **70,** 460–474. ISSN: 0031-899X. doi:10.1103/PhysRev.70.460 (1946).

16. Spaeth, J.-M., Niklas, J. R. & Bartram, R. H. *Structural Analysis of Point Defects in Solids* 375. ISBN: 978-3-642-84407-2. doi:10.1007/978-3-642-84405-8 (Springer Berlin Heidelberg, Berlin, Heidelberg, 1992).
17. Dub, P., Spousta, J. & Zlámal, J. *Kvantová mechanika* tech. rep. (Institute of Physical Engineering, Brno University of Technology, Brno, 2005), 180.
18. Nemec, I., Herchel, R., Kern, M., Neugebauer, P., van Slageren, J. & Trávníček, Z. Magnetic anisotropy and field-induced slow relaxation of magnetization in tetracoordinate CoII compound [Co(CH3-im)2Cl2]. *Materials* **10,** 1–14. ISSN: 1996-1944. doi:10.3390/ma10030249 (2017).
19. Neese, F. & Pantazis, D. A. What is not required to make a single molecule magnet. *Faraday Discuss.* **148,** 229–238. ISSN: 1359-6640. doi:10.1039/C005256F (2011).
20. Ortu, F., Reta, D., Ding, Y. S., Goodwin, C. A., Gregson, M. P., McInnes, E. J., Winpenny, R. E., Zheng, Y. Z., Liddle, S. T., Mills, D. P. & Chilton, N. F. Studies of hysteresis and quantum tunnelling of the magnetisation in dysprosium(iii) single molecule magnets. *Dalton Transactions* **48,** 8541–8545. ISSN: 1477-9234. doi:10.1039/c9dt01655d (2019).
21. Pedersen, K. S., Dreiser, J., Weihe, H., Sibille, R., Johannesen, H. V., Sørensen, M. A., Nielsen, B. E., Sigrist, M., Mutka, H., Rols, S., Bendix, J. & Piligkos, S. Design of Single-Molecule Magnets: Insufficiency of the Anisotropy Barrier as the Sole Criterion. *Inorganic Chemistry* **54,** 7600–7606. ISSN: 1520-510X. doi:10.1021/acs.inorgchem.5b01209 (2015).
22. Liddle, S. T. & van Slageren, J. Improving f-element single molecule magnets. *Chemical Society Reviews* **44,** 6655–6669. ISSN: 0306-0012. doi:10.1039/C5CS00222B (2015).
23. Escalera-Moreno, L., Baldoví, J. J., Gaita-Ariño, A. & Coronado, E. Spin states, vibrations and spin relaxation in molecular nanomagnets and spin qubits: a critical perspective. *Chemical Science* **9,** 3265–3275. ISSN: 2041-6520. doi:10.1039/C7SC05464E (2018).
24. Castro-Alvarez, A., Gil, Y., Llanos, L. & Aravena, D. High performance single-molecule magnets, Orbach or Raman relaxation suppression? *Inorganic Chemistry Frontiers* **7,** 2478–2486. ISSN: 2052-1553. doi:10.1039/D0QI00487A (2020).
25. Zhu, Z., Zhao, C., Feng, T., Liu, X., Ying, X., Li, X. L., Zhang, Y. Q. & Tang, J. Air-Stable Chiral Single-Molecule Magnets with Record Anisotropy Barrier Exceeding 1800 K. *Journal of the American Chemical Society* **143,** 10077–10082. ISSN: 1520-5126. doi:10.1021/jacs.1c05279 (2021).
26. Giansiracusa, M. J., Kostopoulos, A. K., Collison, D., Winpenny, R. E. P. & Chilton, N. F. Correlating blocking temperatures with relaxation mechanisms in monometallic single-molecule magnets with high energy barriers (U eff > 600 K). *Chemical Communications* **55,** 7025–7028. ISSN: 1359-7345. doi:10.1039/C9CC02421B (2019).
27. Gatteschi, D., Sessoli, R. & Villain, J. *Molecular Nanomagnets* 1st, 408. ISBN: 978-0198567530. doi:10.1093/acprof:oso/9780198567530.001.0001 (Oxford University Press, 2007).
28. Stoll, S. & Schweiger, A. EasySpin, a comprehensive software package for spectral simulation and analysis in EPR. *Journal of Magnetic Resonance* **178,** 42–55. ISSN: 1090-7807. doi:10.1016/j.jmr.2005.08.013 (2006).
29. Mohr, P. J., Newell, D. B. & Taylor, B. N. CODATA recommended values of the fundamental physical constants: 2014. *Reviews of Modern Physics* **88,** 035009. ISSN: 0034-6861. doi:10.1103/RevModPhys.88.035009 (2016).
30. Van Slageren, J. *Introduction to Molecular Magnetism* tech. rep. (1. Physikalisches Institut, Universität Stuttgart, 2004), 1–44.

31. Sessoli, R., Gatteschi, D., Caneschi, A. & Novak, M. A. Magnetic bistability in a metal-ion cluster. *Nature* **365,** 141–143. ISSN: 0028-0836. doi:10.1038/365141a0 (1993).
32. Christou, G., Gatteschi, D., Hendrickson, D. N. & Sessoli, R. Single-molecule magnets. *Mrs Bulletin* **25,** 66–71 (2000).
33. Thomas, L., Lionti, F., Ballou, R., Gatteschi, D., Sessoli, R. & Barbara, B. Macroscopic quantum tunnelling of magnetization in a single crystal of nanomagnets. *Nature* **383,** 145–147. ISSN: 0028-0836. doi:10.1038/383145a0 (1996).
34. Lis, T. Preparation, structure, and magnetic properties of a dodecanuclear mixed-valence manganese carboxylate. *Acta Crystallographica Section B Structural Crystallography and Crystal Chemistry* **36,** 2042–2046. ISSN: 0567-7408. doi:10.1107/S0567740880007893 (1980).
35. Schumacher, B. Quantum coding. *Physical Review A* **51,** 2738–2747. ISSN: 1050-2947. doi:10.1103/PhysRevA.51.2738 (1995).
36. Nielsen, M. A. & Chuang, I. L. *Quantum Computation and Quantum Information* 10th, 710. ISBN: 978-1107002173. doi:10.1017/CBO9780511976667 (Cambridge University Press, Cambridge, 2011).
37. DiVincenzo, D. P. The physical implementation of quantum computation. *Fortschritte der Physik* **48,** 771–783. ISSN: 0015-8208. doi:10.1002/1521-3978(200009)48:9/11<771::AID-PROP771>3.0.CO;2-E (2000).
38. Beals, R., Buhrman, H., Cleve, R., Mosca, M. & de Wolf, R. Quantum lower bounds by polynomials. *Journal of the ACM* **48,** 778–797. ISSN: 0004-5411. doi:10.1145/502090.502097 (2001).
39. Grover, L. K. Quantum Mechanics Helps in Searching for a Needle in a Haystack. *Physical Review Letters* **79,** 325–328. ISSN: 0031-9007. doi:10.1103/PhysRevLett.79.325 (1997).
40. Shor, P. W. Polynomial-Time Algorithms for Prime Factorization and Discrete Logarithms on a Quantum Computer. *SIAM Review* **41,** 303–332. ISSN: 0036-1445. doi:10.1137/S0036144598347011 (1999).
41. Cory, D. G., Fahmy, A. F. & Havel, T. F. Ensemble quantum computing by NMR spectroscopy. *Proceedings of the National Academy of Sciences* **94,** 1634–1639. ISSN: 0027-8424. doi:10.1073/pnas.94.5.1634 (1997).
42. Graham, M. J., Zadrozny, J. M., Fataftah, M. S. & Freedman, D. E. Forging Solid-State Qubit Design Principles in a Molecular Furnace. *Chemistry of Materials* **29,** 1885–1897. ISSN: 0897-4756. doi:10.1021/acs.chemmater.6b05433 (2017).
43. Barra, A. L. High-frequency EPR spectroscopy of single-molecule magnets: A case study. *Applied Magnetic Resonance* **21,** 619–628. ISSN: 0937-9347. doi:10.1007/BF03162434 (2001).
44. Hołyńska, M. *Single-Molecule Magnets: Molecular Architectures and Building Blocks for Spintronics* (ed Hołyńska, M.) 320. ISBN: 978-3527809929. doi:10.1002/9783527809929 (Wiley-VCH Verlag GmbH & Co. KGaA, Weinheim, Germany, 2018).
45. Barra, A. L., Gatteschi, D. & Sessoli, R. High-frequency EPR spectra of a molecular nanomagnet: Understanding quantum tunneling of the magnetization. *Physical Review B - Condensed Matter and Materials Physics* **56,** 8192–8198. ISSN: 1550-235X. doi:10.1103/PhysRevB.56.8192 (1997).
46. Barra, A. L., Gatteschi, D. & Sessoli, R. High-frequency EPR spectra of [Fe8O2(OH)12(taCn)6]Br8: A critical appraisal of the barrier for the reorientation of the magnetization in single-molecule magnets. *Chemistry - A European Journal* **6,** 1608–1614. ISSN: 0947-6539. doi:10.1002/(SICI)1521-3765(20000502)6:9<1608::AID-CHEM1608>3.0.CO;2-8 (2000).

47. Frost, J. M., Harriman, K. L. M. & Murugesu, M. The rise of 3-d single-ion magnets in molecular magnetism: Towards materials from molecules? *Chemical Science* **7,** 2470–2491. ISSN: 2041-6539. doi:10.1039/c5sc03224e (2016).
48. Ruette, B., Zvyagin, S., Pyatakov, A. P., Bush, A., Li, J. F., Belotelov, V. I., Zvezdin, A. K. & Viehland, D. Magnetic-field-induced phase transition in BiFeO3 observed by high-field electron spin resonance: Cycloidal to homogeneous spin order. *Physical Review B - Condensed Matter and Materials Physics* **69,** 23–25. ISSN: 1550-235X. doi:10.1103/PhysRevB.69.064114 (2004).
49. Krzystek, J., Ozarowski, A. & Telser, J. Multi-frequency, high-field EPR as a powerful tool to accurately determine zero-field splitting in high-spin transition metal coordination complexes. *Coordination Chemistry Reviews* **250,** 2308–2324. ISSN: 0010-8545. doi:10.1016/j.ccr.2006.03.016 (2006).
50. Krzystek, J., Ozarowski, A., Zvyagin, S. A. & Telser, J. High spin Co(I): High-frequency and -field EPR spectroscopy of CoX(PPh 3) 3 (X = Cl, Br). *Inorganic Chemistry* **51,** 4954–4964. ISSN: 0020-1669. doi:10.1021/ic202185x (2012).
51. Ozarowski, A. The zero-field-splitting parameter D in binuclear copper(II) carboxylates is negative. *Inorganic Chemistry* **47,** 9760–9762. ISSN: 0020-1669. doi:10.1021/ic801560e (2008).
52. Vallejo, J., Pascual-Álvarez, A., Cano, J., Castro, I., Julve, M., Lloret, F., Krzystek, J., De Munno, G., Armentano, D., Wernsdorfer, W., Ruiz-García, R. & Pardo, E. Field-induced hysteresis and quantum tunneling of the magnetization in a mononuclear manganese(III) complex. *Angewandte Chemie - International Edition* **52,** 14075–14079. ISSN: 1433-7851. doi:10.1002/anie.201308047 (2013).
53. Rechkemmer, Y., Fischer, J. E., Marx, R., Dörfel, M., Neugebauer, P., Horvath, S., Gysler, M., Brock-Nannestad, T., Frey, W., Reid, M. F. & van Slageren, J. Comprehensive Spectroscopic Determination of the Crystal Field Splitting in an Erbium Single-Ion Magnet. *Journal of the American Chemical Society* **137,** 13114–13120. ISSN: 0002-7863. doi:10.1021/jacs.5b08344 (2015).
54. Realista, S., Fitzpatrick, A. J., Santos, G., Ferreira, L. P., Barroso, S., Pereira, L. C. J., Bandeira, N. A. G., Neugebauer, P., Hrubý, J., Morgan, G. G., van Slageren, J., Calhorda, M. J. & Martinho, P. N. A Mn(III) single ion magnet with tridentate Schiff-base ligands. *Dalton Transactions* **45,** 12301–12307. ISSN: 1477-9226. doi:10.1039/C6DT02538B (2016).
55. Kultaeva, A., Biktagirov, T., Neugebauer, P., Bamberger, H., Bergmann, J., Van Slageren, J., Krautscheid, H. & Pöppl, A. Multifrequency EPR, SQUID, and DFT Study of Cupric Ions and Their Magnetic Coupling in the Metal-Organic Framework Compound ∞3[Cu(prz-trz-ia)]. *Journal of Physical Chemistry C* **122,** 26642–26651. ISSN: 1932-7455. doi:10.1021/acs.jpcc.8b08327 (2018).
56. Bucinsky, L., Breza, M., Malček, M., Powers, D. C., Hwang, S. J., Krzystek, J., Nocera, D. G. & Telser, J. High-Frequency and -Field EPR (HFEPR) Investigation of a Pseudotetrahedral Cr IV Siloxide Complex and Computational Studies of Related Cr IV L 4 Systems. *Inorganic Chemistry* **58,** 4907–4920. ISSN: 1520-510X. doi:10.1021/acs.inorgchem.8b03512 (2019).
57. Neugebauer, P., Orlita, M., Faugeras, C., Barra, A. L. & Potemski, M. How perfect can graphene be? *Physical Review Letters* **103,** 136403. ISSN: 0031-9007. doi:10.1103/PhysRevLett.103.136403 (2009).
58. Bloos, D., Kunc, J., Kaeswurm, L., Myers-Ward, R. L., Daniels, K., DeJarld, M., Nath, A., van Slageren, J., Gaskill, D. K. & Neugebauer, P. Contactless millimeter wave method for quality assessment of large area graphene. *2D Materials* **6,** 035028. ISSN: 2053-1583. doi:10.1088/2053-1583/ab1d7e (2019).

59. Layfield, R. A. Organometallic Single-Molecule Magnets. *Organometallics* **33,** 1084–1099. ISSN: 0276-7333. doi:`10.1021/om401107f` (2014).

60. Bogani, L. & Wernsdorfer, W. Molecular spintronics using single-molecule magnets. *Nature Materials* **7,** 179–186. ISSN: 1476-4660. doi:`10.1038/nmat2133` (2008).

61. Holmberg, R. J. & Murugesu, M. Adhering magnetic molecules to surfaces. *Journal of Materials Chemistry C* **3,** 11986–11998. ISSN: 2050-7526. doi:`10.1039/C5TC03225C` (2015).

62. Caneschi, A., Gatteschi, D. & Totti, F. Molecular magnets and surfaces: A promising marriage. A DFT insight. *Coordination Chemistry Reviews* **289-290,** 357–378. ISSN: 0010-8545. doi:`10.1016/j.ccr.2014.11.016` (2015).

63. Cornia, A., Mannini, M., Sainctavit, P. & Sessoli, R. Chemical strategies and characterization tools for the organization of single molecule magnets on surfaces. *Chemical Society Reviews* **40,** 3076. ISSN: 0306-0012. doi:`10.1039/c0cs00187b` (2011).

64. Mannini, M., Pineider, F., Sainctavit, P., Danieli, C., Otero, E., Sciancalepore, C., Talarico, A. M., Arrio, M.-A., Cornia, A., Gatteschi, D. & Sessoli, R. Magnetic memory of a single-molecule quantum magnet wired to a gold surface. *Nature Materials* **8,** 194–197. ISSN: 1476-1122. doi:`10.1038/nmat2374` (2009).

65. Mannini, M., Pineider, F., Danieli, C., Totti, F., Sorace, L., Sainctavit, P., Arrio, M.-A., Otero, E., Joly, L., Cezar, J. C., Cornia, A. & Sessoli, R. Quantum tunnelling of the magnetization in a monolayer of oriented single-molecule magnets. *Nature* **468,** 417–421. ISSN: 0028-0836. doi:`10.1038/nature09478` (2010).

66. Mannini, M., Bertani, F., Tudisco, C., Malavolti, L., Poggini, L., Misztal, K., Menozzi, D., Motta, A., Otero, E., Ohresser, P., Sainctavit, P., Condorelli, G. G., Dalcanale, E. & Sessoli, R. Magnetic behaviour of TbPc2 single-molecule magnets chemically grafted on silicon surface. *Nature Communications* **5,** 4582. ISSN: 2041-1723. doi:`10.1038/ncomms5582` (2014).

67. Malavolti, L., Lanzilotto, V., Ninova, S., Poggini, L., Cimatti, I., Cortigiani, B., Margheriti, L., Chiappe, D., Otero, E., Sainctavit, P., Totti, F., Cornia, A., Mannini, M. & Sessoli, R. Magnetic Bistability in a Submonolayer of Sublimated Fe 4 Single-Molecule Magnets. *Nano Letters* **15,** 535–541. ISSN: 1530-6984. doi:`10.1021/nl503925h` (2015).

68. Kiefl, E., Mannini, M., Bernot, K., Yi, X., Amato, A., Leviant, T., Magnani, A., Prokscha, T., Suter, A., Sessoli, R. & Salman, Z. Robust Magnetic Properties of a Sublimable Single-Molecule Magnet. *ACS Nano* **10,** 5663–5669. ISSN: 1936-086X. doi:`10.1021/acsnano.6b01817` (2016).

69. Hrubý, J., Santana, V. T., Kostiuk, D., Bouček, M., Lenz, S., Kern, M., Šiffalovič, P., van Slageren, J. & Neugebauer, P. A graphene-based hybrid material with quantum bits prepared by the double Langmuir–Schaefer method. *RSC Advances* **9,** 24066–24073. ISSN: 2046-2069. doi:`10.1039/C9RA04537F` (2019).

70. Marie, L. S., El Fatimy, A., Hrubý, J., Nemec, I., Hunt, J., Myers-Ward, R., Gaskill, D. K., Kruskopf, M., Yang, Y., Elmquist, R., Marx, R., van Slageren, J., Neugebauer, P. & Barbara, P. Nanostructured graphene for nanoscale electron paramagnetic resonance spectroscopy. *Journal of Physics: Materials* **3,** 014013. ISSN: 2515-7639. doi:`10.1088/2515-7639/ab6af8` (2020).

71. Ciccullo, F., Glaser, M., Sättele, M. S., Lenz, S., Neugebauer, P., Rechkemmer, Y., Van Slageren, J. & Casu, M. B. Thin film properties and stability of a potential molecular quantum bit based on copper(ii). *Journal of Materials Chemistry C* **6,** 8028–8034. ISSN: 2050-7526. doi:`10.1039/c8tc02610f` (2018).

72. Petty, M. C. *Langmuir-Blodgett Films: An Introduction* 234. ISBN: 978-0521424509 (Cambridge University Press, 1996).

73. Gengler, R. *A Modified Langmuir Schaefer Method For the Creation of Functional Thin Films* PhD thesis (University of Groningen, 2010), 161. ISBN: 978-9036746250.

74. Hertz, H. Ueber einen Einfluss des ultravioletten Lichtes auf die electrische Entladung. *Annalen der Physik und Chemie* **267,** 983–1000. ISSN: 0003-3804. doi:10.1002/andp.18872670827 (1887).

75. Einstein, A. Über einem die Erzeugung und Verwandlung des Lichtes betreffenden heuristischen Gesichtspunkt. *Annalen der physik* **4,** 132–148 (1905).

76. Siegbahn, K. & Edvarson, K. β-Ray spectroscopy in the precision range of 1 : 105. *Nuclear Physics* **1,** 137–159. ISSN: 0029-5582. doi:10.1016/s0029-5582(56)80022-9 (1956).

77. Raman, C. V. & Krishnan, K. S. A New Type of Secondary Radiation. *Nature* **121,** 501–502. ISSN: 0028-0836. doi:10.1038/121501c0 (1928).

78. Smith, E. & Dent, G. *Modern Raman Spectroscopy* 2nd, 1–241. ISBN: 978-1119440550. doi:10.1002/9781119440598 (John Wiley & Sons, Hoboken, NJ, 2019).

79. Atkins, P., Paula, d. J. & Friedman, R. *Quanta, Matter, and Change: A Molecular Approach to Physical Chemistry* 1st, 782. ISBN: 978-0716761174 (W. H. Freeman, New York, 2009).

80. Spizzirri, P. G., Fang, J. H., Rubanov, S., Gauja, E. & Prawer, S. Nano-Raman spectroscopy of silicon surfaces. *Materials Forum* **34,** 161–166. ISSN: 0883-2900. doi:1002.2692. arXiv: 1002.2692 (2008).

81. Solé, J. G., Bausá, L. & Jaque, D. *An Introduction to the Optical Spectroscopy of Inorganic Solids* 283. ISBN: 978-0470016046. doi:10.1002/0470016043 (John Wiley & Sons, Ltd, Chichester, UK, 2005).

82. Hollas, J. M. *Modern spectroscopy* 4th, 482. ISBN: 978-0470844151 (John Wiley & Sons, Chichester, West Sussex, England, 2004).

83. Binnig, G., Quate, C. F. & Gerber, C. Atomic Force Microscope. *Physical Review Letters* **56,** 930–933. ISSN: 0031-9007. doi:10.1103/PhysRevLett.56.930 (1986).

84. Vavrečková, Š. *DEPOZICE MOLEKULÁRNÍCH MAGNETŮ NA „2D“ MATERIÁLY* Bachelor Thesis (Brno University of Technology, 2020), 36.

85. Israelachvili, J. *Intermolecular and Surface Forces* 3rd, 710. ISBN: 978-0123751829. doi:10.1016/C2009-0-21560-1 (Elsevier, 2011).

86. Turčan, I. *MIKROSKOPIE MAGNETICKÝCH SIL V PROMĚNNÉM MAGNETICKÉM POLI* Bachelor Thesis (Brno University of Technology, 2014), 38.

87. Perdomo-Ortiz, A., Dickson, N., Drew-Brook, M., Rose, G. & Aspuru-Guzik, A. Finding low-energy conformations of lattice protein models by quantum annealing. *Scientific Reports* **2,** 1–7. ISSN: 2045-2322. doi:10.1038/srep00571 (2012).

88. Gershenfeld, N. & Chuang, I. L. Quantum Computing with Molecules. *Scientific American* **278,** 66–71. ISSN: 0036-8733 (1998).

89. Leuenberger, M. N. & Loss, D. Quantum computing in molecular magnets. *Nature* **410,** 789–793. ISSN: 0028-0836. doi:10.1038/35071024 (2001).

90. Wolf, S. A., Awschalom, D. D., Buhrman, R. A., Daughton, J. M., Von Molnar, S., Roukes, M. L., Chtchelkanova, A. Y. & Treger, D. M. Spintronics: a spin-based electronics vision for the future. *Science* **294,** 1488–1495. ISSN: 0036-8075. doi:10.1126/science.1065389 (2001).

91. Doherty, M. W., Manson, N. B., Delaney, P., Jelezko, F., Wrachtrup, J. & Hollenberg, L. C. The nitrogen-vacancy colour centre in diamond. *Physics Reports* **528,** 1–45. ISSN: 0370-1573. doi:10.1016/j.physrep.2013.02.001 (2013).

92. Koehl, W. F., Buckley, B. B., Heremans, F. J., Calusine, G. & Awschalom, D. D. Room temperature coherent control of defect spin qubits in silicon carbide. *Nature* **479,** 84–87. ISSN: 0028-0836. doi:10.1038/nature10562 (2011).

93. Widmann, M., Lee, S. Y., Rendler, T., Son, N. T., Fedder, H., Paik, S., Yang, L. P., Zhao, N., Yang, S., Booker, I., Denisenko, A., Jamali, M., Ali Momenzadeh, S., Gerhardt, I., Ohshima, T., Gali, A., Janzén, E. & Wrachtrup, J. Coherent control of single spins in silicon carbide at room temperature. *Nature Materials* **14,** 164–168. ISSN: 1476-4660. doi:10.1038/nmat4145 (2015).

94. Christle, D. J., Falk, A. L., Andrich, P., Klimov, P. V., Hassan, J. U., Son, N. T., Janzén, E., Ohshima, T. & Awschalom, D. D. Isolated electron spins in silicon carbide with millisecond coherence times. *Nature Materials* **14,** 160–163. ISSN: 1476-4660. doi:10.1038/nmat4144 (2015).

95. Jelezko, F. & Wrachtrup, J. Single defect centres in diamond: A review. *Physica Status Solidi (A) Applications and Materials Science* **203,** 3207–3225. ISSN: 1862-6300. doi:10.1002/pssa.200671403 (2006).

96. Bader, K., Dengler, D., Lenz, S., Endeward, B., Jiang, S.-d., Neugebauer, P. & Slageren, J. V. Potential Molecular Qubit. *Nature Communications* **5,** 1–5. doi:10.1038/ncomms6304 (2014).

97. Lenz, S., Bader, K., Bamberger, H. & Van Slageren, J. Quantitative prediction of nuclear-spin-diffusion-limited coherence times of molecular quantum bits based on copper(ii). *Chemical Communications* **53,** 4477–4480. ISSN: 1364-548X. doi:10.1039/c6cc07813c (2017).

98. Geim, A. K. & Novoselov, K. S. The rise of graphene. *Nature Materials* **6,** 183–191. ISSN: 1476-1122. doi:10.1038/nmat1849 (2007).

99. Du, X., Skachko, I., Barker, A. & Andrei, E. Y. Approaching ballistic transport in suspended graphene. *Nature Nanotechnology* **3,** 491–495. ISSN: 1748-3395. doi:10.1038/nnano.2008.199 (2008).

100. Lee, C., Wei, X., Kysar, J. W. & Hone, J. Measurement of the elastic properties and intrinsic strength of monolayer graphene. *Science* **321,** 385–388. ISSN: 0036-8075. doi:10.1126/science.1157996 (2008).

101. Seol, J. H., Jo, I., Moore, A. L., Lindsay, L., Aitken, Z. H., Pettes, M. T., Li, X., Yao, Z., Huang, R., Broido, D., Mingo, N., Ruoff, R. S. & Shi, L. Two-dimensional phonon transport in supported graphene. *Science* **328,** 213–216. ISSN: 1095-9203. doi:10.1126/science.1184014 (2010).

102. Novoselov, K. S., Geim, A. K., Morozov, S. V., Jiang, D., Zhang, Y., Dubonos, S. V., Grigorieva, I. V. & Firsov, A. A. Electric Field Effect in Atomically Thin Carbon Films. *Science* **306,** 666–669. ISSN: 1095-9203. doi:10.1126/science.1102896 (2004).

103. Warner, J. H., Mukai, M. & Kirkland, A. I. Atomic structure of ABC rhombohedral stacked trilayer graphene. *ACS Nano* **6,** 5680–5686. ISSN: 1936-0851. doi:10.1021/nn3017926 (2012).

104. VanMil, B. L., Myers-Ward, R. L., Tedesco, J., Eddy Jr., C. R., Jernigan, G. G., Culbertson, J. C., Campbell, P. M., McCrate, J., Kitt, S. & Gaskill, D. K. Graphene Formation on SiC Substrates. *Materials Science Forum* **615-617,** 211–214. ISSN: 1662-9752. doi:10.4028/www.scientific.net/MSF.615-617.211 (2009).

105. Coleman, J. N., Lotya, M., O'Neill, A., Bergin, S. D., King, P. J., Khan, U., Young, K., Gaucher, A., De, S., Smith, R. J., Shvets, I. V., Arora, S. K., Stanton, G., Kim, H. Y., Lee, K., Kim, G. T., Duesberg, G. S., Hallam, T., Boland, J. J., Wang, J. J., Donegan, J. F., Grunlan, J. C., Moriarty, G., Shmeliov, A., Nicholls, R. J., Perkins, J. M., Grieveson, E. M., Theuwissen, K., McComb, D. W., Nellist, P. D. & Nicolosi, V. Two-dimensional nanosheets produced by liquid exfoliation of layered materials. *Science* **331,** 568–571. ISSN: 0036-8075. doi:`10.1126/science.1194975` (2011).

106. Wajid, A. S., Das, S., Irin, F., Ahmed, H. S., Shelburne, J. L., Parviz, D., Fullerton, R. J., Jankowski, A. F., Hedden, R. C. & Green, M. J. Polymer-stabilized graphene dispersions at high concentrations in organic solvents for composite production. *Carbon* **50,** 526–534. ISSN: 0008-6223. doi:`10.1016/j.carbon.2011.09.008` (2012).

107. Paton, K. R., Varrla, E., Backes, C., Smith, R. J., Khan, U., O'Neill, A., Boland, C., Lotya, M., Istrate, O. M., King, P., Higgins, T., Barwich, S., May, P., Puczkarski, P., Ahmed, I., Moebius, M., Pettersson, H., Long, E., Coelho, J., O'Brien, S. E., McGuire, E. K., Sanchez, B. M., Duesberg, G. S., McEvoy, N., Pennycook, T. J., Downing, C., Crossley, A., Nicolosi, V. & Coleman, J. N. Scalable production of large quantities of defect-free few-layer graphene by shear exfoliation in liquids. *Nature Materials* **13,** 624–630. ISSN: 1476-4660. doi:`10.1038/nmat3944` (2014).

108. Vadukumpully, S., Paul, J. & Valiyaveettil, S. Cationic surfactant mediated exfoliation of graphite into graphene flakes. *Carbon* **47,** 3288–3294. ISSN: 0008-6223. doi:`10.1016/j.carbon.2009.07.049` (2009).

109. Hong, J., Bekyarova, E., De Heer, W. A., Haddon, R. C. & Khizroev, S. Chemically engineered graphene-based 2d organic molecular magnet. *ACS Nano* **7,** 10011–10022. ISSN: 1936-0851. doi:`10.1021/nn403939r` (2013).

110. Zhuang, X., Tian, C., Luan, F., Wu, X. & Chen, L. One-step electrochemical fabrication of a nickel oxide nanoparticle/polyaniline nanowire/graphene oxide hybrid on a glassy carbon electrode for use as a non-enzymatic glucose biosensor. *RSC Advances* **6,** 92541–92546. ISSN: 2046-2069. doi:`10.1039/c6ra14970g` (2016).

111. Ricciardulli, A. G., Yang, S., Wetzelaer, G.-J. J. A., Feng, X. & Blom, P. W. Hybrid Silver Nanowire and Graphene-Based Solution-Processed Transparent Electrode for Organic Optoelectronics. *Advanced Functional Materials* **28,** 1706010. ISSN: 1616-3028. doi:`10.1002/adfm.201706010` (2018).

112. Kim, T.-H., Lee, D. & Choi, J.-W. Live cell biosensing platforms using graphene-based hybrid nanomaterials. *Biosensors and Bioelectronics* **94,** 485–499. ISSN: 0956-5663. doi:`10.1016/j.bios.2017.03.032` (2017).

113. Zor, E., Morales-Narváez, E., Alpaydin, S., Bingol, H., Ersoz, M. & Merkoçi, A. Graphene-based hybrid for enantioselective sensing applications. *Biosensors and Bioelectronics* **87,** 410–416. ISSN: 1873-4235. doi:`10.1016/j.bios.2016.08.074` (2017).

114. Wang, X., Yu, S., Liu, W., Fu, L., Wang, Y., Li, J. & Chen, L. Molecular Imprinting Based Hybrid Ratiometric Fluorescence Sensor for the Visual Determination of Bovine Hemoglobin. *ACS Sensors* **3,** 378–385. ISSN: 2379-3694. doi:`10.1021/acssensors.7b00804` (2018).

115. Ciesielski, A. & Samorì, P. Supramolecular Approaches to Graphene: From Self-Assembly to Molecule-Assisted Liquid-Phase Exfoliation. *Advanced Materials,* 6030–6051. ISSN: 1521-4095. doi:`10.1002/adma.201505371` (2016).

116. Le Ferrand, H., Bolisetty, S., Demirörs, A. F., Libanori, R., Studart, A. R. & Mezzenga, R. Magnetic assembly of transparent and conducting graphene-based functional composites. *Nature Communications* **7.** ISSN: 2041-1723. doi:`10.1038/ncomms12078` (2016).

117. Qin, S., Chen, X., Du, Q., Nie, Z., Wang, X., Lu, H., Wang, X., Liu, K., Xu, Y., Shi, Y., Zhang, R. & Wang, F. Sensitive and Robust Ultraviolet Photodetector Array Based on Self-Assembled Graphene/C 60 Hybrid Films. *ACS Applied Materials and Interfaces* **10,** 38326–38333. ISSN: 1944-8252. doi:10.1021/acsami.8b11596 (2018).

118. Ma, B. Q., Gao, S., Wang, Z. M., Liao, C. S., Yan, C. H. & Xu, G. X. Synthesis and structure of bis(dibenzoylmethane) copper(II). *Journal of Chemical Crystallography* **29,** 793–796. ISSN: 1074-1542. doi:10.1023/A:1009543703278 (1999).

119. Hernandez, Y., Nicolosi, V., Lotya, M., Blighe, F. M., Sun, Z., De, S., McGovern, I. T., Holland, B., Byrne, M., Gun'ko, Y. K., Boland, J. J., Niraj, P., Duesberg, G., Krishnamurthy, S., Goodhue, R., Hutchison, J., Scardaci, V., Ferrari, A. C. & Coleman, J. N. High-yield production of graphene by liquid-phase exfoliation of graphite. *Nature Nanotechnology* **3,** 563–568. ISSN: 1748-3387. doi:10.1038/nnano.2008.215 (2008).

120. Mankad, V., Gupta, S. K., Jha, P. K., Ovsyuk, N. N. & Kachurin, G. A. Low-frequency Raman scattering from Si/Ge nanocrystals in different matrixes caused by acoustic phonon quantization. *Journal of Applied Physics* **112.** ISSN: 0021-8979. doi:10.1063/1.4747933 (2012).

121. Ferrari, A. C. Raman spectroscopy of graphene and graphite: Disorder, electron-phonon coupling, doping and nonadiabatic effects. *Solid State Communications* **143,** 47–57. ISSN: 0038-1098. doi:10.1016/j.ssc.2007.03.052 (2007).

122. Malard, L. M., Pimenta, M. A., Dresselhaus, G. & Dresselhaus, M. S. Raman spectroscopy in graphene. *Physics Reports* **473,** 51–87. ISSN: 0370-1573. doi:10.1016/j.physrep.2009.02.003 (2009).

123. Nekoei, A. R., Vakili, M., Hakimi-Tabar, M., Tayyari, S. F., Afzali, R. & Kjaergaard, H. G. Theoretical study, and infrared and Raman spectra of copper(II) chelated complex with dibenzoylmethane. *Spectrochimica Acta - Part A: Molecular and Biomolecular Spectroscopy* **128,** 272–279. ISSN: 1386-1425. doi:10.1016/j.saa.2014.02.097 (2014).

124. Tayyari, S. F., Rahemi, H., Nekoei, A. R., Zahedi-Tabrizi, M. & Wang, Y. A. Vibrational assignment and structure of dibenzoylmethane. A density functional theoretical study. *Spectrochimica Acta - Part A: Molecular and Biomolecular Spectroscopy* **66,** 394–404. ISSN: 1386-1425. doi:10.1016/j.saa.2006.03.010 (2007).

125. Shirley, D. A. High-resolution x-ray photoemission spectrum of the valence bands of gold. *Physical Review B* **5,** 4709–4714. ISSN: 0163-1829. doi:10.1103/PhysRevB.5.4709 (1972).

126. Savu, S. A., Casu, M. B., Schundelmeier, S., Abb, S., Tönshoff, C., Bettinger, H. F. & Chassé, T. Nanoscale assembly, morphology and screening effects in nanorods of newly synthesized substituted pentacenes. *RSC Advances* **2,** 5112–5118. ISSN: 2046-2069. doi:10.1039/c2ra20168b (2012).

127. Savu, S. A., Biswas, I., Sorace, L., Mannini, M., Rovai, D., Caneschi, A., Chassé, T. & Casu, M. B. Nanoscale assembly of paramagnetic organic radicals on Au(111) single crystals. *Chemistry - A European Journal* **19,** 3445–3450. ISSN: 0947-6539. doi:10.1002/chem.201203247 (2013).

128. Ishii, H., Sugiyama, K., Ito, E. & Seki, K. Energy level alignment and interfacial electronic structures at organic/metal and organic/organic interfaces. *Advanced materials* **11,** 605–625. ISSN: 0935-9648. doi:10.1002/(SICI)1521-4095(199906)11:8<605::AID-ADMA605>3.0.CO;2-Q (1999).

129. Sjögren, B., Svensson, S., Naves De Brito, A., Correia, N., Keane, M. P., Enkvist, C. & Lunell, S. The C1s core shake-up spectra of alkene molecules: An experimental and theoretical study. *The Journal of Chemical Physics* **96,** 6389–6398. ISSN: 0021-9606. doi:10.1063/1.462633 (1992).

130. Ghijsen, J., Tjeng, L. H., van Elp, J., Eskes, H., Westerink, J., Sawatzky, G. A. & Czyzyk, M. T. Electronic structure of Cu2O and CuO. *Physical Review B* **38,** 11322–11330. ISSN: 0163-1829. doi:10.1103/PhysRevB.38.11322 (1988).

131. Chawla, S. K., Sankarraman, N. & Payer, J. H. Diagnostic spectra for XPS analysis of CuOSH compounds. *Journal of Electron Spectroscopy and Related Phenomena* **61,** 1–18. ISSN: 0368-2048. doi:10.1016/0368-2048(92)80047-C (1992).

132. Yin, M., Wu, C.-K., Lou, Y., Burda, C., Koberstein, J. T., Zhu, Y. & O'Brien, S. Copper Oxide Nanocrystals. *Journal of the American Chemical Society* **127,** 9506–9511. ISSN: 0002-7863. doi:10.1021/ja050006u (2005).

133. Barreca, D., Fois, E., Gasparotto, A., Seraglia, R., Tondello, E. & Tabacchi, G. How Does CuII Convert into CuI? An Unexpected Ring-Mediated Single-Electron Reduction. *Chemistry - A European Journal* **17,** 10864–10870. ISSN: 0947-6539. doi:10.1002/chem.201101551 (2011).

134. Glaser, M., Ciccullo, F., Giangrisostomi, E., Ovsyannikov, R., Calzolari, A. & Casu, M. B. Doping and oxidation effects under ambient conditions in copper surfaces: a "real-life" CuBe surface. *Journal of Materials Chemistry C* **6,** 2769–2777. ISSN: 2050-7526. doi:10.1039/C7TC04983H (2018).

135. David, L., Crăciun, C., Cozar, O., Chiş, V., Agut, C., Rusu, D. & Rusu, M. Spectroscopic studies of some oxygen-bonded copper(II) β-diketonate complexes. *Journal of Molecular Structure* **563-564,** 573–578. ISSN: 0022-2860. doi:10.1016/S0022-2860(00)00941-8 (2001).

136. Bak, M. & Nielsen, N. C. Repulsion, A Novel Approach to Efficient Powder Averaging in Solid-State NMR. *Journal of Magnetic Resonance* **125,** 132–139. ISSN: 1090-7807. doi:10.1006/jmre.1996.1087 (1997).

137. Von Zelewsky, A. & Fierz, H. Electron spin resonance of copper bis(dibenzoylmethane). Superhyperfine anomalies. *Inorganic Chemistry* **10,** 1556–1557. ISSN: 0020-1669. doi:10.1021/ic50101a060 (1971).

138. Belford, R. L. & Davis, P. H. Anomalous structure in electron paramagnetic resonance spectra of polycrystalline copper complexes. *Inorganic Chemistry* **10,** 1557–1558. ISSN: 0020-1669. doi:10.1021/ic50101a061 (1971).

139. Cinchetti, M., Dediu, V. A. & Hueso, L. E. Activating the molecular spinterface. *Nature Materials* **16,** 507–515. ISSN: 1476-1122. doi:10.1038/nmat4902 (2017).

140. Godfrin, C., Ferhat, A., Ballou, R., Klyatskaya, S., Ruben, M., Wernsdorfer, W. & Balestro, F. Operating Quantum States in Single Magnetic Molecules: Implementation of Grover's Quantum Algorithm. *Physical Review Letters* **119,** 187702. ISSN: 0031-9007. doi:10.1103/PhysRevLett.119.187702 (2017).

141. Ishikawa, N., Sugita, M., Ishikawa, T., Koshihara, S.-y. & Kaizu, Y. Lanthanide Double-Decker Complexes Functioning as Magnets at the Single-Molecular Level. *Journal of the American Chemical Society* **125,** 8694–8695. ISSN: 0002-7863. doi:10.1021/ja029629n (2003).

142. Guo, F.-S., Day, B. M., Chen, Y.-C., Tong, M.-L., Mansikkamäki, A. & Layfield, R. A. Magnetic hysteresis up to 80 kelvin in a dysprosium metallocene single-molecule magnet. *Science* **362,** 1400–1403. ISSN: 0036-8075. doi:10.1126/science.aav0652 (2018).

143. Zadrozny, J. M. & Long, J. R. Slow Magnetic Relaxation at Zero Field in the Tetrahedral Complex [Co(SPh) 4] 2–. *Journal of the American Chemical Society* **133,** 20732–20734. ISSN: 0002-7863. doi:10.1021/ja2100142 (2011).

144. Rechkemmer, Y., Breitgoff, F. D., van der Meer, M., Atanasov, M., Hakl, M., Orlita, M., Neugebauer, P., Neese, F., Sarkar, B. & van Slageren, J. A four-coordinate cobalt(II) single-ion magnet with coercivity and a very high energy barrier. *Nature Communications* **7,** 10467. ISSN: 2041-1723. doi:10.1038/ncomms10467 (2016).

145. Habib, F., Luca, O. R., Vieru, V., Shiddiq, M., Korobkov, I., Gorelsky, S. I., Takase, M. K., Chibotaru, L. F., Hill, S., Crabtree, R. H. & Murugesu, M. Influence of the Ligand Field on Slow Magnetization Relaxation versus Spin Crossover in Mononuclear Cobalt Complexes. *Angewandte Chemie International Edition* **52,** 11290–11293. ISSN: 1433-7851. doi:10.1002/anie.201303005 (2013).

146. Vallejo, J., Castro, I., Ruiz-García, R., Cano, J., Julve, M., Lloret, F., De Munno, G., Wernsdorfer, W. & Pardo, E. Field-Induced Slow Magnetic Relaxation in a Six-Coordinate Mononuclear Cobalt(II) Complex with a Positive Anisotropy. *Journal of the American Chemical Society* **134,** 15704–15707. ISSN: 0002-7863. doi:10.1021/ja3075314 (2012).

147. Huang, X.-C., Zhou, C., Shao, D. & Wang, X.-Y. Field-Induced Slow Magnetic Relaxation in Cobalt(II) Compounds with Pentagonal Bipyramid Geometry. *Inorganic Chemistry* **53,** 12671–12673. ISSN: 0020-1669. doi:10.1021/ic502006s (2014).

148. Chen, L., Wang, J., Wei, J.-M., Wernsdorfer, W., Chen, X.-T., Zhang, Y.-Q., Song, Y. & Xue, Z.-L. Slow Magnetic Relaxation in a Mononuclear Eight-Coordinate Cobalt(II) Complex. *Journal of the American Chemical Society* **136,** 12213–12216. ISSN: 0002-7863. doi:10.1021/ja5051605 (2014).

149. Titiš, J., Miklovič, J. & Boča, R. Magnetostructural study of tetracoordinate cobalt(II) complexes. *Inorganic Chemistry Communications* **35,** 72–75. ISSN: 1387-7003. doi:10.1016/j.inoche.2013.05.031 (2013).

150. Nemec, I., Herchel, R. & Trávníček, Z. Suppressing of slow magnetic relaxation in tetracoordinate Co(II) field-induced single-molecule magnet in hybrid material with ferromagnetic barium ferrite. *Scientific Reports* **5,** 10761. ISSN: 2045-2322. doi:10.1038/srep10761 (2015).

151. Corain, B., Longato, B., Favero, G., Ajò, D., Pilloni, G., Russo, U. & Kreissl, F. Heteropolymetallic complexes of 1,1 -Bis(diphenylphosphino)ferrocene (dppf). III. Comparative physicochemical properties of (dppf)MCl2 (M = Co, Ni, Pd, Pt, Zn, Cd, Hg). *Inorganica Chimica Acta* **157,** 259–266. ISSN: 0020-1693. doi:10.1016/S0020-1693(00)80550-2 (1989).

152. Park, T.-J., Huh, S., Kim, Y. & Jun, M.-J. Dichloro[ferrocene-1,1'-diylbis(diphenylphosphine- P)]cobalt(II). *Acta Crystallographica Section C Crystal Structure Communications* **55,** 848–850. ISSN: 0108-2701. doi:10.1107/S0108270199001183 (1999).

153. Meihaus, K. R., Rinehart, J. D. & Long, J. R. Dilution-Induced Slow Magnetic Relaxation and Anomalous Hysteresis in Trigonal Prismatic Dysprosium(III) and Uranium(III) Complexes. *Inorganic Chemistry* **50,** 8484–8489. ISSN: 0020-1669. doi:10.1021/ic201078r (2011).

154. Nemec, I., Herchel, R. & Trávníček, Z. Ferromagnetic coupling mediated by Co π non-covalent contacts in a pentacoordinate Co(II) compound showing field-induced slow relaxation of magnetization. *Dalton Transactions* **45,** 12479–12482. ISSN: 1477-9234. doi:10.1039/c6dt01539e (2016).

155. Salzner, U. Quantitatively Correct UV-vis Spectrum of Ferrocene with TDB3LYP. *Journal of Chemical Theory and Computation* **9,** 4064–4073. ISSN: 1549-9618. doi:10.1021/ct400322v (2013).

156. Rohmer, M.-M., Veillard, A. & Wood, M. H. Excited states and electronic spectrum of ferrocene. *Chemical Physics Letters* **29,** 466–468. ISSN: 0009-2614. doi:10.1016/0009-2614(74)85146-8 (1974).

157. Lomjanský, D., Varga, F., Rajnák, C., Moncoľ, J., Boča, R. & Titiš, J. Redetermination of Zero-Field Splitting in [Co(qu)2Br2] and [Ni(PPh3)2Cl2] Complexes. *Nova Biotechnologica et Chimica* **15,** 200–211. ISSN: 1338-6905. doi:10.1515/nbec-2016-0020 (2016).

158. Figgis, B. N. & Hitchman, M. A. *Ligand Field Theory and Its Applications* 376. ISBN: 978-0471317760 (Wiley-VCH, 1999).

159. Idešicová, M., Titiš, J., Krzystek, J. & Boča, R. Zero-Field Splitting in Pseudotetrahedral Co(II) Complexes: a Magnetic, High-Frequency and -Field EPR, and Computational Study. *Inorganic Chemistry* **52,** 9409–9417. ISSN: 0020-1669. doi:10.1021/ic400980b (2013).

160. Masaryk, L., Moncol, J., Herchel, R. & Nemec, I. Halogen Bonding in New Dichloride-Cobalt(II) Complex with Iodo Substituted Chalcone Ligands. *Crystals* **10,** 354. ISSN: 2073-4352. doi:10.3390/cryst10050354 (2020).

161. Yeh, J. & Lindau, I. Atomic subshell photoionization cross sections and asymmetry parameters: 1 Z 103. *Atomic Data and Nuclear Data Tables* **32,** 1–155. ISSN: 0092-640X. doi:10.1016/0092-640X(85)90016-6 (1985).

162. Fischer, A. B., Wrighton, M. S., Umana, M. & Murray, R. W. An X-ray Photoelectron Spectroscopic Study of Multilayers of an Electroactive Ferrocene Derivative Attached to Platinum and Gold Electrodes. *Journal of the American Chemical Society* **101,** 3442–3446. ISSN: 1520-5126. doi:10.1021/ja00507a003 (1979).

163. Gassman, P. G., Macomber, D. W. & Hershberger, J. W. Evaluation by ESCA of the Electronic Effect of Methyl Substitution on the Cyclopentadlenyl Ligand. A Study of Tltanocenes, Zirconocenes, Hafnocenes, and Ferrocenes. *Organometallics* **2,** 1470–1472. ISSN: 1520-6041. doi:10.1021/om50004a044 (1983).

164. Woodbridge, C. M., Pugmire, D. L., Johnson, R. C., Boag, N. M. & Langell, M. A. HREELS and XPS Studies of Ferrocene on Ag(100). *Journal of Physical Chemistry B* **104,** 3085–3093. ISSN: 1089-5647. doi:10.1021/jp993235+ (2000).

165. Rosencwaig, A., Wertheim, G. K. & Guggenheim, H. J. Origins of satellites on inner-shell photoelectron spectra. *Physical Review Letters* **27,** 479–481. ISSN: 0031-9007. doi:10.1103/PhysRevLett.27.479 (1971).

166. Frost, D. C., McDowell, C. A. & Woolsey, I. S. Evidence for multiplet splitting of 2p photoelectron lines of transition metal complexes. *Chemical Physics Letters* **17,** 320–323. ISSN: 0009-2614. doi:10.1016/0009-2614(72)87086-6 (1972).

167. Frost, D. C., McDowell, C. A. & Woolsey, I. S. X-ray photoelectron spectra of cobalt compounds. *Molecular Physics* **27,** 1473–1489. ISSN: 1362-3028. doi:10.1080/00268977400101251 (1974).

168. Brown, D. G. & Weser, U. XPS Spectra of Spin-Triplet Cobalt(III) Complexes. *Zeitschrift fur Naturforschung - Section B Journal of Chemical Sciences* **34,** 1468–1470. ISSN: 1865-7117. doi:10.1515/znb-1979-1027 (1979).

169. Poneti, G., Mannini, M., Cortigiani, B., Poggini, L., Sorace, L., Otero, E., Sainctavit, P., Sessoli, R. & Dei, A. Magnetic and spectroscopic investigation of thermally and optically driven valence tautomerism in thioether-bridged dinuclear cobalt-dioxolene complexes. *Inorganic Chemistry* **52,** 11798–11805. ISSN: 0020-1669. doi:10.1021/ic4011949 (2013).

170. Chan, H. S., Andy Hor, T. S., Phang, L. T. & Tan, K. L. Substituted metal carbonyls. XVI. X-ray photoelectron spectroscopic differentiation of chemically distinct phosphorus environments in unidentate complexes of 1,1 -bis(diphenylphosphino)ferrocene. *Journal of Organometallic Chemistry* **407,** 353–357. ISSN: 0022-328X. doi:10.1016/0022-328X(91)86313-F (1991).

171. K. Kouba, J., Pierce, J. L. & Walton, R. A. X-ray photoelectron spectra of inorganic molecules XXlX. The characterization of mixed phosphido-phosphine and phosphido-phosphite complexes of transition metal carbonyl clusters using X-ray photoelectron spectroscopy. *Journal of Organometallic Chemistry* **202,** C105–C107. ISSN: 0022-328X. doi:10.1016/S0022-328X(00)81880-X (1980).

172. Barber, M., Connor, J. A., Derrick, L. M., Hall, M. B. & Hillier, I. H. High energy photoelectron spectroscopy of transition metal complexes. Part 2. - Metallocenes. *Journal of the Chemical Society, Faraday Transactions 2: Molecular and Chemical Physics* **69,** 559–562. ISSN: 0300-9238. doi:10.1039/F29736900559 (1973).

173. Karam, A., Tenia, R., Martínez, M., López-Linares, F., Albano, C., Diaz-Barrios, A., Sánchez, Y., Catarí, E., Casas, E., Pekerar, S. & Albornoz, A. Iron(II) and cobalt(II) tris(2-pyridyl)phosphine and tris(2-pyridyl)amine catalysts for the ethylene polymerization. *Journal of Molecular Catalysis A: Chemical* **265,** 127–132. ISSN: 1381-1169. doi:10.1016/j.molcata.2006.09.048 (2007).

174. Karam, A. R., Catarí, E. L., López-Linares, F., Agrifoglio, G., Albano, C. L., Díaz-Barrios, A., Lehmann, T. E., Pekerar, S. V., Albornoz, L. A., Atencio, R., González, T., Ortega, H. B. & Joskowics, P. Synthesis, characterization and olefin polymerization studies of iron(II) and cobalt(II) catalysts bearing 2,6-bis(pyrazol-1-yl)pyridines and 2,6-bis(pyrazol-1-ylmethyl)pyridines ligands. *Applied Catalysis A: General* **280,** 165–173. ISSN: 0926-860X. doi:10.1016/j.apcata.2004.10.047 (2005).

175. Mannini, M. & Poggini, L. in *Encyclopedia of Interfacial Chemistry* 538–546 (Elsevier, 2018). ISBN: 978-0128098943. doi:10.1016/B978-0-12-409547-2.13184-1.

176. Caneschi, A., Gatteschi, D., Sessoli, R., Barra, A. L., Brunei, L. C. & Guillot, M. Alternating Current Susceptibility, High Field Magnetization, and Millimeter Band EPR Evidence for a Ground S=10 State in [Mn12O12(CH3COO)16(H2O)4].2CH3COOH.4H2O. *Journal of the American Chemical Society* **113,** 5873–5874. ISSN: 1520-5126. doi:10.1021/ja00015a057 (1991).

177. Sessoli, R., Gatteschi, D., Tsai, H. L., Hendrickson, D. N., Schake, A. R., Wang, S., Vincent, J. B., Christou, G. & Folting, K. High-Spin Molecules: [Mn12O12(O2CR)16(H2O)4]. *Journal of the American Chemical Society* **115,** 1804–1816. ISSN: 1520-5126. doi:10.1021/ja00058a027 (1993).

178. Hrubý, J., Dvořák, D., Squillantini, L., Mannini, M., Van Slageren, J., Herchel, R., Nemec, I. & Neugebauer, P. Co(ii)-Based single-ion magnets with 1,1 -ferrocenediyl-bis(diphenylphosphine) metalloligands. *Dalton Transactions* **49,** 11697–11707. ISSN: 1477-9234. doi:10.1039/d0dt01512a (2020).

179. Saywell, A., Magnano, G., Satterley, C. J., Perdigão, L. M., Britton, A. J., Taleb, N., Del Carmen Giménez-López, M., Champness, N. R., O'Shea, J. N. & Beton, P. H. Self-assembled aggregates formed by single-molecule magnets on a gold surface. *Nature Communications* **1,** 1–8. ISSN: 2041-1723. doi:10.1038/ncomms1075 (2010).

180. Rozbořil, J., Rechkemmer, Y., Bloos, D., Münz, F., Wang, C. N., Neugebauer, P., Čechal, J., Novák, J. & Van Slageren, J. Magneto-optical investigations of molecular nanomagnet monolayers. *Dalton Transactions* **45,** 7555–7558. ISSN: 1477-9234. doi:10.1039/c6dt00839a (2016).

181. Lanzilotto, V., Malavolti, L., Ninova, S., Cimatti, I., Poggini, L., Cortigiani, B., Mannini, M., Totti, F., Cornia, A. & Sessoli, R. The Challenge of Thermal Deposition of Coordination Compounds: Insight into the Case of an Fe4 Single Molecule Magnet. *Chemistry of Materials* **28,** 7693–7702. ISSN: 1520-5002. doi:`10.1021/acs.chemmater.6b02696` (2016).

182. Canon-Mancisidor, W., Miralles, S. G., Baldoví, J. J., Espallargas, G. M., Gaita-Arinio, A. & Coronado, E. Sublimable Single Ion Magnets Based on Lanthanoid Quinolinate Complexes: The Role of Intermolecular Interactions on Their Thermal Stability. *Inorganic Chemistry* **57,** 14170–14177. ISSN: 1520-510X. doi:`10.1021/acs.inorgchem.8b02080` (2018).

183. Miralles, S. G., Bedoya-Pinto, A., Baldoví, J. J., Cañon-Mancisidor, W., Prado, Y., Prima-Garcia, H., Gaita-Ariño, A., Mínguez Espallargas, G., Hueso, L. E. & Coronado, E. Sublimable chloroquinolinate lanthanoid single-ion magnets deposited on ferromagnetic electrodes. *Chemical Science* **9,** 199–208. ISSN: 2041-6539. doi:`10.1039/c7sc03463f` (2017).

184. Margheriti, L., Matteo Mannini, Lorenzo Sorace, Lapo Gorini, Gatteschi, D., Caneschi, A., Chiappe, D., Moroni, R., De Mongeot, F. B., Cornia, A., Piras, F. M., Magnani, A. & Sessoli, R. Thermal deposition of intact tetrairon(III) single-molecule magnets in high-vacuum conditions. *Small* **5,** 1460–1466. ISSN: 1613-6810. doi:`10.1002/smll.200801594` (2009).

185. Geim, A. K. & Novoselov, K. S. The rise of graphene. *Nature Materials* **6,** 183–191. ISSN: 1476-1122. doi:`10.1038/nmat1849` (2007).

186. Bae, S., Kim, H., Lee, Y., Xu, X., Park, J. S., Zheng, Y., Balakrishnan, J., Lei, T., Ri Kim, H., Song, Y. I., Kim, Y. J., Kim, K. S., Özyilmaz, B., Ahn, J. H., Hong, B. H. & Iijima, S. Roll-to-roll production of 30-inch graphene films for transparent electrodes. *Nature Nanotechnology* **5,** 574–578. ISSN: 1748-3387. doi:`10.1038/nnano.2010.132` (2010).

187. Atanasov, M., Aravena, D., Suturina, E., Bill, E., Maganas, D. & Neese, F. First principles approach to the electronic structure, magnetic anisotropy and spin relaxation in mononuclear 3d-transition metal single molecule magnets. *Coordination Chemistry Reviews* **289-290,** 177–214. ISSN: 0010-8545. doi:`10.1016/j.ccr.2014.10.015` (2015).

188. Akula, S., Parthiban, V., Peera, S. G., Singh, B. P., Dhakate, S. R. & Sahu, A. K. Simultaneous Co-Doping of Nitrogen and Fluorine into MWCNTs: An In-Situ Conversion to Graphene Like Sheets and Its Electro-Catalytic Activity toward Oxygen Reduction Reaction. *Journal of The Electrochemical Society* **164,** F568–F576. ISSN: 0013-4651. doi:`10.1149/2.0501706jes` (2017).

189. Fiedler, R. & Herzschuh, R. An XPS investigation of the effects of heat treatment on the chlorine surface chemistry of some lignites. *Fuel* **72,** 1501–1505. ISSN: 0016-2361. doi:`10.1016/0016-2361(93)90007-O` (1993).

190. Langley, S. P. The Bolometer and Radiant Energy. *Proceedings of the American Academy of Arts and Sciences* **16,** 342. ISSN: 0199-9818. doi:`10.2307/25138616` (1880).

191. Richards, P. L. & McCreight, C. R. Infrared Detectors for Astrophysics. *Physics Today* **58,** 41–47. ISSN: 0031-9228. doi:`10.1063/1.1897522` (2005).

192. Richards, P. L. Bolometers for infrared and millimeter waves. *Journal of Applied Physics* **76,** 1–24. ISSN: 0021-8979. doi:`10.1063/1.357128` (1994).

193. Fong, K. C., Wollman, E. E., Ravi, H., Chen, W., Clerk, A. A., Shaw, M. D., Leduc, H. G. & Schwab, K. C. Measurement of the Electronic Thermal Conductance Channels and Heat Capacity of Graphene at Low Temperature. *Physical Review X* **3,** 041008. ISSN: 2160-3308. doi:`10.1103/PhysRevX.3.041008` (2013).

194. Wellstood, F. C., Urbina, C. & Clarke, J. Hot-electron effects in metals. *Physical Review B* **49,** 5942–5955. ISSN: 0163-1829. doi:`10.1103/PhysRevB.49.5942` (1994).

195. Castro Neto, A. H., Guinea, F., Peres, N. M., Novoselov, K. S. & Geim, A. K. The electronic properties of graphene. *Reviews of Modern Physics* **81,** 109–162. ISSN: 0034-6861. doi:10.1103/RevModPhys.81.109 (2009).

196. Chen, J. H., Jang, C., Xiao, S., Ishigami, M. & Fuhrer, M. S. Intrinsic and extrinsic performance limits of graphene devices on SiO 2. *Nature Nanotechnology* **3,** 206–209. ISSN: 1748-3395. doi:10.1038/nnano.2008.58 (2008).

197. Tan, Y. W., Zhang, Y., Stormer, H. L. & Kim, P. Temperature dependent electron transport in graphene. *European Physical Journal: Special Topics* **148,** 15–18. ISSN: 1951-6355. doi:10.1140/epjst/e2007-00221-9 (2007).

198. Morozov, S. V., Novoselov, K. S., Katsnelson, M. I., Schedin, F., Elias, D. C., Jaszczak, J. A. & Geim, A. K. Giant intrinsic carrier mobilities in graphene and its bilayer. *Physical Review Letters* **100,** 016602. ISSN: 0031-9007. doi:10.1103/PhysRevLett.100.016602 (2008).

199. Yan, J., Kim, M. H., Elle, J. A., Sushkov, A. B., Jenkins, G. S., Milchberg, H. M., Fuhrer, M. S. & Drew, H. D. Dual-gated bilayer graphene hot-electron bolometer. *Nature Nanotechnology* **7,** 472–478. ISSN: 1748-3395. doi:10.1038/nnano.2012.88 (2012).

200. Han, Q., Gao, T., Zhang, R., Chen, Y., Chen, J., Liu, G., Zhang, Y., Liu, Z., Wu, X. & Yu, D. Highly sensitive hot electron bolometer based on disordered graphene. *Scientific Reports* **3,** 3533. ISSN: 2045-2322. doi:10.1038/srep03533 (2013).

201. El Fatimy, A., Myers-Ward, R. L., Boyd, A. K., Daniels, K. M., Gaskill, D. K. & Barbara, P. Epitaxial graphene quantum dots for high-performance terahertz bolometers. *Nature Nanotechnology* **11,** 335–338. ISSN: 1748-3395. doi:10.1038/nnano.2015.303 (2016).

202. El Fatimy, A., Nath, A., Kong, B. D., Boyd, A. K., Myers-Ward, R. L., Daniels, K. M., Jadidi, M. M., Murphy, T. E., Gaskill, D. K. & Barbara, P. Ultra-broadband photodetectors based on epitaxial graphene quantum dots. *Nanophotonics* **7,** 735–740. ISSN: 2192-8614. doi:10.1515/nanoph-2017-0100 (2018).

203. Goto, M., Yamada, Y., Shimura, A., Suzuki, T., Degawa, N., Yamane, T., Aoki, S., Urabe, J., Hara, S., Nomura, H. & Suzuki, Y. Uncooled sub-GHz spin bolometer driven by auto-oscillation. *Nature Communications* **12,** 536. ISSN: 2041-1723. doi:10.1038/s41467-020-20631-0 (2021).

204. Lee, G.-H., Efetov, D. K., Jung, W., Ranzani, L., Walsh, E. D., Ohki, T. A., Taniguchi, T., Watanabe, K., Kim, P., Englund, D. & Fong, K. C. Graphene-based Josephson junction microwave bolometer. *Nature* **586,** 42–46. ISSN: 0028-0836. doi:10.1038/s41586-020-2752-4 (2020).

205. Kokkoniemi, R., Girard, J.-P., Hazra, D., Laitinen, A., Govenius, J., Lake, R. E., Sallinen, I., Vesterinen, V., Partanen, M., Tan, J. Y., Chan, K. W., Tan, K. Y., Hakonen, P. & Möttönen, M. Bolometer operating at the threshold for circuit quantum electrodynamics. *Nature* **586,** 47–51. ISSN: 0028-0836. doi:10.1038/s41586-020-2753-3 (2020).

206. Accorsi, S., Barra, A.-L., Caneschi, A., Chastanet, G., Cornia, A., Fabretti, A. C., Gatteschi, D., Mortalò, C., Olivieri, E., Parenti, F., Rosa, P., Sessoli, R., Sorace, L., Wernsdorfer, W. & Zobbi, L. Tuning Anisotropy Barriers in a Family of Tetrairon(III) Single-Molecule Magnets with an S = 5 Ground State. *Journal of the American Chemical Society* **128,** 4742–4755. ISSN: 0002-7863. doi:10.1021/ja0576381 (2006).

207. Gregoli, L., Danieli, C., Barra, A.-L., Neugebauer, P., Pellegrino, G., Poneti, G., Sessoli, R. & Cornia, A. Magnetostructural Correlations in Tetrairon(III) Single-Molecule Magnets. *Chemistry - A European Journal* **15,** 6456–6467. ISSN: 0947-6539. doi:10.1002/chem.200900483 (2009).

8. Author publications and outputs

Publications

1. **J. Hrubý**, Š. Vavrečková, L. Masaryk, A. Sojka, J. Navarro-Giraldo, M. Bartoš, R. Herchel, J. Moncol, I. Nemec and P. Neugebauer: Deposition of Tetracoordinate Co(II) Complex with Chalcone Ligands on Graphene, *Molecules*, **25**, 5021 (2020).
2. **J. Hrubý**, D. Dvořák, L. Squillantini, M. Mannini, J. van Slageren, R. Herchel, I. Nemec, and P. Neugebauer: Co(II)-Based single-ion magnets with 1,1 -ferrocenediyl-bis(diphenylphosphine) metalloligands, *Dalton Trans.*, **49**, 11697-11707 (2020).
3. L. A. Gonzaga, V. T. Santana, M. I. B. Bernardi, **J. Hrubý**, P. Neugebauer and A. Mesquita: CeO_2 and CeO_2:Pr nanocrystalline powders prepared by the polymeric precursor method: Yellow and red pigments with tunable color, *J. Am. Ceram. Soc.*, **103**, 6280–6288 (2020).
4. L. St. Marie, A. E. Fatimy, **J. Hrubý**, I. Nemec, J. Hunt, R. Myers-Ward, D. K. Gaskill, M. Kruskopf, Y. Yang, R. Elmquist, R. Marx, J. van Slageren, P. Neugebauer and P. Barbara: Nanostructured graphene for nanoscale electron paramagnetic resonance spectroscopy, *J. Phys. Mater.*, **3**, 014013 (2020).
5. **J. Hrubý**, V. T. Santana, D. Kostiuk, M. Bouček, S. Lenz, M. Kern, P. Šiffalovič, J. van Slageren and P. Neugebauer: A graphene-based hybrid material with quantum bits prepared by the double Langmuir–Schaefer method, *RSC Adv.*, **9**, 24066-24073 (2019).
6. S. Realista, A. J. Fitzpatrick, G. Santos, L. Ferreira, S. Barroso, L. Pereira, N. Bandeira, P. Neugebauer, **J. Hrubý**, G. G. Morgan, J. van Slageren, M. J. Calhorda and P. Martinho: A Mn(III) single ion magnet with tridentate Schiff-base ligands, *Dalton Trans.*, **45**, 12301-12307 (2016).

Conferences

1. 09/2021 – 42nd FGMR Annual Discussion Meeting (online) – Oral contribution
2. 09/2021 – CEITEC PhD 2021 (online) – Flash talk contribution
3. 04/2021 – 54th Annual ESR Spectroscopy Group of the Royal Society of Chemistry (online) – Poster contribution
4. 03/2021 – 2nd International Workshop on Plasmon Enhanced Terahertz Electron Paramagnetic Resonance (online)
5. 11/2019 – 8th EFEPR School (Brno, Czech Republic) – Organisation and Poster contribution
6. 09/2019 – XIth EFEPR Conference (Bratislava, Slovakia) – Poster contribution

7. 06/2019 – CEITEC Joint Retreat 2019 (Kouty, Czech Republic) – Poster contribution
8. 04/2019 – 52nd Annual ESR Spectroscopy Group of the Royal Society of Chemistry (Glasgow, Scotland) – Poster contribution
9. 10/2018 – PETER Summer School (Brno, Czech Republic) – Poster contribution
10. 09/2018 – V School for young scientists on Magnetic Resonance (Roshschino, Saint Petersburg, Russia) – Poster and Oral contribution
11. 07/2018 – International Conference on Nanoscience + Technology (ICN+T) (Brno, Czech Republic) – Poster contribution
12. 04/2018 – CEITEC PhD & Postdoc Retreat (Telč, Czech Republic) – Oral contribution
13. 06/2017 – IUVSTA International Summer School on Physics at Nanoscale (Devět Skal, Czech Republic) – Poster contribution
14. 05/2017 – 10th ESMolNa and 5th Workshop on 2D Materials (El Escorial, Madrid, Spain) – Oral contribution

Supervision

- Bc. Šárka Vavrečková – graduated in 2020, thesis topic: Deposition of molecular magnets on ”2D” materials
- Bc. Martin Bouček – graduated in 2019, thesis topic: Study of behaviour of paramagnetic molecules on surfaces
- Mr. Filip Janko – CEITEC student talent programme, project topic: Development of online framework for data processing

Meeting abstracts

- 03/2021 – L. St. Marie, L. Havlíček, **J. Hrubý**, D. Henry, A. Sojka, J. Navarro, R. Myers-Ward, A. El Fatimy, A. Liu, D. K. Gaskill, I. Nemec, P. Neugebauer and P. Barbara: Spectroscopy of Mn_{12} with modified ligands on graphene bolometers – Bulletin of the American Physical Society
- 03/2020 – L. St. Marie, A. El Fatimy, **J. Hrubý**, I. Nemec, J. Hunt, R. Myers-Ward, D. K. Gaskill, M. Kruskopf, Y. Yang, R. Elmquist, R. Marx, J. van Slageren, P. Neugebauer and Paola Barbara: Graphene quantum dot bolometers for high frequency EPR of single molecule magnets – Bulletin of the American Physical Society
- 03/2019 – L. St. Marie, **J. Hrubý**, J. Hunt, P. Neugebauer, I. Nemec, A. El Fatimy, R. Myers-Ward, D. K. Gaskill, M. Kruskopf, Y. Yang, R. Elmquist and P. Barbara: Deposition of single-molecule magnets on graphene quantum dots – APS March Meeting Abstracts
- 03/2018 – A. El Fatimy, P. Neugebauer, L. St. Marie, **J. Hrubý**, B. Don Kong, A. Boyd, R. Myers-Ward, I. Nemec, K. Daniels, A. Nath, D. Bloos, J. van Slageren, D. K. Gaskill and Paola Barbara: Spectroscopy of single-molecule magnets using graphene quantum dots – APS March Meeting Abstracts

List of abbreviations

HF-ESR	High-frequency electron spin resonance
UHV	Ultra-high vacuum
HV	High vacuum
ESR	Electron spin resonance
EPR	Electron paramagnetic resonance
SMM	Single-molecule magnet
Qubits	Quantum bits
TMDC	Transition metal dichalcogenide
XPS	X-ray photoelectron spectroscopy
AFM	Atomic force microscopy
RS	Raman spectroscopy
SEM	Scanning electron microscopy
OM	Optical microscopy
SI	International system of units
SH	Spin Hamiltonian
ZFS	Zero-field splitting
AC	Alternating current
DC	Direct current
SSD	Solid-state drive
SIM	Single-ion magnet
LFT	Ligand-field theory
DFT	Density functional theory
XMCD	X-ray magnetic circular dichroism
CEITEC	Central European Institute of Technology
BUT	Brno University of Technology
LB	Langmuir-Blodgett

LIST OF ABBREVIATIONS

LS	Langmuir-Schaefer
QCM	Quartz crystal microbalance
TIG	Tungsten inert gas
CF	Conflat
VTI	Variable temperature insert
ESCA	Electron spectroscopy for chemical analysis
BE	Binding energy
CCD	Charge-coupled device
TO	Transverse optical phonons
TA	Transverse acoustic phonons
LO	Longitudinal optical phonons
LA	Longitudinal acoustic phonons
CPEM	Correlative probe and electron microscopy
FLG	Few-layer graphene
CVD	Chemical vapour deposition
TEM	Transmission electron microscopy
CASSCF	Complete active space self-consistent field
NEVPT2	N-electron valence state perturbation theory
UV-VIS	Ultraviolet-visible spectroscopy
NIR	Near infrared region
SOC	Spin-orbit coupling
FWHM	Full width at half maximum
NMR	Nuclear magnetic resonance
COM	Communication port
VISA	Virtual instrument software architecture
A/D	Analog/digital
I/V	Current/voltage
GQD	Graphene quantum dot
NEP	Noise equivalent power
PCB	Printed circuit board

Appendices

Appendix A: Remote DC power supply

The scheme of remote DC power supply control as LabVIEW file is shown in following Figures (8.1 and 8.2).

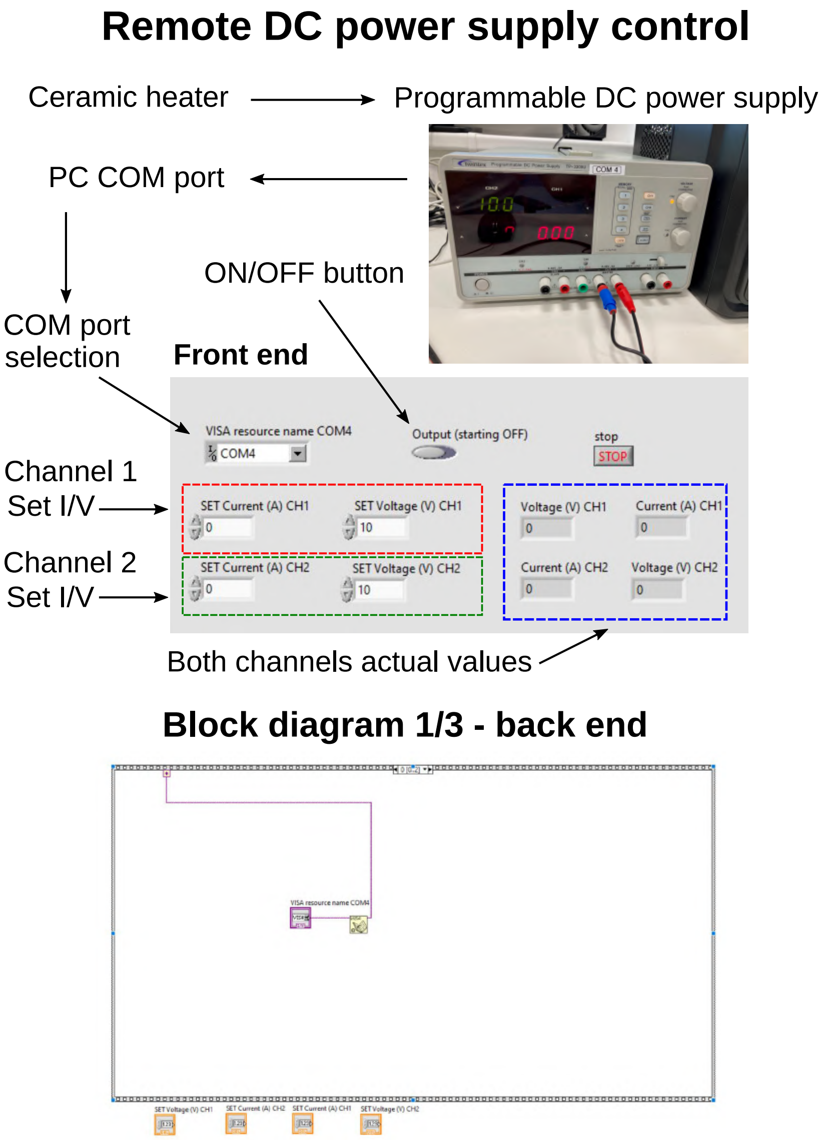

VISA resource name COM4: COM4
Output (starting OFF)
stop
SET Current (A) CH1: 0
SET Voltage (V) CH1: 10
SET Current (A) CH2: 0
SET Voltage (V) CH2: 10
Voltage (V) CH1: 0
Current (A) CH1: 0
Current (A) CH2: 0
Voltage (V) CH2: 0

VISA resource name COM4
SET Voltage (V) CH1
SET Current (A) CH2
SET Current (A) CH1
SET Voltage (V) CH2

Figure 8.1: Scheme of remote DC power supply control. The ceramic heater which heats a crucible with molecules is connected to programmable DC power supply which is fed into PC COM port. The front end allows to switch the supply ON/OFF and adjust current/voltage on both channels. Usually only one channel is necessary to heat the crucible in this configuration. The right section of front end monitors actual values from the power supply.

Block diagram 2/3 - back end

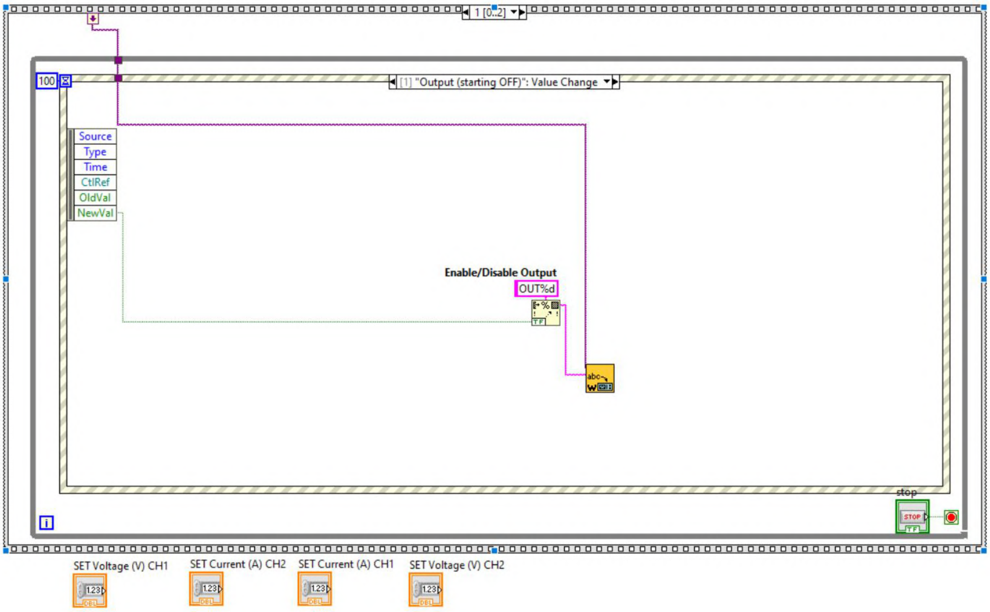

Block diagram 3/3 - back end

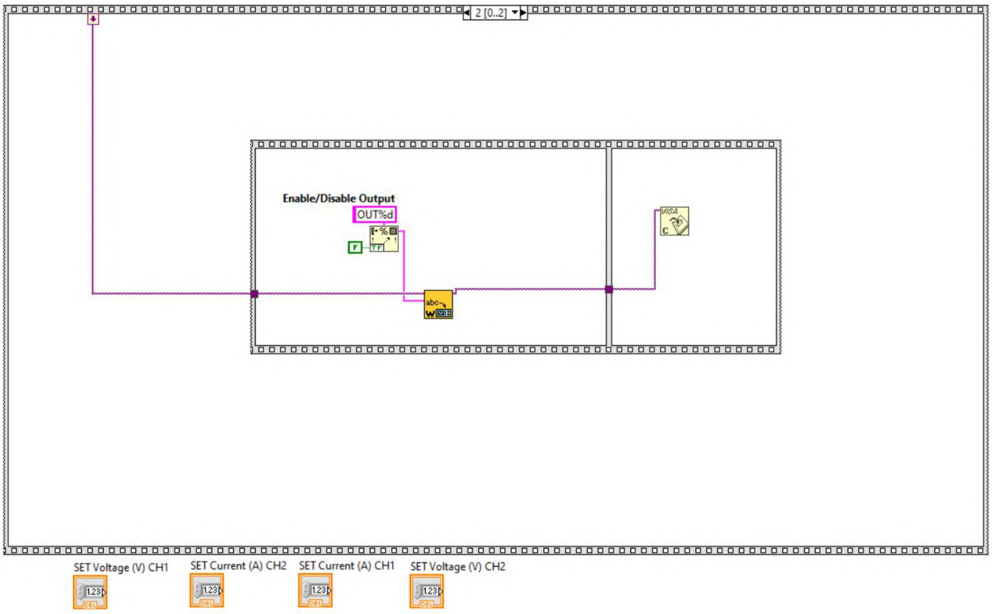

Figure 8.2: Scheme of block diagrams in back end of the remote DC power supply control.

Appendix B: Remote pressure readout

The scheme of remote pressure readout as LabVIEW file for monitoring pressure during sublimations is illustrated in Figure (8.3).

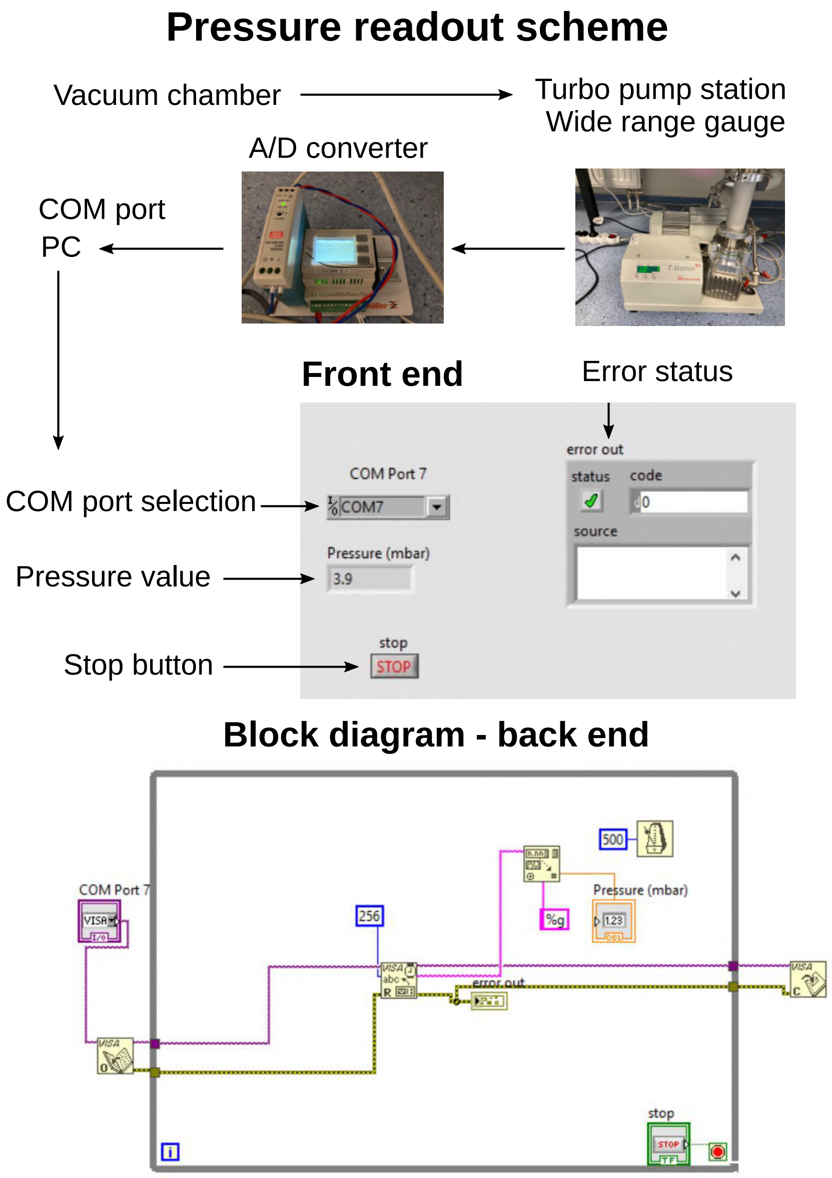

Figure 8.3: Scheme of remote pressure readout for the sublimation chamber. The chamber is connected to turbo pump station with wide range gauge linked via ethernet cable to A/D converter and fed to the PC COM port.